The Henryk Niewodniczański
INSTITUTE OF NUCLEAR PHYSICS
Polish Academy of Sciences
ul. Radzikowskiego 152, 31-342 Kraków, Poland
www.ifj.edu.pl/publ/reports/2010

Report No. 2042/PH

Charged particle multiplicity fluctuations and correlations in heavy-ion collisions in the PHOBOS experiment at RHIC

Krzysztof Woźniak

Habilitation Thesis - Rozprawa Habilitacyjna

Kraków, September 2010

Abstract

The Relativistic Heavy Ion Collider is the first accelerator in which beams of heavy ions collide at an unprecedented energy of $\sqrt{s_{NN}} = 200$ GeV. Collisions of Au nuclei result in creation of a system with extremely high energy density in which a new phase of matter, the strongly interacting Quark-Gluon Plasma, is formed. It manifests itself in suppression of partons with very high transverse momenta and large elliptic flow. A general overview of experimental signals of QGP creation is presented with an emphasis on results from fluctuation and correlation studies.

In a system crossing a phase transition or passing near a critical point enhanced fluctuations that can be visible also in various correlation studies may appear. This work describes in detail the analyzes of multiplicity fluctuations and correlations performed by the PHOBOS Collaboration. They include a search for events with unusually high multiplicities or very large fluctuations of the angular particle density distribution. The results of correlation studies can be explained by production of particles in clusters, which are large and very wide in pseudorapidity. In the analysis of reconstruction of cluster parameters and in calculations of acceptance effects Simple Cluster Model is applied.

The centrality dependence of correlations suggests that they can not be described as decays of heavy resonances only, thus the Wounded Nucleon Model is used to explain these correlations. It is shown that in this model the correlations are partly due to fluctuations of the number of wounded nucleons and that the Wounded Nucleon Model predicts them better than other models.

The more technical aspects of the heavy-ion collisions studies are also described. There is some information on the RHIC accelerator complex and the experiments measuring $Au + Au$ collisions, with a detailed discussion of the PHOBOS detector. In addition to results on multiplicity and charged particle pseudorapidity distributions, the multiplicity reconstruction methods are presented. Several methods of the vertex reconstruction applied in the PHOBOS experiment are discussed, including a novel algorithm based on hits in a single layer of silicon sensors. The system of PHOBOS Monte Carlo simulations and a report on its outcome are presented.

Streszczenie

Zderzacz Relatywistycznych Ciężkich Jonów (RHIC - Relativistic Heavy Ion Collider) jest pierwszym akceleratorem, w którym doprowadzono do zderzeń przeciwbieżnych wiązek ciężkich jąder atomowych o energii nigdy wcześniej w laboratorium nieosiągalnej ($\sqrt{s_{NN}}$ = 200 GeV). W wyniku zderzeń jąder zlota uzyskana zostala bardzo wysoka gęstość energii, dzięki czemu wytworzona zostala nowa faza materii, Plazma Kwarkowo-Gluonowa. O jej powstaniu świadczy przede wszystkim tlumienie produkcji partonów o dużych pędach poprzecznych oraz obecność silnego przeplywu eliptycznego. W pracy zostaly pokrótce przedstawione także inne wyniki eksperymentalne otrzymane w badaniach zderzeń jądro-jądro, a najwięcej uwagi zostalo poświęcone badaniom fluktuacji i korelacji.

Silne fluktuacje różnych parametrów ukladu termodynamicznego pojawiają się często przy przejściu fazowym albo gdy jego ewolucja przebiega w pobliżu punktu krytycznego. Szansę na wykrycie ich obecności daje analiza różnego rodzaju korelacji. W tej pracy szczegółowo opisane zostaly badania fluktuacji i korelacji krotności cząstek naladowanych dokonane w ramach eksperymentu PHOBOS. Poszukiwane byly przypadki o nadzwyczaj wysokiej krotności wyprodukowanych cząstek lub bardzo silnych fluktuacjach ich rozkladu kątowego. Analizowane byly korelacje dwucząstkowe, korelacje między symetrycznymi obszarami kinematycznymi oraz korelacje z cząstką o wysokim pędzie poprzecznym.

Źródlem korelacji międzycząstkowych może być produkcja cząstek w klastrach. Prosty model klastrów (Simple Cluster Model) zastosowano do analizy wyników eksperymentalnych oraz wyznaczenia wplywu akceptacji detektora na parametry klastrów uzyskiwane doświadczalnie.

Zaobserwowane w eksperymencie PHOBOS korelacje są zależne od centralności zderzenia jąder i odpowiadają klastrom o dużych krotnościach i szerokościach, które nie mogą być wyjaśnione wylącznie poprzez rozpady rezonansów. Jakościowe wyjaśnienie zależności od centralności dostarcza Model Zranionych Nukleonów (Wounded Nucleon Model), który zaklada znaczący wplyw fluktuacji liczby zranionych nukleonów na parametry klastrów otrzymywane z analizy korelacje krotności oraz korelacji dwucząstkowych. Przewidywania tego modelu są zgodne z wynikami doświadczalnymi lepiej niż przewidywania z innych modeli zderzeń jądro-jądro.

Praca zawiera także opis bardziej technicznych aspektów badania zderzeń ciężkich jonów zwlaszcza dotyczących eksperymentu PHOBOS. Podane zostaly podstawowe informacje o akceleratorze RHIC i dzialających przy nim eksperymentach. Bardziej szczegółowo omówiony jest detektor eksperymentu PHOBOS. Przedstawione zostaly metody rekonstrukcji krotności cząstek naladowanych na potrzeby odtworzenia ich rozkladu kątowego i analizy korelacji. W opisie algorytmów rekonstrukcji pierwotnego wierzcholka oddzialywania szczególną uwagę należy zwrócić na metodę wyznaczania wierzcholka na podstawie informacji z pojedynczej warstwy detektorów krzemowych. Przedstawiony zostal także system symulacji Monte Carlo w eksperymencie PHOBOS i rezultaty jego dzialania.

Contents

1 Introduction

Since the middle of the 20th century, progress in understanding the physics of processes occurring at high energies has been connected with accelerators. They provide beams of particles with energies otherwise available only from cosmic rays at very low rates. Almost every increase in the energy reached by a new accelerator has led to important discoveries for which Nobel prizes were awarded.

The highest collision energies were always achieved for elementary particles, protons and antiprotons or electrons and positrons. The majority of elementary particles were discovered in accelerator experiments; to name just a few: the antiproton and plenty of resonances (in the Bevatron at Lavrence Berkeley National Laboratory), particles containing charm (in SPEAR at the SLAC National Accelerator Laboratory and in AGS at the Brookhaven National Laboratory), the W and Z bosons (in SPS at CERN), and the top quark (in the Tevatron at the Fermi National Accelerator Laboratory). Equally important were detailed studies and tests of theories describing elementary forces, at first of the theory of electroweak interactions and later of the Standard Model, which unifies also strong interactions (in the Tevatron at FNAL, in LEP at CERN and in HERA at DESY).

The interactions involving more complicated objects, nuclei, were at first available only from cosmic rays, but in fixed-target experiments at accelerators soon after interactions of elementary particles also hadron-nucleus collisions were studied. It was discovered that the particles created in a collision inside the nucleus do not produce intranuclear cascades, and to explain this observation the concept of delayed creation of secondary particles (formation time) was introduced.

Later it was appreciated that a hadron accelerator can usually also be used to accelerate heavier particles – multiply-charged ions – even if it is technically more complicated and reaching an equally high energy of collisions is not possible. Studies of collisions of nuclei at high energies sparked widespread interest once it was realized from theoretical considerations that in heavy-ion collisions a new phase of matter can be created. It was estimated that the energy density is sufficiently large to create enough quark-antiquark pairs and gluons that the hadronic matter could be transformed into a Quark-Gluon Plasma (QGP). The predicted most probable signatures of QGP creation included an enhanced production of strangeness, a suppression of J/ψ particle production, smaller net-charge fluctuations, and unusual properties of events indicating phenomena connected with a phase transition. The collisions of nuclei were first studied in fixed target experiments at AGS at BNL and at the Super Proton Synchrotron at CERN. The search for QGP was performed for collisions of different types of nuclei, up to $Pb + Pb$, at energies per a nucleon-nucleon pair, $\sqrt{s_{NN}}$, up to 19 GeV. Although some effects resembling predicted signals were found, alternative theoretical explanations of observed phenomena started to appear. A few years later a much higher collision energy ($\sqrt{s_{NN}} = 200$ GeV) was reached in the Relativistic Heavy Ion Collider at the Brookhaven National Laboratory (see Appendix A). Contrary to initial expectations the signals observed at lower energies did not become more significant, but different and unexpected phenomena were found. The suppression of high-p_T particles and strong elliptic flow were found, which signal creation of a dense and strongly interacting matter.

The theoretical studies, which started from predictions of a first order phase transition, led to the conclusion that most probably such a transition is present at high net baryon densities for low or moderate temperatures and ends with a critical point. In the case of heavy-ion collisions at high energies only a second order phase transition or a smooth crossover is thus

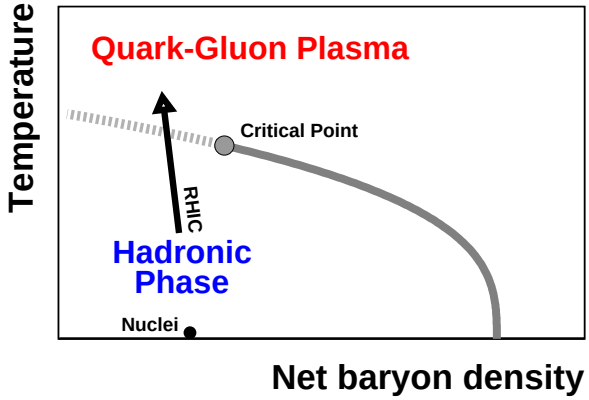

Fig. 1.1: The schematic phase diagram of the transition between Quark-Gluon Plasma and hadronic matter. The continuous line represents the first order phase transition, the dashed line denotes the crossover region and the arrow indicates the change in the system created in heavy ion collisions at RHIC.

expected, as shown in Fig. 1.1.

One of the signals of a phase transition or a critical point may be a change of medium properties, which can be then detected as a discontinuity or a change (usually an increase) of fluctuations of some observables. This work reports the experimental studies of multiplicity fluctuations and correlations performed using measurements from the PHOBOS experiment at RHIC. They are based on measurements that do not identify particle species, but extend to kinematical regions not accessible to other experiments that have less than one-third of our acceptance.

This work is divided into several sections devoted to presentation of experimental results and their discussion, while more technical aspects, such as a description of analysis methods, may be found in the Appendices.

A review of the most important results providing evidence for creation of a QGP is presented in Section 2. It contains also a discussion of the signals for which theoretical predictions were not confirmed or an unambiguous interpretation has not been reached. Some predictions for fluctuations and description of methods proposed to detect them are included, but the review of results on fluctuations is deferred to the following sections. Section 3 presents the PHOBOS experiment, starting from the description of the PHOBOS detector followed by a discussion of the most interesting results. Studies of multiplicity fluctuations and correlations performed by the PHOBOS experiment and similar analyses carried out by other experiments at RHIC are presented in Section 4. They are then discussed in the context of a simple cluster model in Section 5, but an additional analysis of kinematical properties of clusters are deferred to Appendix F. The predictions from the Wounded Nucleon Model on fluctuations and correlations are shown in Section 6. In order to complete the presentation of fluctuation studies results obtained for observables other than multiplicity, such as elliptic flow in the PHOBOS experiment and transverse momentum, electric charge and particle ratios measured in other experiments are briefly described in Section 7. All sections conclude with a short summary of their content, and a final résumé of the search for signals of QGP is presented in Section 8.

For the reader looking for more details or unfamiliar with the physics of heavy ion collisions at RHIC, the first two Appendices provide especially useful additional information. The description of the RHIC complex and a short summary of the properties of the detectors in the experiments at RHIC are included in Appendix A. The parameters describing collisions of nuclei and methods used to determine collision centrality are broadly discussed in Appendix B. Other Appendices are devoted to more technical aspects of the PHOBOS experiment. The methods of multiplicity reconstruction are discussed in Appendix D. Several algorithms of

vertex reconstruction and their performance are presented in Appendix C. There is also additional information on the Monte Carlo simulations performed for the PHOBOS experiment in Appendix E.

The author of this work has been an active member of the PHOBOS Collaboration since its inception, starting from the preparation of the Letter of Intent, the Proposal, and the PHOBOS Detector Conceptual Design Report. Since then his main responsibility has been Monte Carlo simulations: writing of the PHOBOS specific simulation code, creation of an automatized system of job processing and the direct supervision of simulations of nearly 250,000,000 events (described in Appendix E). He took part in the studies which led to optimization of the PHOBOS detector and later developed the vertex reconstruction algorithms using the Vertex detector and the single layer Multiplicity detector (Appendix C). In the analysis of the data he was involved in the studies of multiplicity fluctuations and correlations described in Section 4 and especially their interpretation based on the Simple Cluster Model (Section 5 and Appendix F) and Wounded Nucleon Model (Section 6).

As a result of 6 years of operation of the PHOBOS experiment and several more years of analysis of the data, 39 papers [1]-[39] have been published and many contributions to conferences have been presented. The author of this work has presented PHOBOS experiment capabilities and early results [40, 41], performance of the vertex reconstruction algorithms [42] and results of the studies of correlations and fluctuations [43, 44, 45, 46, 47].

2 Physics of ultra-relativistic heavy-ion collisions

After decades of studies of interactions of elementary particles and concurrent developments in theory the basic processes occurring in them are well known and understood. The Standard Model provides formulas describing three fundamental types of interactions: electromagnetic, weak, and strong. While calculations in the electro-weak part can be performed with high precision, reliable and accurate results for processes involving strong interactions, described by Quantum Chromodynamics (QCD), are much more difficult to obtain. In Quantum Electrodynamics higher order corrections, multiplied by powers of $\alpha \approx 1/137$, decrease rapidly, but the coupling constant in QCD is much closer to 1 and higher order terms are much more important. As it is impossible to include all of them, approximate calculations for strong processes are less precise.

Strong interactions between the constituents of nucleons, quarks and gluons, dominate in the collisions of nuclei at high energies. This makes the theoretical description of collisions of nuclei more ambiguous. Nevertheless, numerical lattice QCD calculations provide interesting predictions for a system characterized by its energy density, that can be created in heavy ion collisions. Assuming that colliding nucleons are to a large extent stopped and a thermalization of quarks and gluons occurs, a new type of matter should be created, in which the basic components are not hadrons, but quarks and gluons [48, 49]. Quantum Chromodynamics thus predicts the creation of a new type of matter, called the Quark-Gluon Plasma (QGP). Much less clear is the energy of colliding nuclei at which this may occur, and especially the properties of the QGP. Experimental studies of heavy ion collisions are thus necessary to learn more about properties of the matter at extremely high energy density. The results may be used to verify theoretical models and calculations. Such studies may also shed light on the evolution of the Universe after the Big Bang, during which similar conditions existed at a much larger scale.

Theoretical calculations (lattice QCD) provide predictions on the temperature and energy density of a system at which hadronic matter should undergo a transition to the quark-gluon phase. Usually the critical temperature is estimated as $T_c \sim 155 - 185$ MeV, which corresponds to an energy density of the order of 1 GeV/fm^3 [50, 51].

Determination of the conditions created in an experiment is more difficult and ambiguous. The PHOBOS Collaboration estimates them from the energy available for thermalized partons, E_{tot}, using the energy carried by the particles created in heavy ion collisions, calculated from [22]:

$$E_{tot} = 2E_{part} \left.\frac{dN_{ch}}{d\eta}\right|_{|\eta|\leq 1} f_{neut} f_{4\pi} \tag{2.1}$$

where the factor of 2 accounts for integration over the interval $-1 < |\eta| < 1$, $dN_{ch}/d\eta$ is the particle density at midrapidity, f_{neut} and $f_{4\pi}$ are corrections accounting for undetected neutral particles and the incomplete solid angle coverage, 1.6 and 1.3 respectively. The energy per charged particle, $E_{part} \sim 600$ MeV, is estimated using the average transverse momentum $\langle p_T \rangle \sim 500$ MeV/c. This gives $E_{tot} \approx 1600$ GeV for the 6% of the most central $Au + Au$ collisions at $\sqrt{s_{NN}} = 200$ GeV, only about 4% of the total energy. The volume in which this energy is released is defined in the transverse direction by the dimensions of colliding nuclei, and is assessed to be 2 fm in the longitudinal direction, similar to the value proposed by Bjorken [52]. The final, most conservative estimate, taking into account also the expansion of the system, gives an energy density ≥ 3 GeV/fm^3 [22]. This is 20 times larger than the density inside a nucleus, 6 times larger than the density of nucleons and ~ 3 times larger than the critical density from theoretical estimates.

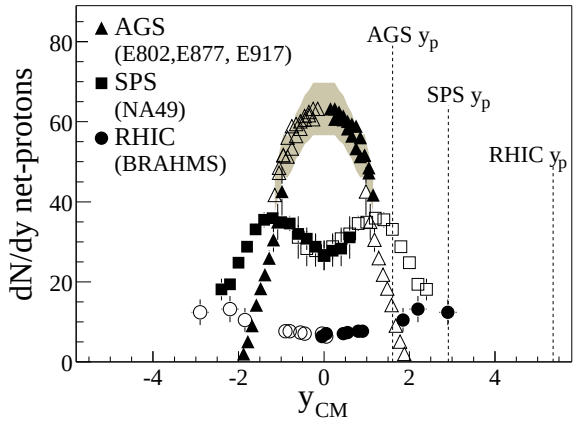

Fig. 2.1: Rapidity density of net protons (i.e., number of protons minus number of antiprotons) measured at AGS ($Au + Au$ at $\sqrt{s_{NN}} =$ 5 GeV [53]), SPS ($Pb + Pb$ at $\sqrt{s_{NN}} = 17$ GeV [54]), and RHIC ($Au + Au$ at $\sqrt{s_{NN}} = 200$ GeV [55]) for central nucleus-nucleus collisions.

In an analogous analysis performed by the PHENIX Collaboration three types of density estimates were considered: *general energy density* during nuclei overlap ($\langle\varepsilon\rangle = 3150$ GeV/fm^3), *formed energy density* involving created particles ($\langle\varepsilon\rangle = 15$ GeV/fm^3) and *thermalized energy density* at the moment when a local thermal equilibrium is first achieved, estimated to be 5.4 to 9.0 GeV/fm^3. The last, *thermalized energy density*, with a value of the same order as the estimate from the PHOBOS experiment, should be compared with theoretical predictions.

Experimental energy density estimates for heavy ion collisions at RHIC are much higher than the expected critical value. For similar collisions at the CERN SPS, at $\sqrt{s_{NN}} = 17$ GeV, analogous values are at least a factor of 2 smaller, but still the conditions for creation of aQGP may be fulfilled. In the following subsections observables that may be used as signals of such a transition are discussed, mostly with relation to RHIC experiments, but also mentioning some results at lower energies.

Theoretical studies of the Quark-Gluon Plasma are usually performed for the case of baryon-free matter, as the calculations are simpler when the system has the total quantum numbers of the vacuum. It is thus interesting to know the net-baryon density in heavy ion collisions. The BRAHMS Collaboration has measured the net proton density at RHIC [55] and compared it with results obtained at lower energies (Fig. 2.1). At the highest RHIC energy, at $y = 0$, the net proton density is about 10 times smaller than that observed at AGS. The opposite relation is observed for the number of produced particles, charged particle density increases about 20 times in this case [6, 56]. Thus we observe a change from a baryon-dominated system to an (almost) baryon-free system. This increases the chance that even approximate theoretical calculations may be applicable at RHIC energies.

2.1 Properties of Quark Gluon Plasma

Unlike other elementary particles, quarks and gluons are characterized by an additional quantum number, color. From many experiments we know that quarks do not exist as free particles, but are confined in larger, composite and colorless objects: hadrons. The energy of strong interactions between quarks increases rapidly with the distance separating them. The additional energy supplied to confined quarks, rather than forcing separation of them, is used to produce an additional quark-antiquark pair with appropriate colors, and two colorless hadrons appear. On the other hand the QCD coupling constant between color partons decreases when

the distance between them is smaller than the hadron size, and this effect is called "asymptotic freedom" [57, 58]. By producing in some volume an energy density sufficiently high to generate many quark-antiquark pairs, a system can be created in which each parton is always close to other partons and interacts with them very weakly. It seems thus natural that a system of such a large density should behave as an ideal quark-gluon gas, which is now frequently called the weakly interacting QGP (wQGP).

The physical picture presented above has several consequences. At high energy density, creation of heavier quark-antiquark pairs becomes more probable, which leads to an increase of the strange quark contribution, eventually seen as an enhanced production of strange particles. The matter in wQGP is color-transparent, thus the quarks from a $c\bar{c}$ pair, rather than forming a bound state just after creation, may easily drift away - an effect that leads to a suppression of charmonium (J/ψ) production [59].

Studying the properties of a QGP, once created, is complicated by its undergoing several transformations before the final appearance in the form of produced particles. A hot and dense system of quarks and gluons has to achieve thermal equilibrium, then expands and cools. At a sufficiently low temperature and density quarks form colorless particles again and a gas of hadrons exists until the final observed particles can escape from it at so-called freeze out. In the evolution of the system the properties predicted for the QGP may be modified by these later processes. On the other hand, study of effects connected to later phases may strengthen the evidence for QGP creation, if they depend on the initial conditions. For example it was argued that the size of the particle source, measured using the Hanbury-Brown-Twiss (HBT) method, should be larger and different for pions and kaons [60]. It was also predicted [61] that interactions of particles originating from decays of resonances in the hot hadronic matter may be seen as an increase of the width of the resonances for the $\phi(1020) \rightarrow K^+K^-$ decay by a factor of 2-3.

The above presented expectations for the QGP were at least partially met by the experimental results obtained at the CERN SPS in heavy ion collisions at $\sqrt{s_{NN}} = 17$ GeV [62]. The strange particle yields are in this case larger than in proton-nucleus collisions. Production of charmonium is suppressed in the most central $Pb + Pb$ collisions by a factor of about 2 with respect to the expectations for a normal nuclear absorption pattern [63, 64]. On the other hand open charm production is enhanced by a factor of 3.5 relative to an extrapolation based on results from $p + A$ collisions [65].

The studies of $Au + Au$ collisions delivered by RHIC at much higher than previously energy have led to new, unexpected results. Rather than a weakly coupled QGP, a strongly interacting matter (sQGP) was found [66]. A summary of experimental evidences for sQGP creation was published as a set of "White Papers" from all experiments at RHIC [22, 67, 68, 69]. The clearest sign of strong interactions is the suppression of high-p_T particles originating from energetic partons created in the hard binary scattering of quarks or gluons. Equally important is the observation of a strong elliptic flow resulting from pressure gradients which modify the collective expansion of the system. Strange particle yields and particle ratios suggest that thermal equilibrium was reached at some stage of the system evolution. Interesting results are obtained from a variety of correlation and fluctuation studies. These subjects are discussed in more detail later, here some other results which do no provide previously expected signals of QGP creation are mentioned.

Predicted increase of the width of $\phi(1020)$ resonance was tested by the STAR Collaboration [70], but the observed mass and width are consistent with the values from Particle Data Group tables [71].

Increase of the yields of low-p_T particles is expected if droplets of cold plasma are created. Yields measured by the PHOBOS Collaboration (see Section 3.5) do not show any significant enhancement [72].

Yields of charmonium observed at SPS energies [63, 64] are a factor of 2 smaller than expected from binary scaling of $p+p$ data. At RHIC a similar suppression was found [73, 74], but for large transverse momenta J/ψ yields agree with binary scaling, while for larger rapidities the suppression level increases. These trends are not reproduced by models of charmonium interactions in a quark-gluon medium [75, 76].

Experimental results obtained at RHIC also provide information on the initial states of nuclei, prior to the collision. In the earlier studies of $e+p$ interactions it was found that the proton can be treated as an object composed not only of valence quarks, but also of sea quarks and gluons. The basic parameter is the fraction of the longitudinal momentum, x, that is carried by these gluons. Because each gluon can radiate another one with a smaller momentum, the number of gluons at small x increases rapidly and seems to diverge. However, below some characteristic momentum the number of gluons saturates [77] and for a probing particle (for example γ) the cross section at small Bjorken variable x becomes only a function of $Q^2R_0(x)$, the photon virtuality Q^2 multiplied by the saturation radius, $R_0(x)$, which defines a saturation scale, $Q^2_{sat} = 1/R_0(x)$ [78]. Saturation can be understood as a competition between extra gluon radiation and gluon fusion, which is possible thanks to the large gluon density. As the gluons at small x are generated from partons with large momenta, they are contained in a Lorenz contracted area and for the probing particle have a form of a gluonic wall. The properties of low x gluons evolve slowly (as in a glass) due to their connection with fast partons for which time dilation occurs. Large gluon density causes the quantum mechanical states of the system to be multiply-occupied and thus to share some properties of a Bose condensate. To summarize the properties of this system of colored gluons, it was named a Color Glass Condensate (CGC) [79, 80, 81]. For a recent review see Ref. [82, 83].

The Color Glass Condensate concept supports the saturation models [84], and its prediction of weak dependence of particle densities on the number of nucleons participating in the collisions, N_{part}:

$$\frac{1}{N_{part}}\frac{dN}{dy} \sim \frac{1}{\alpha_S(Q^2_{sat})} \sim \log N_{part} \tag{2.2}$$

agrees with experiments (see Section 3.3 and 3.4). It also explains results for high-p_T suppression in $d+Au$ collisions, mentioned later in this Section. However, it is still unclear if the evidence is sufficient to establish the existence of the CGC.

2.2 Size of the particle source from interferometry

It was expected that the system created in a heavy-ion collision expands before particles are produced. The size of the source from which particles are emitted can be measured using the Hanbury-Brown and Twiss (HBT) correlations of identical particles. The correlation function for two particles with four-momenta $\mathbf{p}_1$ and $\mathbf{p}_2$:

$$C(\mathbf{q}) = C(\mathbf{p}_1 - \mathbf{p}_2) = \frac{P(\mathbf{p}_1, \mathbf{p}_2)}{P(\mathbf{p}_1)P(\mathbf{p}_2)}, \tag{2.3}$$

where P is a two- or single-particle probability function, can be described using Bertsch-Pratt parameterization as a function of relative four-momentum, $\mathbf{q}$:

$$C(\mathbf{q}) = 1 + \lambda e^{-(q_o^2R_o^2 + q_s^2R_s^2 + q_l^2R_l^2 + 2q_oq_l^2R_{ol}^2)} \tag{2.4}$$

and can be used to measure the source size, R_o, R_s and R_l, in *out*, *side* and *long* directions, respectively[1]. The measured radii for identical pion pairs are of the order of 6 fm in all directions [23, 85] and no significant increase with energy is observed. Presence of strong position-momentum correlations [23] suggests that particles are emitted by a source moving collectively at the same rapidity. Another analysis performed by STAR Collaboration involving pion-kaon correlations indicates that pions and kaons are not emitted at the same average space-time point [86]. All interferometry studies provide results that are consistent with a collective transverse expansion of the system driven by initial pressure gradients.

2.3 Suppression of high-p_T particles

The most convincing evidence for strong interactions in the system created by heavy ion collisions comes from the study of particles with large transverse momenta. The STAR experiment has measured the azimuthal angle correlations of a trigger hadron with $p_T > 4$ GeV and other particles with $p_T > 2$ GeV [87, 88, 89]. In elementary $p + p$ interactions the correlation plot features a double peaked distribution, with two maxima at $\Delta\phi = 0°$ and $\Delta\phi = 180°$, which is a sign of two jets produced by fragmentation of a pair of partons emitted back-to-back ($q\bar{q}$ or gluon-gluon). In central $Au + Au$ collisions the peak at $\Delta\phi = 180°$ disappears (see Fig. 2.2). Such an effect is expected when a pair of partons is created near the surface of a region of strongly interacting matter. The parton escaping outwards delivers a jet associated with the trigger particle, while the second parton, which has to traverse a long path through the matter, looses its energy and can not produce high-p_T particles. This is not the case for $d + Au$ collisions, where a few nucleon-nucleon collisions do not lead to the creation of a sQGP and the second parton does not interact [88] (Fig. 2.2 (left)). Further evidence is provided by the study of correlations in semi-central $Au + Au$ collisions [89] presented in Fig. 2.2 (right), where the correlation is analyzed separately for trigger hadrons emitted parallel to the event reaction plane ("in-plane") or perpendicular to it ("out-of-plane"). In the first case only partial suppression of hadrons at $\Delta\phi = 180°$ is observed, but the peak disappears for the "out-of-plane" case. This is consistent with the geometry of the collision: the path traversed by the parton in the medium is longer for the "out-of-plane" direction and much smaller for the "in-plane" direction[2].

The suppression of high-p_T particles can also be studied using average particle yields. Usually, they are scaled by the yields from $p + p$ interactions to obtain the nuclear modification factor, R_{AA}, defined as:

$$R_{AA} = \frac{\sigma_{pp}^{inel}}{N_{coll}} \frac{d^2 N_{AA}}{dp_T d\eta} d^2\sigma_{pp}/dp_T d\eta \tag{2.5}$$

which normalizes particle production in $A+A$ collisions by elementary $p+p$ yields and accounts for an increased probability of hard processes by dividing by the number of nucleon-nucleon collisions, N_{coll}. Properties of the R_{AA} observable are described in Section 3.5 where measurements performed by the PHOBOS Collaboration are presented. These studies confirm a decrease of the yields of charged particles at high-p_T. Analyses from other RHIC experiments provide also more exclusive information. The STAR Collaboration found that protons and anti-protons are less suppressed than π^+ and π^- in the range $1.5 < p_T < 6$ GeV/c, but R_{AA} is the same at

[1] For detail discussion of Eq. 2.4 and reconstruction of R_o, R_s and R_l see Refs. [23, 85]

[2] For collisions in the rest frame of one of the nuclei or in the case of collisions of parallel beams, the reaction plane is defined by the vector between the centers of the nuclei at their closest approach and the momentum of a nucleus

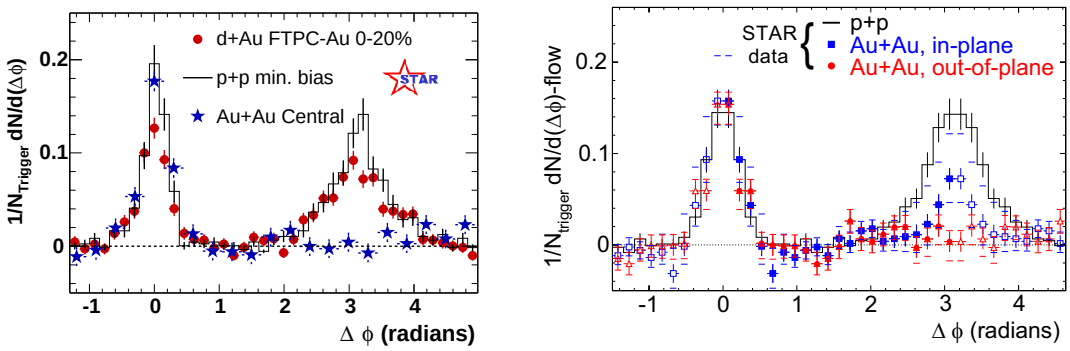

Fig. 2.2: Dihadron azimuthal correlations at high-p_T, in central $d+Au$ and central $Au+Au$ collisions [88] (left) and for different orientations of the trigger hadron relative to the reaction plane in 20-60% central $Au+Au$ collisions [89] (right). In both cases background-subtracted distributions are shown and compared with an appropriate distribution obtained for $p+p$ interactions.

larger momenta [90], while the PHENIX Collaboration observed a suppression of π^0 similar to that found for charged pions [91]. The BRAHMS Collaboration extended R_{AA} measurements to large rapidities (up to $\eta = 3.2$) and found a suppression of the yields in $d+Au$ collisions for smaller emission angles [92]. This last observation is consistent with Color Glass Condensate predictions: at larger rapidities partons created in the initial collision are more energetic and thus probe gluons with smaller x values. As the number of gluons increases with decreasing x the suppression due to parton multiple scattering on gluons is larger [66].

2.4 Collective effects observed as elliptic flow

The colliding nuclei usually do not hit head-on, but more or less miss each other. In such a case only some fraction of nucleons interact inelastically - those from the area of the overlap of nuclei, when viewed along their direction of flight (see Fig. B.1 in Appendix B). The shape of this area is thus not fully symmetric in the transverse plane and resembles an almond or a lens. This asymmetry is later reflected in the final products of the collision [93]. It can be described by the parameters of a Fourier expansion of particle density as a function of the azimuthal angle, ϕ:

$$\frac{dN}{d\phi} \sim 1 + 2v_1 \cos(\phi - \phi_R) + 2v_2 \cos 2(\phi - \phi_R) + \ldots \tag{2.6}$$

where the vector between the centers of nuclei at closest approach defines the azimuthal angle of the reaction plane, ϕ_R. Usually only the first two parameters, v_1 (directed flow) and v_2 (elliptic flow) are sufficient for the description of the particle density distribution, and effects of the elliptic flow prevail over those due to directed flow. The magnitude of elliptic flow, v_2, is studied as a function of several parameters: the type of colliding nuclei, the centrality of the collision, the type of the particles analyzed, and their transverse momentum or pseudorapidity. The PHOBOS experiment has measured almost all of the above characteristics [7, 18, 21, 28, 31], and STAR and PHENIX have provided flow measurements also for identified particles [94, 95, 96].

The elliptic flow measurements in heavy ion collisions were performed starting from very small energies. At low energies, $\sqrt{s_{NN}} < 4$ GeV, the value of v_2 is negative [97], as the matter is "squeezed out" from the almond shaped overlap area by geometric shadowing of the non-

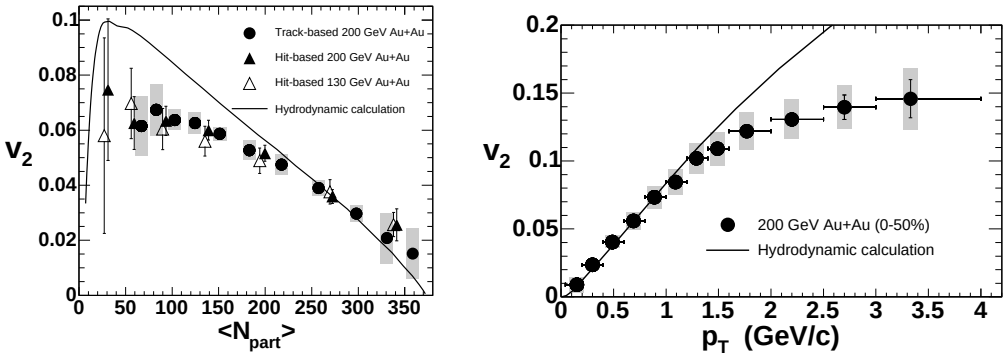

Fig. 2.3: Elliptic flow, v_2, as a function of the number of nucleons participating in the $Au+Au$ collisions (left) and as a function of the transverse momentum of particles (right) measured at $\sqrt{s_{_{NN}}} = 130$ GeV and $\sqrt{s_{_{NN}}} = 200$ GeV [21]. The lines represent calculations based on a hydrodynamic model [98].

interacting part of the nuclei [99, 100]. Above $\sqrt{s_{_{NN}}} = 4$ GeV v_2 values are positive, as the shadowing weakens and finally disappears. Then effects of pressure gradients in the reaction zone cause more particles to be emitted along the shorter axis of the almond. A further increase of v_2 is observed at the CERN SPS [100] and continues at RHIC. At an energy $\sqrt{s_{_{NN}}} \approx 200$ GeV the magnitude of elliptic flow reaches values which are consistent with predictions from hydrodynamic models [98]. In Fig. 2.3 the dependencies of elliptic flow on event centrality and on transverse momentum of particles are shown. The observed flow values are large, which in the hydrodynamic models implies very small viscosity [101]. The analysis of v_2 for different particles [94] shows that elliptic flow in the range $p_{_T} < 1$ GeV/c is largest for pions, smaller for kaons, and smallest for protons [94, 95]. This is also consistent with hydrodynamic calculations based, for example, on the model described in Ref. [102] with a first-order phase transition and a freeze-out temperature of 120 MeV. It appears that this behavior may be mostly a meson-baryon difference, as after rescaling of v_2 and $p_{_T}$ by the number of valence quarks, n_q, a universal dependence $\frac{v_2}{n_q}(\frac{p_T}{n_q})$ is observed for K^0_s, $p+\overline{p}$, $\Lambda+\overline{\Lambda}$, $\Xi^- + \overline{\Xi^+}$ and $\Omega^- + \overline{\Omega^+}$ [96]; only for $\pi^+ + \pi^-$ is it different.

2.5 Strangeness production and particle ratios

Increased creation of strange quarks in the hot quark-gluon matter and thus an enhanced production of strange particles was among the first proposed signals of QGP creation [103]. The yields of strange baryons, particularly these containing 2 or 3 strange quarks, should be specially sensitive to the properties of the matter created in heavy ion collisions [104]. As production of particles depends on the energy and centrality of the collision, the correct observable to be studied is the relative yield of strange particles measured in $A + A$ and $p + p$ collisions:

$$E = \frac{Yield^{AA}\langle N^{NN}_{part}\rangle}{Yield^{NN}\langle N^{AA}_{part}\rangle} \tag{2.7}$$

where NN denotes either a $p+p$ or a $p+A$ collision. The numbers of nucleons participating in the collision, $\langle N^{AA}_{part}\rangle$ and $\langle N^{NN}_{part}\rangle$ for $A+A$ and $p+p$ (or $p+A$), are used in order to obtain correct normalization. Such yields obtained for protons, Λ, Ξ^-, $\overline{\Lambda}$, $\overline{\Xi}^+$, Ω^- and $\overline{\Omega}^+$ [105, 106, 107] are

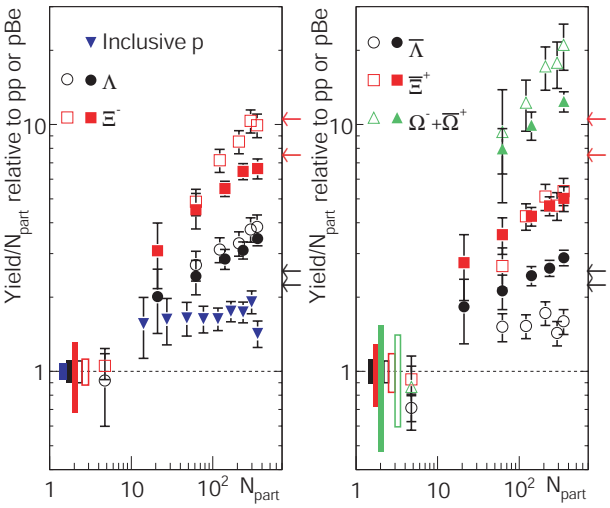

Fig. 2.4: Centrality dependence of the yields of strange baryons in $Au + Au$ collisions at $\sqrt{s_{NN}} = 200$ GeV [105] (filled symbols) and $Pb+Pb$ collisions at $\sqrt{s_{NN}} = 17$ GeV [106, 107] (open symbols) relative to the yields obtained in $p + p$ interactions. The uncertainties of the measurements in $A+A$ collisions are represented by errors for the data points, the errors due to uncertainties of $p + p$ reference are depicted by boxes. More information can be found in Ref. [105].

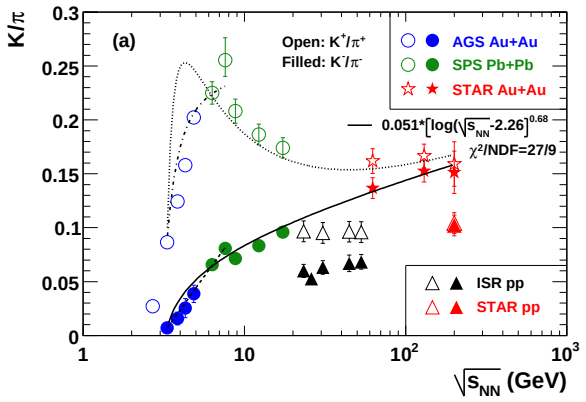

Fig. 2.5: K^+/π^+ and K^+/π^+ ratios as a function of collision energy in p+p and central heavy-ion collisions [108].

shown in Fig. 2.4.

As expected the largest enhancement is observed for Ω^- and $\overline{\Omega}^+$ baryons and reaches about 20 in the most central collisions. Values obtained at RHIC and SPS, for energies different by an order of magnitude, are similar, whereas from theoretical calculations using the Grand Canonical ensemble approach [109] a significant decrease with collision energy is expected [105].

The lightest and most abundantly produced particles containing strange quarks are kaons, thus the global strangeness enhancement should be visible in the K/π ratio. This ratio was measured in many experiments, at AGS, at SPS and at RHIC. At low energies the ratio of total multiplicities for K^+/π^+ is larger than the ratio for K^-/π^- and grows faster with the collision energy. While K^-/π^- increases continuously with energy the ratio K^+/π^+ reaches a maximum at about $\sqrt{s_{NN}} = 9$ GeV, then drops by about 30% and remains constant up to RHIC energies [108] (see Fig. 2.5). Larger K^+ yields may be partly related to associated production of K^+ mesons in the interactions of nucleons (for example in the reaction $p + p \rightarrow p + \Lambda + K^+$), which do not lead to K^- production. Such differences can happen only in regions with significant net-baryon densities. At RHIC energies the difference between K^-/π^- and K^-/π^- is very small except at large rapidities [110, 111]. The structure in the energy dependence of the K^+/π^+ ratio is well described by a statistical model assuming the creation of a QGP [112], and may thus represent the onset of deconfinement.

The yields of particles, and especially the antiparticle to particle ratios, can be used to asses

the degree of equilibrium and calculate the temperature and the baryon chemical potential, μ_B. In central $Au + Au$ collisions at RHIC the $\overline{p}/p$ ratio reaches about 0.73, which indicates that the value of the baryon chemical potential, μ_B, is small. Statistical model calculations [113] provide an estimate of the ratio $\mu_B/T = 0.17$ which is consistent with that extracted from the experimental K^+/K^- ratio [9].

2.6 Fluctuations as a sign of a phase transition

A study of observables event-by-event is the most promising way of detecting new physical phenomena if the change of properties of the system created in the collisions of heavy nuclei is neither step-like nor very rapid. Also in the case when a new type of matter is created in only a fraction of events, such an analysis may more easily unveil its properties. In both cases studies of fluctuations of many different observables make it possible to collect useful information. A more detailed description of experimental results on fluctuations is deferred to the following Sections, here theory-based motivation for using specific observables, proposed methods, and a few predictions are presented.

It is obvious that in a system that can be described by thermodynamics and which undergoes a transition between two very different states, some type of phase transition should occur. For the system that is created in heavy ion collisions at RHIC energies, with high temperature and moderate or even relatively low net-baryon density, the QCD favors a rather smooth second-order phase transition [114]. The first-order phase transition should be present at lower temperatures, but only for very large net-baryon densities. It is thus also expected that somewhere in the phase diagram of nuclear matter there is a critical point at which the phase transition changes its order [115, 116]. Only in the case of a first-order phase transition is a discontinuity in the basic thermodynamic parameters expected. In a system that crosses a second order phase transition, or in particular that passes near a critical point, enhanced fluctuations are much more likely [117, 118, 119, 120, 121]. Also if the quark-gluon matter forms small droplets [122] or if areas of Disoriented Chiral Condensate (DCC) appear [123], they may be visible as an enhanced production of particles in a narrow rapidity interval. However, effects related to these new phenomena must be distinguished from fluctuations occurring in the hadron gas [124, 125].

It is possible to find several examples of relations between the fluctuations and the thermodynamical properties of the system [126, 127]. The fluctuations of the energy in a part of a finite system in a thermal equilibrium are connected with the heat capacity:

$$\langle (\Delta E)^2 \rangle = T^2 C_V(T) \tag{2.8}$$

The energy can be determined experimentally, but it is easier to measure the multiplicity of the produced particles. By measuring multiplicity fluctuations the changes of the heat capacity can be detected. A similar relation is valid for the fluctuations of the system temperature:

$$\frac{\langle (\Delta T)^2 \rangle}{T^2} = \frac{1}{C_V(T)} \tag{2.9}$$

Although the temperature is not directly measurable, it is connected with the transverse momenta of particles; thus fluctuations of the mean $p_{_T}$ are useful in studies of thermodynamic systems.

Charge fluctuations, which in thermodynamical systems are proportional to the square of the charge of particles present in them, seem particularly interesting. They are very different

in a hadron gas of pions ($Q^2_{\pi^\pm} = 1$) and in a quark-gluon gas ($Q^2_{u,\bar{d}} = 4/9$ and $Q^2_{\bar{d},\bar{u}} = 1/9$). However, the contribution from resonances produced in the hadronization process decreases the fluctuations expected for the hadron gas and the simplest estimates for quarks cited above underestimate fluctuations - thus this signal is not so unambiguous, as discussed in Section 7.3.

As we are looking for any change in the properties of the system, fluctuations of other observables are also potentially interesting. In this context, fluctuations of the ratios: baryon to pion, kaon to pion, and $\pi^0/\pi^\pm$ can be examined [127]. A characteristic signal of deconfinement - enhanced production of neutral pions, if domains of Disoriented Chiral Condensate (DCC) appear [128, 129] - can be detected as fluctuations of the ratio $\pi^0/\pi^\pm$. When a tri-critical point is present in the phase diagram of the chemical potential μ and the temperature T, the fluctuations of the soft particle multiplicity should be enhanced. They may be visible either directly as an excess in the p_T spectra at low p_T, or via increased event-by-event fluctuations at low p_T, but at the same time fluctuations for pions with larger momenta should be anomalously suppressed [116].

Large but localized fluctuations are also possible if a new phase of matter has very distinctive properties and is created only in some small areas of the system. This type of fluctuation can be revealed by intermittency analyses [130] using higher order factorial moments. It was found that such correlations in $p+p$ interactions are stronger than in $A+A$ collisions, which indicates that they are mainly due to resonances and jets. Reversal of this trend due to a second order phase transition was suggested in several papers [131, 132, 133], but there are no experimental indications that it is observed at RHIC energies.

Beside many possible observables there are also numerous methods of quantifying fluctuations and detecting unusual properties [134, 135, 136]. Many other methods for detecting phase transition effects have been proposed, in addition to the analyses described in this work. However, many theoretically very attractive observables are difficult to analyze experimentally.

Several problems arise in the study of fluctuations aimed at uncovering new phenomena. As has been mentioned, fluctuations created in a QGP or appearing as an effect of a phase transition have to be different from those expected for a hadron gas. Even so, the difference may disappear if they are substantially altered during the hadronization phase of the nuclear collision. In studies of $A + A$ collisions, observables often depend on the centrality of the collision, and fluctuations of the number of nucleons participating in the collision may strongly modify thermodynamical fluctuations [137, 138, 139, 140].

There are also other purely experimental effects which need to be carefully accounted for in correctly reconstructing the original fluctuations. If background particles produced in secondary interactions are not readily recognized and rejected, their contribution may affect registered fluctuations. Also the effects connected with limited acceptance of the detector may be very important. A striking example is seen in fluctuations of the number of charged particles measured as the variance of the N_{ch} distribution divided by the mean multiplicity:

$$\omega_{N_{ch}} = \frac{\langle (N_{ch} - \langle N_{ch} \rangle)^2 \rangle}{\langle N_{ch} \rangle} \tag{2.10}$$

studied in Ref. [140] using events from Monte Carlo generators. For selected semi-central $Au+Au$ collisions in the full phase space, $\omega_{N_{ch}}$ can reach ≈ 83.6, but after restricting particles to those detected by the PHOBOS Spectrometer ($0 < \eta < 2$ and $|\phi| < 0.087$ rad), $\sim$40 times lower values ($\omega_{N_{ch}} \approx 1.92$) are obtained .

In the analysis of fluctuations we are searching not only for "unusual" properties of the

events, detected as very large fluctuations. Fluctuations can also exhibit smaller-than-expected deviations of an observable that cannot be explained as a statistical variation. In order to quantify this difference several measures of fluctuations are used. Very frequently in the definitions of these measures ratios of observables appear, as they can cancel some fluctuations or other effects that we are not interested in. It is also very convenient when for purely statistical fluctuations the selected measure has a well defined value, for example 0 or 1. The ω measure defined by Eq. 2.10 is the most appropriate, when the quantity (here N_{ch}) is expected to follow a Poisson distribution for which the variance is equal to $\langle N_{ch} \rangle$, as in this case $\omega = 1$. Another popular function is the Φ function proposed in Ref. [141]:

$$\Phi_x = \sqrt{\frac{\langle Z^2 \rangle}{\langle N \rangle}} - \sqrt{\bar{z^2}} \tag{2.11}$$

where for an observable x we have: $z = x - \bar{x}$, $Z = \sum_{i=1}^{N} x_i - \bar{x}$, N is the number of particles, the bars denote averaging over inclusive single particle distributions and the brackets $\langle ... \rangle$ denote averaging over events. This fluctuation measure equals 0 when in each event only statistical fluctuations are present. Other fluctuation measures are described together with the results of studies in which they were used. However, in the case when statistical fluctuations are much larger than the fluctuations from dynamical sources, and in the studied event sample the multiplicity is large and has a narrow distribution, all measures are related to each other and can be derived from the covariance of the analyzed observable [142].

The studies of multiplicity fluctuations, with special consideration of those performed by the PHOBOS Collaboration, are presented in Section 4. In Section 7 the results of fluctuation studies obtained by other RHIC experiments, using observables unavailable in the PHOBOS experiment, are described. No studies provide unambiguous evidence of a phase transition or a critical point. More sensitive methods and a scan of collision energy will probably be necessary to find such phenomena. It may be necessary to look at other observables, for example strangeness fluctuations [143] and correlations between baryon number and strangeness [144], or to search for rare processes [145], or use other novel methods [146]. Higher moments of experimental observables, which are however more difficult to analyze experimentally, may be very sensitive to these effects [147].

Section summary

In collisions of heavy nuclei a system characterized by a very large energy density is created. For such a system Quantum Chromodynamics predicts the formation of a medium with quarks and gluons instead of hadrons. It was discovered in the experiments at RHIC that the quark-gluon matter is strongly interacting, as indicated by suppression of high-p_T particles and large elliptic flow. The rather smooth dependences of most observables on collision energy and centrality do not provide unambiguous evidence on the location of a phase transition or a critical point. Studies of dynamical fluctuations are expected to deliver more information in this area.

3 Results from the PHOBOS experiment

This Section is devoted to the presentation of the PHOBOS detector and the most interesting results obtained by the PHOBOS Collaboration. The analyses included here are not connected directly with the subject of this work, nevertheless their results deserve some attention. Only multiplicity studies are presented in more detail, while particle spectra and flow measurements are only briefly mentioned.

3.1 PHOBOS Detector

The general view of the PHOBOS detector [148] is shown in Fig. 3.1 where all important subsystems of the apparatus are labeled. The beams of ions travelling in the beam pipe arrive from opposite directions and collide near the nominal interaction point which is located in the center of the figure. Close to it is the conventional magnet (in Fig. 3.1 the upper part of the magnet is removed), which delivers 2 Tesla field. In the approximately constant magnetic field two Spectrometer arms are located; however, first 8 layers of the Spectrometer are placed in a very weak field. Near the beam pipe the elements of the Multiplicity detector and of the trigger system are positioned. The Vertex detector and details of the central part of the apparatus are shown in Fig. C.1 in Appendix C. Active elements of the most important detector systems are built of silicon sensors [149, 150], but also scintillator and Čerenkov detectors are used.

In the PHOBOS coordinates system the z-axis is directed along the beam, the x-axis is horizontal and the y-axis points vertically upwards. Elements of the Multiplicity detector and some of the trigger system are placed approximately symmetrically with respect to $z = 0$, and have a high degree of symmetry in azimuthal angle. Two Spectrometer arms are mirror reflections in x, while the Vertex detector is symmetric with respect to each axis.

The Spectrometer consists of two symmetric arms on both sides of the beam pipe, each of them has 16 layers of silicon sensors. Starting from the interaction point there are first the sensors with pixels (1×1 mm^2), then with rectangular pads (0.427×6 mm^2) and finally with vertical strips (0.667 mm wide, 7.5, 15 or 19 mm high). Together there are 274 sensors with almost 112000 electronics channels. The highest occupancy in the Spectrometer, for the most central $Au + Au$ events is about 4%.

Particles can be identified using the energy loss in the silicon, dE/dx, measured by the electronics with very good resolution in the momentum range 0.1 to 0.6 GeV/c for pions, 0.15 to 0.65 GeV/c for kaons and 0.2 to 1.0 GeV/c for protons and antiprotons [2]. In the studies that require the average number of particles only, fitting of the dE/dx distribution as a sum of contributions from π, K, and p allows us to extend the identification for pions and kaons to $p < 0.9$ GeV/c and for protons and antiprotons to $p < 1.4$ GeV/c [29]. A different procedure is used for particles with very low momenta which stop in the fifth layer of the Spectrometer (described in Ref. [15]), which allows for identification of pions between 0.03 and 0.05 GeV/c, kaons between 0.09 and 0.13 GeV/c and protons/antiprotons between 0.14 and 0.21 GeV/c, however without determining the sign of the charge of the particle.

First 8 layers of the Spectrometer are placed in an area with a very weak magnetic field, the remaining layers are inside the conventional magnet producing ~ 2 Tesla magnetic field. The magnetic field in Spectrometer arms is vertical, but in one arm pointing up and in the other one - down. This causes that particles of the same type emitted at 45° bend in both arms either towards the beam pipe or away from it - depending on the sign of their charge.

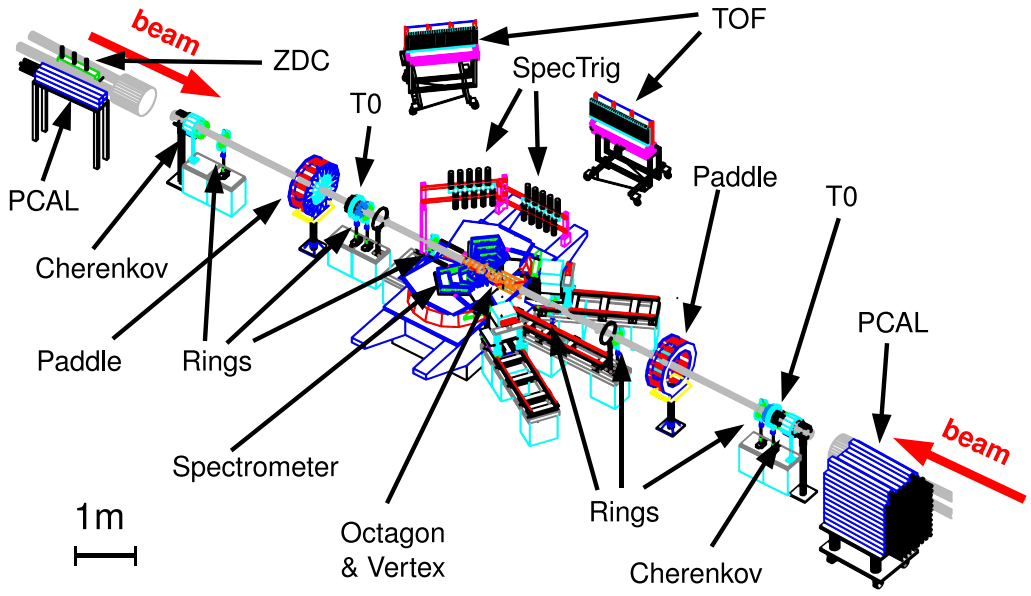

Fig. 3.1: The elements of the PHOBOS detector: trigger system (Paddle, T0, Čerenkov, ZDC, SpecTrig, PCAL), Multiplicity detector (Octagon, Rings), Spectrometer, Vertex detector and time of flight system (TOF).

Measurements were thus always performed with a varying polarization of the magnet to collect similar samples of events in which particles with opposite signs have the same acceptance. The acceptance of the Spectrometer strongly depends on the vertex position and the particle type, usually particles are measured in the range $|\eta| < 0.5$, but especially for pions it may be extended to $\eta \approx 1.3$ or even farther [13].

Momenta of particles traversing all silicon layers of the Spectrometer are measured with an error about 1% for $p \approx 1$ GeV/c that increases with p, but is still less than 5% for $p = 8$ GeV/c [29].

The Time of Flight system (TOF) is located behind the Spectrometer at a distance of about 4 m from the interaction point and covers the pseudorapidity range $0 < \eta < 1.24$. It consists of 240 scintillator modules which measure the arrival time of charges particles with a resolution better than 100 ps. Using TOF it is possible to measure particle velocity, v, with an accuracy sufficient to separate pions from kaons up to $p < 1.2 - 1.4$ GeV/c and kaons from protons up to $p < 2.0$ GeV/c [148]. By fitting the $1/v$ distribution particle identification can be extended to higher momenta, even up to 3 GeV/c [29].

The Multiplicity detector is placed closest to the beam pipe and consists of a 1.1 m long central octagonal part and six rings placed symmetrically at about ± 1.12 m, ± 2.35 m and ± 5.05 m from the interaction point. The Octagon covers the pseudorapidity range of approximately $|\eta| < 3$ while the Rings extend the coverage to $|\eta| < 5.4$. The Octagon has four windows, two at the sides before the first sensors of both Spectrometer arms and two at the bottom and top before the Vertex detector. The Multiplicity detector is built of silicon sensors: rectangular in the Octagon (with 120 pads 2.708×8.71 mm^2) and trapezoidal in the rings (with 64 pads of varying area, covering $2\pi/64$ in ϕ and about 0.1 unit in η). It has only one layer of sensors, with very small overlaps, thus the charged primary particles are leaving

usually only one hit. The number of pads in the Multiplicity detector (3072 in the Rings, 11000 in the Octagon) is relatively small. Due to coarse segmentation the occupancy is large and in most central $Au + Au$ events ranges from 28% to 66%. This causes that the event multiplicity can not be obtained by simple counting of hits and more elaborate methods have to be applied (see Appendix D).

The Vertex detector is the smallest silicon system with only 24 sensors, arranged in two parts above and below the nominal interaction point, each with two layers. In the inner layers sensors with 4 rows of 473 μm wide and 12 mm long strips are used, in the outer layers there are two times more sensors with 2 rows of 473 μm wide and 24 mm long strips. The hits measured in the Vertex detector are used in the basic method of reconstruction of the interaction point in two dimensions (z and y). More details on vertex reconstruction are given in Appendix C.

The trigger system includes several different detectors: Paddle counters [151], Time-zero (T0), Čerenkov [152], SpecTrig and PCAL. Usually only a few of them were used in the online trigger condition, but information from the remaining was sometimes included in an off-line selection of events.

The Paddle counters, built of scintillators, are placed at ± 3.21 m from the interaction point and cover the range $3 < |\eta| < 4.5$. This detector is a part of the trigger for interactions of ions, but in addition the signal from it is used for the determination of the centrality of events. The standard trigger condition required signals in this detector both at negative and positive z side with a time difference less than 8 ns. This requirement rejects false events caused by a beam halo (for which the time difference is about 21 ns - the time necessary to traverse the distance between Paddle counters with the speed of light). The central $Au + Au$ collisions were selected by requiring signal in many "paddles" at both sides.

In the PHOBOS experiment there are two systems incorporating Čerenkov detectors. The system installed from the very beginning at the distance ± 5.5 m from the interaction point, called simply Čerenkov detector, comprise 12 tubes at each side. The later addition, Time-zero (T0) system consists of two rings of 10 tubes each. It was placed either at ± 5.31 m for heavy ion collisions or at 2.55 m and -1.31 m for $p+p$ interactions. Both systems measured the arrival time of particles and allowed us to select events in which collisions occurred near the nominal interaction point, $z = 0$.

Zero Degree Calorimeters (ZDC) were positioned at the largest distance ± 18.5 m from the interaction point, already behind the first magnet of RHIC accelerator [153]. They registered signals from spectator neutrons which did not interact inelastically, but also were not contained in larger fragments of the colliding nuclei. As identical detectors were installed at each interaction point they can be used for comparison of trigger conditions between all RHIC experiments.

Remaining subdetectors were relatively rarely used. SpecTrig detector was applied in triggering for particles with high momenta. The PCAL detector (proton calorimeter) was intended to register spectator protons - as an extension of ZDC capabilities.

The trigger definition was chosen depending on the type of colliding beams (heavy ions, $d + Au$, or $p + p$), the beam energy and required sample of events (inclusive or central). Details on trigger method are provided in the original publications as part of the description of the collected data for example in Ref. [1] for $Au + Au$, Ref. [10] for $d + Au$ and Ref. [19] for $p + p$.

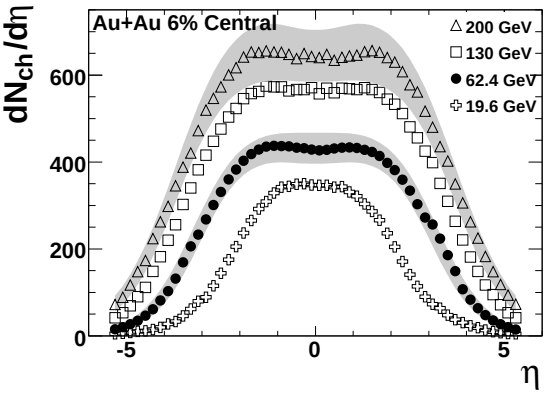

Fig. 3.2: Particle density distributions $dN_{ch}/d\eta$ for 0-6% central $Au + Au$ collisions at several beam energies.

3.2 Pseudorapidity distributions of charged particles

One of the goals of the PHOBOS experiment that determined the design of the detector was the measurement of charged particles in almost the full solid angle. This was achieved using the Multiplicity detector with the largest acceptance among experiments at RHIC. It registers only one hit from a primary particle, but this information is sufficient to reconstruct the charged particle density distribution, $dN_{ch}/d\eta$, as described in more datail in Appendix D. General properties of particle production were studied for different beam energies, projectile types and collision centralities:

- $Au + Au$ at $\sqrt{s_{NN}}$ = 19.6 GeV [8, 34], 64 GeV [25], 130 GeV [3] and 200 GeV [4, 8];
- $Cu + Cu$ at $\sqrt{s_{NN}}$ = 22 GeV, 62 GeV and 200 GeV [34];
- $d + Au$ at $\sqrt{s_{NN}}$ = 200 GeV [20];
- $p + p$ at $\sqrt{s_{NN}}$ = 200 and 410 GeV [154].

Experimental results are compared to predictions from Monte Carlo generators, most frequently the HIJING model [155, 156] and AMPT model [157].

The $dN_{ch}/d\eta$ dependence on collision energy follows the trends observed at lower energies: the distribution becomes wider and the height of the central area increases. There is a continuous approximately linear change of these parameters with $\ln(\sqrt{s_{NN}})$. As an example the distributions for central $Au + Au$ collisions at four energies are shown in Fig. 3.2. Complete data can be found in references given above.

In the case of nucleus-nucleus collisions, the $dN_{ch}/d\eta$ dependence on centrality was studied. The integral of the $dN_{ch}/d\eta$ distribution scales with the number of nucleons participating in the collision, N_{part}. This is discussed in more detail in Section 3.4. The shape of the distribution, although constant at first glance, slowly changes with centrality (Fig. 3.3). This becomes evident only in a detailed comparison, for example if the distributions are scaled to the same height. The width of $dN_{ch}/d\eta$ becomes smaller for more central collisions, as can be seen in Fig. 3.3 (right).

Generally, the $dN_{ch}/d\eta$ distributions in symmetric collisions (Au+Au or Cu+Cu) follow the same trends [34]. The distributions obtained for similar N_{part}, shown in Fig. 3.4, agree within their systematic errors at 200 GeV. At lower energies there are more particles in $Au + Au$ collisions than in $Cu + Cu$ collisions. An increased number of spectator nucleons in collisions of heavier nuclei is most probably responsible for this effect, especially as at the lowest energy the

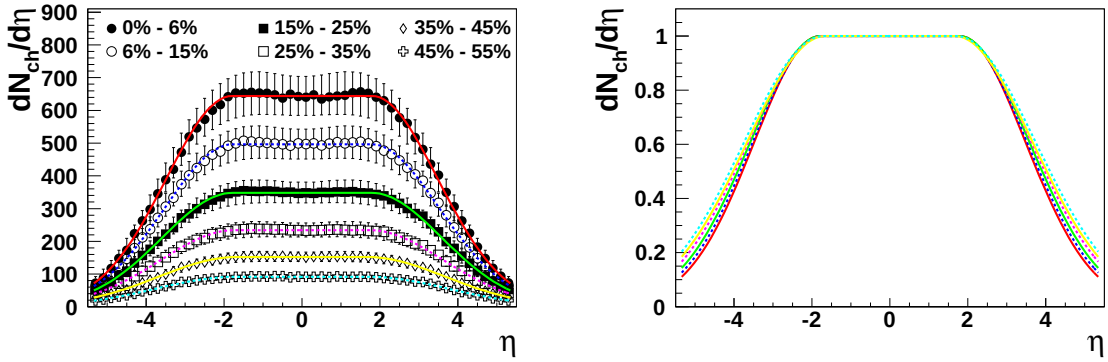

Fig. 3.3: Charged particle pseudorapidity density $dN_{ch}/d\eta$ in $Au+Au$ collisions at $\sqrt{s_{NN}}$=200 GeV for six centrality bins (described in the left panel). In order to compare the shapes of $dN_{ch}/d\eta$ distributions, they were fitted by a function (constant in the central area with gaussian "wings"). Right panel shows the functions, fitted to the data in the left panel, after scaling to the same height at η=0.

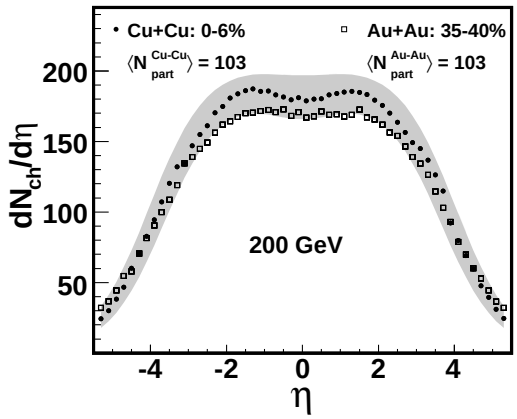

Fig. 3.4: Charged particle pseudorapidity density $dN_{ch}/d\eta$ for $Au+Au$ and $Cu+Cu$ collisions at $\sqrt{s_{)NN}} = 200$ GeV. The central $Cu+Cu$ collisions are compared to semi-peripheral $Au+Au$ collisions (35-45%) in order to obtain the same number of nucleons participating in the collision.

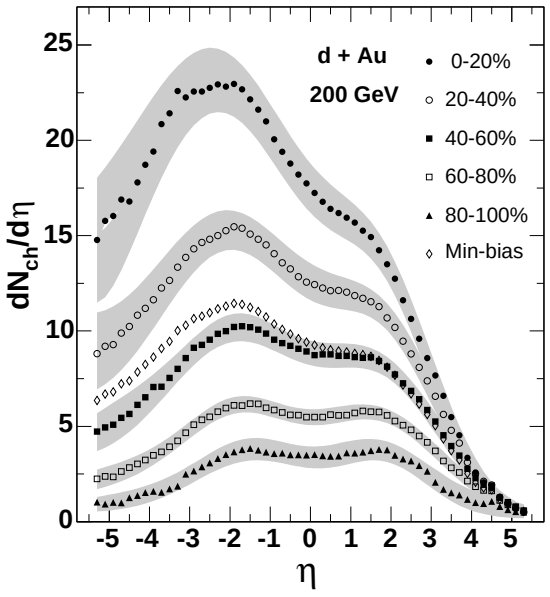

Fig. 3.5: Charged particle pseudorapidity density $dN_{ch}/d\eta$ for $d+Au$ collisions at $\sqrt{s_{)NN}} =$ 200 GeV for several centralities.

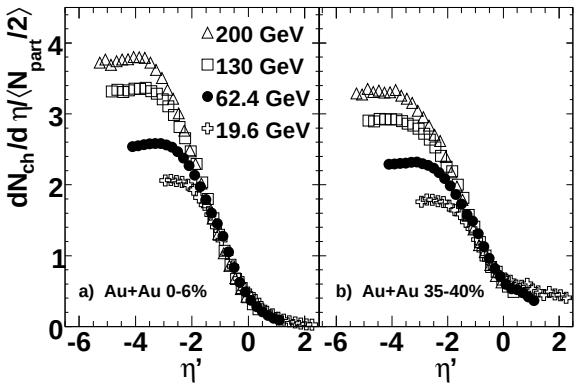

Fig. 3.6: Charged particle density $dN_{ch}/d\eta'$ scaled to one pair of participating nucleons for four different energies, obtained in the most central (a) and peripheral (b) $Au + Au$ collisions.

broad acceptance range of the PHOBOS detector reaches pseudorapidities $|\eta| > y_{beam}$, where particles originating from excited remnants of colliding nuclei may be present.

In asymmetric $d + Au$ collisions $dN_{ch}/d\eta$ distributions are distinctly different, as shown in Fig. 3.5. Many more particles are produced on the negative η (Au side) than at positive η (deuteron side). This asymmetry is larger for more central events, in agreement with the Wounded Nucleon Model interpretation of $d + Au$ collisions [158]. The comparison to $p + p$ collisions presented in Ref. [20] shows that for $\eta \approx 5$ the particle density is similar to that from elementary collisions, but grows relative to $p + p$ while moving to the Au side and increases by a factor up to 20 for $\eta \approx$ -5.

The unique capability of measuring $dN_{ch}/d\eta$ for large $|\eta|$ in the PHOBOS experiment allows the study of the particle density in the rest frame of one of colliding nuclei. In this case the variable $\eta' = \eta - y_{beam}$, where y_{beam} is the rapidity of the selected projectile in the laboratory frame, has to be used. The distributions $dN_{ch}/d\eta'$ obtained in the fragmentation region, $\eta' \approx 0$, were predicted to scale for different collision energies (hypothesis of limiting fragmentation [159]).

In Fig. 3.6 the $dN_{ch}/d\eta$ distributions for $Au + Au$ collisions with the same centralities, but different collision energies, shifted to the rest frame of one of the nuclei and scaled by $\langle N_{part}\rangle/2$ are compared. These distributions overlap in the fragmentation region, and the range of η' over which $dN_{ch}/d\eta'$ is identical grows with collision energy. A similar effect was seen in elementary $p + \overline{p}$ collisions [160] and hadron-nucleus collisions [161]. To emphasize this broadening of the scaling range, which is no longer restricted to the typical fragmentation region, this effect was renamed to *extended longitudinal scaling*.

The scaling in the fragmentation region is valid only for the same centralities of the collision. This is a consequence of the dependence of the $dN_{ch}/d\eta$ shape on centrality (Fig. 3.3) - the widths of the distributions are not the same, thus in the rest frame of the nuclei they are slightly different. The importance of a proper selection of centrality is manifested in the comparison of $d + Au$ [20] and proton-emulsion [162, 163, 164] results. The normalization of the distributions that accounts for the difference between $\langle N_{part}^{d+Au}\rangle$ and $\langle N_{part}^{p+Em}\rangle$ is not sufficient. Only if in addition the centrality of the $d + Au$ collisions is appropriately selected to match as closely as possible the values of the ratios $\langle N_{part}^{Au}\rangle/\langle N_{part}^{d}\rangle$ and $\langle N_{part}^{Em}\rangle/\langle N_{part}^{p}\rangle$ the extended longitudinal scaling is observed [20].

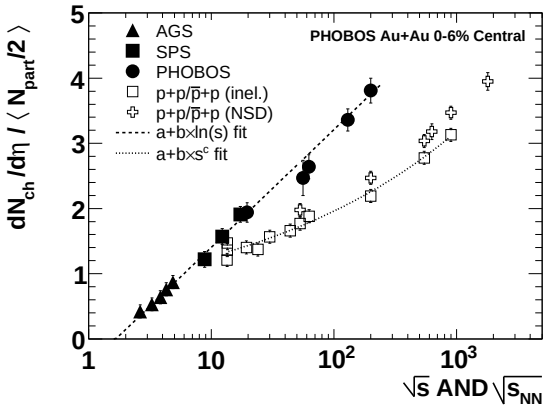

Fig. 3.7: Charged particle density at midrapidity, $dN_{ch}/d\eta|_{|\eta|<1}$, normalized to one pair of nucleons participating in the collision, as a function of collision energy, $\sqrt{s_{NN}}$, for the most central $Au + Au$ collisions compared with $p + p$, $p + \overline{p}$ and lower-energy $A + A$ data. Two fits: to the PHOBOS data (dashed line) and to the elementary collisions data (dotted line) are also shown [25].

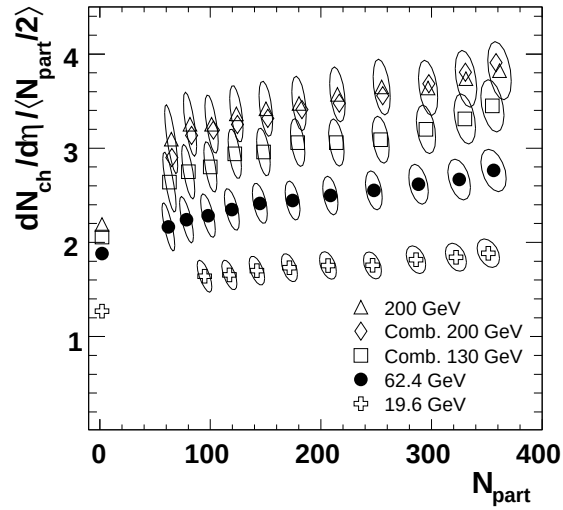

Fig. 3.8: Charged particle density at midrapidity, $dN_{ch}/d\eta|_{|\eta|<1}$, normalized to one pair of nucleons participating in the collision, as a function of N_{part} for four $Au + Au$ collision energies. For comparison, the points for inelastic $p + p$ collisions are included (measured data or extrapolations to the required energy, as described in Ref. [25]); the systematic errors are shown as ellipses corresponding to 90% C.L.

3.3 Charged particle density at η=0

The central rapidity region is very important in studies of the properties of the system created in the collisions, as the energy density released is related to the particle density at $\eta \approx 0$. This was the first measurement of the PHOBOS experiment [1], which showed that the particle density in the central region grows approximately linearly with $ln(\sqrt{s_{NN}})$ (Fig. 3.7). Before the first experimental results were obtained, most theoretical models predicted larger particle densities [165].

In a more differential approach presented in Fig. 3.8, the particle density at midrapidity, $dN_{ch}/d\eta|_{|\eta|<1}$, normalized to one pair of interacting nucleons, is shown as a function of collision centrality represented by N_{part} [5, 6, 14, 25]. A slow increase of the particle yield with centrality is observed; however, even for peripheral collisions this yield is larger than in elementary $p + p$ collisions. The observed centrality dependence can be fitted by a simple two-component parameterization [166] as a superposition of two terms, one from soft collisions, proportional to $\langle N_{part}\rangle$, and the other from hard collisions, multiplied by $\langle N_{coll}\rangle$:

$$\frac{dN_{ch}}{d\eta} = n_{pp}\left((1-x)\frac{\langle N_{part}\rangle}{2} + x\langle N_{coll}\rangle\right). \tag{3.1}$$

Precise determination of both n_{pp} and x, treated as free parameters, is not possible, but the dependencies for two extreme energies are compatible within systematic uncertainties with a similar fraction of hard collisions, x=0.13±0.01(stat)±0.05(syst) [14], while an increase of x with

energy is expected. The observed centrality dependence is in a better agreement with calculations from the saturation model [84, 167], than with predictions from the HIJING model [156].

3.4 Total charged particle multiplicity

The most obvious global observable for collisions of high energy particles and nuclei is the total multiplicity. In this Section the total charged particle multiplicity, which is easier to obtain experimentally than the number of all particles, is discussed. All neutral particles are rarely detected, even if undetectable neutrinos are excluded from consideration. Even for charged particles the acceptance of the detector is usually limited, which makes such a measurement difficult, as the number of observed particles has to be corrected using model dependent extrapolations. The PHOBOS experiment provides measurements in a very large range $|\eta| < 5.4$. The total multiplicity can be obtained after integrating the $dN_{ch}/d\eta$ distribution presented in Section 3.2. Only a few percent of particles are produced outside the acceptance of the detector, but as this fraction changes with the energy and the centrality of the collision, an extrapolation to the full phase space is necessary [26]. In this case the "limiting fragmentation" property of the $dN_{ch}/d\eta$ distributions can be used [8]. After the pseudorapidity distribution obtained at $\sqrt{s_{NN}}$=19.6 GeV is shifted by the difference in rapidities of the beams at two energies, for example for 200 GeV: $\Delta\eta = y_{beam,200} - y_{beam,19.6} = 2.32$, it overlaps near y_{beam} the $dN_{ch}/d\eta$ distribution at larger energy, which allows us to extend it significantly. With such an extrapolation the total multiplicity in the full phase space can be obtained. Larger uncertainty arises from the integration of the $dN_{ch}/d\eta$ distribution. The difference between direct sum of the experimental points and the integral of a smooth functional fit can reach up to 15% in the most peripheral data considered.

The results for four energies and many centralities of $Au + Au$ collisions are summarized in Fig. 3.9, where the total multiplicity scaled to one pair of participating nucleons as a function of N_{part} is presented. They confirm that within the errors N_{ch} is directly proportional to N_{part}. However, the value of $\langle N_{ch}\rangle/\langle N_{part}/2\rangle$ is about 40% larger than $\langle N_{ch}\rangle$ for $p + p$ or $p + \overline{p}$, and agrees rather with the multiplicity in $e^+ + e^-$ reactions [26].

The last observation can be verified in a comparison of $\langle N_{ch}\rangle/\langle N_{part}/2\rangle$ from nucleus-nucleus collision with $\langle N_{ch}\rangle$ from elementary interactions (Fig. 3.10). As the earlier observable is practically independent of collision centrality, it is necessary to show only the values for the most central collision. In addition to previously presented $Au + Au$ collisions at RHIC energies [25] also the $d + Au$ data at $\sqrt{s_{NN}}$=200 GeV [11], the $Au + Au$ data at $\sqrt{s_{NN}}$= 2.6-4.3 GeV (E895 experiment at AGS [56]) and the $Pb + Pb$ data at $\sqrt{s_{NN}}$= 8.6-17.3 GeV (NA49 experiment at SPS [168]) are shown. At high energies only $d + Au$ point coincide with $p + p$, while data for collisions of heavier nuclei are close to $e^+ + e^-$. Below 20 GeV $\langle N_{ch}\rangle/\langle N_{part}/2\rangle$ for $A + A$ collisions decreases faster than $\langle N_{ch}\rangle$ for elementary interactions and even drops below $p + p$, as is clearly shown in Fig. 3.10.

The difference between $e^+ + e^-$ and $p + p$ disappears when for the latter $\sqrt{s}$ is rescaled by a factor of 1/2 (the diamonds in Fig. 3.10). This is interpreted as the "leading particle" effect: the energy available for particle production in $p + p$ collisions is equal to the $p + p$ center of mass energy minus the energy of leading particles [169, 170]. In heavy ion collisions, for all centralities considered, each participating nucleon suffers on average 3 or more inelastic collisions. Obviously after experiencing several collisions the final "leading particle" has smaller momentum than in $p+p$ and this may explain the fact that no evidence of the "leading particle" effect is seen at RHIC energies.

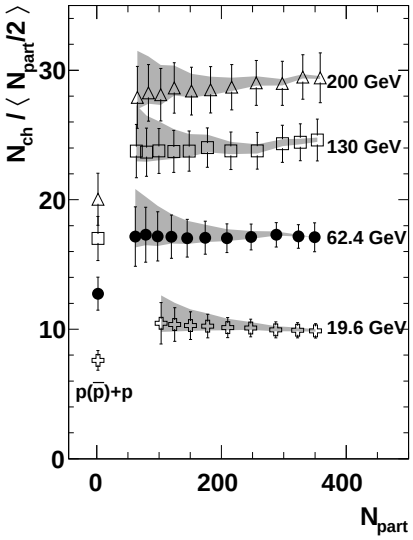

Fig. 3.9: The total charged particle multiplicity scaled to one pair of interacting nucleons, $\langle N_{ch}\rangle/\langle N_{part}/2\rangle$ as a function of centrality of the collision, represented by N_{part}, for four beam energies [25]. The error includes also the uncertainty of the N_{ch} and N_{part} scales. The shaded band shows the uncertainty of the extrapolation procedure (90% C.L.) described in the text. The points for elementary $p+p$ or $\bar{p}+p$ interactions were calculated according to a parameterization from Ref. [127].

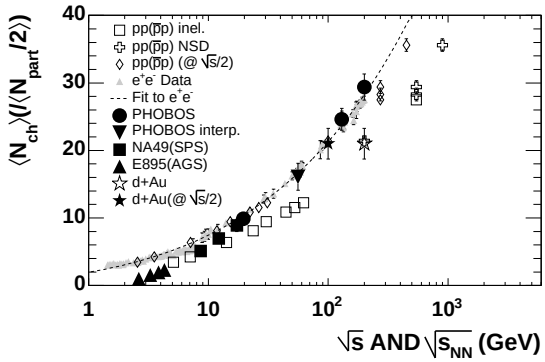

Fig. 3.10: The total charged particle multiplicity $\langle N_{ch}\rangle$ for $e^+ + e^-$, $p+p$ and $p+\overline{p}$ and scaled values $\langle N_{ch}\rangle/\langle N_{part}/2\rangle$ for nucleus-nucleus collisions ($d+Au$, $Au+Au$ and $Pb+Pb$) as a function of $\sqrt{s}$ or $\sqrt{s_{NN}}$ respectively [26]. The data for elementary interactions were taken from Ref. [171]; the nucleus-nucleus data are described in the text. For $p+p$, $p+\overline{p}$ and $d+Au$ points at $\sqrt{s}$ and at $\sqrt{s}/2$ are shown.

At lower collision energies another mechanism becomes important. The fraction of net baryons, proportional to N_{part}/N_{ch}, which is only about 5% at $\sqrt{s_{NN}}$=200 GeV, rises to 50% at AGS energy. This means that a large part of the energy that could be used for the production of particles in collisions at small $\sqrt{s_{NN}}$ is absorbed by the baryons.

3.5 Particle spectra

In the PHOBOS experiment momenta of particles were measured in a limited acceptance of the Spectrometer and particle spectra are thus available only at midrapidity. However, it is possible to reconstruct charged particles with very small momenta, starting from p_T= 30 MeV/c [15]. In Fig. 3.11 the yields for pions, kaons and protons are shown. They agree with extrapolations of the fits (performed in the higher p_T range) of models assuming expansion of the system [72].

The charged hadron production was studied also at larger momenta, in $Au+Au$ collisions [12], $d+Au$ collisions [10] and $Cu+Cu$ collisions [27]. In Fig. 3.12 the scaled yields obtained for central collisions of different nuclei are compared. In $d+Au$ collisions the value of R_{AA} (defined in Eq. 2.5) at large p_T is close to 1, indicating no suppression of high-p_T particles. In the most central $Au+Au$ collisions R_{AA} drops below 0.4 for $p_T > 3$ GeV/c, while

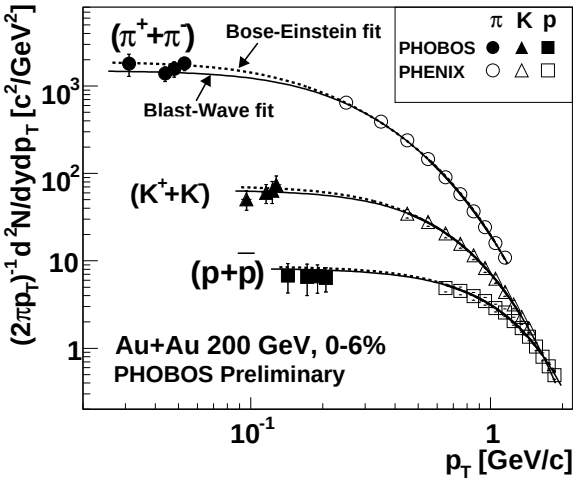

Fig. 3.11: Identified particle spectra near mid-rapidity in $Au + Au$ collisions at $\sqrt{s_{NN}}$=200 GeV. The Blast-Wave (solid lines) and Bose-Einstein (dotted lines) parameterizations were fitted to the PHENIX experiment data [172] at larger p_T and extrapolated to the lowest p_T points measured by the PHOBOS experiment, for details see Ref. [72].

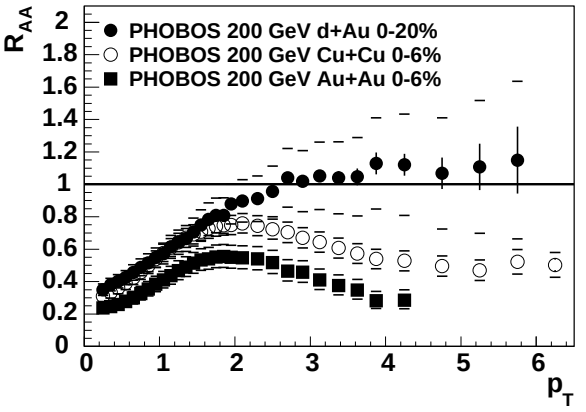

Fig. 3.12: Yields of charged particles in the central nucleus-nucleus collisions, scaled to the elementary interactions, as a function of transverse momentum [10, 12, 27]

for smaller systems like $Cu + Cu$ the suppression is also present, but with smaller magnitude. When the scaled yields are studied as a function of the centrality of $Au + Au$ or $Cu + Cu$ collisions a rather smooth evolution is observed [12, 27]. A comparison of R_{AA} at two different energies, $\sqrt{s_{NN}} = 62$ GeV and $\sqrt{s_{NN}} = 200$ GeV [17, 27] is also interesting. The R_{AA} values at the lower of these energies are much larger, close to 1, but also decrease with the centrality of the collision.

In $Au+Au$ and $Cu+Cu$ collisions the dependence of R_{AA} as a function of N_{part} (in the same p_T bins) is very similar [27]. This observation is consistent with predictions from a simple jet absorption model that includes a Glauber-based collision geometry and a quadratic dependence of absorption on a path length in an expanding medium [173], which predicts N_{part} scaling. However, in addition to the geometry of the collision and parton energy loss in the dense medium, which probably most significantly influence particle production in the high-p_T range, several other effects, like p_T broadening due to initial or final state multiple scattering ("Cronin effect"), a parton recombination, and collective velocity fields, may modify the observed yields.

3.6 Elliptic flow

In Section 2.4 the definition and properties of elliptic were already presented; the centrality and p_T dependences of elliptic flow were shown in Fig. 2.3. These results were obtained for particles at mid-rapidity, but the PHOBOS experiment measures the elliptic flow also as a function of

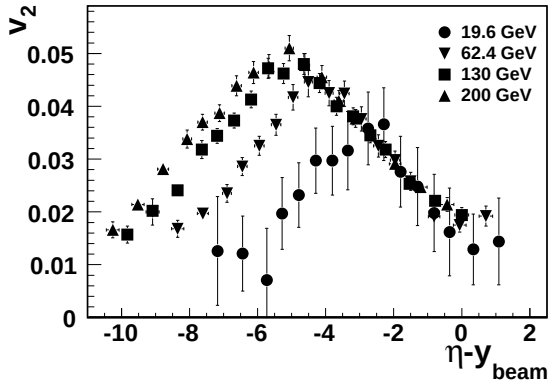

Fig. 3.13: Elliptic flow, v_2, as a function of pseudorapidity, after a translation to the rest frame of one of the colliding nuclei, in $Au + Au$ collisions at four different energies [18].

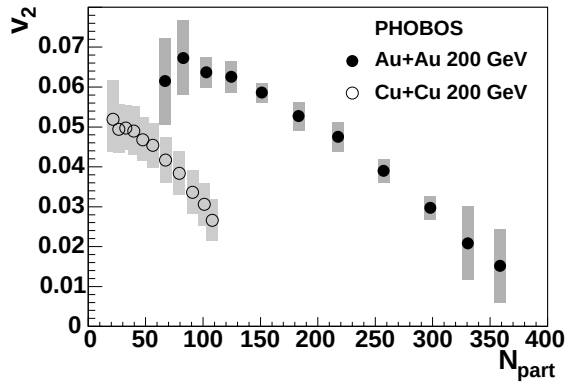

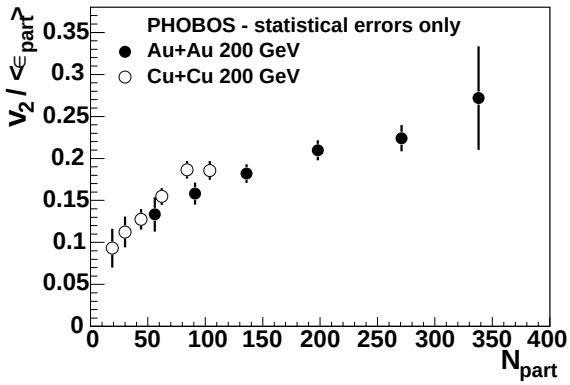

Fig. 3.14: Elliptic flow, v_2, at mid-rapidity as a function of the number of nucleons participating in the $Au + Au$ and $Cu + Cu$ collisions at $\sqrt{s_{NN}} = 200$ GeV(left) and the same dependences for the values of v_2 divided by the participant eccentricity, ϵ_{part} [31] (right).

pseudorapidity over a very wide range. As a function of pseudorapidity, v_2 is largest at $\eta = 0$ and decreases linearly for larger $|\eta|$ values [18]. In Fig. 3.13 the $v_2(\eta')$ distributions are shifted by beam rapidity, $\eta' = \eta - y_{beam}$, and thus represent dependences as seen in the rest frame of one of the nuclei. In this case scaling of $v_2(\eta')$ with energy is observed over a wide η' range that increases with energy of collisions. This feature is similar to the extended longitudinal scaling found earlier for the $dN/d\eta$ distribution (see Section 3.2).

Studies of the elliptic flow for different collision systems, $Au + Au$ and $Cu + Cu$, provide interesting results. A direct comparison of v_2 values, presented in Fig. 3.14 (left) as a function of N_{part}, gives distinctly different dependences; moreover in the most central collisions the value of v_2 is larger in $Cu + Cu$ collisions than in $Au + Au$ collisions. In Fig. 3.14 (right), agreement is reached when v_2 is divided by the participant eccentricity (described in Appendix B), which is a measure of the deviation of the area defined by nucleons participating in the collision from a circle [31]. This clearly indicates that elliptic flow is directly connected with collision geometry.

Section summary

The PHOBOS Collaboration has performed several studies that are unique among RHIC experiments. The charged particle pseudorapidity distribution was measured in a very wide range

$|\eta| < 5.4$. A smooth evolution of the $dN_{ch}/d\eta$ distribution as a function of collision energy and centrality was found. In the fragmentation area, an *extended longitudinal scaling* was observed in an increasing η' range. The particle density in the central region grows with collision energy as $\ln \sqrt{s_{_{NN}}}$. The total multiplicity increases with collision energy faster - approximately as $\ln^2 \sqrt{s_{_{NN}}}$.

The particle spectra measured at the lowest transverse momenta at RHIC do not show anomalous enhancement and are consistent with expansion of the system created in heavy-ion collisions. The yields of high-$p_{_T}$ are suppressed for the most central collisions and a smooth energy and centrality is observed.

The elliptic flow as a function of pseudorapidity has a triangular shape, with a maximum at midrapidity. In the rest frame of one of colliding nuclei a scaling similar to the *extended longitudinal scaling* found for particle density distributions is observed.

4 Charged particle multiplicity fluctuations and correlations

The study of general features of particle density distributions averaged over many events reveals at RHIC a rather smooth continuation of dependencies established at lower collisions energies. However, entering the unexplored area we may encounter new phenomena, which may be present only in a small fraction of events and can thus be detected in event-by-event analysis of fluctuations or in studies of correlations.

In the PHOBOS experiment a search for events with unusually high multiplicity or with the $dN_{ch}/d\eta$ distribution deviating strongly from the average shape was carried out. The search was performed for the most central $Au + Au$ collisions at the highest available energy $\sqrt{s_{NN}} = 200$ GeV (Section 4.1). Less spectacular fluctuations may be detected in the analysis of the difference of multiplicities in symmetric pseudorapidity bins. The variance of $C = \frac{N_F - N_B}{\sqrt{N_F + N_B}}$ was studied at the same energy, but in addition to the central events also semi-peripheral events were separately analyzed (Section 4.2). The studies of correlations include general two-particle correlations between all charged particles in a very wide pseudorapidity interval and correlations with a high-p_T trigger particle (Section 4.3 and Section 4.4, respectively). Results on multiplicity fluctuations and correlations from other RHIC experiments are presented in Section 4.5.

4.1 Search for unusual events

Fluctuations in particle production might appear both in the first order and in the second order phase transition. Observation of events with large multiplicities in nucleus-nucleus collisions at extreme energies, found in cosmic ray interactions by the JACEE Collaboration [174], gave rise to speculation that they might be a sign of a QGP creation. Any observation of both a large total multiplicity and fluctuations in a limited pseudorapidity and azimuthal angle range are interesting. At the SPS energies such fluctuations were analyzed by NA44 Collaboration [175] and WA80 Collaboration [176]. The first of these studies was sensitive to local fluctuations involving at least 3% of particles measured in a relatively small acceptance ($1.4 < \eta < 3.7$), and the probability that they exceed statistical fluctuations by more than 3 RMS was found to be less than 10%. The multiplicity and transverse energy distributions measured by the WA80 Collaboration have Gaussian tails, thus the probability of finding events characterized by much larger energy density than the average is limited. At the much larger energy in $Au + Au$ collisions, the PHOBOS Collaboration tested the hypothesis of large fluctuations using multiplicity and angular distributions measured in almost the full solid angle.

The most interesting event sample in which unusual fluctuations may appear consists of the most central $Au + Au$ collisions, selected by a 3% centrality cut. In the PHOBOS experiment over 1,900,000 such events were measured at energy $\sqrt{s_{NN}} = 200$ GeV. In this study the raw number of particles without occupancy corrections, as obtained by "hit counting" method (described in Section D), was used. The distribution of the total multiplicity counted in the range $|\eta| < 5.4$ has a small tail of large multiplicities (Fig. 4.1). The fraction of such events is less than 0.1% and was found to be correlated with the luminosity of the accelerator at the time of the measurement [177] (Fig. 4.2). This clearly indicates that the most probably source of such events is a pile-up effect. At RHIC two beams of gold nuclei are divided into 60 bunches of ions each. These bunches collide several times in the read-out time of the silicon detectors which

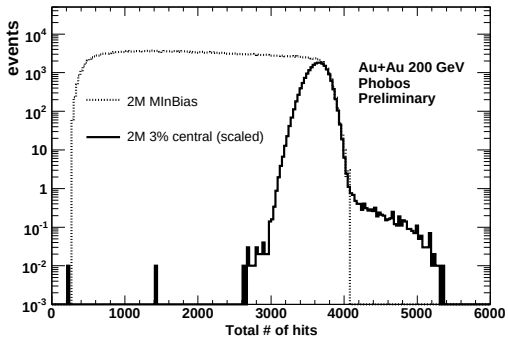

Fig. 4.1: The distribution of the total number of charged particles registered in the Multiplicity detectors for events without centrality selection and in the 3% most central $Au + Au$ collisions.

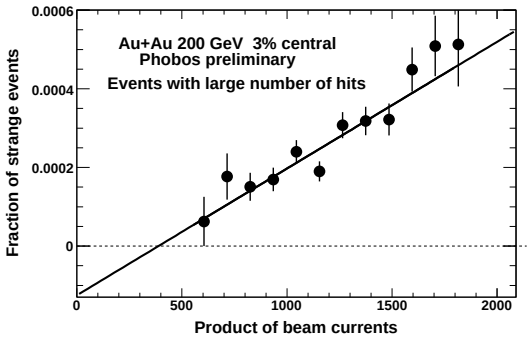

Fig. 4.2: The number of events with more than 4400 detected charged particles as a function of luminosity represented here by the product of the currents in two RHIC beams.

measure the multiplicity of charged particles. Although luminosity is not very high and usually a nucleus-nucleus collision happens once per many bunch crossings it is still possible that in the time between the trigger signal from the fast scintillator detectors and the completion of the measurement in the silicon other $Au + Au$ collisions occur and the total multiplicity registered is the sum of the multiplicities of two or more collisions. Even if cuts intended to remove such events are applied, some of these events are not rejected. The estimated remaining pile-up ratio is consistent with the observed tail of large multiplicities. In addition the fraction of events with large multiplicities extrapolated to luminosity equal zero is consistent within errors with zero (Fig. 4.2).

In the second attempt [44] a more efficient pipe-up rejection method was applied and the analysis was focused on the fluctuations of the $dN_{ch}/d\eta$ distribution. For each central event we determined the raw angular distribution of charged particles as a function of pseudorapidity, $M(\eta)$, and calculated the mean value $\langle M(\eta)\rangle$ and variance $\sigma^2_{\rm M}(\eta)$ in narrow bins of vertex position (to minimize acceptance fluctuations). The deviation of the η distribution from the average was then measured by:

$$\chi^2_{\rm NDF} = \frac{1}{N_{\eta\rm bins}} \sum_{\eta} \frac{(M(\eta) - S\langle M(\eta)\rangle)^2}{\sigma^2_{\rm M}(\eta)} \tag{4.1}$$

where $N_{\eta\rm bins}$ denotes the number of bins in η in which $M(\eta)$ is defined and S is the fitted scaling factor accounting for varying total multiplicity. We defined as unusual any events with $\chi^2_{\rm NDF} > 3$. For the 51 degrees of freedom in the fit such large values of $\chi^2_{\rm NDF}$ should not happen in our sample. Without any pile-up cuts we obtained several hundreds of such events. This is not very surprising, as for events containing two collisions at different vertex positions one expects a non-statistical deformation of the $M(\eta)$ distribution.

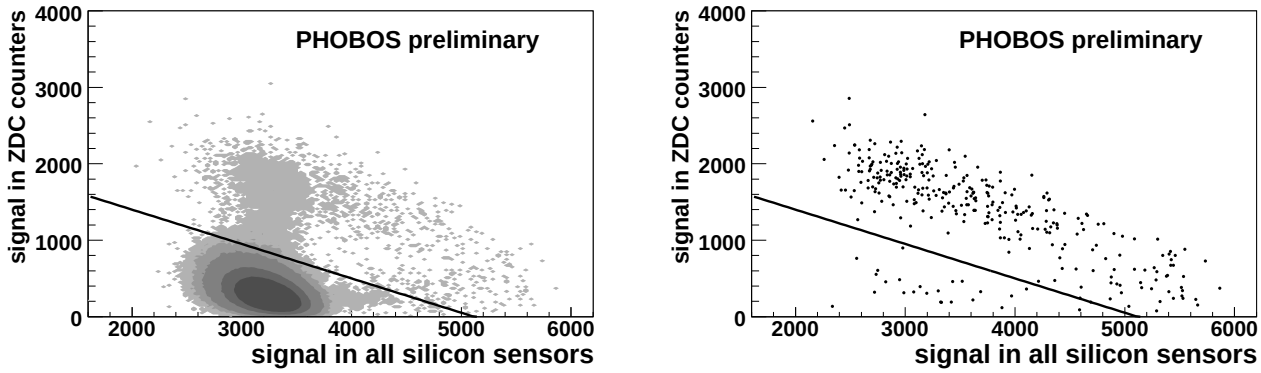

Fig. 4.3: Rejection of pile-up events using the signal from Zero Degree Calorimeters and from the Multiplicity detector (*pile-up cut II*). The rejected pile-up events lie above the line; the left plot was obtained for all most central events, the right plot for events with unusual $dN_{ch}/d\eta$ distributions.

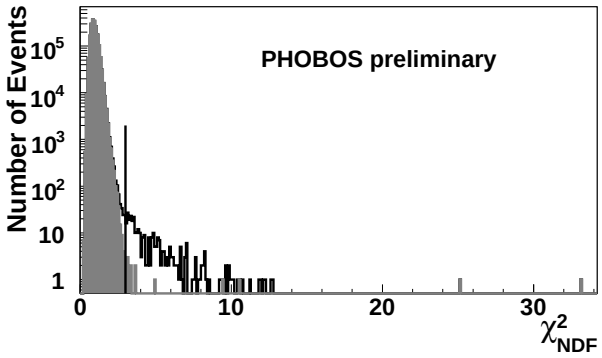

Fig. 4.4: The distribution of χ^2_{NDF} for all most central events (histogram) and those accepted by pile-up *cut I* and *cut II* (shaded area).

In the first paper [177] only the *pile-up cut I* was applied, which compared the signals in the silicon detectors (long integration time) with signals in the trigger paddle scintillator counters (registering particles created during only one beam crossing). Events with a large number of particles (hits) registered in the silicon for which the signal in the paddles was not proportionally high were rejected. This eliminated events containing two $Au + Au$ collisions which occurred at different bunch crossings. Still the double collisions occurring in the same beam crossing pass this *pile-up cut I* and need to be identified by a different method. This is possible with the help of the Zero Degree Calorimeters (ZDC), which register spectator neutrons from the interacting nuclei. In the case of a central $Au + Au$ collision practically all nucleons interact and thus the signal in the ZDC should be very low. Presence of the signal means that in addition to the central collision also a semi-central or a peripheral collision occurred in the same bunch crossing. There are still two types of pile-up cases that are not visible in the ZDC. The additional collision has either to be another extremally central collision (without spectator nucleons) or a very peripheral collision (in which colliding nuclei do not break into single nucleons but survive as one or a few heavier, charged fragments). The events with two collisions, one very central and a second semi-central, are rejected by the *pile-up cut II*, as shown in Fig. 4.3(left). At the multiplicity typical for the most central events (i.e. signal in the silicon sensors approximately between 2500-4000) the *pile-up cut II* removes the events with one central and one semi-peripheral collision. The pile-up events with two very central collisions

should have about double the total multiplicity, and are also rejected as the maximal accepted signal in the silicon sensors is 5000.

The effect of the *pile-up cut II* involving the ZDC signal on the selected unusual events is presented in Fig. 4.3 (right). We can see that the majority of unusual events lie above the line and are rejected. Some of the remaining events are rejected by the *pile-up cut I*. The χ^2_{NDF} distribution before and after the cuts is shown in Fig. 4.4. The final ratio of central events with an unusual shape of the $dN_{ch}/d\eta$ distribution is smaller than 10^{-5}. It can not be excluded that these events do not differ from the typical central $Au + Au$ interaction and their unusual properties are due to some unclear detector effects.

In the study of the most central Au+Au collisions measured in the PHOBOS experiment very few events with unusually large multiplicities or large fluctuations of particle density were found. This allows us to set only an upper limit on the probability of observing unusual phenomena at the level of 10^{-5}.

4.2 Forward-backward multiplicity correlations

The futile search for large fluctuations in the total multiplicity and the shape of $dN_{ch}/d\eta$ distribution does not imply that only purely statistical fluctuations occur in the process of particle production in heavy ion collisions. If the fluctuations are frequent, but relatively small, they have no chance to be detected in the study presented in the previous section, but may be revealed using a different approach.

It is difficult to detect the difference between an observable obtained for one event and its mean value characterizing a sample of events if the sample is not fully homogeneous. The variation of the values observed in the sample may contain both the contribution from dynamical fluctuations and the dependence of the mean value on a parameter which is not fully controlled. One such parameter that may obscure other sources of fluctuations is the centrality of the collision.

To be sensitive to small and frequent fluctuations from other sources it is better to look at observables on an event-by-event basis for events for which the centrality dependence is removed. Such a possibility is offered by the asymmetry parameter

$$C = \frac{N_B - N_F}{\sqrt{N_F + N_B}} \tag{4.2}$$

where N_F and N_B denote the number of particles measured in pseudorapidity bins symmetric with respect to $\eta = 0$, at positive and negative η, respectively. In symmetric collisions this observable has several useful features:

- the particles counted in N_F and N_B belong to the same kinematical; regions
- the mean value $\langle C \rangle = 0$;
- if the particles are randomly partitioned to the F and B bins with probability $p = 0.5$ then the variance $\sigma^2_C = \sigma^2(C) = 1$.

In the presence of positive correlations decreasing the difference $N_F - N_B$ values of $\sigma^2_C < 1$ are expected. Values of σ^2_C larger than one occur in two cases: a negative correlation between N_F and N_B or the presence of short range correlations, which also enhance the difference between N_F and N_B.

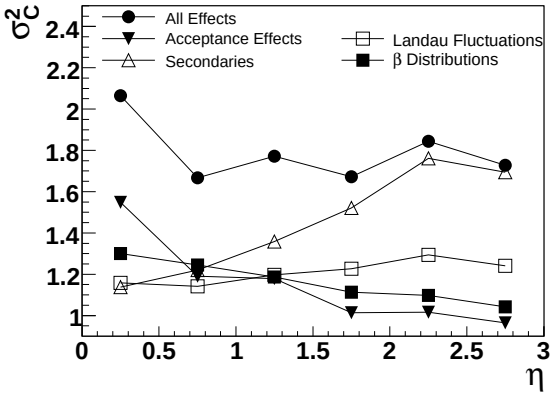

Fig. 4.5: Contributions from detector effects and background to σ_C^2 obtained for bins with the same width $\Delta\eta = 0.5$ but different positions of the center, η.

The latter case can be easily explained by a simple example. If particles are produced always in pairs and not the particles, but the pairs, are partitioned randomly in the bins, then we observe $2N_F$ and $2N_B$ particles (where N_F and N_B denote now the number of pairs) in F and B bins. In this case:

$$\sigma_C^2 = \left\langle \frac{(2N_B - 2N_F)^2}{2N_B + 2N_F} \right\rangle = 2 \left\langle \frac{(N_B - N_F)^2}{N_B + N_F} \right\rangle \tag{4.3}$$

The same reasoning can be repeated for any number of particles produced together. It might be surprising that the study of correlations between distant kinematical regions might provide any information on *local* properties of the particle production. It is however possible only if there exists a *global* correlation that ensures similar production, with statistical deviations only, in both η regions considered.

The σ_C^2 observable is thus suitable for detection of clusters, objects which break into finally observed particles with close values of η. In the general case we expect that some particles are still produced independently and there are clusters with different sizes, K. In addition the limited width of the pseudorapidity bins means that some of the correlated particles from a cluster are not counted in N_F (or N_B). All this means that K varies following an (unknown) distribution. The apparent change $\sigma_C^2 \mapsto K_{eff}\sigma_C^2$ involves the effective cluster size, K_{eff}, which is defined as:

$$K_{eff} = \langle K \rangle + \sigma_K^2 / \langle K \rangle \tag{4.4}$$

The analysis of forward-backward correlations was performed by the PHOBOS Collaboration using the $Au + Au$ data at $\sqrt{s_{NN}} = 200$ GeV [24, 43]. Charged particles emitted in the pseudorapidity range $|\eta| < 3$ were registered in the Octagonal Multiplicity detector. Only half of the azimuthal acceptance was used, as the ϕ segments with the holes for the Spectrometer and the Vertex detector were omitted in order to avoid problems with incomplete acceptance in pseudorapidity. The number of particles in each η bin analyzed was reconstructed using the energy loss of hits registered in this bin. Hits with low signals were removed in order to reject electronic noise, while a high-energy threshold was applied to reduce effects of low-momentum secondaries. For each event and η bin the sum of energy losses corrected for the incidence angle was calculated and divided by the average energy loss per particle. The values of $\langle C \rangle$ were calculated as a function of pseudorapidity bin, primary vertex position and centrality of the $Au + Au$ collision. The non-zero values of $\langle C \rangle$ were then corrected to remove acceptance effects due to the asymmetry of small gaps between the octagon sensors for events with different vertex positions.

The values of $\sigma^2_{C,raw}$ obtained in the above described procedure are still strongly affected by detector related effects: acceptance, secondary particles, the tail of the Landau distribution of energy loss and variation of energy loss for different velocities β of particles. The importance of each source of modifications was studied in simulations in which only one of the effects was present. In Fig. 4.5 results obtained for the bins with $\Delta\eta = 0.5$ are shown as a function of pseudorapidity. The acceptance effects dominate only in the case of very close bins; for larger η the contribution from secondary particles is the most important. The primary particles emitted at small angles traverse a much longer path in the beam pipe, thus the number of secondary background particles increases with $|\eta|$. The values of $\sigma^2_{C,raw}$ increase also due to fluctuations in the energy losses from the long tail of the Landau distribution and the variation of velocities of particles with different masses. According to simulations, these contributions combine in quadrature; the value of $\sigma_C - 1$ obtained for *All Effects* in Fig. 4.5 is a sum of $\sigma_C - 1$ values from independent sources (note: *Landau Fluctuations* are already included in contribution for *Secondaries*). To remove the undesired contributions we can thus use the formula

$$\sigma^2_C = \sigma^2_{C,raw} - (\sigma^2_{C,det} - 1) \tag{4.5}$$

where σ^2_C denotes the forward-backward correlation between primary particles and $\sigma^2_{C,det}$ is an additional contribution from all detector effects[3].

The value of $\sigma^2_{C,det}$ was determined separately for each analyzed η bin using simulations of standard HIJING and AMPT events and the same events after modifications that removed any intrinsic non-statistical correlations To achieve this, the signs of η for all particles were randomly generated without changing $|\eta|$ thus preserving the kinematical properties of events. Finally, the values obtained for half-azimuth acceptance were corrected to the full ϕ acceptance:

$$\sigma^2_{C,\Delta\phi=2\pi} = 2(\sigma^2_{C,\Delta\phi=\pi} - 1) + 1 \tag{4.6}$$

The validity of this formula was confirmed by Monte Carlo simulations. Further details of the reconstruction procedure presented here can be found in Ref. [24].

The study of forward-backward correlations was performed for two centrality classes, 20% of the most central events (denoted as 0-20%) and the peripheral events (denoted as 40-60%). Two types of pseudorapidity bins were analyzed:

- bins of constant width, $\Delta\eta = 0.5$, but varying positions of the centers from $\eta = 0.25$ to $\eta = 2.75$ (from $\eta = -0.25$ to $\eta = -2.75$ for B bin)
- bins with the same positions of the centers, $\eta = 2$ ($\eta = -2$ for B bin), but the width of the bins changing from $\Delta\eta = 0.25$ to $\Delta\eta = 2$

In Fig. 4.6 the values of σ^2_C corrected for all detector effects are presented and compared to results from two Monte Carlo generators, HIJING and AMPT. Even after a brief examination it is obvious that the experimental values and model predictions follow similar trends, but the data points are systematically higher than the model predictions.

In the case of the dependence on the position of the bins in η (upper panels in Fig. 4.6) an increase of the variance is observed. When there is no gap between the bins ($\eta = 0.25$) σ^2_C is very close to 1, as it is expected for purely statistical fluctuations. This can be explained easily

[3]In simulations used in Fig. 4.5 the number of primary particles in the F and B bins was statistically fluctuating, thus the values were always greater than 1. From the value of $\sigma^2_{C,det}$ shown in Fig. 4.5 the contribution from statistical fluctuations has to be subtracted in Eq. 4.5

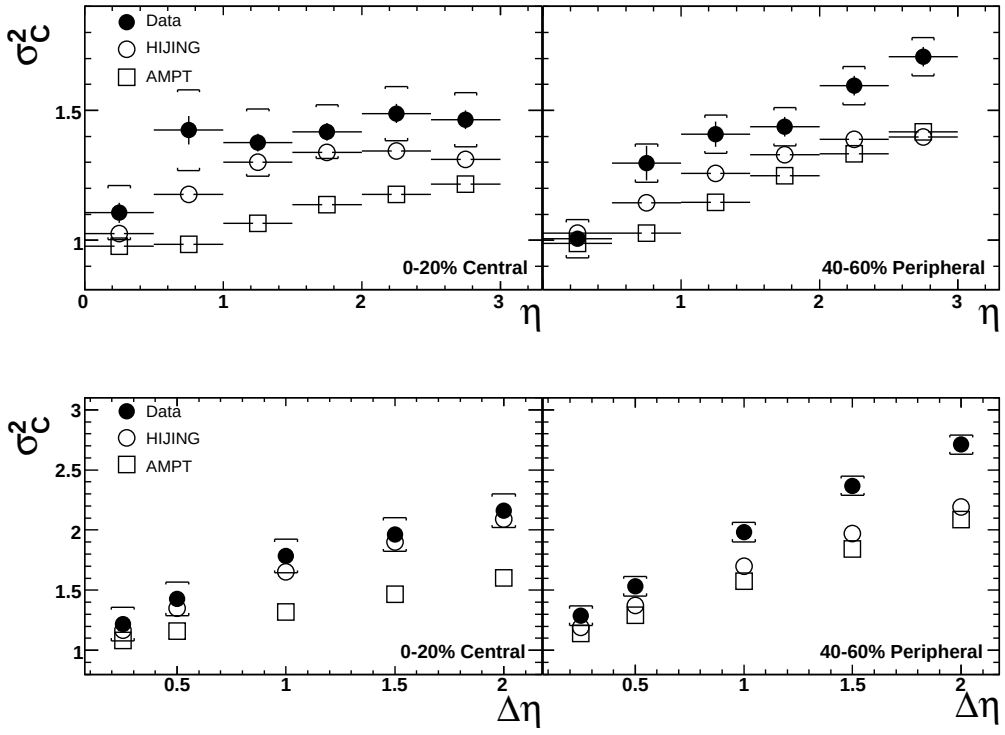

Fig. 4.6: Variance of the C parameter in $Au + Au$ collisions at $\sqrt{s_{NN}} = 200$ GeV for the most central events (left side) and peripheral events (right side), presented as a function of pseudorapidity (the center of the F bin) for bins of the constant size $\Delta\eta = 0.5$ (upper plots) and as a function of the bin width $\Delta\eta$ for bins centered at the same position ($\eta = 2$ for F bin) (lower plots). The statistical errors are denoted by the vertical bars, the systematic errors by the brackets. For comparison, results of calculations for primary charged particles from the HIJING and AMPT generators are shown.

in the context of cluster production: the enhancement caused by clusters registered in one of the bins (which contribute only to N_F or only to N_B) is compensated by the clusters which contribute *both* to N_F and to N_B. The σ^2_C values grow with increasing separation of the bins.

A monotonic rise of σ^2_C is observed when it is studied as a function of bin width $\Delta\eta$ (lower panels in Fig. 4.6). In the case of production and decay of clusters such a dependence is again expected as an acceptance effect: in the narrow bins usually only one particle from a cluster is accepted, while for very wide bins many clusters are fully accepted and the effective cluster size is large.

Because of relatively large systematic errors it is difficult to establish any centrality dependence for the narrow η bins (plots in the upper panels in Fig. 4.6). The centrality dependence is conspicuous for wider bins (plots in the lower panels) - the peripheral events are characterized by much larger σ^2_C values than the central events. This can be explained by larger cluster size in the peripheral events, but also other phenomena may contribute to the difference. The HIJING model predicts larger σ^2_C values than AMPT, and is thus always closer to the data points. However, the AMPT model exhibits the same centrality dependence as the data, even

if it always significantly underestimates the forward-backward correlations.

The forward-backward multiplicity correlations were studied for Au+Au collisions at $\sqrt{s_{NN}} = 200$ *GeV in a very wide pseudorapidity range using the asymmetry variable C defined for symmetric* η *bins (Eq. 4.2) and its variance* σ_C^2*. The observed values* $\sigma_C^2 > 1$ *and dependencies on bin size and separation can be interpreted qualitatively as effects of the production of clusters that decay into finally observed particles. Correlations obtained for peripheral events are stronger than for central events. The Monte Carlo generators, HIJING and AMPT, do not describe the experimental data.*

4.3 Two-particle correlations

More detailed information on particle production may be provided by a direct analysis of correlations between pairs of particles. Such study was performed by the PHOBOS Collaboration for $p+p$ collisions at $\sqrt{s} = 200$ GeV and $\sqrt{s} = 410$ GeV [30] and later for $Cu+Cu$ and $Au+Au$ collisions at $\sqrt{s_{NN}} = 200$ GeV [36]. In the calculations the charged particle pair distribution

$$\rho_n^{\mathrm{II}}(\eta_1, \eta_2, \phi_1, \phi_2) = \frac{1}{n(n-1)\sigma_n} \frac{d^4\sigma_n}{d\eta_1 d\eta_2 d\phi_1 d\phi_2}$$

, and the single particle density distribution

$$\rho_n^{\mathrm{I}}(\eta, \phi) = \frac{1}{n\sigma_n} \frac{d^2\sigma_n}{d\eta d\phi}$$

, are used to obtain the inclusive two-particle correlation function:

$$R(\eta_1, \eta_2, \phi_1, \phi_2) = \left\langle (n-1) \left(\frac{\rho_n^{\mathrm{II}}(\eta_1, \eta_2, \phi_1, \phi_2)}{\rho_n^{\mathrm{I}}(\eta_1, \phi_1)\rho_n^{\mathrm{I}}(\eta_2, \phi_2)} - 1 \right) \right\rangle . \tag{4.7}$$

For the further analysis the function defined in the 4-dimensional space is less convenient then the correlation function of the difference between the pseudorapidities and azimuthal angles of two particles:

$$R(\Delta\eta, \Delta\phi) = \left\langle (n-1) \left(\frac{\rho_n^{\mathrm{II}}(\Delta\eta, \Delta\phi)}{\rho^{\mathrm{mixed}}(\Delta\eta, \Delta\phi)} - 1 \right) \right\rangle . \tag{4.8}$$

This function is obtained from $\rho_n^{\mathrm{II}}(\eta_1, \eta_2, \phi_1, \phi_2)$ by averaging over the acceptance of the detector, $-3 < \eta < 3$ and $-\pi < \phi < \pi$ for the PHOBOS experiment. The single particle density functions are replaced in this case by a background distribution of $\Delta\eta$ and $\Delta\phi$ obtained for pairs of uncorrelated particles taken randomly from different events. The factor $(n-1)$ in Eq. 4.8 compensates for a faster growth of the number of uncorrelated pairs than correlated pairs [178]. This factor ensures that if $A + A$ collisions are a simple superposition of $p + p$ interaction the correlation function is the same in both cases. In the following discussion the correlation functions averaged over one of the variables, $\Delta\eta$ or $\Delta\phi$, are used. They are defined as:

$$R(\Delta\eta) = \left\langle (n-1) \left(\frac{\int \rho_n^{\mathrm{II}}(\Delta\eta, \Delta\phi) d\Delta\phi}{\int \rho^{\mathrm{mixed}}(\Delta\eta, \Delta\phi) d\Delta\phi} - 1 \right) \right\rangle , \tag{4.9}$$

and

$$R(\Delta\phi) = \left\langle (n-1) \left(\frac{\int \rho_n^{\mathrm{II}}(\Delta\eta, \Delta\phi) d\Delta\eta}{\int \rho^{\mathrm{mixed}}(\Delta\eta, \Delta\phi) d\Delta\eta} - 1 \right) \right\rangle . \tag{4.10}$$

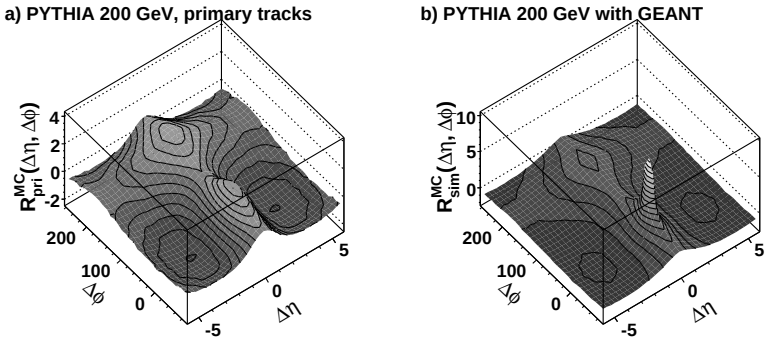

Fig. 4.7: Two-particle correlation function in $p+p$ interactions at $\sqrt{s_{NN}} = 200$ GeV for primary particles from the PYTHIA generator (a) and for the hits obtained in simulations of the same events (b).

In the PHOBOS experiment hits of charged particles registered in the Octagonal Multiplicity detector are used. The multiplicity in $p+p$ interactions is very low and almost every registered hit is produced by a single particle. For $Cu+Cu$ collisions and especially for $Au+Au$ collisions the occupancy in this detector is much larger and frequently two or more particles traverse the same pad in a silicon sensor. However, the ionization energy loss registered in the silicon sensor is larger when several particles traverse the same element. This allows the determination of the probability that a given hit was left by one, two, or more particles and the calculation of the particle density functions using this information [36].

The hits registered in the detector are left not only by primary particles, but also by products of secondary interactions (mostly in the beam pipe and in support structures of the detector) and by decays. The procedure of the hit reconstruction and the acceptance of the detector also affect the raw correlation function. The magnitude of these effects can be observed in Fig. 4.7, where the correlation function for the primary charged particles (Fig. 4.7a) is compared with the same function calculated using hits obtained in the GEANT Monte Carlo simulations of the same events (Fig. 4.7b). Using the results of the simulations, the raw correlation function obtained from the experimental data can be corrected:

$$R^{\mathrm{data}}_{\mathrm{final}}(\Delta\eta, \Delta\phi) = A \times [R^{\mathrm{data}}_{\mathrm{raw}}(\Delta\eta, \Delta\phi) - S(\Delta\eta, \Delta\phi)]. \tag{4.11}$$

The function $S(\Delta\eta, \Delta\phi)$ represents the contribution from secondary particles and decays, while the A parameter compensates for the holes in the detector acceptance. The sharp peak at $\Delta\eta = 0$ and $\Delta\phi = 0$ present in the raw data and in the GEANT simulations (see Fig. 4.7b), due mostly to δ-electrons, is not completely removed by the correction procedure. Most probably it arises from background sources or detector effects that are not included in the simulations, although unknown physical effects can not be excluded. For the analysis of correlations at larger distances the particle pairs from the region ($|\Delta\eta| < 0.15$ and $|\Delta\phi| < 5.625°$) are rejected.

The analysis of data from the PHOBOS experiment was performed for $p+p$ collisions at center-of-mass energies 200 GeV and 410 GeV [30], and for $Cu+Cu$ and $Au+Au$ collisions at $\sqrt{s_{NN}} = 200$ GeV [36]. About 500,000 and 800,000 events from $p+p$ interactions at two beam energies and about 4 million events for both $Cu+Cu$ and $Au+Au$ collisions were used. Examples of the correlation function $R(\Delta\eta, \Delta\phi)$ are shown in Fig. 4.8. Quantitative study of the correlations is simpler for a function of only one variable, averaged over the second one (Eqs. 4.9 and 4.10). As an example the correlation function in pseudorapidity, $R(\Delta\eta)$, in $p+p$ collisions is shown in Fig. 4.9. It can be fitted by the parameterization proposed in

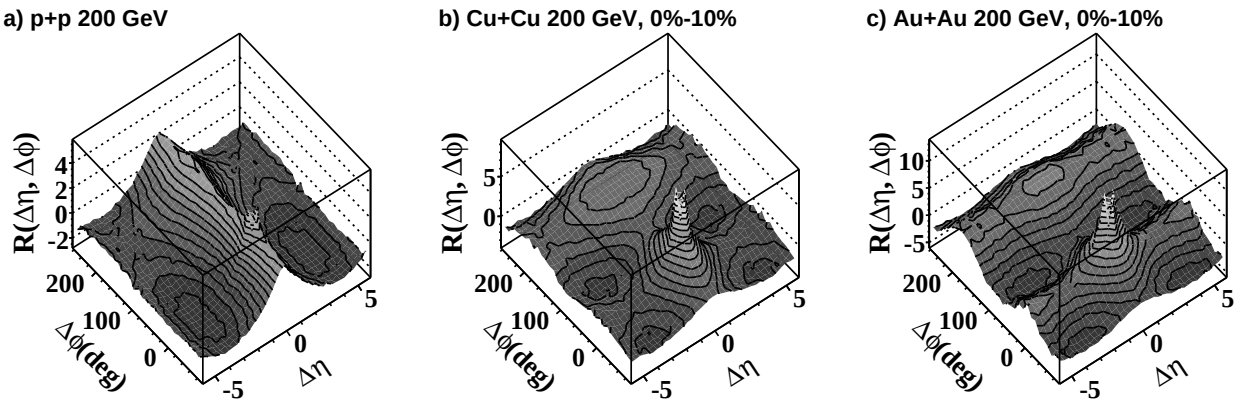

Fig. 4.8: The reconstructed two-particle correlation function in $p+p$ interactions (a), for the most central $Cu+Cu$ collisions (b), and the most central $Au+Au$ collisions (c) at energy $\sqrt{s_{NN}} = 200$ GeV.

Ref. [179], slightly modified here, which is appropriate for describing correlations as the result of independent emission and decay of clusters:

$$R(\Delta\eta) = \alpha \left[\frac{\Gamma(\Delta\eta)}{\rho^{\text{mixed}}(\Delta\eta)} - 1 \right] \tag{4.12}$$

where the background distribution $\rho^{\text{mixed}}(\Delta\eta)$ is obtained by mixing particles from different events, $\Gamma(\Delta\eta) \propto exp[-(\Delta\eta)^2/(4\delta^2)]$. The correlation strength parameter α is connected with the number of particles in the cluster decay, K, by the relation:

$$\alpha = K_{eff} - 1 \tag{4.13}$$

where the effective cluster size is calculated as

$$K_{eff} = \langle K \rangle + \frac{\sigma_K^2}{\langle K \rangle} \tag{4.14}$$

and where σ_K^2 denotes the variance of the K distribution. By measuring correlations it is not possible, in the general case of a mixture of different clusters, to extract the mean number of particles in the decay of the cluster, $\langle K \rangle$, but only the effective cluster size, K_{eff}. The second parameter, δ, is equal to the RMS of the distance in pseudorapidity, $\Delta\eta$, between the particles from the cluster. For clusters with fixed size K:

$$\delta = \sqrt{\frac{K}{K-1}}\ \sigma_\eta \tag{4.15}$$

where σ_η denotes the RMS of the pseudorapidity distribution of particles in the cluster with respect to its center:

$$\sigma_\eta = \sigma(\eta_{particle} - \eta_{cluster}) \tag{4.16}$$

The azimuthal correlation function, $R(\Delta\phi)$, obtained by averaging the two-dimensional function $R(\Delta\eta, \Delta\phi)$ over pseudorapidity, is shown in Fig. 4.10. The experimental results are very similar to the calculations for the particles obtained from the PYTHIA generator [180]. In Section 5.1 it is shown that the transverse momentum conservation effects determine the shape

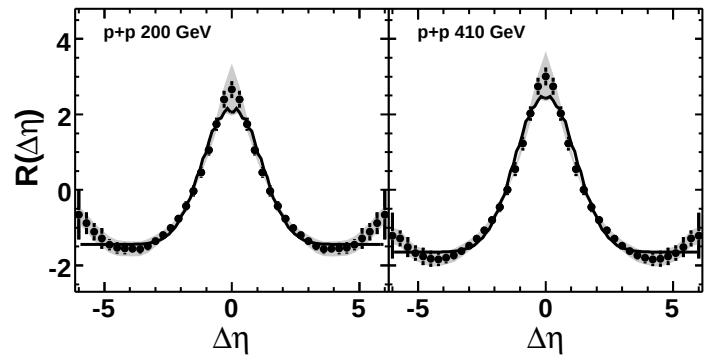

Fig. 4.9: The two-particle pseudorapidity correlation function in $p + p$ interactions (points). The statistical errors are negligible; the error bars correspond to point-to-point systematic errors and the shaded bands correspond to the overall scale error. The solid lines were obtained from the fit of the function defined in Eq. 4.12.

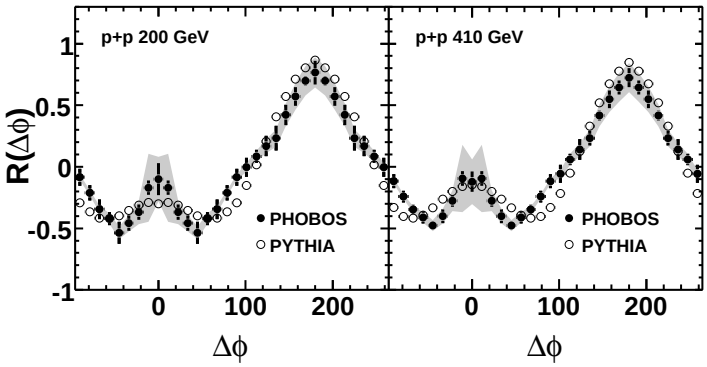

Fig. 4.10: The two-particle azimuthal correlation function in $p + p$ interactions obtained from PHOBOS experimental data and for particles generated using PYTHIA. The meaning of the errors is the same as in Fig. 4.9.

of the azimuthal correlation function. It is thus not surprising that the experimental data and the realistic model of $p + p$ interactions (which takes momentum conservation into account) give similar results.

The most interesting results that can be obtained from the two-particle correlations analysis are thus the cluster parameters K_{eff} and δ extracted from $R(\Delta\eta)$. In Fig. 4.11 the results for $p + p$ interactions are shown as a function of collision energy. The effective cluster size is increasing with $\sqrt{s_{NN}}$ but the δ values are similar for all available energies. The two models of $p + p$ interactions, PYTHIA and HIJING predict similar δ but much lower cluster size.

It is necessary to note here that the values shown in Fig. 4.11 were measured in the experiments with slightly different acceptances: $|\eta| < 4$ (but with a hole in azimuth) for the ISR data [178], $|\eta| < 3$ for the PHOBOS experiment [30], and $|\eta| < 4$ for the SPS-UA5 data [181] and thus only the PHOBOS data and the values obtained from PYTHIA and HIJING models (using PHOBOS acceptance cuts) are directly comparable. The clusters near the acceptance boundary are only partially registered and their contribution to reconstructed values of K_{eff} and δ are smaller than the real cluster parameters. For a long time these effects were considered negligible for the acceptance of 6 pseudorapidity units or more, however more detailed studies of the Simple Cluster Model (presented in Section 5) have shown that the effect is very important. The modification of cluster parameters due to limited acceptance can be easily determined for events with identical clusters. However, in the experimental data we have always a mixture of clusters with different parameters. Unfortunately the correction appropriate for a mixture of

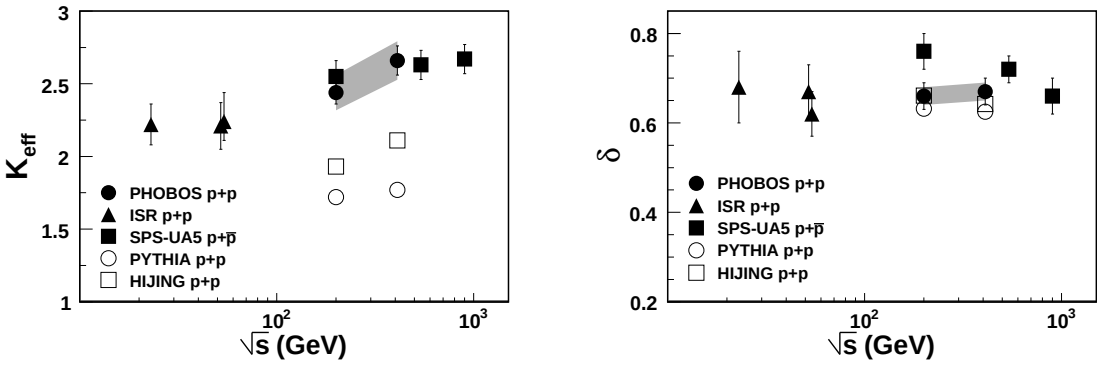

Fig. 4.11: The cluster parameters K_{eff} (left) and δ (right) in $p+p$ interactions as a function of the collision energy. The values shown were not corrected for the limited acceptance effects.

clusters can not be calculated using clusters with some effective parameters as it depends on the cluster composition in a complicated way (see Section 5.3 for details).

The acceptance correction can not be thus obtained in a fully model independent way. In the PHOBOS experiment it was calculated using several different models, by performing the same reconstruction procedure as for the experimental data either with acceptance cuts applied (denoted by a superscript $|\eta| < 3$) or without any cuts (denoted by a superscript $|\eta| < \infty$). In Fig. 4.12 two ratios of cluster parameters $K_{eff} - 1$ and δ are drawn for several generators. The simple independent cluster model (ICM) assumes isotropic decay of clusters in their rest frames. In some cases the η distribution of particles from clusters was artificially widened to obtain large values of $\delta^{|\eta|<3}$ [36]. The results for $p+p$ collisions are obtained from PYTHIA generator and those for nucleus-nucleus collisions from HIJING and AMPT generators.

After applying the above described acceptance correction to PHOBOS experimental $p+p$ data at $\sqrt{s_{NN}} = 200$ GeV shown in Fig. 4.11 we obtain $K_{eff}^{|\eta|<\infty} = 3.02$ and $\delta^{|\eta|<\infty} = 0.9$ (without this correction 2.44 and 0.66, respectively). The results from other experiments can not be corrected using the functions from Fig. 4.12, because of different acceptance ranges and different width of the $dN_{ch}/d\eta$ distribution, possible are only some speculations. The correction for UA5 data should be most probably smaller than for the PHOBOS data (larger $|\eta|$ range and the acceptance at least partially accounted for [181]). At the ISR energies the pseudorapidity range $|\eta| < 4$ is sufficient to accept almost full $dN_{ch}/d\eta$ distribution, but the size of the clusters is affected by the hole in the azimuth. It seems thus that corrected cluster parameters at different energies should became closer, although the observation that the clusters are smaller at ISR energies should still be valid.

Very similar analyses were performed by the PHOBOS Collaboration using the data for $Cu+Cu$ and $Au+Au$ collisions at $\sqrt{s_{NN}} = 200$ GeV [36, 182]. In the case of nucleus-nucleus collisions the multiplicity of charged particles is many times larger than in $p+p$ interactions, thus the occupancy in the silicon sensors has to be taken into account. Special care was thus taken to correctly account for merging of hits from two or more particles into one signal, as described in Section D. Thanks to the large number of measured events (4 million in each sample) it was possible to reconstruct two-particle correlations in many bins of centrality. If the reconstructed cluster parameters are presented as functions of the number of nucleons participating in the collision, N_{part}, the dependences for $Cu+Cu$ and $Au+Au$ collisions are different. However, when events with similar geometry of the collision, represented by the fractional cross section,

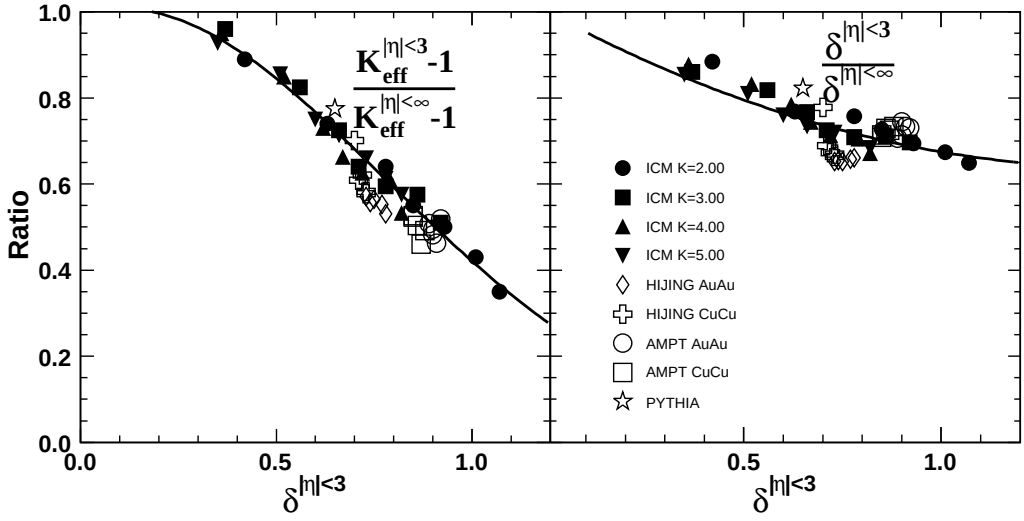

Fig. 4.12: The plots used in the calculations of corrections of reconstructed cluster parameters for the limited acceptance of the PHOBOS detector, for the $p+p$ or $A+A$ collisions at $\sqrt{s_{NN}} = 200$ GeV: the ratio of $K_{eff}^{|\eta|<3} - 1$ to $K_{eff}^{|\eta|<\infty} - 1$ (left) and the ratio of $\delta^{|\eta|<3}$ to $\delta^{|\eta|<\infty}$ (right) as a function of reconstructed cluster width parameter $\delta^{|\eta|<3}$. The solid lines are smooth functions fitted to the points from all models.

$1 - \sigma/\sigma_0$, are compared, the results for both types of nuclei become identical within the errors (Fig. 4.13). For both types of colliding systems the width of the cluster δ is larger than that observed in the $p + p$ interactions. The cluster size K_{eff} is slightly smaller in the most central collisions than in $p + p$ interactions, but in the peripheral collisions becomes much larger and even without acceptance correction exceeds 3. The AMPT generator gives similar width δ of the clusters, and reproduces qualitatively the centrality dependence of K_{eff}, but generally gives a smaller cluster size.

After applying the acceptance correction using the fitted dependences from Fig. 4.12 the cluster parameters increase significantly (compare Fig. 4.13 and Fig. 4.14). The cluster size is now identical for the most central $A + A$ collisions and $p + p$ interactions, but increases while going to more peripheral collisions, reaching a maximum of 6 charged particles in the cluster. For the most peripheral $Au + Au$ sample studied some decrease of K_{eff} is visible. AMPT also predicts a similar centrality dependence of K_{eff}, but with a maximum reaching only 4.73. The cluster width δ varies from 1 for the most central collisions to 1.4 for the semi-peripheral ones. For the isotropic decay of an object into many particles the value of δ is about 1 only for a decay at rest ($p_{T,cluster} = 0$) and decreases for non-zero $p_{T,cluster}$. Much larger δs observed in the experiment indicate that the correlations found in this study can not be explained exclusively by the kinematics of the decay.

The parameters of clusters can be extracted not only using all pairs of particles, but also after selecting them according to the distance in azimuth. In Ref. [36] the values K_{eff} and δ obtained from the near-side ($\Delta\phi < 90°$) and the away-side ($\Delta\phi > 90°$) correlations are presented. The near-side cluster width δ is smaller than that for the away-side, while results obtained for all pairs are in-between them. Near-side cluster size changes weakly with centrality, while

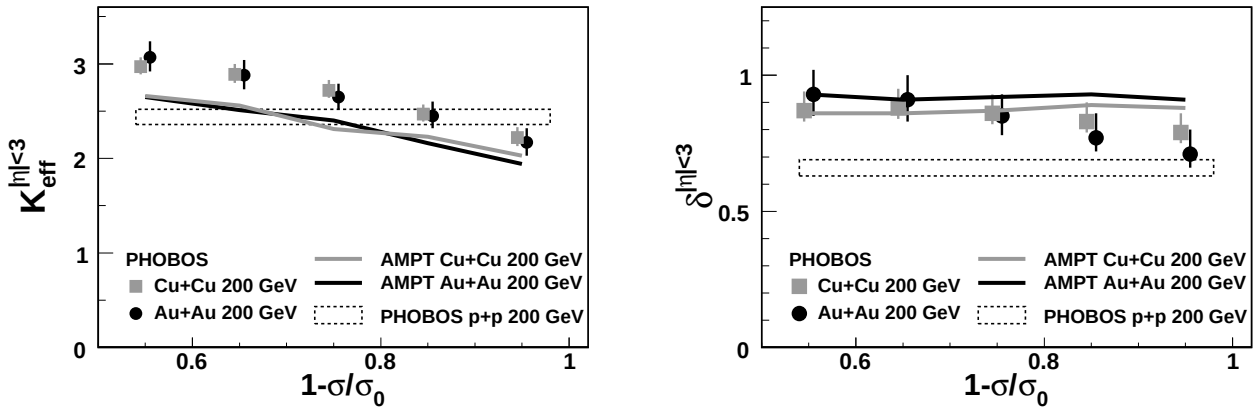

Fig. 4.13: The cluster parameters K_{eff} (left) and δ (right) reconstructed in the limited acceptance of the PHOBOS detector for the Cu+Cu (squares) and Au+Au (circles) interactions at $\sqrt{s_{NN}} = 200$ GeV as a function of the fractional cross section representing the centrality of the collision (the most central data are at $1-\sigma/\sigma_0 \approx 1$). For comparison the cluster parameters for events from the AMPT generator with acceptance cuts applied are shown as the lines and those obtained for p+p interactions are marked by the boxes. The error bars represent the systematic errors of the reconstruction procedure.

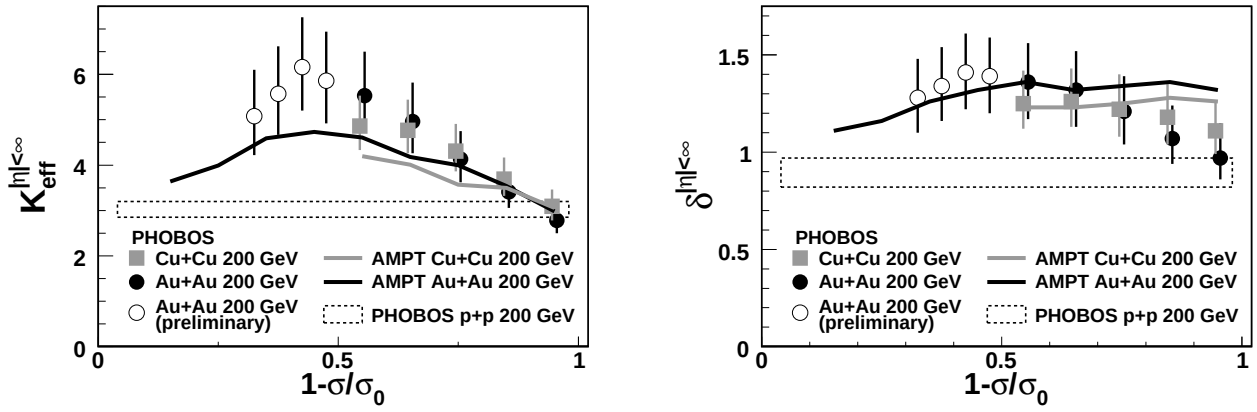

Fig. 4.14: The cluster parameters K_{eff} (left) and δ (right) as in Fig. 4.13 after correcting the reconstructed values for the detector acceptance. In addition the preliminary results for semi-peripheral $Au + Au$ data [182] are shown. The error bars represent both the systematic error of the parameters obtained from the reconstruction procedure and the uncertainty of the acceptance correction (12% for K_{eff} and 9% for δ).

the away-side cluster size decreases rapidly with centrality. The acceptance correction, which is much larger when the reconstructed $\delta^{|\eta|<3}$ is large, additionally enhances this trend. Any explanation of these dependences has to account for strong correlations in azimuth introduced by transverse momentum conservation.

The analysis of two-particle correlations in $p + p$, $Cu + Cu$ and $Au + Au$ collisions reveals clustering effects stronger than those resulting from known hadronic resonances and extending to larger distances in pseudorapidity than expected from the kinematics of the particle decay.

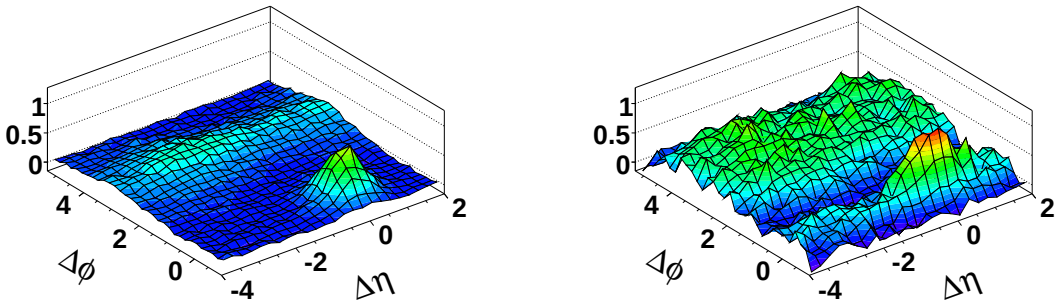

Fig. 4.15: The yield of the particles correlated with a high p_t trigger particle in $p+p$ PYTHIA events (left) and $Au+Au$ 0-30% central collisions (right) at $\sqrt{s_{NN}}$=200 GeV as a function of $\Delta\eta$ and $|\Delta\phi|$.

The large size of the clusters may be at least partially explained as jets fragmenting into a large number of particles. Correlations involving many particles may also be due to fluctuations of the $dN_{ch}/d\eta$ distribution. The strong centrality dependence of the reconstructed cluster size K_{eff}, which in addition scales with the geometry of the collision, is another unexpected result.

4.4 Correlations with a high p_T trigger particle

One of the first and most important discoveries indicating unexpected properties of the matter created in $Au+Au$ collisions at RHIC is the observation of the suppression of particles with very high transverse momenta. In the case of the PHOBOS experiment this is seen as the decrease of the yield of particles with large p_T with respect to the scaled $p+p$ yields (see Fig. 3.12 and Ref. [10]). The source of high-momentum particles is hard scattering of nucleon components (quarks or gluons), in which pairs of partons are created and emitted back-to-back. The very large acceptance in azimuth of the detector used by the STAR Collaboration allows it to observe directly the suppression of one of two leading particles in central $Au+Au$ collisions [87, 88]. In $p+p$ and $d+Au$ collisions the trigger particle with high p_T is correlated with another such particle at opposite direction in azimuth, but no such correlation is seen for the most central $Au+Au$ collisions (Fig. 2.2). This effect is explained by strong interactions of partons traversing the matter created in $Au+Au$ collisions, which have the result that only partons produced near the surface of the collision volume and emitted in the outside direction can survive.

In order to study the stopping of energetic partons in the dense strongly interacting matter, it is necessary to look also at particles with lower transverse momenta, which may carry a part of the energy of the stopped partons. In this context charged di-hadron correlations [183, 184] (in the PHENIX and STAR experiments), and correlations of three particles [185, 186] (in the STAR experiment) were measured, while the PHOBOS Collaboration studied the correlations of all charged particles with a high-p_T trigger particle ($p_T > 2.5$ GeV/c). The correlations are measured as a function of $\Delta\eta$ and $\Delta\phi$ - the difference between the pseudorapidity and the azimuthal angle of the trigger particle and all remaining charged particles. Measured yields are corrected for the presence of an elliptic flow [37, 182]. The two-dimensional correlation functions for $p+p$ and $Au+Au$ are compared in Fig. 4.15. They both feature a high peak when both $\Delta\eta$ and $\Delta\phi$ are close to zero. On the opposite side $\Delta\phi \approx 180°$ a wide maximum is present, which may be due to momentum conservation. However, only in the case of $Au+Au$ collisions, correlations with the trigger particle at $\Delta\phi \approx 0$ are significant also at very large $\Delta\eta$

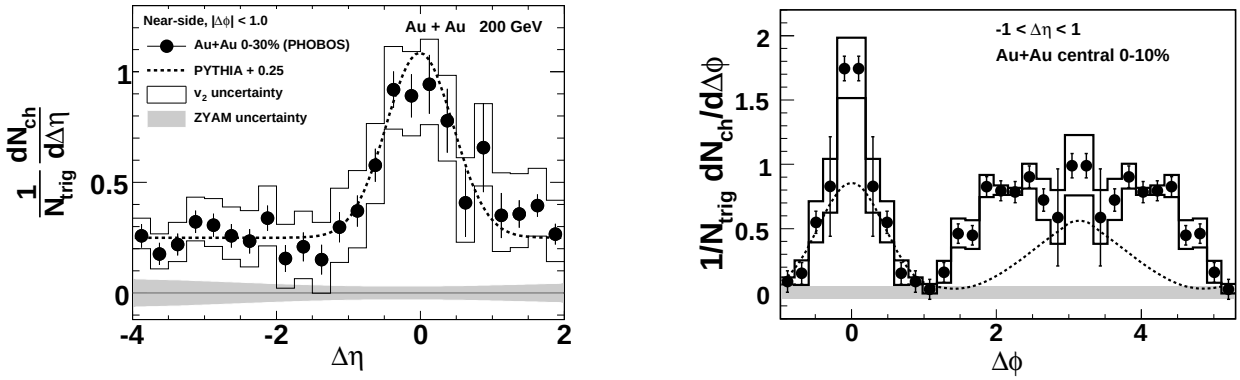

Fig. 4.16: The yield of the particles correlated with a high p_t trigger particle in $Au + Au$ collisions at $\sqrt{s_{NN}}$=200 GeV: the dependence on $\Delta\eta$ in the near-side ($|\Delta\phi| < 1$) for central collisions (0-30%) (left) and the dependence on $\Delta\phi$ in the short-range ($|\Delta\eta| < 1$) for the most central collisions (0-10%)(right).

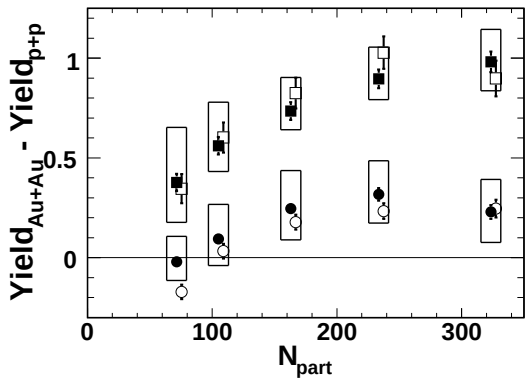

Fig. 4.17: The yield of the particles correlated with a high p_t trigger particle in $Au + Au$ collisions at $\sqrt{s_{NN}}$=200 GeV, after subtracting the yield from $p + p$ collisions, for all combinations of applied selections: the near side ($\Delta\phi \approx 0$ - circles) or the away side ($\Delta\phi \approx \pi$ - squares) and the short range ($|\Delta\eta| < 1$ - open symbols) or the long range ($-4 < \Delta\eta < -2$ - full symbols), shown as a function of event centrality (represented by the number of nucleons participating in the collision, N_{part}).

values, up to at least $\Delta\eta = -4$ which is the maximum distance measurable using the PHOBOS detector.

More quantitative results can be obtained using projections of the 2D histogram on one axis. In Fig. 4.16 (left) the yield of correlated particles emitted at approximately the same azimuthal angle ($\Delta\phi \approx 0$) is shown as a function of $\Delta\eta$. The peak at $\Delta\eta \approx 0$ and the "ridge" (a non-zero value) extending to a large distance in pseudorapidity are clearly visible. The comparison with elementary $p + p$ collisions (from the PYTHIA generator) shows that the yield in $Au + Au$ collisions can be described as a constant term (of about 0.25) plus the $p + p$ yield.

Similarly, the yields of correlated particles can be presented as a function of $\Delta\phi$. They are studied in two pseudorapidity intervals: the short range ($|\Delta\eta| < 1$) and the long range ($-4 < \Delta\eta < -2$). An example of such correlations in the most central $Au+Au$ events is shown in Fig. 4.16(right); the full set of correlation functions for both ranges and all centralities can be found in Ref. [37]. The peak at the near side ($\Delta\phi \approx 0$) is always narrower than that at the opposite (away) side. The height and the area under the peaks vary with the centrality

of the collisions and are different in the short and the long range in $\Delta\eta$. However, the area under each peak is almost always larger than the corresponding area for the same correlation in elementary $p+p$ interactions. Both peaks are biggest in the most central events and become smaller for more peripheral collisions. The narrow peak at $\Delta\phi \approx 0$ is much higher in the short range than in the long range in $\Delta\eta$, while the broad peak at away side looks similar in both ranges. Much more similar are the results in the short and long range when from the yield observed in $Au+Au$ collisions the yield from elementary $p+p$ interactions is subtracted. Such surplus yields are shown in Fig. 4.17, where four combinations of ranges in $\Delta\eta$ and $\Delta\phi$ are included. The enhancement over elementary collisions is practically the same at short and long range, but it is larger for the away side than for the near side. For peripheral events all these additional yields decrease, and the near-side ridge seems to disappear at about $N_{part} = 80$.

In a study of a high-p_T trigger particle correlations with other charged particles, several interesting results were obtained. In Au+Au collisions the correlation in the near-side ($\Delta\phi \approx 0$) features a "ridge" extending a considerable distance in pseudorapidity. There is a surplus of correlated particles over the yield observed in the $p+p$ interactions both at near-side and away-side, but it decreases for semi-peripheral collisions.

4.5 Multiplicity fluctuations measured in other experiments

The two big experiments at RHIC, PHENIX and STAR, performed several similar or complementary studies of multiplicity correlations and fluctuations. In some cases, when identified particles are involved, results are more precise and some aspects not accessible for the PHOBOS experiment can be analyzed. However, PHENIX and STAR always are limited by a relatively small acceptance range in pseudorapidity and in the case of PHENIX also by incomplete coverage in the azimuthal angle.

The STAR Collaboration has studied forward-backward correlations for $Au+Au$ and $p+p$ collisions at $\sqrt{s_{NN}} = 200$ GeV [187] by comparing charged particle multiplicities N_F and N_B in pseudorapidity bins 0.2 unit wide, symmetric with respect to $\eta = 0$, using the observable

$$b = \frac{\langle N_F N_B \rangle - \langle N_F \rangle \langle N_B \rangle}{\langle N_F^2 \rangle - \langle N_F \rangle^2}. \tag{4.17}$$

Positive values of b indicate a correlation between forward and backward bins. Values of b are analyzed as a function of the distance between the bins for different centralities. The acceptance of the detector for this study is limited to $|\eta| < 1$; thus the largest possible distance between F and B bins is only 1.8. The centrality of collisions is defined according to multiplicity registered in a subrange of $|\eta| < 1$ that does not overlap the bin actually considered. The largest values, $b \approx 0.6$, are obtained for the most central events (0-10%), while for the most peripheral $Au+Au$ events (centrality 50-80%) and for inclusive $p+p$ interactions, values $b < 0.12$ are obtained. HIJING and Parton String Model [188] simulations predict smaller than the observed b values for the most central events. These results are interpreted as a possible sign of multiple parton-parton interactions (see the discussion in Ref. [187]). However, the definition of centrality based on the multiplicity of particles in bins very close to those for which a correlation is measured severely complicates the interpretation of the results [189]. Also production of particles from clusters affects the b parameter; the expectations from a simple cluster model are discussed in Section 5.5.

The full azimuthal coverage and relatively large pseudorapidity acceptance of the STAR

detector allows it to be used to study two-particle or even three-particle correlations [185]. In the analysis of autocorrelations between particles with low momenta, starting form the lowest measured $p_T \approx 0.15$ MeV/c, several contributions have been identified and extracted. Their functional forms are selected to represent dependencies expected for transverse momentum conservation and elliptic flow, local charge conservation, fragmentation of longitudinal color strings, and minijets [190]. In the study of like-sign and unlike-sign particle correlations, fits with many more (~ 15) parameters are necessary [191, 192]. These results are however always obtained in a limited pseudorapidity range, usually $|\eta| < 1$ and only sometimes extended to $|\eta| < 1.3$. This may cause effects that are important at larger distances ($\Delta\eta > 1$) to be suppressed by the limited acceptance. The reconstructed short-range correlations are thus not sensitive to the presence of the very wide clusters observed by PHOBOS Collaboration, and are dominated by minijets contribution. Analyses of correlations between particles, which are used to extract mean p_T fluctuations [193] or to study local parity violation [194], are described in more detail in Section 7.2.

There are also numerous correlation studies focused on particles with higher momenta, which are used for the analysis of jet properties [195, 196, 197, 184, 190, 185]. Similar results to those presented in Section 4.4 were obtained earlier [195], but in a much narrower pseudorapidity range, $|\eta| < 1$. An interesting result is obtained in a three-particle correlation study [185] in which a conical emission of particles at an angle $\theta = 1.37$ rad was found. This effect may indicate a Mach-cone shock wave and in this case the angle is related to the speed of sound in the medium.

The PHENIX Collaboration has measured very precisely charged particle multiplicity distributions in the range $|\eta| < 0.26$ for different centralities and p_T ranges [198]. They were fitted using the Negative Binomial (NB) function:

$$P(n, \bar{n}, k) = \frac{\Gamma(n+k)}{\Gamma(n+1)\Gamma(k)} \left(\frac{\bar{n}}{k}\right)^n \left(1 + \frac{\bar{n}}{k}\right)^{-n-k} \tag{4.18}$$

where $\bar{n}$ is the mean multiplicity, $\langle N_{ch} \rangle$, and k is an additional parameter. The multiplicity distribution in this form is sufficient for calculation of many fluctuation measures; for example,

$$\omega_{ch} = \frac{\langle N_{ch}^2 \rangle - \langle N_{ch} \rangle^2}{\langle N_{ch} \rangle} \tag{4.19}$$

can be calculated using the NB distribution parameters:

$$\omega_{ch} = 1 + \frac{\bar{n}}{k}. \tag{4.20}$$

Owing to specific properties of the NB distribution, acceptance effects can be easily accounted for:

$$\omega_{ch,acc} = 1 + f_{acc}(1 - \omega_{ch}), \tag{4.21}$$

assuming that a fraction f_{acc} of all particles used to calculate ω_{ch} is randomly registered and reconstructed in the acceptance of the detector. However, Eq. 4.21 is only approximately valid if there are correlations between particles registered inside and outside the detector acceptance. The values of ω_{ch} even for narrow centrality bins contain both dynamical effects in particle production and contributions connected with fluctuations in the numbers of nucleons participating in the collisions, N_{part}. After removing the latter contribution using Monte Carlo simulation

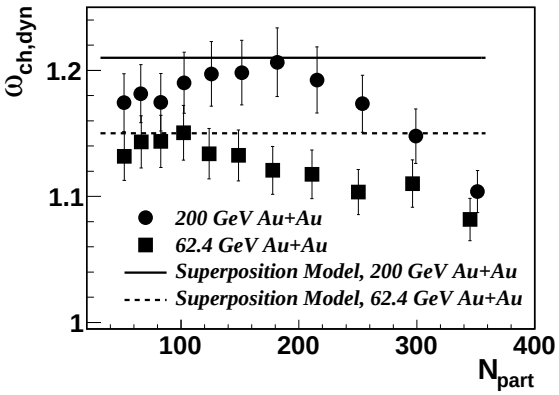

Fig. 4.18: Fluctuations expressed as the scaled variance $\omega_{ch,dyn}$, with the contribution due to fluctuations of collision geometry removed, as a function of centrality represented by N_{part} in $Au + Au$ collisions at $\sqrt{s_{NN}}$ = 200 GeV and $\sqrt{s_{NN}}$ = 62.4 GeV, compared with the expectation from a superposition model based on $p + p$ data [198].

studies, the extracted dynamical fluctuations, $\omega_{ch,dyn}$, are obtained. They are consistent with or below the expectations from the superposition model of participant nucleons (Fig. 4.18). The multiplicity fluctuations decrease with centrality, dropping for the most central sample much below predictions from superposition of nucleon-nucleon collisions [198]. This trend is expected for the contribution from elliptic flow not removed from $\omega_{ch,dyn}$.

Values of $\omega_{ch,dyn}$ calculated for particles of the same sign or in bins of transverse momentum are consistent within errors with the scaling expected for the appropriate acceptance correction (Eq. 4.21), although for the lowest momenta, $0.2 < p_T < 0.5$ GeV/c, they are systematically larger. There are thus no signs of anomalously increased fluctuations, which could be evidence of a phase transition or a critical point.

The experimental results are also compared with predictions from the HIJING generator and analyzed in the context of a clan model. HIJING gives much larger $\omega_{ch,dyn}$ values, but becomes consistent with the data when the jet production parameter is turned off. The clan model [199] is a specific variant of a cluster model that assumes that clusters are produced according to a Poisson distribution and decay into some number of secondary particles. The number of clusters, $\bar{N}_c$, and the mean cluster size, $\bar{n}_c$, can be calculated from the parameters of the Negative Binomial distribution:

$$\bar{N}_c = k \ln(1 + \bar{n}/k)\bar{n}_c = (\bar{n}/k)/\ln(1 + \bar{n}/k). \tag{4.22}$$

The mean number of particles per cluster, $\bar{n}_c$, for elementary $p + p$ and $p + \bar{p}$ interactions, is a rapidly growing function of the number of clusters, $\bar{N}_c$. For events with the largest multiplicities it reaches $\bar{n}_c \approx 4$ and $\bar{n}_c \approx 3$ at $\sqrt{s_{NN}} = 540$ GeV and $\sqrt{s_{NN}} = 200$ GeV, respectively [200]. For $A + A$ collisions the $\bar{n}_c$ values lie within the range 1.0-1.1 which indicates practically no clustering, in disagreement with results presented earlier in this Section. Taking into account that also the results for elementary interactions are qualitatively different than for $A + A$, the clan model seems inadequate for description of these data. Most probably the assumption that the number of clusters, $\bar{N}_c$, can be described by a Poisson distribution is inconsistent with the properties of the interactions.

Studies of multiplicity fluctuations were also performed at SPS energies. The WA98 Collaboration studied fluctuations of the number of charged particles and photons [201] using the ω_{ch} and ω_γ observables. Observed dependence on the rapidity window agrees with acceptance effects like those discussed in Ref. [140], while the decrease of fluctuations with centrality of the collision is consistent with results obtained from a simple participant model that takes into account impact parameter fluctuations and multiplicity fluctuations in nucleon-nucleon interactions.

The NA49 Collaboration observed larger than statistical fluctuations for the total measured multiplicity and for the particle density at midrapidity. In the forward rapidity region distributions of the number of positively charged and negatively charged particles are narrower than the Poisson distribution, which is interpreted as an effect of conservation laws [202, 203].

Section summary

Analyses of multiplicity fluctuations and correlations at RHIC using different techniques and observables did not identify strong effects that could be considered as a clear sign of a phase transition or a critical point. Results of the search for events with very large multiplicities or unusual fluctuations of the $dN_{ch}/d\eta$ distribution allow one only to establish an upper limit for such phenomena. The studies of forward-backward correlations and two-particle correlations performed by PHOBOS do not reveal any significant discontinuities and are consistent with the hypothesis of production of clusters that decay into the finally observed particles. After applying acceptance corrections, which are very important even for an acceptance range as wide as $|\eta| < 3$, very wide clusters with effective size up to 6 charged particles are reconstructed. The correlations between a high-p_T particle and other charged particles extends to large distance, at least $\Delta\eta \approx 4$, and are strongest for the most central collisions.

Results from experiments other than PHOBOS indicate the presence of fluctuations that are larger than purely statistical, but also only of moderate magnitude. They can be used to verify models of particle production, but a detailed comparison and careful examination of acceptance effects needs to be performed in each case.

5 Simple Cluster Model and short range correlations

The concept of clusters appeared as a phenomenological explanation for experimentally observed short range correlations between produced particles [178, 179, 181, 204, 205, 206, 207, 208]. The physics picture behind any cluster model is a description of the particle production as a two step process: at first some intermediate objects (clusters) are created which then decay into some number of particles; isotropic decays in the rest frame of the cluster are postulated. There are thus direct correlations only between particles originating from the same cluster. Other correlations may arise from correlations between clusters, but they are usually neglected.

Natural candidates for clusters are hadronic resonances, but mini-jets have similar features [209]. There are also other processes that can not be treated as particle decays, but which may be responsible for observed "cluster-like" correlations: string fragmentation [210], wounded nucleons or wounded quarks fragmentation (Section 6).

The cluster parameters, which may be accessible in the correlation studies, are cluster size, (K - number of particles originating from it) and the width in rapidity (or pseudorapidity) of their distribution, $\sigma(\eta)$, as described in Section 4.2 and 4.3. The parameters of the cluster treated as a particle, its momentum, its mass, and the number of secondaries in the decay, can be treated as free parameters that have to be adjusted to describe the observed correlations and other properties of the events, especially the rapidity (or pseudorapidity) and transverse momentum distributions. In Appendix F many aspects of the kinematics of the decay are extensively studied, here only a résumé is presented. In a modeling of cluster parameters the cluster size is fixed by selection of the parent particle and its decay mode. The width of the cluster (in y or η) formed by the decay products depends also on the momentum of the parent and details of the decay process. In the simplest case of isotropic decay at rest the cluster width $\sigma(\eta) \approx 0.9$, regardless of the cluster size. This is the largest possible value, as practically all modifications that make the cluster properties more realistic lead to a decrease of the cluster width. As it is shown in Appendix F the width of best known resonances varies from 0.2 (for $\phi(1020)$ meson) to 0.62 (for $\rho(770)$ meson) and is always lower than 0.9 expected for an isotropic decay at rest.

In two-particle correlation studies a width parameter δ is extracted. According to Eq. 4.15 it is a factor of $\sqrt{K/(K-1)}$ larger than $\sigma(\eta)$. For clusters of two particles decaying at rest $\delta_{isotropic} \approx 1.3$ is possible, but it decreases to $\delta_{isotropic} \approx 1$, if the size of the cluster reaches 6, as obtained from semi-peripheral $Au+Au$ data (Fig. 4.14). Experimental values of δ, reaching up to $\delta^{|\eta|<\infty} \approx 1.4 \pm 0.2$, are larger than $\delta_{isotropic}$. Kinematical decays of resonances are thus not sufficient to reproduce such clusters. In the calculation of acceptance corrections (described in Section 4.3) the realistic clusters were modified by artificial rescaling of pseudorapidities of secondary particles leading to the required widening of the clusters [36].

The Simple Cluster Model (SCM) used in the studies presented in this Section takes another route. It starts from defining the position of the cluster in pseudorapidity, η_{cl}. Secondary particles are not generated kinematically, but are obtained from a Gaussian distribution centered at η_{cl}, in agreement with the function Eq. 4.12 used in the fit performed to obtain K_{eff} and δ in two-particle correlation studies [30, 36]. SCM is thus more convenient for studying acceptance effects, because it uses cluster parameters that are extracted from two-particle correlations. Clusters with more realistic η-shapes may be approximated by a mixture of clusters with Gaussian shapes. If the acceptance of Gaussian clusters and the results of mixing them are known, it is also possible to predict the acceptance of clusters with other shapes.

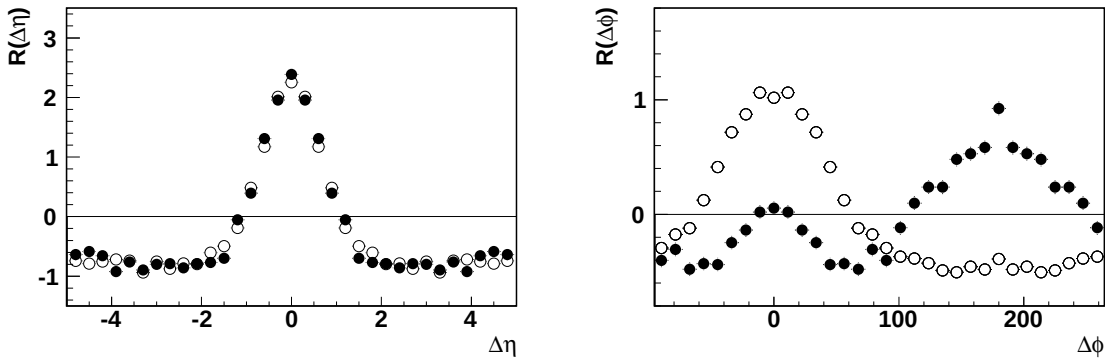

Fig. 5.1: Two-particle correlation functions: $R(\Delta\eta)$ (left) and $R(\Delta\phi)$ (right) (see Section 4.3 for definitions), obtained for events with identical clusters (decays: $\omega(782) \to \pi^+\pi^-\pi^0$). Results shown with open circles were obtained for an independent generation of the clusters; filled circles represent events for which the momenta of all particles in the event were transformed from the laboratory frame to the center of mass frame (in which the sum of momenta of all particles in the event equals zero) [47].

5.1 Momentum conservation effects in two-particle correlations

The analysis of momentum conservation effects requires clusters treated as particles with realistic momenta and decaying kinematically. As an example events with $\omega(782)$ resonances (decaying into three pions) with $\langle p_T \rangle$=0.92 were generated. The same events were used to create a second sample in which all momenta of final particles were transformed to the center of mass system of the event, enforcing total momentum conservation.

Both samples were analyzed using the reconstruction procedure for two-particle correlations and the $R(\Delta\eta)$ and $R(\Delta\phi)$ functions were obtained. They are shown in Fig. 5.1 and should be compared to experimental functions in Fig. 4.10. The correlations in pseudorapidity are almost identical for both samples, but the shape of the azimuthal angle correlation function $R(\Delta\phi)$ strongly depends on the presence or the absence of correlations due to total momentum conservation. In the case of an independent generation of clusters, $R(\Delta\phi)$ is peaked at $\Delta\phi$=0. This shape reflects the ϕ distribution within the clusters: as the transverse momentum of the cluster is relatively large, the decay products are usually emitted in the same direction. Particles from other independent cluster decays are distributed uniformly in ϕ, thus their contributions effectively cancel. After the transformation to the center of mass frame of the event the momentum of each cluster is compensated by the momenta of other clusters. In the transverse direction, this means that a selected charged particle has one charged companion from the same decay at small $\Delta\phi$ and on average two charged particles from other clusters at the opposite side ($\Delta\phi \approx 180^\circ$). The correlation in pseudorapidity is practically unaffected; a small difference of the correlation function $R(\Delta\eta)$ in Fig. 5.1 (left) is due to a small difference in the $\langle p_T \rangle$ of clusters (p_T calculated in the lab frame is slightly changed after the transformation to the C.M. frame) rather than to a real change of correlations in η.

Analysis of two particle correlations in azimuthal angle for events with kinematically decaying clusters reveals their strong dependence on the presence or absence of momentum conservation during generation of events.

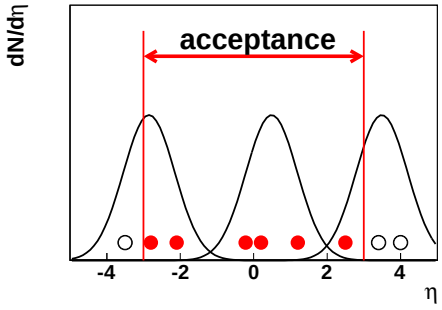

Fig. 5.2: Effects of limited η range used in the two-particle correlation studies: some clusters have fewer particles accepted (decrease of the effective cluster size) and the particles from them seem to be closer in η (smaller effective width of clusters).

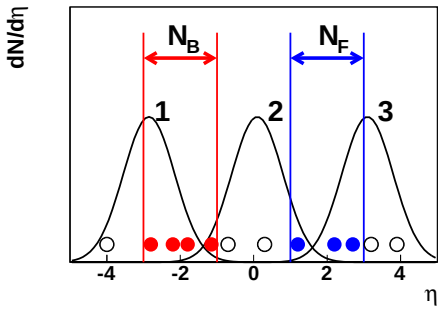

Fig. 5.3: Effects of limited width of η bins used in the forward-backward correlation studies: some particles (from clusters 1 and 3) are not accepted (smaller effective cluster size) and particles from the same cluster emitted near $\eta = 0$ (like cluster 2) may be registered in both forward and backward bins.

5.2 Acceptance effects in the Simple Cluster Model

In the reconstruction of two-particle correlations, only hits measured in the octagonal part of the Multiplicity detector ($|\eta| < 3$) are used. The same detector is used in the forward-backward correlations studies, but in addition much narrower η bins are used. This means that all particles belonging to the same cluster are not always registered. As shown in Fig. 5.2 and 5.3, a lower effective cluster size and a smaller effective cluster width are thus expected. An even stronger decrease of the "visible" cluster size is expected in the forward-backward correlations using narrower η bins to count the number of particles in the forward and backward bins (N_F and N_B). In this case an additional effect becomes also important, especially if the separation of bins is very small or zero: the particles from the same cluster may fall into both forward and backward bins, inducing a positive correlation between N_F and N_B (see Fig. 5.3), which decreases the difference $N_F - N_B$ and reduces the value of $\sigma^2(C)$.

The acceptance effects depend strongly on the ratio of the widths of the clusters to the width of the acceptance range or the widths of the η bins considered. An example is shown in Fig. 5.4 where results from two-particle correlation reconstructions with a changing acceptance cut $|\eta| < \eta_{max}$ for events from SCM are presented. In generated events it is possible to find particles belonging to each cluster and determine how many of them fit in the acceptance range. Using this information the expected effects of the acceptance cut can be precisely calculated (continuous lines in Fig. 5.4). The results of the standard reconstruction procedure, obtained from all accepted particles, correctly reproduces the cluster parameters only for the full η range. For smaller η_{max} both the cluster size and width are underestimated, even with respect to the calculated effects of the acceptance cut.

In the case of forward-backward correlations, acceptance effects are even stronger. The values of $\sigma(C)$ grow with increasing $\Delta\eta$ and there is no clear sign of saturation (see Fig. 4.6 in Section 4.2), which is expected when the bin width $\Delta\eta$ becomes much larger than the cluster width. This means that even for the widest bins ($\Delta\eta$=2) the asymptotic value $\sigma(C)$=K_{eff} still

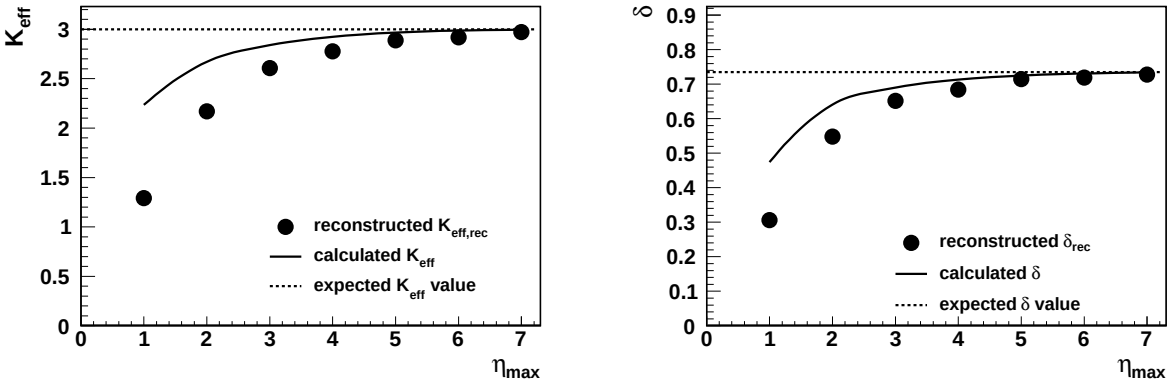

Fig. 5.4: Reconstruction of cluster parameters: cluster size $K_{eff,rec}$ (left) and cluster width δ_{rec} (right) obtained from two-particle correlations for different acceptance cuts $|\eta| < \eta_{max}$. The events from an SCM generation of identical clusters (K=3, $\sigma(\eta)$=0.6 and thus δ=0.735) are used. The raw results of the standard two-particle reconstruction (points) and the cluster parameters calculated directly using the true information on clusters (continuous lines) are presented. For the full acceptance the true values of cluster parameters are reproduced (horizontal dashed lines).

was not approached.

For the two-particle correlation reconstruction these acceptance effects were studied using many samples of SCM events with identical clusters, testing a full grid of K and δ values (Fig. 5.5). As expected, the larger the width of clusters, the more the results of reconstruction differ from the true cluster parameters.

In the forward-backward correlation analysis a simultaneous determination of both K_{eff} and δ (or $\sigma(\eta)$) is not possible. The dependence of $\sigma^2(C)$ on $\Delta\eta$ can be equally well described using clusters with size K=3 and K=8 if the width of the clusters is appropriately adjusted (Fig. 5.6 (left)). Similar ambiguity is present in the case of the dependence of $\sigma^2(C)$ on the bin position in pseudorapidity (Fig. 5.6 (right)). For the peripheral events sample $\sigma^2(C)$ values are generally larger than for the central events (especially in Fig. 5.6 (left)). If this difference reflects properties of clusters, then clusters observed in the peripheral events are either narrower

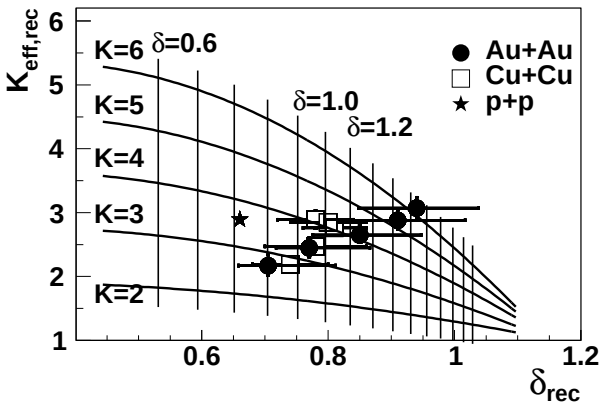

Fig. 5.5: Parameters of clusters: cluster size $K_{eff,rec}$ and cluster width δ_{rec} obtained either from experimental data (points) or for SCM events with identical clusters (crossings of grid lines), without corrections for acceptance cut $|\eta|$ <3. Points represent raw reconstruction results for $p+p$, $Cu+Cu$ and $Au+Au$ collisions at $\sqrt{s_{NN}} = 200$ GeV. The grid was obtained for clusters with sizes K=2, 3, 4, 5 and 6 and widths $\delta = 0.6, 0.7, ..., 2.0$, The distribution of η of clusters was adjusted to reproduce the experimental $dN_{ch}/d\eta$ distribution.

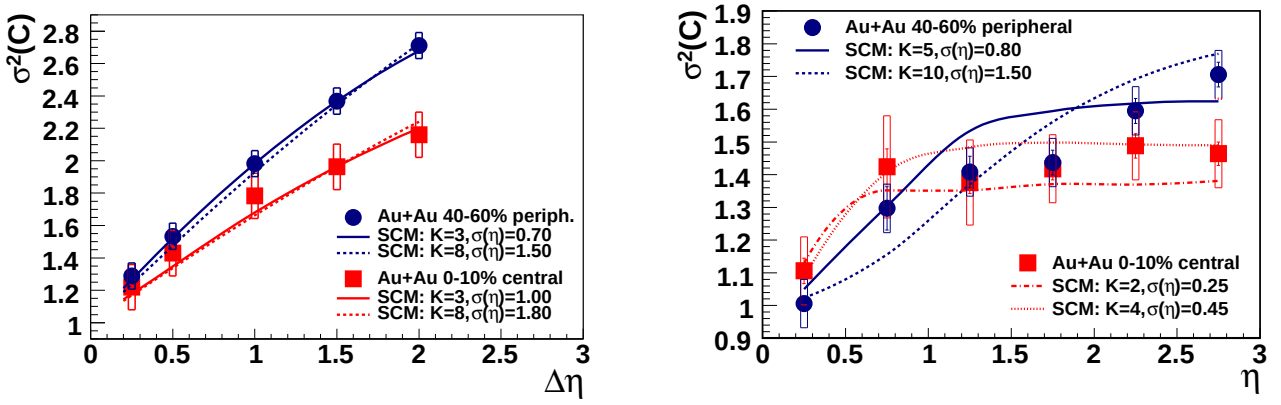

Fig. 5.6: Reconstructed forward-backward correlations presented as $\sigma^2(C)$ dependence on the width of pseudorapidity bin $\Delta\eta$ (left) or as the position of bins with the same width ($\Delta\eta$=0.5) in pseudorapidity η (right) compared with the calculated values obtained from the events generated in the Simple Clusters Model using clusters with several different values of cluster size K and width $\sigma(\eta)$.

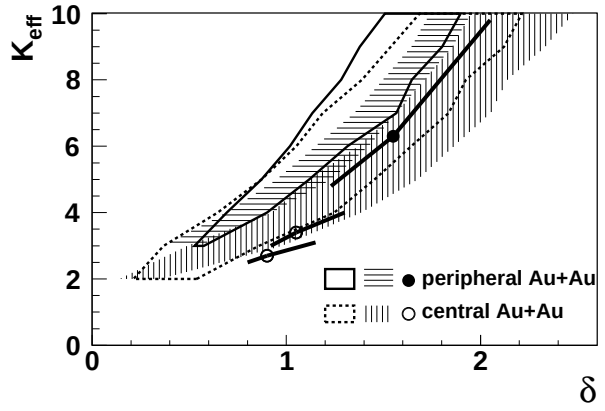

Fig. 5.7: The values of cluster parameters K_{eff} and δ in SCM that agree with the experimental results on forward-backward correlations for peripheral (40-60%) or central (0-20%) data, for $\sigma(C)$ dependence on the bin position in η (contours) and on the bin width $\Delta\eta$ (hatched areas). In each case the area corresponds to 90% confidence level. The points represent results from two-particle correlations for the same centralities: central (0-10%, 10-20%) and peripheral (40-50%), with the acceptance correction calculated using SCM (Fig. 5.5).

or consist of more particles.

The dependencies of $\sigma^2(C)$ (on η and $\Delta\eta$) measured for events from the two centrality classes are compared in Fig. 5.6 with several SCM predictions obtained for clusters with different parameters. However, predictions for clusters with many more different sizes (K=2, ..., 10) and width were calculated. Using deviations of SCM predictions from experimental $\sigma^2(C)$ values the probability that clusters were compatible with the data was obtained. After accepting those cluster parameters for which the probability was larger than 0.1, the areas of 90% confidence were found. They are shown in Fig. 5.7 for two centralities and two dependencies analyzed. According to these results the observed correlations may be reproduced by many types of clusters, from small and relatively narrow to very large but also very wide. The dependence based on the bin width $\Delta\eta$ gives more restrictive limits; however the dependence on position in η increases the lower limit for the size of clusters. There is a very limited overlap of acceptance areas obtained from the $\Delta\eta$ dependence for central and peripheral collisions. This suggest a difference of cluster parameters, but identical clusters can not be excluded.

In Fig. 5.7 a direct comparison of forward-backward and two-particle correlations results is possible. The central event sample used in the first analysis (centrality 0-20%) corresponds to two points (centrality 0-10% and 10-20%) from two-particle correlations studies, while for the peripheral sample (centrality 40-60%) one data point (centrality 40-50%) is included. In both cases the points from two-particle correlations are at the edge of the area allowed by the results from forward-backward correlations. The next Section explains why the cluster size observed in two-particle correlations may be smaller than that deduced from $\sigma^2(C)$ measurement.

The analysis of acceptance effects based on the Simple Cluster Model illustrates their importance even for the PHOBOS experiment, which has very large coverage in pseudorapidity, $-3 < \eta < 3$, used in the correlation studies. It provides acceptance corrections for two-particle correlation results and clearly shows that the width of clusters obtained from such an analysis exceeds that expected for resonance decays.

5.3 Mixture of clusters with different sizes and widths

The analysis of SCM events with one type of clusters is useful to learn basic properties of the production of particles in two steps. However, in the real events clusters of different sizes and widths are expected, even if only a few resonances are considered. It is thus necessary to test conclusions from the previous Section using mixtures of different clusters.

The easiest to calculate are effects expected for clusters with the same width, but different sizes. This includes also uncorrelated particles - they may be treated as clusters of size K=1 for any required width and are thus compatible with all types of clusters with bigger size. It is easy to show that for a perfect detector accepting all particles it is sufficient to replace the constant K value by

$$K_{eff} = \langle K \rangle + \frac{\sigma^2(K)}{\langle K \rangle}. \tag{5.1}$$

In the case of the two-particle correlation fit described in Section 4.3, the correlation strength parameter is directly connected with K_{eff}:

$$\alpha = \frac{\langle K(K-1) \rangle}{\langle K \rangle} = \langle K \rangle + \frac{\sigma^2(K)}{\langle K \rangle} - 1 = K_{eff} - 1 \tag{5.2}$$

For the value of $\sigma^2(C)$ the same can be proven by analytical calculations under the following assumptions:

- the events in the sample consists of clusters of different sizes, but the number of clusters with the size K which fall into either forward or backward bins considered, M_K, is the same in all events;
- the clusters are so narrow that acceptance effects can be neglected;
- clusters are randomly assigned to the bins and there are $\sum_K M_{K,F}$ and $\sum_K M_{K,B}$ clusters in the forward and backward bins, respectively.

As a consequence of the last assumption, fluctuations of the number of clusters in the bins are purely statistical, and for clusters with size K:

$$\sigma^2(C_{M_K}) = \left\langle \left(\frac{M_{K,F} - M_{K,B}}{\sqrt{M_{K,F} + M_{K,B}}} \right)^2 \right\rangle = 1 \tag{5.3}$$

and because $M_K = M_{K,F} + M_{K,B}$ is constant:

$$\langle (M_{K,F} - M_{K,B})^2 \rangle = M_K \tag{5.4}$$

Denoting the number of particles produced from cluster of size K registered in the forward and backward bins as $N_{K,F}$ and $N_{K,B}$ we have $N_{K,F} = KM_{K,F}$ and $N_{K,B} = KM_{K,B}$. For all particles:

$$\sigma^2(C) = \left\langle \left(\frac{\sum_K N_{K,F} - \sum_K N_{K,B}}{\sqrt{\sum_K N_{K,F} + \sum_K N_{K,B}}} \right)^2 \right\rangle =$$

$$\left\langle \left(\frac{\sum_K K(M_{K,F} - M_{K,B})}{\sqrt{\sum_K K(M_{K,F} + M_{K,B})}} \right)^2 \right\rangle =$$

$$\left\langle \frac{\sum_K \sum_J KJ(M_{K,F} - M_{K,B})(M_{J,F} - M_{J,B})}{\sum_K K(M_{K,F} + M_{K,B})} \right\rangle$$

. Taking into account that $M_K = M_{K,F} + M_{K,B}$ is constant, the denominator is the same for all events. In the numerator the averaging over events can be done inside the sums, which leads to removal of terms with $K \neq J$, thus:

$$\sigma^2(C) = \frac{\sum_K K^2 \langle (M_{K,F} - M_{K,B})^2 \rangle}{\sum_K K M_K} \tag{5.5}$$

Finally, $\langle (M_{K,F} - M_{K,B})^2 \rangle$ may be replaced by M_K, transforming the above equation into:

$$\sigma^2(C) = \frac{\langle K^2 \rangle}{\langle K \rangle} = \langle K \rangle + \frac{\sigma^2(K)}{\langle K \rangle} \tag{5.6}$$

where averaging is done no longer over events, but over clusters in the event.

The above calculations also remain valid when clusters are not fully randomly partitioned to the bins, but the values of $\sigma^2(C_{M_K})$ are the same for each K. It is only necessary to multiply the right side in Eq. 5.6 by the common value $\sigma^2(C_M)$:

$$\sigma^2(C) = \left(\langle K \rangle + \frac{\sigma^2(K)}{\langle K \rangle} \right) \sigma^2(C_M) \tag{5.7}$$

Tests using generated events prove also that when the multiplicity of the events is not fixed and acceptance effects are present Eq. 5.7 is at least approximately valid.

Results of reconstruction of cluster parameters or $\sigma^2(C)$ for events with a mixture of clusters with two different widths should fall between those obtained separately for events with only narrow or only wide clusters. There should be an intermediate "effective width", such that the correlations for the mixture are very similar to those obtained for identical clusters with that width. One may expect that such effective width is close to $RMS(\eta - \eta_{cl})$ and the effective δ close to $RMS(\eta_i - \eta_j)$ (where η_{cl} is the center of the cluster, $\eta_i - \eta_j$ is the η difference calculated for particles from the same cluster).

For the values of $\sigma^2(C)$ these predictions are almost fully confirmed. In Fig. 5.8 results for a mixture of clusters with different widths but also different sizes are shown. Values obtained for the mixture are very close to those that are obtained for clusters with the effective width and size. The effective width is in this case very close to the $RMS(\eta - \eta_{cl})$ within the clusters.

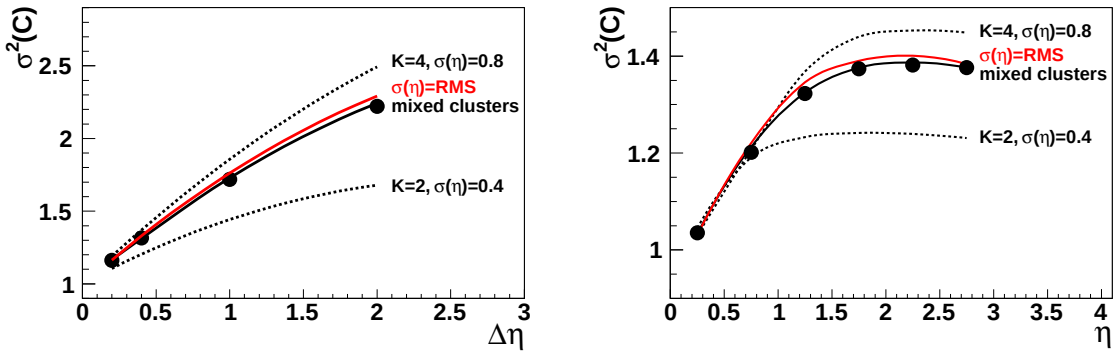

Fig. 5.8: Reconstructed forward-backward correlations presented as $\sigma^2(C)$ dependence on the width of pseudorapidity bin $\Delta\eta$ (left) or as the position of bins with the same width ($\Delta\eta$=0.5) in pseudorapidity η (right), obtained for events from SCM for mixtures of clusters with different sizes ($K = 4$ or $K = 2$) and different widths $\sigma(\eta)$. As a reference, dotted lines represent clusters of the same type. The "mixed clusters" sample (continuous black line) was obtained by mixing clusters with K=4, $\sigma(\eta)$=0.8 and K=2, $\sigma(\eta)$=0.4, 50% of each type. The red line denoted as "$\sigma(\eta) = RMS$" was obtained for a mixture of clusters with sizes K=2 and K=4 and with $\sigma(\eta)$=0.69, which corresponds to the effective cluster width for the "mixed clusters" sample. The points show the calculations according to Eq. 5.8.

However, the best agreement is obtained if the values of $\sigma^2(C_1)$ and $\sigma^2(C_2)$ calculated for the two types of clusters separately are used in the formula

$$\sigma^2(C) = \frac{m_1\sigma^2(C_1) + m_2\sigma^2(C_2)}{m_1 + m_2} \tag{5.8}$$

where m_1 and m_2 denote the numbers of charged particles from cluster 1 and cluster 2 in the event.

In the case of two-particle correlations a mixture of clusters with different widths gives much less predictable results. In Fig. 5.9 results for clusters with the same size, K=3, but different widths, selected in such a way that the $RMS(\eta_i - \eta_j)$ of the η distance between particles (effective δ) is the same in each sample [4], are shown. As expected, acceptance effects calculated directly from the "truth" information are very close for all samples, however the reconstructed cluster parameters for mixtures with the same effective δ are not identical. For samples with bigger spreads of cluster widths, both the reconstructed cluster size K, and the reconstructed cluster width δ are usually smaller, but the difference is more significant for the latter.

The presence of clusters with different widths is a natural consequence of the fact that at least some of finally observed particles are decay products of resonances. First, as shown in Appendix F, resonances, which are present as an intermediate step in the particle production, are characterized by a variety of widths. Second, the shape of the η distribution of particles from a resonance is not exactly Gaussian and in the simplest approach such a resonance may be treated as a mixture of two or more types of clusters with the same size and Gaussian shapes, but with different widths.

[4] When mixtures comprise clusters of the same size K, as in the following discussion, different samples characterized by the same $RMS(\eta_i - \eta_j)$ have also the same values of $RMS(\eta - \eta_{cl})$, as $\delta = \sqrt{K/(K-1)}\sigma(\eta)$ in this case.

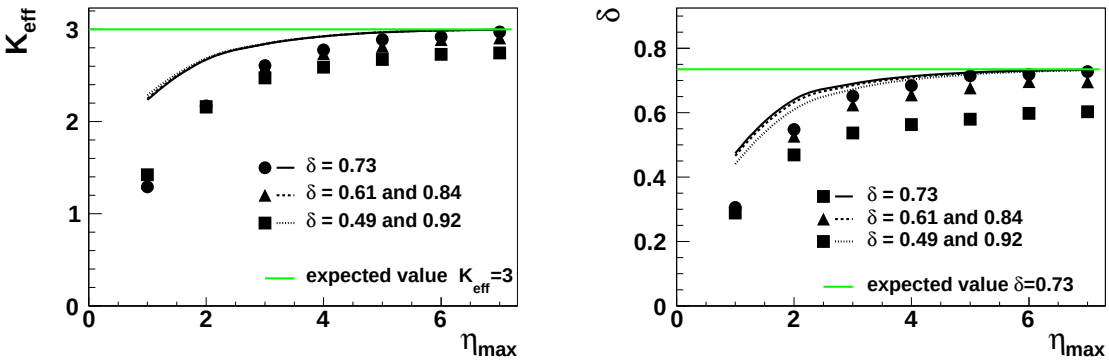

Fig. 5.9: Reconstruction of cluster size K_{eff} (left) and cluster width δ (right) with different acceptance cuts for events from SCM with clusters having the same size (K=3) but different widths δ. In all cases the calculated effective δ for all clusters is the same (δ=0.73), but event samples contain either identical clusters or a 50% mixture of narrow and wide clusters (either δ=0.61 and δ=0.84 or δ=0.49 and δ=0.92). The raw results of the standard two-particle reconstruction (points) and the cluster parameters calculated directly using the true information on clusters (continuous lines) are presented. The true values of cluster parameters (horizontal green lines) are reproduced for the full acceptance in the calculations and in the reconstruction of the sample with identical clusters, but not in the reconstruction performed on the mixtures.

For a mixture of different clusters the two-particle correlations procedure generally gives lower values of cluster parameters than those expected for effective clusters. However, the effective clusters give a good approximation of any cluster mixture in the forward-backward correlations analysis. This means that results from both studies are not fully compatible, as indicated in Fig. 5.7. To account for effects of cluster mixing, additional correction of results from the reconstruction of two-particle correlations is necessary. It is obvious that this should increase both K_{eff} and δ, but the exact magnitude of the change depends on the mixture of clusters in the data, which is unfortunately not known. However, it is not clear whether a better agreement in Fig. 5.7 is then reached, because simultaneous increase of K_{eff} and δ will most probably move the points in this Figure approximately along the error lines.

The Simple Cluster Model offers a convenient method for analysis of acceptance effects for events with a variety of different clusters. Studies of samples of events with mixtures of clusters confirm that in the case of forward-backward correlations the results of reconstruction can be represented by an average cluster, and can be analytically predicted if this mixture is known. For the two-particle correlations, acceptance effects have a more complicated dependence on the composition of the mixture. Reconstructed cluster parameters, K_{eff} and δ, are in this case lower than expected from accurate calculations and are thus more difficult to interpret.

5.4 Effects from fluctuations of $dN/d\eta$ distribution

In all previous studies in this Section it was assumed that in the first stage of the process of particle production the positions of the clusters are randomly generated from the same η distribution, and thus in the $dN/d\eta$ distribution of final particles only statistical fluctuations are present. It is however interesting to know how the results obtained in previous subsections may

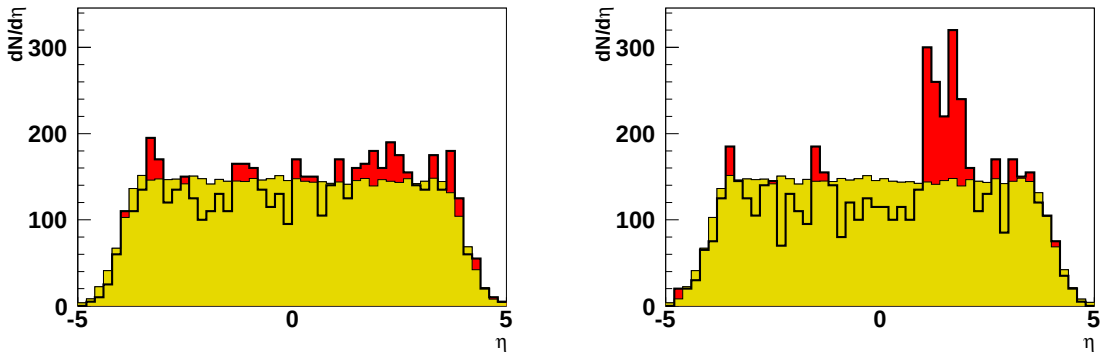

Fig. 5.10: Examples of fluctuations of $dN/d\eta$ shape: enhanced particle production in one hemisphere ($\eta > 0$) (left) and additional particles in a limited η range ($1 < \eta < 2$) (right). The black contour histogram was obtained for a single event with such a fluctuation, the yellow shaded histogram shows the average shape of $dN/d\eta$ calculated from 100 events, and the red areas indicate the excess of particles in the event with respect to the mean due to statistical and non-statistical fluctuations. In this example 10% of particles come from the fluctuation; they were added in the appropriate η range to the symmetric histogram, which contained 90% of expected total multiplicity.

change in the presence of non-statistical fluctuations of the particle density $dN/d\eta$. In order to answer this question it is now assumed that the emission angles of clusters are generated from a $dN_{cl}/d\eta$ distribution that changes from event to event.

In this study two simple types of fluctuations are considered, a global increase of particle density in one hemisphere and a "bump" of additional particles in a well defined η range (selected range is $1 < |\eta| < 2$). Examples of events with these types of fluctuation are presented in Fig. 5.10. The first scenario is a simplified version of the Wounded Nucleon Model, discussed in Section 6, while the second is similar to production of particle "bursts" or "bubbles" [211]. In order to obtain finally a symmetric $dN/d\eta$ distribution, the fluctuations are generated with 50% probability for positive and negative pseudorapidity.

The analysis of the impact of such fluctuations on results from two-particle correlations requires the generation of events and reconstruction of "raw" cluster parameters. It was assumed that events contain clusters with K=3 and width δ=1.0, and the fluctuation is already present during the production of clusters. Samples of events with each type of fluctuation and varying fluctuation strength characterized as the fraction of additional clusters are analyzed. In Fig. 5.11 (left) results for events with the same multiplicity are compared. As expected, the stronger the fluctuation, the larger the deviation of raw reconstructed cluster parameters from those obtained in the absence of such fluctuations. If $dN/d\eta$ fluctuations are present, they lead primarily to overestimation of the cluster size K, although the reconstructed width δ of the cluster also increases. The fluctuations limited to narrow η bins give larger K values than for similar fluctuations in the full hemisphere. The fluctuations of the second type lead to a larger reconstructed width δ; however, in order to obtain $\delta \approx 1.5$ as seen in the data, the clusters in the events should be wider than what was assumed in the studies discussed here.

The dependence of reconstruction results on event multiplicity for a fixed fluctuation strength (2%) is shown in Fig. 5.11 (right). Such fluctuations have only a small effect for event samples with a low total multiplicity, but the deviation of reconstructed cluster parameters from those expected for the case without fluctuations grows with the number of charged particles. This is

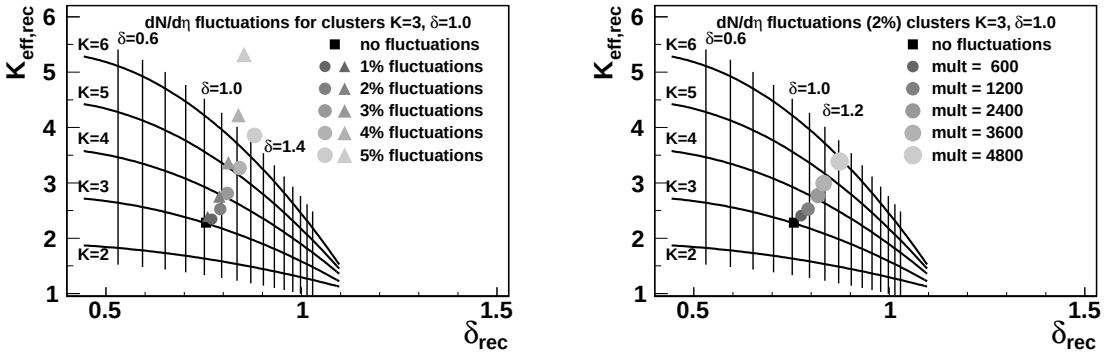

Fig. 5.11: Reconstruction of cluster parameters from two-particle correlations for events containing clusters with size K=3 and width δ=1.0 in which fluctuations of $dN/d\eta$ shape are present: the events have the same total multiplicity of charged particles (1200), but the fraction of particles involved in the fluctuations is changing (left); the fraction of particles involved in the fluctuations is constant (2%), but the total multiplicity of charged particles varies from 600 to 4800 (right). The circles denote results obtained for fluctuations in one full hemisphere, the triangles denote results obtained for fluctuations limited to the $1 < |\eta| < 2$ range and the square marks results for the sample without $dN/d\eta$ fluctuations. The grid is the same as presented and described in Fig. 5.5.

a natural effect of the constant strength of additional fluctuations (2%), which become more significant when statistical fluctuations decrease with multiplicity. This trend is opposite to that observed in the experimental results, where the smallest cluster size and width is found in the most central $Au + Au$ collisions [36].

The sensitivity of forward-backward correlations to the fluctuations of the $dN/d\eta$ shape can be estimated analytically. Let's assume that an additional N_x particles are registered in one of the bins. Then the modified C_x parameter is equal to

$$C_x = \frac{(N_F + N_x) - N_B}{N_F + N_B + N_x} \quad \text{or} \quad \mathrm{C_x} = \frac{\mathrm{N_F} - (\mathrm{N_B} + \mathrm{N_x})}{\mathrm{N_F} + \mathrm{N_B} + \mathrm{N_x}} \tag{5.9}$$

when the additional particles are registered in forward or backward hemisphere, respectively. Assuming that the fluctuations occur with the same probability at positive and negative η, the variance of C_x can be calculated as:

$$\sigma^2(C_x) = \left\langle \frac{(N_F + N_x - N_B)^2}{2(N_F + N_B + N_x)} + \frac{(N_F - N_B - N_x)^2}{2(N_F + N_B + N_x)} \right\rangle \tag{5.10}$$

and then:

$$\sigma^2(C_x) = \left\langle \frac{(N_F - N_B)^2 + N_x^2}{N_F + N_B + N_x} \right\rangle . \tag{5.11}$$

Denoting the sum $N_F + N_B + N_x$ by N and the fraction of additional particles by x ($x = N_x/N$), the formula can be simplified to:

$$\sigma^2(C_x) = \left\langle \frac{(N_F - N_B)^2}{N} + \frac{(xN)^2}{N} \right\rangle = \left\langle \frac{(N_F - N_B)^2}{N_F + N_B} \frac{N_F + N_B}{N} + x^2 N \right\rangle \tag{5.12}$$

thus

$$\sigma^2(C_x) = \left\langle \frac{(N_F - N_B)^2}{N_F + N_B}(1 - x) + x^2 N \right\rangle . \tag{5.13}$$

Assuming that the fraction of additional particles x is not correlated with N or $N_F - N_B$ we obtain:

$$\sigma^2(C_x) = \sigma^2(C)\langle 1-x\rangle + \langle x^2\rangle\langle N\rangle. \tag{5.14}$$

The reconstructed $\sigma^2(C_x)$ is larger than the $\sigma^2(C)$ for events without $dN/d\eta$ fluctuations if $xN > \sigma^2(C)$, i.e. the fluctuations comprise more particles than the average number of particles from one cluster in the η bin considered. The value of $\sigma^2(C_x)$ grows with event multiplicity providing that the cluster properties and the fluctuations size (x) are not changing. The above formula enables us also to calculate the upper limit for the size of $dN/d\eta$ fluctuation that is still in agreement with the experimentally measured $\sigma^2(C_{exp})$. Assuming fully random production of particles, which gives $\sigma^2(C)$=1, the maximal value of x for large N is almost exactly equal to:

$$x_{max} = \sqrt{\frac{\sigma^2(C_{exp}) - 1}{\langle N\rangle}} \tag{5.15}$$

The most reliable upper limit of x can be obtained using the widest η bin centered at $|\eta|$=2 ($\Delta\eta$=2). The reproduction of the $\sigma^2(C_{exp})$=2.16 and $\sigma^2(C_{exp})$=2.71 (for central and peripheral event samples, respectively) solely by $dN/d\eta$ fluctuations would require x_{max}=2.5% and x_{max}=6.7% for central and peripheral collisions, respectively.

Studies of events from the Simple Cluster Model generated for a fluctuating pseudorapidity distribution reveal the sensitivity of results from correlation analyses to such global fluctuations. Both in two-particle correlations and in the forward-backward correlations the cluster size and width seems to increase substantially even for relatively small fluctuations. On the basis of analytical calculations it is possible to determine the upper limit on the fraction of particles that can be involved in such non-statistical fluctuations.

5.5 Forward-backward multiplicity correlations measured by STAR Collaboration

In the study performed by the STAR Collaboration [187] the correlation is represented by the parameter

$$b = \frac{\langle N_F N_B\rangle - \langle N_F\rangle\langle N_B\rangle}{\langle N_F^2\rangle - \langle N_F\rangle^2}, \tag{5.16}$$

in which multiplicities of charged particles registered in pseudorapidity bins symmetric with respect to $\eta = 0$ are used. Considering the production of particles in clusters of K particles, we may first examine effects of a simultaneous transformation: $N_F \to KN_F$ and $N_B \to KN_B$. As N_F and N_B appear in the numerator and denominator in the same order, this modification does not change the value of b, thus this parameter is not directly sensitive to production of particles in clusters. However, such a simple transformation corresponds to an idealized case in which all particles belonging to a cluster have the same pseudorapidity and thus are registered in the same η bin. For clusters with large widths the correlations become more complicated and are worth studying using the Simple Cluster Model. This is especially justified as in this analysis the centrality determination is based on the multiplicity in an η range, which is very close to the η bins for which b is calculated.

For the purpose of analyzing forward-backward correlations measured using the b parameter, several samples of events were generated according to the Simple Cluster Model. In each case

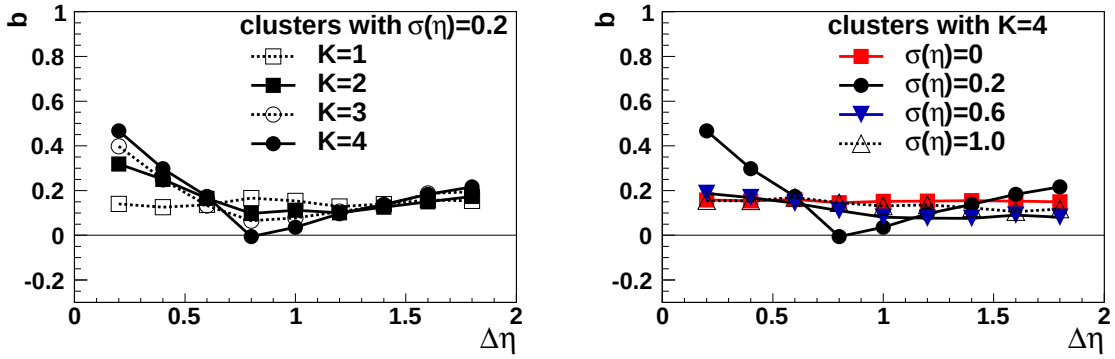

Fig. 5.12: Forward-backward correlation strength parameter b, as a function of the distance, $\Delta\eta$, between the η bins, obtained for events with clusters with the same cluster width and changing cluster size (left) or with the same cluster size and changing cluster width (right).

the $dN/d\eta$ distribution of clusters and also of particles originating from them is flat in the pseudorapidity acceptance of the STAR detector, $|\eta| < 1$. The number of clusters, selected randomly for each event, was generated in such a range that all multiplicities observed by STAR experiment for $|\eta| < 1$ are present also in the simulations. Following the STAR analysis [187], the multiplicity of particles N_F and N_B in 9 pairs of corresponding, symmetric η bins were calculated. The width of the bins was 0.2, and they were separated by a pseudorapidity gap (distance between bin centers, $\Delta\eta$) varying from 0.2 to 1.8. Also the multiplicity, N_{ch}, used as a measure of the event centrality, was counted in one of three η ranges: $|\eta| < 0.5$, $|\eta| < 0.3$ or $0.8 < |\eta| < 1.0$, and $|\eta| > 0.5$ (for the distance between the actually used bins $\Delta\eta = 1.2$, 1.4, 1.6 and 1.8, $\Delta\eta = 0.2$, 0.4, 0.6 and $\Delta\eta = 0.8$, 1.0, respectively). As suggested by STAR Collaboration, fits of $\langle N_F \rangle$, $\langle N_B \rangle$, $\langle N_F^2 \rangle$ and $\langle N_F N_B \rangle$, as a function of N_{ch} were performed. This allows us to calculate the b parameter at any N_{ch}, using the values of fitted functions.

The basic properties of the observable b are analyzed using the values calculated for a single value of $N_{ch} = 350$. This is equivalent to selecting events with the same N_{ch} from the full multiplicity distribution; the fits only allow us to reduce the impact of statistical fluctuations. Such a choice does not impact the final conclusions, as tests performed for many different multiplicities and also in the multiplicity range corresponding to the centrality selection used by the STAR Collaboration always give similar results.

In the first analyzed sample of events single particles were generated randomly (i.e. $K = 1$). Naively, one would expect $b = 0$ in such a case; however, from the simulations $b \approx 0.15$ is obtained, the same value for any $\Delta\eta$. The same result is obtained for K=2, 3, 4 if the width of clusters is zero (all particles from a cluster have the same η). In order to explain this rather unexpected result, it is necessary to understand the properties of the events over which the averaging takes place. In our case, events with the same N_{ch} (in the bins used to determine event centrality) are selected and then N_F and N_B are obtained and used in the calculations. However, the same N_{ch} does not mean that the total number of particles (in the full η range) is the same. We have thus a mixture of events for which the total number of particles varies slightly. For accepted events with the total multiplicity larger than the average in this sample, the values of N_F and N_B are also systematically and simultaneously larger. Similar effect is present for events with lower multiplicity, thus a correlation between originally uncorrelated N_F and N_B appears. This positive correlation, called from now *the correlation with the total*

multiplicity, makes b larger than 0.

A much more complicated pattern of correlations appears, when for $K > 1$ the cluster width is larger than zero. A good illustration of this is furnished by the analysis of the event samples with $\sigma(\eta) = 0.2$ and several K values, shown in Fig. 5.12 (left). The *correlation with the total multiplicity* described above increases b to about 0.15, as is observed for clusters with $K = 1$. A much larger b value is obtained for the first pair of adjacent bins (-0.2, 0) and (0, 0.2) if K is larger than 1. In this case a cluster centered at $\eta = 0$ populates the forward and backward bins with equal probability and induces a strong positive correlation between N_F and N_B. Clusters centered at larger $|\eta|$ add larger contribution to only one of the bins. The larger the cluster size K, the more probable that a pair of particles from it belong to different bins; thus b at $\Delta\eta = 0.2$ increases with K. When the distance between the bins grows, the probability that particles from the same cluster are registered in both the forward and backward bins decreases and the positive short range correlation becomes smaller. This probability becomes negligible for $\Delta\eta > 0.5$ and only the correlation originating from the common total multiplicity determines the value of b.

An interesting effect is observed for $\Delta\eta = 0.8$ (i.e. bins (-0.5, -0.3) and (0.3, 0.5)) for which the value of b for $K > 1$ is smaller than that for $K = 1$. This is again explained by the contribution of particles from one cluster to two different bins, in this case to N_F and N_{ch} (or N_B and N_{ch}), which is possible because the interval (-0.3, 0.3) used to determine N_{ch} is adjacent to the bins in which values of N_F and N_B are calculated. Because of correlation between N_{ch} and N_F (and N_{ch} and N_B) effects of *the correlation with the total multiplicity* are partly cancelled.

The clusters with the width $\sigma(\eta) = 0.2$ were considered only to make the explanations more perspicuous. Realistic clusters are much wider, and the effects expected for clusters with larger widths are presented in Fig. 5.12 (right). A strong dependence on the distance between forward and backward bins, observed for very narrow clusters ($\sigma(\eta) = 0.2$), is already much weaker for clusters with $\sigma(\eta) = 0.6$, and for the clusters with $\sigma(\eta) = 1.0$ the parameter b is practically the same as for the events not affected by production of particles in clusters (represented by $\sigma(\eta) = 0$). This indicates that the dependence of b on the distance between the η bins is on average rather weak, which agrees with the observation made by STAR Collaboration [187].

This study of the forward-backward correlation strength parameter b confirms that short-range correlations due to the production of particles in clusters are cancelled in this observable. If extremely narrow clusters are produced in the events, the short range correlations might modify the dependence on the distance between the bins. However, the global correlation connected with the total multiplicity plays an important role.

Section summary

The Simple Cluster Model provides only an approximate description of the correlations observed in particle production, but it allows us to determine the basic properties of several observables. Its main success was the disclosure of the importance of acceptance effects even in the case when a very wide pseudorapidity range, (-3,3), is used in the studies. Results shown in this section and in the Appendix F clearly demonstrate that correlations observed in nucleus-nucleus collisions can not be attributed only to decays of resonances. The range of the correlations measured as cluster width δ (or $\sigma(\eta)$) is even larger than that expected for resonance decays at rest.

6 Fluctuations and correlations in Wounded Nucleon Model

Particle production in collisions of nuclei depends on geometrical parameters of the collision, which determine the number of elementary $N+N$ collisions, N_{coll}, and the number of nucleons participating in the collisions, N_{part}. The latter parameter is approximately linearly correlated with the total multiplicity and the particle density at $\eta \approx 0$.

The Wounded Nucleon Model (WNM) [212, 158] provides a simple description of nucleus-nucleus collisions that is consistent with the above mentioned observations. It assumes that the collision of nuclei can be treated as a specific superposition of collisions between nucleons. The finally observed particles are produced in a process of independent fragmentation of nucleons participating in $N+N$ collisions, called in this model wounded nucleons. In the original model, this fragmentation does not depend on the number of collisions a nucleon has suffered. Recently, the centrality dependence of pseudorapidity distributions measured in $d+Au$ collisions [20] was successfully described using the Wounded Nucleon Model [158]. This Section presents predictions from WNM for multiplicity fluctuations [213] and two-particle correlations [47].

The assumption that in high energy collisions the fragmenting objects are wounded nucleons and that the yield of particles does not depend on the number of collisions, in which the fragmenting nucleon took part, is a simplification of real processes and can be valid only approximately. For the central $A+A$ collisions the original Wounded Nucleon Model does not perfectly describe the data [214]. It is thus reasonable to consider also other possibilities, taking into account composite structure of nucleons and treat it as composed of tree valence quarks or a quark and a diquark. The collisions of nucleons should be regarded in this case as collisions between quarks or diquarks and particles are then produced by fragmentation of quarks or diquarks [215]. The model with valence quarks was used in the context of π-nucleus [216] and proton-nucleus interactions [217]. The wounded quark and diquark model was recently successfully applied to describe pseudorapidity distributions in $Au+Au$ collisions at RHIC energy [218, 219]. It appears that the wounded quark and diquark model describes better $A+A$ collisions than the original Wounded Nucleon Model [220]. However, simplicity of both models causes that perfect agreement with the experimental data can not be expected. For example discrepancies between experiment and predictions from superposition models for the scaled dispersion of multiplicity distribution are shown in Ref. [221].

Predictions from models with wounded quarks and wounded nucleons may become very close when in the WNM some dependence of the fragmentation on the number of collisions is introduced. The fragmentation function of the nucleon can be treated as a sum of the fragmentation functions of the quark and a diquark weighted by the probability of wounding each of them in a single nucleon-nucleon collision (Fig. 6.1). Both approaches are equivalent in the pseudorapidity range, where the contribution from spectator quarks (diquarks) is negligible (i.e. $|\eta| < 3.5$). The Wounded Nucleon Model with such modification was used in Ref. [213] and the analysis from it is presented in a shortened version in this Section.

In Wounded Nucleon Model the particle density in elementary $p+p$ collisions is described as $\rho(\eta)+\rho(-\eta)$. In the case of nucleus-nucleus collision it is the sum of these functions multiplied by the number of wounded nucleons in the appropriate nucleus [158]:

$$\frac{dN}{d\eta} = \langle w_{_F} \rangle \, \rho(\eta) + \langle w_{_B} \rangle \, \rho(-\eta) \tag{6.1}$$

where $\langle w_{_F} \rangle$ and $\langle w_{_B} \rangle$ are the mean numbers of wounded nucleons in the forward and backward

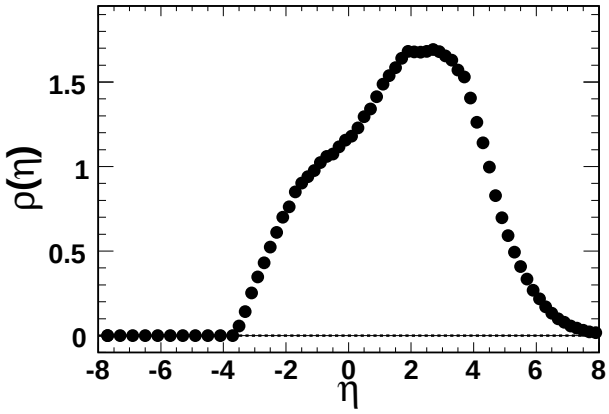

Fig. 6.1: Wounded nucleon fragmentation function $\rho(\eta)$ used in the presented analysis: pseudorapidity density of produced particles from the forward-moving wounded nucleon at $\sqrt{s_{NN}} = 200$ GeV [213].

moving nucleus, respectively. At midrapidity the particle density in $A + A$ collisions becomes simply

$$dN/d\eta|_{\eta=0} = \langle w_{_F} + w_{_B} \rangle \, \rho(0) \tag{6.2}$$

and should be $\langle w_{_F} + w_{_B} \rangle /2$ times larger than in elementary collisions. However, the experimental particle density $dN/d\eta|_{\eta=0}$ is larger than $\langle w_{_F} + w_{_B} \rangle \, \rho(0)$ [6]. In order to remove this discrepancy a centrality dependence of the fragmentation function has to be introduced. It is sufficient to use a factor γ, determined for each centrality class, which represents the average increase of the multiplicity of particles generated in the fragmentation of a wounded nucleon that underwent many inelastic collisions. The scaling factor γ in WNM is related to the increase of probability of wounding more than one constituent of the nucleon in the wounded quark and diquark model.

Wounded Nucleon Model can be used not only to describe average $dN/d\eta$ distribution, but provides also interesting predictions for multiplicity correlations and fluctuations. According to this model the charged particles pseudorapidity distribution in a single nucleus-nucleus collision equals:

$$\frac{dN}{d\eta} = w_{_F} \rho_{_F}(\eta) + w_{_B} \rho_{_B}(\eta), \tag{6.3}$$

where in contrast to Eq. 6.1 actual values $w_{_F}$ and $w_{_B}$ of the number of wounded nucleons in forward and backward moving nuclei, respectively, and actual fragmentation functions (averaged only within this event) are used. Of course averaging over many events gives:

$$\langle \rho_{_F}(\eta) \rangle = \rho(\eta) \quad \text{and} \quad \langle \rho_{\mathrm{B}}(\eta) \rangle = \rho(-\eta). \tag{6.4}$$

Difference between $\rho(\eta)$ and $\rho(-\eta)$ is sufficiently large that even in a single event the shape of $dN/d\eta$ tends to be asymmetric when $w_{_F}$ and $w_{_B}$ are different. Because of this effect Wounded Nucleon Model naturally predicts fluctuations connected with the geometry of the collision, which determines values of $w_{_F}$ and $w_{_B}$.

6.1 Forward-backward fluctuations in the Wounded Nucleon Model

The variance σ_C^2 of the asymmetry variable $C = (N_F - N_B)/\sqrt{N_F + N_B}$ (Eq. 4.2 discussed in Section 4.2) is used by PHOBOS Collaboration as a measure of the forward-backward fluctuations. The values of N_F and N_B denote the number of particles in η bins placed symmetrically

with respect to $\eta = 0$. They can be calculated in the Wounded Nucleon Model by multiplying the wounded nucleon fragmentation function (integrated in the appropriate η interval) by the number of wounded nucleons. However, for the calculation of event-by-event values, both the fluctuations of the number of wounded nucleons and the fluctuations in the fragmentation of them have to be included. This requires additional stipulations, more precisely defining the model:

(a) regardless of the number of particles produced in the fragmentation of a wounded nucleon, the shape of the fragmentation function $\rho(\eta)$ is the same;

(b) the number of particles produced in the combined pseudorapidity bin $B+F$ can be parameterized by negative binomial (NB) distribution:

$$P(n,\bar{n},k) = \frac{\Gamma(n+k)}{\Gamma(n+1)\Gamma(k)} \left(\frac{\bar{n}}{k}\right)^n \left(1+\frac{\bar{n}}{k}\right)^{-n-k}, \tag{6.5}$$

where $\bar{n}$ is the average multiplicity in the combined interval $B+F$, $1/k$ measures deviation from Poisson distribution and $\Gamma(n)$ is the generalized factorial function ($n! = \Gamma(n+1)$);

(c) particles registered in the $F+B$ bin can be randomly assigned to bin F and bin B with the probability p and $1-p$ which is obtained from the integration of $\rho(\eta)$ in appropriate intervals:

$$p = \frac{\int_F \rho\,(\eta)\,d\eta}{\int_B \rho\,(\eta)\,d\eta + \int_F \rho\,(\eta)\,d\eta}; \tag{6.6}$$

(d) the correct centrality dependence of the fragmentation function is ensured by the γ factor;

(e) the actual values of $w_{_F}$ and $w_{_B}$ are obtained from Monte Carlo generations, as described below.

The point (b) is justified by experimental studies of $p+p$ interactions [222], in which the negative binomial distribution was fitted to measured experimental distributions in selected pseudorapidity bins. It is straightforward to show that if such a parameterization is valid for $p+p$ interactions then the multiplicity distribution from a single wounded nucleon follows also a NB distribution, but with $\bar{n}$ and k substituted by $\bar{n}/2$ and $k/2$, respectively [223].

The centrality dependence of the wounded nucleon fragmentation is introduced by multiplying $\bar{n}/2$ by a scaling factor γ. It is not clear if the $k/2$ parameter should also be modified, thus two possibilities are considered: $k/2$ unchanged or multiplied by γ. The latter is justified if nucleons can be treated as composed of a quark and a diquark that populate particles independently.

The most realistic values of $w_{_F}$ and $w_{_B}$ for events from a given centrality class can be obtained from simulations using events from the HIJING generator (for which $w_{_F}$ and $w_{_B}$ are known), selected by cuts compatible with those for the PHOBOS experimental data. As it is shown later, the most important is correct reproduction of the variance of the asymmetry variable C_w, this time calculated not for multiplicity, but for the number of wounded nucleons:

$$C_w = (w_{_F} - w_{_B})/\sqrt{w_{_F} + w_{_B}}. \tag{6.7}$$

The values of $\sigma^2_{C_w}$ obtained using the experimental selection of centrality classes are shown in Fig. 6.2. They are compared with the values obtained using cuts based on charged particle multiplicity, impact parameter, and $w_{_F} + w_{_B}$, which all give very close results. While it is not

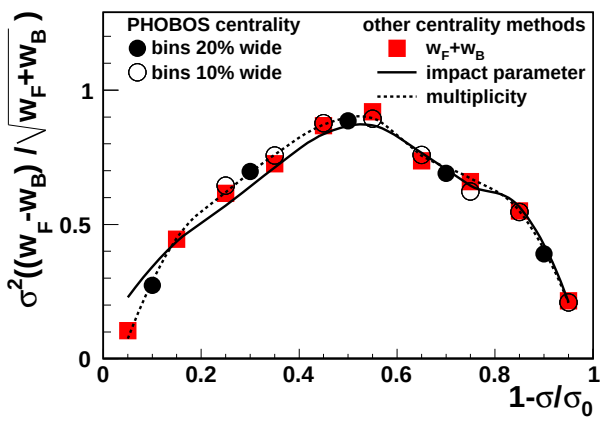

Fig. 6.2: The variance $\sigma^2_{C_w}$ of the asymmetry variable C, calculated for the number of wounded nucleons: $C_w = (w_F - w_B)/\sqrt{w_F + w_B}$, as a function of centrality represented by the fractional cross section $1-\sigma/\sigma_0$. The values of w_F and w_B were obtained from HIJING events with different centralities (as determined using the centrality cuts compatible with experimental cuts in the PHOBOS experiment). For comparison $\sigma^2_{C_w}$ was also calculated for events assigned to centrality classes using cuts on $w_F + w_B$, impact parameter and charged particles multiplicity.

surprising in the case of the total multiplicity, as the detector signals used in the experimental centrality cut is proportional to multiplicity in a selected η range, so close agreement with the remaining types of cuts is rather unexpected.

6.2 Toy model simulations and analytical calculations

The predictions of Wounded Nucleon Model for the variance of asymmetry variable C were obtained by a toy model simulations. Three types of generation are used:

(A) events have a fixed number of wounded nucleons $w_F = w_B$ and each wounded nucleon adds its contribution to $F + B$ bins; these contributions are generated independently according to an NB distribution; then the generated particles are randomly assigned to bins F and B according to probability p and $1 - p$ (defined by Eq. 6.6);

(B) events with fluctuating w_F and w_B, from HIJING model, but without fluctuations in the wounded nucleon fragmentation: each wounded nucleon adds the same mean number of particles to the bins F and B;

(C) the most realistic generation with the fluctuating w_F and w_B, as in the case (B), and the final particles generated from the NB distribution, as it is done in the case (A).

Calculations were done for several pseudorapidity bins, either with fixed position (at $|\eta| = 2$) and changing bin width or with fixed bin width ($\Delta\eta = 0.5$) but changing position in pseudorapidity - just like in the PHOBOS experiment [24]. Also the same centrality bins: central 0-20% and peripheral 40-60% were used. The parameters of the NB distribution and the probability p can be found in Ref. [213]. The γ factor was estimated by comparing $\langle w \rangle \rho(0)$ and the PHOBOS data on $dN/d\eta$ at midrapidity [6], and equals $\gamma = 1.35 \pm 0.15$ and $\gamma = 1.6 \pm 0.1$ for peripheral and central collisions, respectively. Using values of N_F and N_B for events from toy model simulations the variable C and then its variation σ^2_C were calculated.

The case (A) allows us to study effects of simple superposition of nucleon-nucleon collisions, by changing the number of wounded nucleons. An increase of σ^2_C is observed, but it saturates soon, as for $w_F > 10$ the changes are very small (see the results for $w_F = 30$ and $w_F = 140$ in

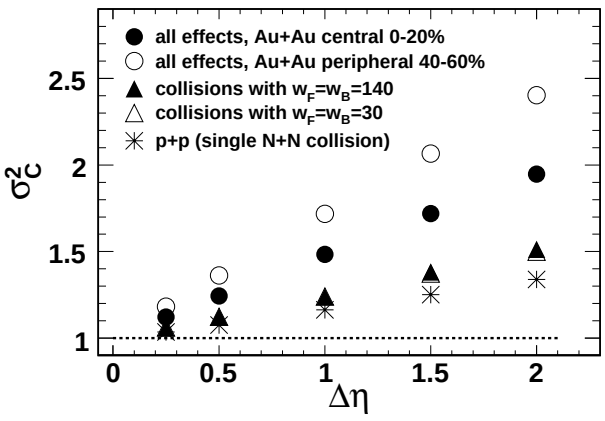

Fig. 6.3: Wounded Nucleon Model predictions for σ_C^2 values obtained for pseudorapidity bins centered at η=2 with changing width, $\Delta\eta$. The model calculations for central $0-20\%$ ($\langle w_{_F}\rangle = 140$) and peripheral $40-60\%$ ($\langle w_{_F}\rangle = 30$) $Au+Au$ collisions with all effects included (full and open circles) are compared with results for collisions with exactly 140 and 30 wounded nucleons in each nuclei (full and open triangles), fluctuations in the number of wounded nucleons are responsible for the difference between corresponding sets of points. In addition predictions for $p+p$ collisions are also shown (stars).

Fig. 6.3). It means that superposition of many collisions increases fluctuations, but it is not responsible for the difference between the most central and semi-central collisions.

The case (B) contains only fluctuations in the number of wounded nucleons without any contributions from other effects thus σ_C^2 (calculated for the registered particles) is directly proportional to the variance of

$$C_w = \frac{w_{_F} - w_{_B}}{\sqrt{w_{_F} + w_{_B}}} \tag{6.8}$$

(denoted from now by $\sigma_{C_w}^2$). The centrality dependence of $\sigma_{C_w}^2$ is shown in Fig. 6.2, it reaches the highest value for semi-peripheral collisions and decreases for the most central events sample.

The case (C) contains all sources of fluctuations: those present in the elementary $p+p$ interactions (hidden in the NB distribution), effects of superposition of fragmentation of many wounded nucleons and caused by probabilistic nature of the collision on nuclei. Because these sources are independent, the value of σ_C^2 obtained in case (C) is a direct sum of the values of this variance in cases (A) and (B).

For Wounded Nucleon Model with additional specifications enumerated at the beginning of this Section an analytical calculation of σ_C^2 is possible [213]. When the terms of the order $1/\langle w_{_F}\rangle$ are neglected a relatively simple formula can be derived:

$$\sigma_C^2 \approx 1 + \bar{n}(2p-1)^2 \left[\frac{1}{k} + \frac{1}{2}\gamma \left\langle \frac{(w_{_F} - w_{_B})^2}{w_{_F} + w_{_B}} \right\rangle\right] \tag{6.9}$$

This formula agrees with the results from the toy model simulations with an accuracy better than 3%. It also clearly shows that values of $\sigma_C^2 > 1$ can be obtained only when $p \neq 0.5$, i.e. the fragmentation function is asymmetric with respect to $\eta = 0$.

Presented calculations combine the effects present in elementary $p+p$ interactions (and contained in the multiplicity distribution), with the fluctuations of the number of wounded nucleons that both increase values of σ_C^2. For nucleus-nucleus collisions predictions from the Wounded Nucleon Model can be obtained from a relatively simple formula.

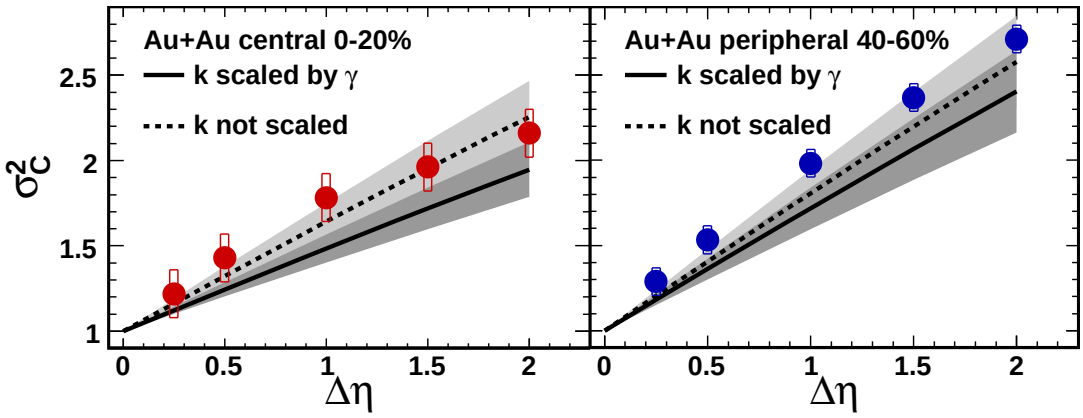

Fig. 6.4: The variance of the forward-backward asymmetry variable $C = (N_F - N_B)/\sqrt{N_F + N_B}$ as a function of the width of the forward and backward intervals for the most central collisions (left) and the semi-peripheral collisions (right). The position of the center of each bin is fixed at $\eta_F = 2$ and $\eta_B = -2$. The PHOBOS data points are compared with predictions of the modified Wounded Nucleon Model (continuous and dashed lines, for the scaled and unmodified k parameter respectively). The grey bands reflect the systematic error of model calculations, due to the uncertainty of model parameters.

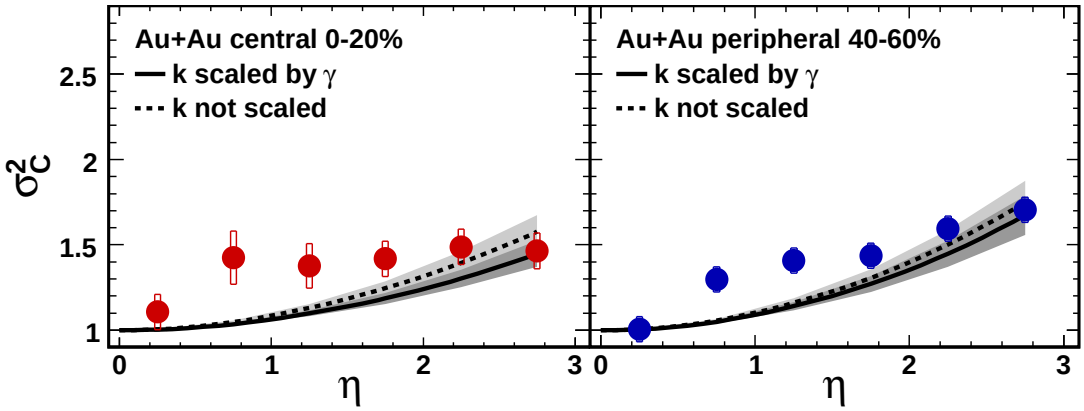

Fig. 6.5: The same as in Fig. 6.4 but now as a function of the position of the center of the forward bin, η, for fixed width of each bin ($\Delta\eta = 0.5$) is.

6.3 Comparison with experimental data

The model calculations were performed for the same pseudorapidity intervals as those used to obtain experimental results for $Au + Au$ collisions at $\sqrt{s_{NN}} = 200$ GeV [24] presented already in the Section 4.2. In Fig. 6.4 the dependence of σ^2_C on the bin width $\Delta\eta$ is shown, while the dependence on the relative separation of the bins with identical width is presented in Fig. 6.5. As described previously, there is some uncertainty with regard to the centrality dependence of the k parameter in the Negative Binomial parameterization of the multiplicity distribution and two extreme variants of it (k multiplied by γ and k not scaled) are included. Each of the parameters of the model ($\bar{n}$, k and p) is known with limited precision (relative errors are 7%, 20% and 10%, respectively). Systematic errors of model calculations, represented in Fig. 6.4

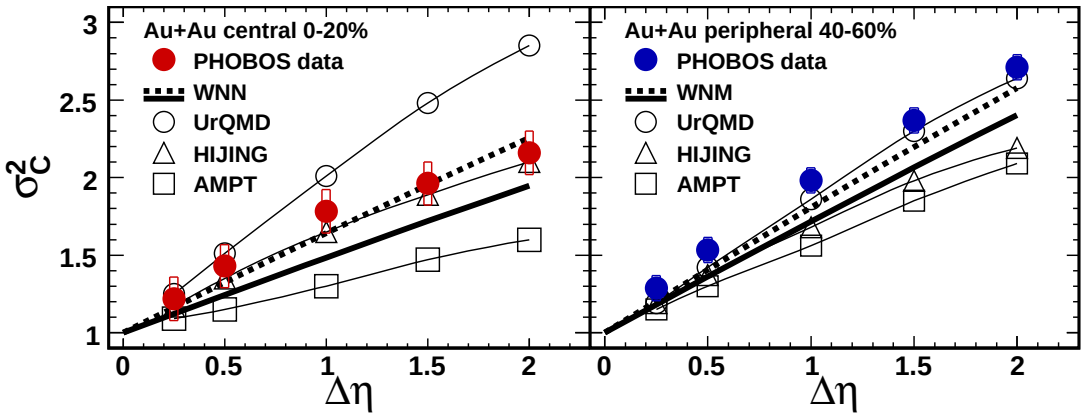

Fig. 6.6: Wounded Nucleon Model (WNM) predictions for σ_C^2 values obtained for the pseudorapidity bins centered at $\eta = 2$ with changing width $\Delta\eta$. Results for wounded nucleon model are shown for two cases, k parameter scaled and not scaled, as continuous and dashed lines respectively. UrQMD [224], HIJING and AMPT [24] predictions are represented by open symbols described in the plot.

and 6.5 by grey bands, take into account these uncertainties.

In both cases presented in Fig. 6.4 and in Fig. 6.5 the general trends of the data and model predictions agree. The version with k parameter not scaled is closer to the data points, however the experimental values of σ_C^2 are systematically larger than it is expected from the model. This is not necessarily a failure of the model, but may be due to short range correlations, which are only partially reflected in the multiplicity distribution measured in $p+p$ interactions and thus are not included in the model.

It is interesting to compare the experimental data also with predictions from other models. For this purpose the dependence of σ_C^2 on the bin width $\Delta\eta$ was chosen, because it is more challenging for the models, as it includes points with the largest values of σ_C^2, measured with the smallest relative errors. In Fig. 6.6 in addition to WNM also three other models are included. The UrQMD [224] reproduces only experimental results obtained for peripheral collisions and deviates strongly for central collisions, as it predicts a slight increase of σ_C^2 with centrality instead of a significant drop. The HIJING model [24] agrees for the central data, but has no centrality dependence of σ_C^2 and thus for peripheral collisions underestimates this observable. Finally the AMPT model predicts correct trend for centrality dependence, but both for central and peripheral collisions significantly underestimates σ_C^2 values.

Wounded Nucleon Model correctly reproduces centrality dependence of forward-backward correlations. In comparison of predicted σ_C^2 values from several models, these from Wounded Nucleon Model are the closest to the experimental results.

6.4 Two-particle correlations

Fluctuations of the number of wounded nucleons from forward and backward moving nuclei cause that the particle density distribution, $dN/d\eta$, is asymmetric - more particles are produced on the side of this nuclei, in which more nucleons were wounded. It has similar effect as the fluctuations of $dN/d\eta$ distribution discussed earlier in Section 5.4 as a potential source of modifications both in the case of σ_C^2 and reconstructed parameters of clusters. Successful

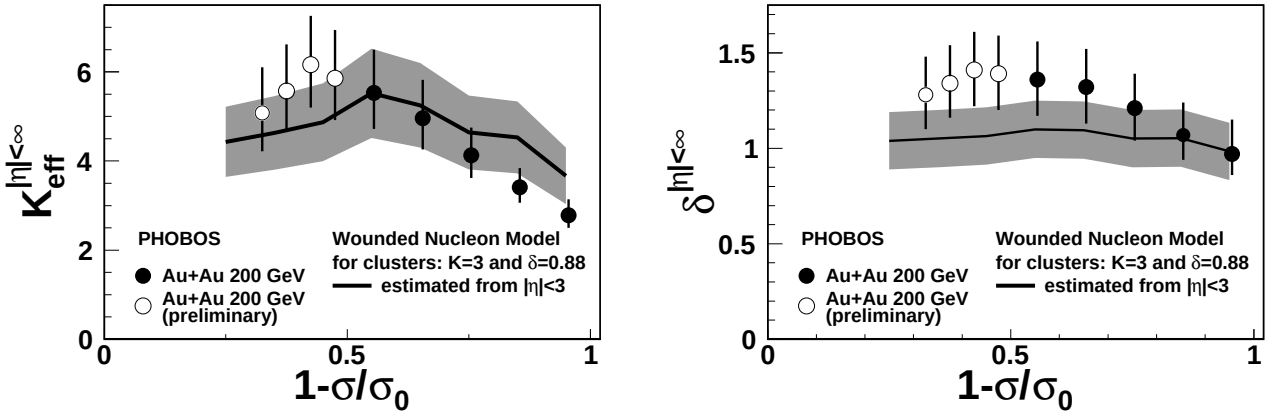

Fig. 6.7: The effective cluster size (left) and the width parameter δ (right) for $Au + Au$ collisions compared with the predictions from the Wounded Nucleon Model in which we assume fragmentation of the wounded nucleons into clusters similar to those observed in $p + p$ interactions [47].

description of the first observable, σ_C^2, by Wounded Nucleon Model encourages to use this model to obtain also predictions for the two-particle correlations. Obviously, some modifications of the model are needed as the main source of two-particle correlations, production of particles in clusters, has to be combined with the effects originating from fluctuations of the number of wounded nucleons. It is thus reasonable to assume that wounded nucleons fragment not into particles, but into clusters that are decaying later into finally observed particles. However, there are still two questions to be answered: what kind of clusters are produced and how looks the fragmentation function of wounded nucleons into clusters.

From the analysis of $p + p$ interactions we know the values of the effective cluster size, $K_{eff} \approx 3$ and the width, $\delta \approx 0.88$. The studies presented in Section 5.3 show that a mixture of different clusters does not look in the reconstruction like clusters with averaged parameters, thus information on effective cluster parameters is not sufficient for precise calculations of combined effects from WNM and clusters. Nevertheless, we can use the clusters with $K_{eff} = 3$ and $\delta = 0.88$ as representatives to obtain at least qualitative predictions from WNM [47].

Realistic model requires that, regardless of the assumed size of clusters, the final number of produced particles should agree with that measured experimentally. If the wounded nucleons fragment into clusters of the size K_{eff} then the integral of the wounded nucleon fragmentation function (into clusters) has to be K_{eff} times smaller than the integral of the function obtained for finally observed particles and presented in Fig. 6.1. In order to obtain the same properties of observed particles, the width of the fragmentation function into clusters should be smaller than that for final particles. However, the widening effect is small for a fragmentation function extending over about 10 pseudorapidity units, as the width from decay of clusters adds in quadrature and can increases the total width by a few % only.

Predictions from Wounded Nucleon Model can be obtained in simple simulations similar to those used in the case of σ_C^2 study. The number of wounded nucleons $w_{_F}$ and $w_{_B}$ is generated for a given centrality so that the mean numbers of wounded nucleons $\langle w_{_F} \rangle$, $\langle w_{_b} \rangle$ and variance of their difference $\sigma(w_{_F} - w_{_B})$ are consistent with values expected from the Glauber model. For each wounded nucleon positions of clusters in η are generated according to the wounded nucleon fragmentation function, and then the η values for K particles are obtained by adding a shift

generated from the gaussian function with the appropriate width (consistent with the value of δ). Events constructed this way are then processed by the reconstruction algorithm in order to obtain effective cluster parameters that are presented in Fig. 6.7. The cluster parameters are calculated in a fit to the $R(\Delta\eta)$ dependence (like that in Fig. 4.9), and systematic errors of WNM predictions represent uncertainties in the fitting procedure. Other sources of systematic uncertainties are less important and they do not increase the systematic errors significantly.

The trends observed for centrality dependence of reconstructed cluster parameters from experimental data are qualitatively reproduced by the Wounded Nucleon Model. Reconstructed effective cluster size is larger for peripheral then for central collisions and the width δ of the clusters is bigger when fluctuations of wounded nucleons are present. Even if the data points and model predictions agree within errors, the systematic discrepancies may be genuine and can be related to the fact, that in place of a correct (but unknown) mixture of clusters only identical clusters of one type were used in the simulations.

Section summary

Wounded Nucleon Model provides a simple description of particle production by fragmentation of nucleons that took part in the collision. For correct description of $A + A$ collisions it was necessary to modify the model and introduce a centrality dependence of the number of particles created in the fragmentation a wounded nucleon. Knowing the multiplicity distribution measured in $p + p$ interactions and the distribution of the number of wounded nucleons in the forward and backward moving nuclei it was possible to predict, using this modified model, the multiplicity fluctuations represented as the variance σ^2_C of the asymmetry parameter C. These calculations agree better with the experimental data obtained in the PHOBOS experiment than the prediction from other, more sophisticated models of $A + A$ collisions.

Fluctuations of the number of wounded nucleons affect also the values of cluster parameters obtained from the reconstruction procedure used in the analysis of two-particle correlations. In this case short range correlations are introduced by an assumption that wounded nucleons fragment into clusters, rather than directly into final particles observed experimentally. If such clusters are similar to those found in $p + p$ interactions the predictions from the Wounded Nucleon Model agree qualitatively with the trends observed in the $Au + Au$ collisions.

7 Other fluctuations in $A + A$ collisions at RHIC

In earlier Sections a detailed description of multiplicity fluctuations and correlations studies, and their interpretation in Simple Cluster Model and Wounded Nucleon Model are presented. However, in searches for phenomena related to Quark-Gluon Plasma formation and the onset of deconfinement many other observables are considered. This Section briefly describes the most interesting of such studies.

The elliptic flow fluctuations were analyzed by the PHOBOS Collaboration. Studies, for which identified particles are necessary, were performed at RHIC energies by the STAR and PHENIX Collaborations. The experimental investigation of heavy ion collisions at RHIC was at first concentrated on measuring global characteristics and searches for the most promising signals of a new phase of matter. Currently, after collecting large samples of events, more complicated and advanced correlations and fluctuations studies became possible. As it is impossible to present a complete and final summary of this still expanding research field, more attention is given to these types of fluctuations, which were considered as possible signals of critical phenomena and were analyzed from the very beginning: fluctuations of transverse momentum, charge and particle ratios. There are also other studies, for which more details can be found in the referenced papers:

- analysis using a discrete wavelet expansion method, which reveals large scale angular correlations for $p_T < 2.1$ GeV/c interpreted as minijets [225];
- measurement of three particle correlations, which are sensitive to local parity violation [194];
- study of fluctuations of net-charge and net-protons using higher order moments [226];
- detailed study of charged particles 2D correlations in azimuthal angle and pseudorapidity, divided into unlike-sign charged pairs and like-sign charged pairs, which are transformed into charge-dependent (CD) signals and charge-independent (CI) signals [191, 192];
- extensive analysis of inclusive charged particle distributions with an extraction of longitudinal correlations [227], in which a local maximum of $\alpha\xi$ (a parameter related to susceptibility) at $N_{part} \sim 90$ is seen, and which may suggest a critical phase boundary in the interpretation based on Ginzburg-Landau framework [228];
- numerous correlation studies using particles with higher momenta which are focused on determination of jet properties and their interactions in the dense matter created in heavy-ion collisions [190, 183, 184, 229, 185, 230].

7.1 Elliptic flow fluctuations

The strong elliptic flow, v_2, measured in heavy ion collisions at RHIC is an important confirmation of the creation of the strongly interaction new phase of matter - Quark-Gluon Plasma (see Section 2.1 for more details and Eq. 2.6 for definition of v_2). Further insight into its properties provide more detailed studies of this observable, including fluctuations of v_2.

The elliptic flow is related to the geometrical asymmetry of the overlap area of colliding nuclei and the magnitude of flow is proportional to the eccentricity of the overlap [93]. However, rather then the standard eccentricity defined by the shape of the common part of the circles representing colliding nuclei in the plane transverse to their motion, the participant eccentricity (Eq. B.4) calculated using geometrical positions of nucleons involved in inelastic interactions is relevant (see Section 2.4 and Refs. [31, 32]). This implicates that even for events

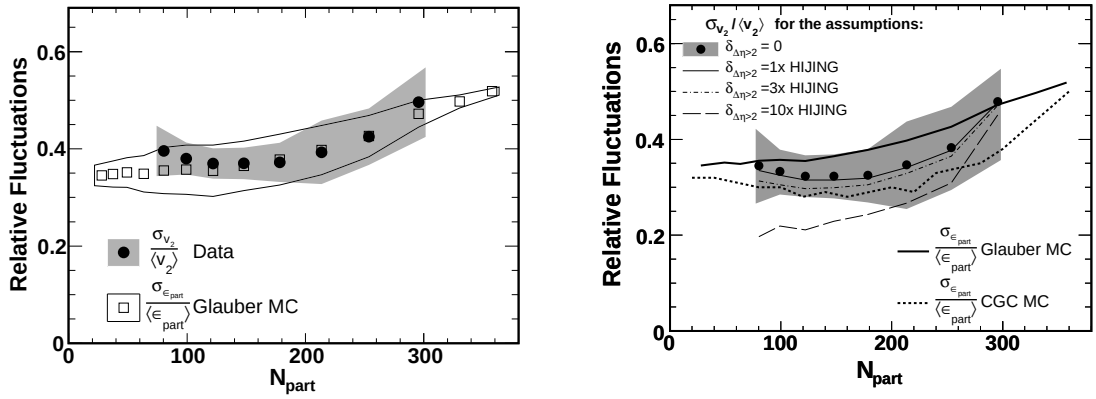

Fig. 7.1: Elliptic flow fluctuations, $\sigma_{v_2}/\langle v_2\rangle$, as a function of the number of nucleons participating in $Au + Au$ collisions at $\sqrt{s_{NN}} = 200$ GeV, without subtraction of non-flow contributions (left) and the same $\sigma_{v_2}/\langle v_2\rangle$ fluctuations with several types of corrections for contributions from non-flow effects (right), for details of correction procedures see Ref. [38]; for comparison eccentricity fluctuations, $\sigma_{\epsilon_{part}}/\epsilon_{part}$, from Glauber MC calculations [32] and from Color Glass Condensate model [231] are shown.

with fixed number of participating nucleons, N_{part}, in which the area and shape of the common part of circles are similar, fluctuations of eccentricity connected to varying positions of participant nucleons are large, $\sigma(\epsilon_{part})/\langle\epsilon_{part}\rangle \approx 40\%$. Slightly smaller eccentricity fluctuations, $\sigma(\epsilon_{part})/\langle\epsilon_{part}\rangle \approx 30\%$, are obtained in calculations from the Color Glass Condensate (CGC) approach [231].

The experimental determination of elliptic flow fluctuations is difficult due to relatively large systematic errors [39]. Although some of the uncertainties cancel in the ratio, $\sigma_{v_2}/\langle v_2\rangle$, the contributions from non-flow sources need to be subtracted to obtain corrected values corresponding to initial fluctuations. In Fig. 7.1 (left) the uncorrected relative fluctuations are shown, which are only slightly larger than the fluctuations of eccentricity from Glauber MC calculations [32]. The estimation of the correction for non-flow contributions need additional assumptions. It is well known that the dominant correlations are short-range and thus correlations for $|\Delta\eta| > 2$ are small. One can also use the information provided by Monte Carlo event generators, like HIJING, which give the non-flow ratio $\langle\delta\rangle/\langle v_2\rangle$. In Fig. 7.1 (right) the elliptic flow fluctuations corrected for non-flow effects are shown [38] and are similar to predictions for eccentricity fluctuations from the two models (Glauber and CGC). This supports a conclusions that the fluctuations of geometric origin are important for the observed elliptic flow.

7.2 Transverse momentum fluctuations

Event-by-event fluctuations of the transverse momentum may reflect fluctuations of temperature of the system created in heavy-ion collisions; their enhancement was considered as one of signals of a critical point. There are several observables that can be used in this type of studies. The most obvious is the mean transverse momentum, calculated for each event:

$$M_{p_T} = \frac{1}{N}\sum_{i=1}^{N} p_{T,i}, \tag{7.1}$$

where N is the number of accepted particles and $p_{T,i}$ is the transverse momentum of i-th particle. Fluctuations of this observable are quantified on the basis of comparison to M_{p_T} distribution with statistical fluctuations. The variance of M_{p_T} can be easily calculated from measured $\langle p_T \rangle$, σ_{p_T}, and $\langle N \rangle$ if p_T distribution is described by a Gamma function and the multiplicity distribution follows a Negative Binomial distribution [232]. Alternatively, it is obtained using Monte Carlo techniques for generation or mixing of events. The p_T fluctuations are analyzed using several different methods. The PHENIX Collaboration uses $\omega_{M_{p_T}}$ (defined by Eq. 2.10 in which N_{ch} is substituted by M_{p_T}) [233, 234], the STAR Collaboration calculates the difference of the variance of the distribution of quantity $\sqrt{n}(\langle p_T \rangle - \bar{p}_T)$ and a reference variance $\sigma^2_{\bar{p}_T}$ [235] ($\langle ... \rangle$ denotes averaging within one event and bar averaging over the whole sample of events) or analyzes p_T correlations and presents results as $(dN/d\eta)\langle \Delta p_{T,i} \Delta p_{T,j} \rangle$ [193]. The NA49 Collaboration uses the Φ_{p_T} function [236, 237] (defined in Eq. 2.11).

The fluctuations of transverse momentum were studied for $Au+Au$ collisions at RHIC [233, 234, 235, 193] and $Pb+Pb$, $Pb+Au$, $Si+Si$, $C+C$ and $p+p$ collisions at SPS [236, 237, 238]. In nucleus-nucleus collisions at RHIC, an enhancement of the M_{p_T} fluctuations over the statistical fluctuations was observed. This excess is largest for mid-central $Au + Au$ events, where the fluctuation measure ω_{p_T} reaches 3.5% [233, 234]. At SPS energies the enhancement is smaller and maximal fluctuations are observed at peripheral collisions [236], while results for the most central $Pb + Pb$ collisions are consistent with purely statistical fluctuations [237].

The increase of transverse momentum fluctuations with energy is usually attributed to mini-jets. The STAR Collaboration has shown that two-particle correlations can be described as contributions from flow and a jet-like structure [196, 190]. Also the PHENIX Collaboration argued that the experimental dependencies of fluctuations on collision centrality and p_T range can be reproduced when the contributions form hard-scattering processes and elliptic flow are added to random particle production [234].

Interesting is the elucidation provided in Ref. [141] that there is a direct connection of M_{p_T} fluctuations with multiplicity fluctuations if only the mean transverse momentum is correlated to the particle multiplicity in $A + A$ collisions. This explains similar centrality dependence of transverse momentum and multiplicity fluctuations. In the presence of such connection, fluctuation studies using different observables are investigating the same basic properties.

Although jets can be a source of enhanced fluctuations, also less energetic clusters may introduce correlations between particles affecting observed fluctuations. If all particles originate from clusters the variance of M_{p_T}, with statistical fluctuations subtracted, equals:

$$\sigma^2_{dyn} = \sigma^2_{M_{p_T}} - \sigma^2_{M_{p_T},mix} = \frac{\langle K(K-1) \rangle}{\langle K \rangle \langle N_{ch} \rangle} cov^*, \tag{7.2}$$

where K is the number of charged particles in the cluster and $2cov^*$ is the average covariance per a pair of particles from the cluster [239]. In the case of limited acceptance a the number of observed particles is proportionally lower:

$$\langle N_{obs} \rangle = a \langle N_{ch} \rangle, \tag{7.3}$$

but the number of pairs from the cluster decreases as a^2. This causes that dynamical fluctuations drop proportionally to the acceptance:

$$\sigma^2_{dyn} = a \frac{\langle K(K-1) \rangle cov^*}{\langle K \rangle \langle N_{obs} \rangle}, \tag{7.4}$$

In order to explain the values observed by the PHENIX Collaboration, clusters with 4-10 charged particles are necessary [239]. Large effective cluster sizes are consistent with results obtained by the PHOBOS Collaboration from the analysis of two-particle correlations described in Section 4.3.

7.3 Charge fluctuations

Fluctuations of charge distributions are considered to be a potential signal of Quark-Gluon Plasma as the charges of basic components, quarks and hadrons in the QGP and in the hadron gas, respectively, are different. Study of the charge Q of all particles registered in a limited kinematical region provides information on properties of this system and its evolution. The most straightforward physical interpretation has the observable:

$$D = 4\frac{\langle (Q - \langle Q \rangle)^2 \rangle}{\langle N_{ch} \rangle}, \tag{7.5}$$

which is a measure of the charge fluctuations per unit entropy. Early predictions suggested $D_{HG} = 4$ for a hadron gas and $D_{QGP} \approx 0.75$ for a Quark-Gluon Plasma with massless quarks. However, estimates for QGP obtained from lattice calculations are larger, $D_{QGP,lattice} \approx 1 - 1.5$, while the value for hadron gas decreases to $D_{HG,resonance} \approx 3$ if resonances are taken into account [240, 241]. Observation of $D < 2$ would provide a strong evidence for existence of QGP, however larger D values do not rule it out, as there is a number of effects at the hadronization stage that modify this observable [242].

In order to remove volume fluctuations that are related to varying centrality of heavy-ion collisions, it is better to use ratios: $F = (N_+ - N_-)/(N_+ + N_-)$ or $R = N_+/N_-$, or functions of them [240]. In experimental studies several other fluctuation measures are used. The PHENIX Collaboration calculates the values of the observable $\omega_Q = (\langle Q^2 \rangle - \langle Q \rangle^2)/\langle N_{ch} \rangle$ (called originally ν_q [243]) which is directly connected with D, as $D = 4\omega_Q$. The NA49 Collaboration uses the Φ_q function defined in Eq. 2.11 [244] where the observable considered is the electric charge of particles, q. The STAR Collaboration uses the observable proposed in Ref. [136]:

$$\nu_{+-} = \left\langle \left(\frac{N_+}{\langle N_+ \rangle} - \frac{N_-}{\langle N_- \rangle} \right)^2 \right\rangle, \tag{7.6}$$

where N_+ and N_- denote the number of particles with positive and negative charge, respectively. For purely statistical fluctuations the values of ν_{+-} are non-zero:

$$\nu_{+-,stat} = \frac{1}{\langle N_+ \rangle} + \frac{1}{\langle N_- \rangle}, \tag{7.7}$$

thus the dynamical fluctuations measured as

$$\nu_{+-,dyn} = \nu_{+-} - \nu_{+-,stat} \tag{7.8}$$

are used in the studies [245, 246]. All presented fluctuation measures can be related using simple formulas in the case when $\langle N_+ \rangle$ and $\langle N_- \rangle$ are large and similar.

Experimental results on net-charge fluctuations were obtained for $Pb + Pb$ collisions at $\sqrt{s_{NN}} = 6 - 17$ GeV by the NA49 Collaboration [244], for $Au + Au$ collisions at $\sqrt{s_{NN}} = 130$ GeV by the PHENIX Collaboration [243] and the STAR Collaboration [245] and more recently

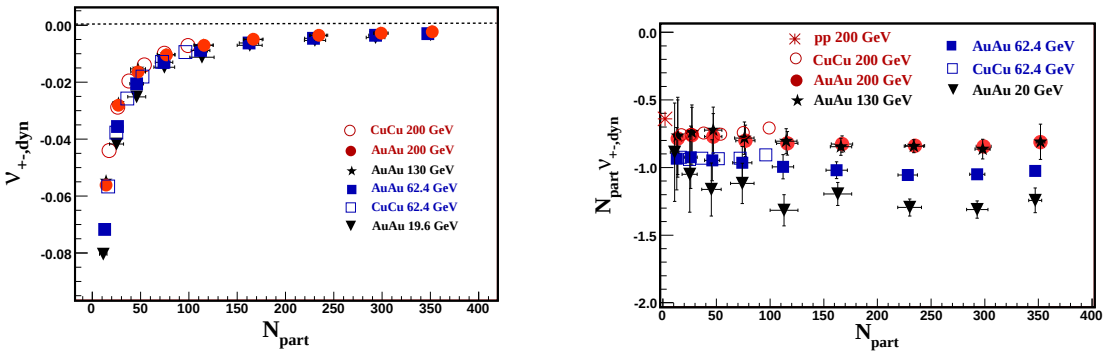

Fig. 7.2: Net-charge fluctuations for several types of collisions and different energies (described in the figures) as a function of centrality represented by the number of participant nucleons [246], for dynamical fluctuations $\nu_{+-,dyn}$ (left) or scaled by N_{part} dynamical fluctuations $N_{part}\nu_{+-,dyn}$ (right).

for $Au + Au$ at $\sqrt{s_{NN}} = 19.6 - 200$ GeV, $Cu + Cu$ at $\sqrt{s_{NN}} = 62 - 200$ GeV and $p + p$ at $\sqrt{s_{NN}} = 200$ GeV by the STAR Collaboration [246]. At the lowest energies values of Φ_q function are close to zero as expected for a gas of hadrons. Similarly, ω_Q obtained by the PHENIX Collaboration after corrections for limited acceptance reaches values much larger than expected for QGP, $\omega_Q = 0.78 - 0.86$. The STAR Collaboration measures net-charge fluctuations in the largest acceptance ($|\eta| < 1$, full azimuthal coverage) for largest range of energies and these results are discussed in more detail. The values of $\nu_{+-,dyn}$ were obtained as a function of energy, centrality and type of colliding systems, as shown in Fig. 7.2 (left). There is only a weak dependence on beam energy, the magnitude of fluctuations ($|\nu_{+-,dyn}|$) is the largest at the lowest energy ($Au + Au$ at $\sqrt{s_{NN}} = 19.6$ GeV). For different nuclei, colliding at the same energy, dynamical fluctuations are very similar. The most prominent is the dependence on collision centrality, represented by N_{part}. The values of $\nu_{+-,dyn}$, initially negative for peripheral collisions, increase and approach 0 for the most central collisions.

The dependence of dynamical fluctuations on energy for the most central collisions is most probably due to global charge conservation. It implies a minimal value of $\nu_{+-,dyn,CC}$, of the order of $-4/N_{ch,4\pi}$ where $N_{ch,4\pi}$ is the total charged particle multiplicity. After subtracting this contribution, the corrected fluctuations do not show any energy dependence for the most central $Au + Au$ collisions, but a dependence on the size of collision system remains [246].

The dependence of dynamical fluctuations on centrality can be understood as a dilution of two-particle correlations for increasing number of particle sources. If the collisions of nuclei were a superposition of independent nucleon-nucleon collisions, dynamical fluctuations would be inversely proportional to multiplicity or the number of participating nucleons. It is thus reasonable to multiply $\nu_{+-,dyn}$ by N_{part} as it was done in Fig. 7.2 (right). After this change the dependence on centrality disappears or becomes very weak, but the dependence on beam energy becomes evident. Alternative scaling methods, multiplying by the particle density, $dN/d\eta$, and especially by the number of binary collisions, do not lead to removal of centrality dependence [246].

Additional information on the size of net-charge fluctuations can be obtained from charge dependent two-particle correlations. In a study of such correlations as a function of the pseudorapidity difference $(\eta_1 - \eta_2)$ and azimuthal angle difference $(\phi_1 - \phi_2)$, an evolution from a 1D

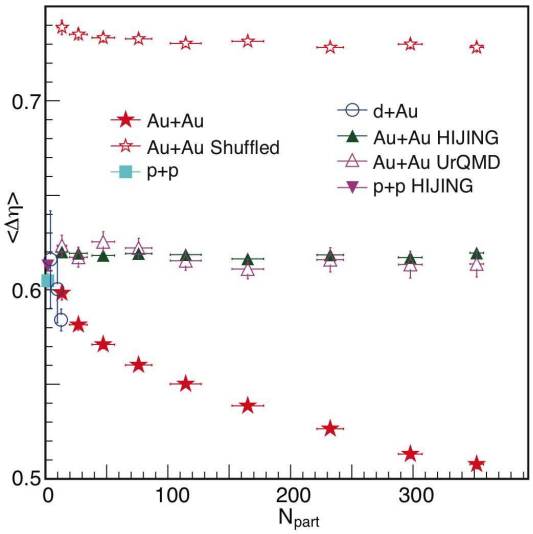

Fig. 7.3: Width of the balance function in pseudorapidity for all charged particles from $Au + Au$, $d + Au$ and $p + p$ collisions at $\sqrt{s_{NN}} = 200$ GeV together with predictions from HIJING and UrQMD models. As an upper limit results of calculations for shuffled $Au + Au$ events are also shown [250].

structure (in η) seen in $p+p$ to a 2D structure in central $Au+Au$ collisions was observed [247]. Large scale correlations are consistent with local charge conservation or canonical suppression of the net-charge, but do not agree with decays of hadronic resonances.

The disagreement of experimental results on net-charge fluctuations with the properties expected for the early stage of QGP does not prove that this phase of matter is not created in heavy-ion collisions. Larger fluctuations may be explained by coalescence scenario, in which gluons are attached to quarks (forming constituent quarks) and hadrons are produced from $q - \bar{q}$ pairs. This way contribution of gluons to entropy and production of hadrons is small. The number of hadrons is then $\langle N_h \rangle \approx \langle N_q \rangle/2$ and the number of charged particles $\langle N_{ch} \rangle \approx \langle N_q \rangle/3$. The denominator in Eq. 7.5 decreases which leads to $D \approx 10/3$ [248]. Net-charge fluctuations are also sensitive to fluctuations in the number of participant nucleons, details of the hadronization phase and resonance decays, and are rather insensitive to the initial QGP dynamics [249].

7.4 Balance functions

The evolution of the system created in the collisions can also be studied using the balance function defined as:

$$B(\Delta y) = \frac{1}{2}\left(\frac{\Delta_{+-} - \Delta_{++}}{N_+} - \frac{\Delta_{-+} - \Delta_{--}}{N_-}\right), \tag{7.9}$$

where Δ denotes the density of pairs of particles (with the signs defined by subscripts) in a given range of rapidity or pseudorapidity, for example for Δ_{+-} the pion pairs such that $|y(\pi^+) - y(\pi^-)| < \Delta y$ (or $|\eta(\pi^+) - \eta(\pi^-)| < \Delta\eta$). The width of the balance function measures the separation between the pairs: particle and antiparticle, created together, which arises from an expansion of the system and interactions with other particles.

The balance function for charged particles was studied in $Au+Au$ collisions at $\sqrt{s_{NN}} = 130$ GeV [251], and recently in $Au+Au$, $d+Au$ and $p+p$ collisions at $\sqrt{s_{NN}} = 200$ GeV. In this second analysis it was also calculated for pions and for kaons. The experimentally observed width of the balance function in pseudorapidity decreases with centrality of the collision, unlike results for events from HIJING and UrQMD models which predict a constant value (Fig. 7.3). This narrowing is consistent with trends predicted by models incorporating delayed hadronization, but is also expected in the presence of a radial flow. In the blast-wave model it corresponds

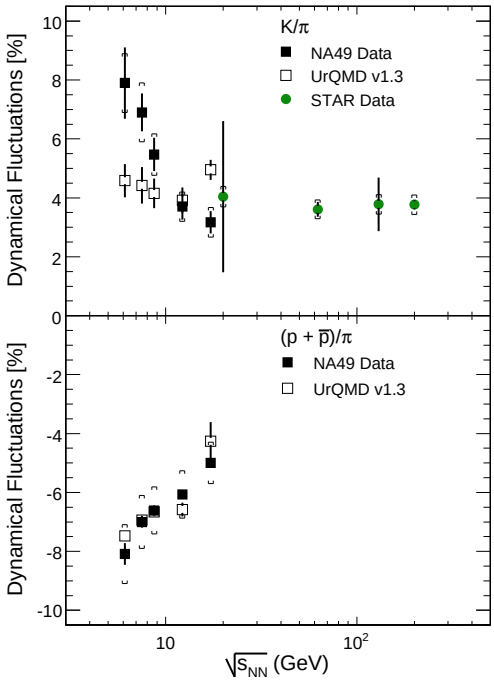

Fig. 7.4: Energy dependence of the event-by-event fluctuations σ_{dyn} of the ratios $(N_{K^+} + N_{K^-})/(N_{\pi^+} + N_{\pi^-})$ and $(N_p + N_{\bar{p}})/(N_{\pi^+} + N_{\pi^-})$ [252]. In addition to data points for the most central $Pb + Pb$ collisions from NA49 experiment (full squares) the predictions from UrQMD model (open squares) and the data points for central $Au + Au$ collisions from STAR experiment [253] (full circles) are shown.

to a correlation of the balancing charges at the moment of a breakup; either because of their late creation or, if they are created early, because they did not separate much due to a very limited diffusion. This last explanation is consistent with a very short mean free path in the medium. Width of the balance function in pseudorapidity for kaons shows no or little centrality dependence and this observation may be interpreted as an early creation of strangeness.

7.5 Fluctuations of particle ratios

The enhancement of strange particle production was one of the first proposed signals of QGP creation. Also the fluctuations of the strange/non-strange particles ratio are expected to increase in the vicinity of a phase transition or a critical point [254] and an analysis of strangeness production may unveil them [255]. These predictions triggered studies of K/π ratio on event-by-event basis.

Such ratios were analyzed for $Pb+Pb$ collisions at SPS in the energy range $\sqrt{s_{NN}} = 6.3-17.3$ GeV [256, 252]. In the first study the width of the distribution of the $(N_{K^+}+N_{K^-})/(N_{\pi^+}+N_{\pi^-})$ ratio was compared with results for mixed events. For the most central $Pb + Pb$ collisions at $\sqrt{s_{NN}} = 17.3$ GeV very similar values ($\sigma_{data} = 23.27\%$ and $\sigma_{mixed} = 23.1\%$) were found. In the study performed for the full range of energies available at SPS [252] also fluctuations of the $(N_p + N_{\bar{p}})/(N_{\pi^+} + N_{\pi^-})$ ratio were analyzed. The non-statistical fluctuations defined as :

$$\sigma_{dyn} = sign(\sigma^2_{data} - \sigma^2_{mixed})\sqrt{|\sigma^2_{data} - \sigma^2_{mixed}|} \tag{7.10}$$

shown in Fig. 7.4 are positive in the case of K/π ratio and negative for p/π ratio. In decays of baryonic resonances the p or $\bar{p}$ and π particles are frequently produced, thus the negative values of σ_{dyn} may be attributed to this type of correlations. This guess is additionally supported by an agreement of experimental results with UrQMD model predictions for p/π ratio fluctuations.

The dynamical fluctuations of K/π ratio decrease with increasing $\sqrt{s_{NN}}$ in the SPS energy range, but becomes constant for RHIC energies [253]. Interpretation of a large increase of K/π fluctuations at low energies is difficult, as the acceptance of NA49 detector covers different parts of $dN/d\eta$ distribution when the energy of collision changes, which may affect reconstructed dynamical fluctuations [257].

The STAR Collaboration used a measure of dynamical fluctuations proposed in Ref. [136]:

$$\nu_{dyn,K\pi} = \frac{\langle N_K(N_K-1)\rangle}{\langle N_K\rangle^2} + \frac{\langle N_\pi(N_\pi-1)\rangle}{\langle N_\pi\rangle^2} - \frac{2\langle N_K N_\pi\rangle}{\langle N_K\rangle\langle N_\pi\rangle}. \tag{7.11}$$

The analysis of $\nu_{dyn,K\pi}$ as a function of energy ($\sqrt{s_{NN}} = 19.6-200$ GeV) and collision centrality was performed [253]. The scaling with energy is observed not only for the most central events (as shown in Fig. 7.4) but also the centrality dependence (represented as a function of particle density $dN_{ch}/d\eta$) is very similar and can be fitted as

$$\nu_{dyn,K\pi}(dN_{ch}/d\eta) = c + d/(dN_{ch}/d\eta). \tag{7.12}$$

The scaled dynamical fluctuations, $(dN_{ch}/d\eta)\nu_{dyn,K\pi}$, increase with centrality in the experimental data, but remain constant for the HIJING model predictions. This behavior may be interpreted as an onset of radial flow or result of later state hadronic rescattering, which destroys correlations among particles from resonance decays [253].

Very interesting theoretically, but difficult to measure, are fluctuations of the ratio of neutral to charged particles. They are supposed to increase if domains of disoriented chiral condensate (DCC) appear during evolution of the system created in heavy-ion collisions [123, 128, 129]. A detailed study of multiplicity of charged particles and photons was performed by the WA98 Collaboration for $Pb+Pb$ collisions at SPS[258, 259]. The fluctuations of N_γ and N_{ch} were found to be similar to those for mixed events; only an upper limit for the size of DCC domains and the frequency of their occurrence was thus obtained. For the most central collisions, the DCC domains with the size in azimuthal angle larger than 30° may be present in less than 1% of events [259].

Section summary

In a search for signals of critical phenomena in heavy-ion collisions fluctuations of numerous observables were studied. The fluctuations of elliptic flow are similar to the fluctuations of participant eccentricity; a direct connection between them is thus likely. The fluctuations of the transverse momentum are increasing with energy of nucleus-nucleus collisions as expected from increasing contribution from mini-jets. After taking into account acceptance effects the extracted effective size of clusters is large, in the range 4-10. Charge fluctuations are consistent with those expected for a hadron gas, but there are many reasons why initially small fluctuations expected for QGP may increase in the later stages of the system evolution. The balance function width is consistent with either a late creation of particles or a very limited diffusion, indicating a short mean free path in the medium. The fluctuations of neutral-to-charged pions ratio are small and allow only to set an upper limit on a Disoriented Chiral Condensate production. The K/π ratio features an increase of fluctuations at low energies, which is difficult to explain and may be an onset of critical phenomena.

8 Summary

The Relativistic Heavy Collider is the first accelerator that delivers head-on collisions of two beams of high energy heavy ions. It provides $Au+Au$ interactions at the center-of-mass energy over 10 times larger than its predecessor in this research field - the Super Proton Synchrotron at CERN. In such collisions very large energy is released in a small volume thus the energy density exceeds 3 GeV/fm^3. The theory of strong interactions - Quantum Chromodynamics - predicts in this case a creation of a new phase of matter consisting of quarks and gluons. However, in place of the expected weakly interacting Quark-Gluon Plasma a dense and strongly interacting matter was found.

The most apparent signals of the strongly interacting Quark-Gluon Plasma are large elliptic flow and a suppression of energetic partons (jets) traversing the system created in the collision. Both these observations confirm a short mean free paths in the dense matter, the first of them indicates also that the matter behaves like a perfect liquid with very small viscosity. The elliptic flow is small in the most central collisions, in which the asymmetry of the overlap area of nuclei is small, but increases in peripheral collisions. Both the size of the elliptic flow and the fluctuations of it are connected with the eccentricity, ϵ_{part}, of the interaction area calculated using positions of participant nucleons. In the most central $Au + Au$ collisions at $\sqrt{s_{NN}} = 200$ GeV the trigger particle with very large transverse momentum does not have a partner at the opposite azimuthal angle; this means that one of back-to-back emitted partons, created in a hard scattering of quarks or gluons, is stopped in the medium. This effect is not observed in $d + Au$ collisions, which implies that it is not a result of the initial state of the Au nuclei. The same conclusion can be derived from the fact that the particle yields at high-p_T are much smaller than in peripheral collisions. However, the magnitude of this suppression smoothly increases with the collision energy and the size of the colliding system, without any indication of a sharp transition.

Enhanced production of strange particles and suppression of J/ψ particle are considered as signs of deconfinement. The yields of strange baryons relative to elementary interaction increase with centrality of collisions, especially for multiply-strange particles. However these results are difficult to interpret because nuclear effects and hadronization process may modify or mimic these signals.

There are also several observables that were considered as possible signs of QGP formation, but do not provide such evidence. It was predicted that a large size of particles source will be found using HBT method while in reality a small size is measured; this is explained by a collective transverse expansion. There are no indications of modified width of resonances (like ϕ) and the yields of particles with very low p_T do not show anomalous increase expected in the case of formation of QGP droplets.

Fluctuations of different observables were proposed as signals of a phase transition or a critical point. However, in most cases they are relatively small and do not indicate unusual phenomena or discontinuities. The search of very large total multiplicities or strong fluctuations of particle density, $dN/d\eta$, allowed us to establish only an upper limit for such effects. Non-statistical fluctuations of transverse momentum are observed, and they increase with the energy of collisions, but this trend is consistent with expectations for the enhanced production of mini-jets. Very promising signal of strong decrease of charge fluctuations in the system with quarks (charges $\pm 1/3$ and $\pm 2/3$) relative to a system with hadrons (charges ± 1) is not observed, the measured fluctuations are consistent with these expected for a hadron gas with resonance decays. There are no indications of creation of Disoriented Chiral Condensate domains, only an

upper limit for such phenomenon is calculated from the measured neutral to charged particles ratios. The only unexplained result is an increase of K/π ratio at low collision energies at SPS. These negative results do not however mean that they contradict creation of Quark-Gluon Plasma, but they indicate a relatively smooth phase transition and a strong modification of fluctuations in the hadronization phase.

Even if the fluctuation studies do not yield any direct evidence of critical phenomena they, together with analyzes of correlations, supply useful information on processes that occur in heavy-ion collisions at very high energies. They indicate importance of the hadronization step in which many observables are modified. Both from direct two particle correlation measurements, forward-backward correlation studies and analysis of transverse momentum fluctuations a consistent picture of production of particles in large clusters emerges. The clusters are composed of many charged particles (up to 6, as deduced from two-particle correlations) and have large width - exceeding the width that can be obtained in isotropic decays of clusters at rest. Larger clusters are observed in peripheral than in the most central nucleus-nucleus collisions and the properties of clusters seem to scale with the geometry of the system expressed as the fractional cross section. A different measurement of correlations of particles with a high-p_T trigger particle shows that the fragmentation of an energetic parton and the interaction of it with the medium influences the particle production at large distances - up to 4 units in pseudorapidity.

For the analysis of production of particles in clusters simple cluster models are used. They allow us to determine quantitatively the acceptance effects that modify the reconstructed parameters of clusters. Even if the correlations studies are done in a 6 units wide pseudorapidity range the acceptance corrections are in some cases very large. Effects of the total momentum conservation are also very important even for events with very large multiplicities - they significantly change the azimuthal correlations. Calculations of parameters of clusters created in decays of the lightest resonances show that they are different than these found in the nucleus-nucleus collisions - most striking is a large width of the clusters that exceeds expectations for resonance decays, even if the parent particle decays at rest. Simple Cluster Model enables the analysis of acceptance effects for clusters with any parameters, including mixtures of different clusters, and in the presence of additional effects, like fluctuations of the shape of pseudorapidity distribution.

The Wounded Nucleon Model provides a simple description of the particle production in nucleus-nucleus collisions as superposition of fragmentation of nucleons that took part in inelastic nucleon-nucleon interactions. The number of wounded nucleons is calculated from a Glauber model, thus the number of produced particles and fluctuations of them are directly connected with the geometry of the collision. From $dN/d\eta$ distributions measured in $d + Au$ collisions the fragmentation function of wounded nucleon was extracted. This fragmentation function, fluctuations of the number of wounded nucleons from the Glauber model, and multiplicity distributions in elementary $p+p$ collisions described by parameters of Negative Binomial distribution are used to calculate forward-backward correlations measured in the PHOBOS experiment. Wounded Nucleon Model correctly describes the centrality dependence of these correlations and agrees better with the data than other, more sophisticated models of heavy-ion collisions. Asymmetry of the fragmentation function of wounded nucleons together with fluctuations of the number of wounded nucleons may explain qualitatively also the centrality dependence of two-particle correlations, if it is assumed that wounded nucleons fragment into clusters.

The PHOBOS experiment proves that valuable results can be often obtained using a rela-

tively simple apparatus but well suited for specific tasks. The information from the PHOBOS Multiplicity detector with a single layer of silicon sensors allows us to reconstruct $dN_{ch}/d\eta$ distribution in exceptionally large angular range that results in observation of extended longitudinal scaling of particle density and elliptic flow. This detector enables the study of correlations at very large distances that reveal such of their properties, which otherwise are undetectable or can be easily overlooked. The reconstruction of the primary vertex in the PHOBOS experiment is a second example proving that limited capabilities of the detector can be sometimes overcome by more elaborate software fully utilizing the information contained in the data. The other software task, simulations of Monte Carlo events, is similar in the scope for all experiments.

After 10 years of RHIC operation extensive data on the properties of the matter created in heavy-ion collisions is collected, but all details of the phase transition are not understood yet. The statements written a few year ago by M. Gyulassy and L. McLerran [66] can still be repeated:

> *The experiments have demonstrated that a new form of matter, the sQGP, exists. The harder long term task of mapping out more of its novel properties can now confidently proceed at RHIC.*

However, in the advent of the first heavy-ion run at the Large Hadron Collider at CERN, it has to be added that studies of sQGP will continue at much higher collision energies. We can also expect that new results obtained at SPS energies may provide a novel insight in this research area.

Acknowledgments

I would like to thank all members of the PHOBOS Collaboration, who contributed to the success of our experiment. The hard work on the PHOBOS detector and later on the analysis of the data has brought many interesting results, only partly described in this report. It is impossible to recognize properly the contributions from all PHOBOS members in a few sentences, but I would like to mention at least those cooperating with me longest or working on similar tasks.

The first is Wit Busza who invited the group from Kraków to join a new experiment at RHIC. The group from the Institute of Nuclear Physics included Roman Holyński, Andrzej Olszewski, Marek Stodulski, Adam Trzupek and Barbara Wosiek, but many other persons from INP were also involved in the preparation of the experiment. Equally early started fruitful collaboration with Mark Baker, Günther Roland, Peter Steinberg, George Stephans, Robin Verdier, Bolek Wyslouch from the Massachusetts Institute of Technology. Many younger colleagues joined the Collaboration later; among them were Burak Alver, Zhengwei Chai, Alexander Mott, Wei Li, and Edward Wenger, who were involved in the correlation and fluctuation analyses.

I highly appreciate a friendly atmosphere and widespread willingness to help in the PHOBOS Collaboration. It was also a great pleasure to gain friends from many countries, including those as distant as Taiwan.

I warmly remember my work with Adam Bzdak on the interpretation of multiplicity fluctuations in the Wounded Nucleon Model.

I would like to thank my Wife and my Family for their support and patience, especially when I was working for the experiment abroad.

A The Relativistic Heavy Ion Collider

The Relativistic Heavy Ion Collider (RHIC) was designed to accelerate and collide two beams of heavy nuclei up to the energy of 100 GeV/nucleon each [260, 261]. The heaviest nucleus available from the ion source is gold (Au), but it is possible to accelerate lighter nuclei (so far Cu, deuterons and protons were delivered). Although the first $Au + Au$ collisions in the year 2000 were obtained for $\sqrt{s_{NN}}$=56 GeV, very soon the energy of collisions reached $\sqrt{s_{NN}}$=130 GeV. In the year 2001 $Au + Au$ collisions at the design energy were provided. In the year 2000 the luminosity was very low, allowing collisions at the rate of a few Hz, but constant improvements led to the maximal luminosity reaching $30 \times 10^{26}[cm^{-2}s^{-1}]$ for $Au+Au$ collisions (Run-7 in 2007) to $35 \times 10^{30}[cm^{-2}s^{-1}]$ for $p+p$ collisions (Run-6 in 2006). The planned upgrades of RHIC [262, 263] should fist lead to an increase of the average luminosity by a factor of 10. Then, after construction of a small electron accelerator providing electron beams with the energy 5-10 GeV, studies of $e + A$ collisions will be possible (eRHIC project).

The complex of accelerators at Brookhaven National Laboratory comprises several elements shown in Fig. A.1. The acceleration of ions, which then collide at RHIC, is performed in several steps [261]. The ions created in the Pulsed Sputter Ion Source have an additional electron and are thus negatively charged. They are accelerated in the Tandem Van de Graaff operating at 14 MV. A partial stripping of the electrons is achieved during a passage through a carbon layer and the ions become positively charged (Au^{+12}). After turning back to the Tandem they pass it in opposite direction and are accelerated to the energy of about 1 MeV/nucleon. These ions undergo a second stripping of electrons (to Au^{+32}) and then are transfered to the Booster, a circular accelerator, in which their energy increases to 100 MeV/nucleon. In the next step, the already almost fully ionized atoms (Au^{+77}) enter the Alternating Gradient Synchrotron (AGS) and are accelerated to about 8.6 GeV/nucleon. With this energy, after loosing last two electrons, they fill two rings of the Relativistic Heavy Ion Collider in which they reach the desired final energy of the collisions. Proton or deuteron beam is obtained in a simpler process: ionized positive ions are accelerated in the Proton Linac and after entering the Booster follow the same path as the heavier ions.

At RHIC there are four places, where the beams of ions were planned to collide, thus four experiments were accepted for construction and operation.

The STAR experiment (the Solenoidal Tracker At RHIC) [264] has the most universal detector, which is capable to measure precisely particles in the largest integrated acceptance. The Silicon Vertex Tracker, which is closest to the interaction point, covers $|\eta| < 1$. The large central Time Projection Chamber (TPC) measures particles emitted at $|\eta| < 1.8$ while the Forward TPCs (FTPC) extend the acceptance to smaller angles, $2.5 < |\eta| < 4$. All these detectors have full azimuthal symmetry. In addition a ring imaging Čerenkov and Time of Flight detector (TOF) extend particle identification capabilities. The electromagnetic calorimeter (EMC) enables detection of neutral particles.

The PHENIX experiment (the Pioneering High Energy Nuclear Interaction eXperiment) [265] has smaller acceptance of the subdetectors, but features more precise measurements at higher momenta. The silicon Multiplicity-Vertex Detector covering $|\eta| < 2.6$ and $\Delta\phi = 2\pi$ is used to determine primary vertex position and measure $dN/d\eta$ distribution of charged particles. In the central spectrometer arms ($|\eta| < 0.35$, $\Delta\phi = \pi/2 \times 2$) particles are measured in Pad Chambers, Drift Chambers and Time Expansion Chamber. Their identification is ex-

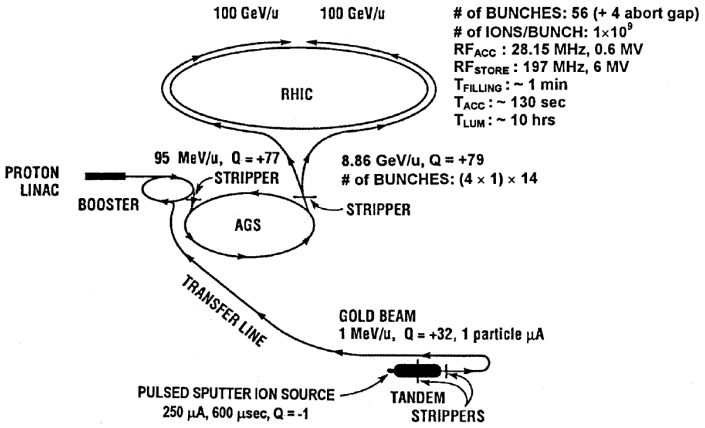

Fig. A.1: The schematic drawing of the Relativistic Heavy Ion Collider complex at BNL.

tended to higher momenta using the information obtained from the Time of Flight and the Ring-Imaging Čerenkov. The pions and kaons are separated up to 2.5 GeV/c and protons are identified up to 5 GeV/c. Neutral particles are measured in the Electromagnetic Calorimeter. The two forward muon spectrometers were designed to measure precisely the J/ψ particles.

The BRAHMS detector [266] was designed to enable reconstruction and identification of charged particles in the widest range of rapidity ($0 < y < 4$). This was achieved using two movable spectrometers covering different intervals of emission angles. The forward spectrometer measures particles with the angles $2.3° - 30°$ allowing separation of $\pi/K/p$ up to ~ 25 GeV/c. The midrapidity spectrometer covers the angles $30° - 95°$ and enables π/K separation to momenta of 2 GeV/c and K/p separation to momenta of 3.5 GeV/c. The central multiplicity detector covers $|\eta| < 2.2$ range, a few other subdetectors are used for triggering and measuring global characteristics of events.

The PHOBOS experiment has again a more universal detector [148], measuring emission angles of charged particles in almost the full solid angle; the acceptance range ($|\eta| < 5.4$) is the largest among RHIC experiments. For most of registered charged particles only their pseudorapidity is known, but for a small fraction (about 1%) of charged particles, emitted at midrapidity ($0 < \eta < 2$), their momenta are measured and they are identified. The PHOBOS experiment is capable to identify particles with lowest transverse momenta (starting from 30 MeV/c for pions). Details of the construction and properties of the detector are given in Section 3.1.

B Determination of the centrality in $A + A$ collisions

In contrast to collisions of elementary particles ($e^+ + e^-$, but also $p + p$) the collisions of nuclei can not be described without taking into account the fact that they are composed of nucleons: protons and neutrons. Nuclei have larger size than protons and nucleons from it in the inelastic collisions at high energies do not interact coherently. In the case of elementary particles (especially electrons), we may treat the collision as occurring in one point, but for nuclei the situations in more complicated. Geometrically, the most important parameter is the distance between nuclei centers, called the impact parameter, b, measured in the plane perpendicular to the direction of the motion of nuclei. It determines the size and shape of the area of an overlap of nuclei, when they are viewed along their direction of flight. Nucleons that happen to be in this overlap area have a chance to interact with the partners from the opposite nuclei. Obviously, collisions involving much different numbers of nucleons have distinctly different properties.

The direct connection between the geometry of the collision and the properties of the registered events manifests clearly in the varying properties of the registered particles. Only the nucleons that did not interact (called *spectators*) follow almost the same direction as the nucleus to which they belonged. They are often contained in larger objects - multi-charged fragments, but with the mass smaller than that of their former nuclei. Spectator nucleons, especially at the highest RHIC energies, are present only at very small emission angles and thus a large $|\eta|$. The *participant nucleons* from the overlap area involved in the interactions (called shortly participants or wounded nucleons) usually can not be recognized, as they either loose their identity and disappear or have momenta similar to the momenta of produced particles. Both participant nucleons and produced particles have larger emission angles, most of them are contained in the range $|\eta| \leqslant y_{beam}$. Generally the number of produced particles is monotonically dependent on the number of participant nucleons.

Centrality of the collision can be thus characterized using one of the following parameters:

- b - impact parameter, the distance between the nuclei centers at their closest approach, changing from 0 for the most central collisions to $R_1 + R_2$, the sum of the radii of the nuclei, for the most peripheral collisions;
- N_{part} - number of participant nucleons, starting from the sum of the mass numbers of nuclei, $A_1 + A_2$, for the most central collisions and decreasing to 0 for the most peripheral collisions,
- N_{spect} - number of spectator nucleons, ranging from 0 for the most central collisions to the sum of the mass numbers of nuclei, $A_1 + A_2$, for the most peripheral collisions;
- N_{coll} - number of nucleon-nucleon collisions, even two times smaller than N_{part} for the most peripheral collisions, but a few times larger for the most central collisions.

The definitions of these parameters of the collision are best explained by the schematic illustration of the collision shown in Fig. B.1.

The impact parameter b and the number of participant nucleons N_{part} are not detectable experimentally. There is no chance to directly measure the impact parameter as this requires determination of relative positions of nuclei with unattainable accuracy. It is also practically impossible to recognize and count the participant nucleons which either loose their identity or are hidden among produced particles. We can thus estimate the centrality of the collision either using the number of spectator nucleons (if they are measured) or from the multiplicity of the event.

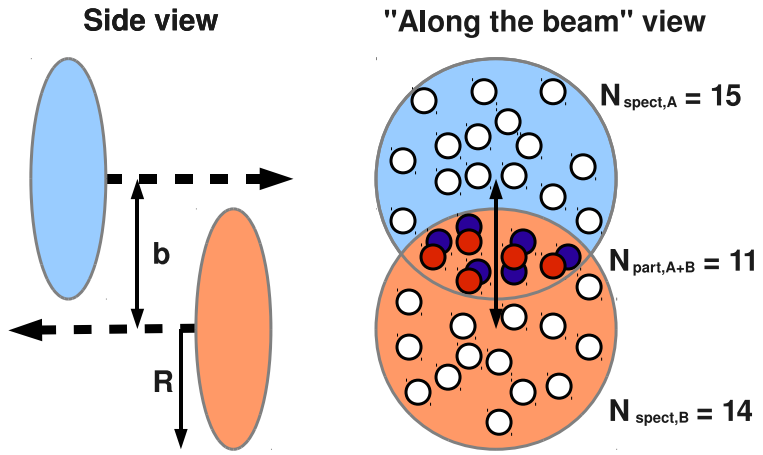

Fig. B.1: Schematic illustration of the $A + A$ collision with definitions of several parameters. The collision is presented in a side view (left) and "along the beam view" - as it can be seen looking in the direction of the flight of nuclei (right). The impact parameter, b, and nucleus radius, R, are shown by thin arrows, the direction of flight of nuclei is depicted by dashed arrows. On the right side the nucleons are also shown: spectators (white) and participants (red or blue). In this example $N_{spect} = 29$, $N_{part} = 11$ and $N_{coll} = 6$ (one of the red nucleons from the nucleus B interacts with two blue nucleons from the nucleus A).

The connection between geometry of the collisions and the number of participant and spectator nucleons is usually provided by the Glauber model. In this approach positions of the nucleons in each nuclei are randomly generated according to a density function. The nuclei are then positioned at the required distance (impact parameter) and the distances between nucleons from different nuclei in the plane perpendicular to the directions of flight of the nuclei are examined. The pairs of nucleons from different nuclei that pass close enough to each other have a chance to interact (with appropriate probability). Simulations based on Glauber model can thus be used to determine correlations between the impact parameter, b, the number of participant nucleons, N_{part}, the number of spectators, N_{spect}, and the number of binary collisions, N_{coll}.

B.1 Estimation of the number of spectator nucleons

The experimental determination of the geometry of the collision or the collision centrality (these two terms can be treated as synonyms) is not always straightforward. Obviously, if we know N_{part} or N_{spect} we can estimate the impact parameter using the dependencies derived from the Glauber model. Potentially the easiest to determine is the number of spectator nucleons. At sufficiently high energies spectators have smaller emission angles than produced particles, and can be thus directly recognized. However, in order to obtain N_{spect} we have to measure both spectator protons and neutrons, emitted as separate particles or as the components of larger fragments, what is possible only with the help of calorimeters. In the case of collider experiments an additional problem is due to the fact that fragments follow very close the direction of the beams, an can not be thus detected. Only the neutral particles escaping the beam pipe are easy to measure in Zero Degree Calorimeters, ZDC. As free neutrons are the only spectators

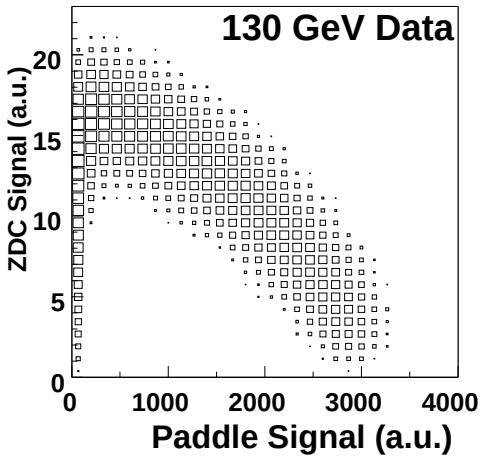

Fig. B.2: The signal in Zero Degree Calorimeters as a function of the signal registered in the Paddle trigger detector (in both cases arbitrary units) for $Au + Au$ collisions at $\sqrt{s_{NN}} = 130$ GeV.

registered in this detector, a low signal may mean either a very central collision with low value of N_{spect}, or opposite, a peripheral collision with very few free spectator neutrons - because most of the spectator nucleons are contained in heavier, undetected multi-charged fragments. This ambiguity can be resolved only using additional information related to the multiplicity of particles produced in the collision. Example of such correlation is shown in Fig. B.2 where ZDC signal as a function of the signal in the Paddle trigger counters, proportional to the multiplicity of particles in the range $3.2 < |\eta| < 4.5$, is shown. The signal registered in ZDC grows rapidly from 0 observed in the most peripheral events with very low multiplicity, reaches a maximum for semi-peripheral events and then slowly decreases to low values measured in the most central events characterized by very large multiplicities. As already mentioned such dependence is determined by the properties of breakup of the non-interacting part of the nuclei:

- in very peripheral collisions only a few nucleons, very distant from the center of nuclei, are interacting inelastically, thus the remaining part of nuclei tends to survive as a big fragment containing almost all spectator nucleons, few if any free neutrons are thus released,
- in slightly less peripheral collisions non-interacting part becomes excited and breaks into several smaller fragments, free spectator neutrons are thus more numerous,
- in more central collisions the nuclei breaks completely, the probability that spectators are not bound in any fragment increases; but as the total number of spectator nucleons decreases there are fewer and fewer candidates for free neutrons thus the signal in ZDC very fast reaches a maximum and then slowly decreases,
- for the most central collisions the number of spectator nucleons becomes so low that the signal in the ZDC may go down to 0.

Although the ambiguity introduced by similar ZDC signals for the most peripheral and the most central signals can be easily resolved, this measurement has a large uncertainty due to the fact that in heavy-ion collisions at RHIC usually only a relatively small fraction of spectator nucleons is registered in ZDC. The described below method based on the connection between the multiplicity of produced particles and N_{part} is thus more precise.

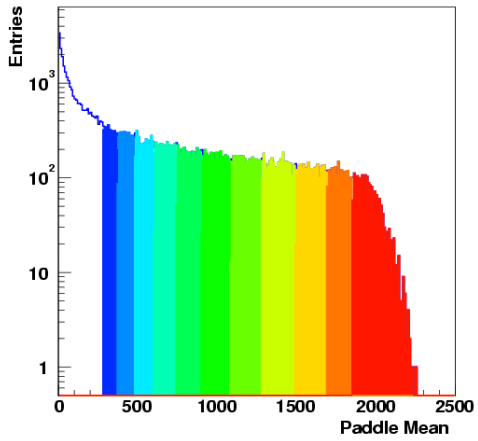

Fig. B.3: The distribution of the signal registered by the Paddle trigger counters for $Au+Au$ collisions at $\sqrt{s_{NN}} = 200$ GeV used in the definition of the centrality of collisions. Different colors filling the histogram denote different centrality classes (described in the text).

B.2 Centrality based on the number of registered particles

The number of produced particles as a function of N_{part} can not be determined from the Glauber model, in order to obtain predictions for this dependence complete models of heavy ion collisions have to be used (HIJING, AMPT, etc.). However, for selection of events with similar centralities knowledge of such a functional dependence is not mandatory. A monotonic relation between N_{part} and the observable/signal is sufficient to divide events into centrality classes. The events with largest signals have then also very large values of N_{part} and when the mean value of the signal decreases also N_{part} becomes smaller. Precision of such centrality selection depends on the strength of the correlation between the signal and N_{part}.

In the PHOBOS experiment the mean value of signals registered in the Paddle trigger counters is usually used for defining centrality. The signals from this detector are included in the trigger conditions, they can thus be easily used for online selection of central events. Furthermore, it was found that they are useful also in the off-line analysis. In Fig. B.3 the distribution of this signal ("Paddle Mean") is shown. In order to define the centrality classes we calculate the values of the signal which divide the sample of events into subsamples containing required fraction of events. The centrality is defined as the range of this fraction: starting from the most central events (with the largest values of the signal) and following classes are selected: 0-3%, 3-6%, 6-10%, 10-15%, 15-20%, etc. Such procedure requires prior estimation of trigger efficiency, to account for missing events, and can not be applied for the most peripheral events. In Fig. B.3 only for 50% of events the centrality class is assigned. It is possible to extend centrality determination to more peripheral events, but for $\sim 30\%$ of the most peripheral events it becomes much less reliable and large systematic errors are expected.

The observable used for centrality determination may be connected with the total charged particles multiplicity or with multiplicity of particles in some η range. The latter approach seems to be more appropriate, if we want to avoid effects from short range correlations. For example in a study of centrality dependence of particle density at $\eta \approx 0$ it is better to use particles from a distant η range. This is why in the PHOBOS experiment the signal measured in the Paddle trigger counters covering the range $3.2 < |\eta| < 4.5$, was the basis of the standard method of the centrality determination.

However, this η range is appropriate only for collisions at high energies, $\sqrt{s_{NN}} = 130$ GeV and $\sqrt{s_{NN}} = 200$ GeV. At lower energies, especially $\sqrt{s_{NN}} = 19.6$ GeV, there are few produced particles in this area and a range closer to $\eta \approx 0$ have be selected. The boundaries of the

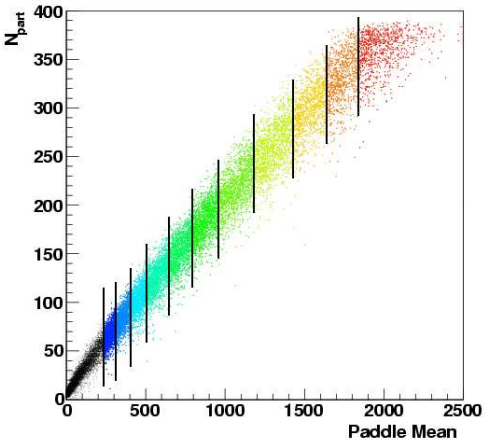

Fig. B.4: The dependence of the number of nucleons participating in the $Au + Au$ collision at $\sqrt{s_{NN}} = 200$ GeV, N_{part}, on the signal registered by the Paddle trigger counters, used for centrality determination. Different colors denote different centrality classes, the same as in Fig. B.3.

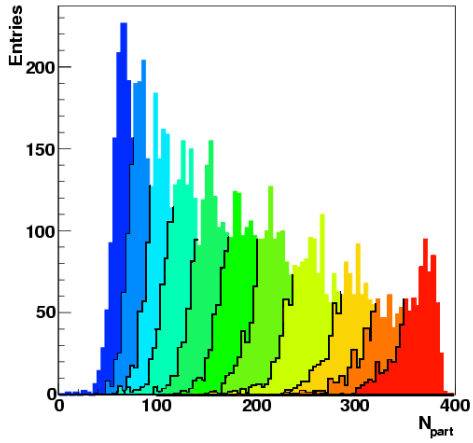

Fig. B.5: The distributions of the number of nucleons participating in the $Au + Au$ collision at $\sqrt{s_{NN}} = 200$ GeV, N_{part}, for different centrality classes (the same as in Fig. B.3) denoted by different colors.

interval corresponding to the acceptance of Paddle trigger counters can be scaled by the ratio of beam rapidities ($y^{beam}_{19.6}/y^{beam}_{200} = 0.563$) and thus a corresponding range is $1.8 < |\eta| < 2.5$. In this case the hits registered in the Octagonal Multiplicity detector are used as the signal for the centrality determination [14].

The relation between the observable that is used to define centrality classes and N_{part} (or other centrality parameter) is obtained using HIJING model and PHOBOS Monte Carlo simulations. These studies confirm the monotonic dependence between the "Paddle Mean" signal and N_{part} (Fig. B.4). They provide also the N_{part} distribution for the events in each centrality class shown in Fig. B.5, from which the mean value and the variance of N_{part} can be calculated. They depend not only on the type of colliding nuclei ($Au + Au$, $Cu + Cu$ or $d + Au$) but also slightly on the energy of the collisions. Interestingly, the difference between $\langle N_{part} \rangle$ estimated using the signal from Paddle trigger counters obtained from the simulations (including fluctuations in the particle production) and for the events divided into centrality classes according to N_{part} distribution differ less than 2% [5]. Such small difference is an outcome of strong correlations between N_{part} and the signal from Paddle trigger counters.

The systematic errors in this procedure are due mostly to the uncertainty of the estimation of the trigger efficiency. In $Au + Au$ collisions at $\sqrt{s_{NN}} = 130$ GeV this efficiency was 97% with a systematic error of 3%. Unfortunately, even this relatively small uncertainty causes that the systematic error of $\langle N_{part} \rangle$ is of the order of 5% for $N_{part} < 100$ [5].

B.3 Eccentricity

Another important parameter connected with the geometry of the collision is the eccentricity [267, 32], which quantitatively represents the shape of the interaction area. It is used in the context of the source of particles and describes the anisotropy of it. The basic formula defines it as:

$$\epsilon = \frac{R_y^2 - R_x^2}{R_y^2 + R_x^2}, \tag{B.1}$$

where R_x^2 and R_y^2 characterize the size of the source in x and y direction, respectively. For the almond shaped area of the overlap of two circles (Fig. B.1) the length of the x and y axis of an ellipsis approximating it should be used. In the case of nuclei collisions the *standard eccentricity*, ϵ_{std}, was commonly calculated using the values of $\langle x^2 \rangle$ and $\langle y^2 \rangle$ averaged over the positions of participant nucleons from many events. In each event x axis coincides with the direction of the impact parameter vector.

$$\epsilon_{std} = \frac{\langle y^2 \rangle - \langle x^2 \rangle}{\langle y^2 \rangle + \langle x^2 \rangle}. \tag{B.2}$$

A straightforward generalization of the standard eccentricity for a single event is the *reaction plane eccentricity* defined as:

$$\epsilon_{RP} = \frac{\sigma_y^2 - \sigma_x^2}{\sigma_y^2 + \sigma_x^2}, \tag{B.3}$$

where σ_x^2 and σ_y^2 are variances of the participant nucleon distribution, but calculated in a single event. PHOBOS Collaboration has proposed [267] a different method of eccentricity calculation, in which the axes are redefined in each event to be consistent with the positions of the participant nucleons (regardless of the reaction plane direction), maximizing ϵ value. This participant eccentricity can be calculated using the formula:

$$\epsilon_{part} = \frac{\sqrt{(\sigma_y^2 - \sigma_x^2)^2 + 4\sigma_{xy}^2}}{\sigma_y^2 + \sigma_x^2} \tag{B.4}$$

The value of participant eccentricity ϵ_{part} was found to better represent the source properties, especially when N_{part} is relatively small, than previously used ϵ_{std} or ϵ_{RP}. The proper method of estimation of eccentricity is important for interpretation of results obtained in the studies of elliptic flow (Section 2.4 and 7.1).

Section summary

In nucleus-nucleus collisions the area of the nuclei overlap and thus the number of nucleons participating in inelastic interactions depends on the distance between the centers of nuclei. Thanks to monotonic relation between the number of participants and the signal registered in the Paddle trigger counters or the number of hits in the Octagonal Multiplicity detector it is possible to define centrality classes into which similar events are assigned. This allows us to study the properties of events as a function of N_{part} or compare collisions of different systems ($Au + Au$ and $Cu + Cu$) with similar geometry.

Using simulations based on Glauber model, other parameters describing the geometry of the collision can also be determined. One of such parameters is the eccentricity of the area of the collision, and a proper measure of it is the participant eccentricity, ϵ_{part}.

C Vertex reconstruction algorithms

A reliable and correct reconstruction of the primary vertex is very important for any further reconstruction of primary tracks in the Spectrometer and even for obtaining $dN_{ch}/d\eta$ distribution from hits registered in the Multiplicity detector. In the PHOBOS experiment this task is challenging as there is no subdetector that would always give satisfactory results. The dedicated Vertex detector consists of the sensors providing precise information on hit positions only in y and z directions; there is thus no information on the position of the vertex in x. By design the Vertex detector can be used to find vertices from a limited range in z: between -24 cm and 24 cm from the nominal center of the PHOBOS detector. The Spectrometer, which enables the reconstruction of the vertex position in three dimensions, covers a small solid angle (accepts about 1% of charged particles); in events with small multiplicity usually there were not enough tracks registered in the Spectrometer to reconstruct the vertex position. In some runs collision vertices were spread in a very wide z range (sometimes even ± 1 m); if in an event the real vertex position was outside the acceptance of the Vertex detector and the Spectrometer a false vertex candidate inside their acceptance range was sometimes found. Such events can be recognized using the information from the Octagonal Multiplicity detector that allows estimation of the vertex position in z with an error of about 1 cm, but with a high efficiency and in a wide z range. If vertex positions obtained from different methods do not agree, results from the less effective and thus less reliable algorithms are neglected.

Several vertex reconstruction algorithms were developed both to determine the vertex position with the highest possible accuracy and to provide the cross checks necessary to reject false vertex candidates. They are presented and compared in Ref. [42], while a more detailed description of the reconstruction method using a single layer Octagonal Multiplicity detector is given in Ref. [268].

C.1 Reconstruction using the Vertex detector

The PHOBOS Vertex detector consists of two parts placed above and below the beam pipe, each with 2 layers of silicon sensors with strips 473 μm wide and 1.2 or 2.4 cm long. The sensors are placed at $y \approx \pm 5.7$ cm (inner layer) or $y \approx \pm 11.8$ cm (outer layer) and they cover the z range from -12 cm to 12 cm. Sensor from the inner layers have four rows of shorter strips. Two corresponding sensors of the outer layer with two times longer strip are placed above or below each inner layer sensor (Fig. C.1). The strips are perpendicular to the beam direction

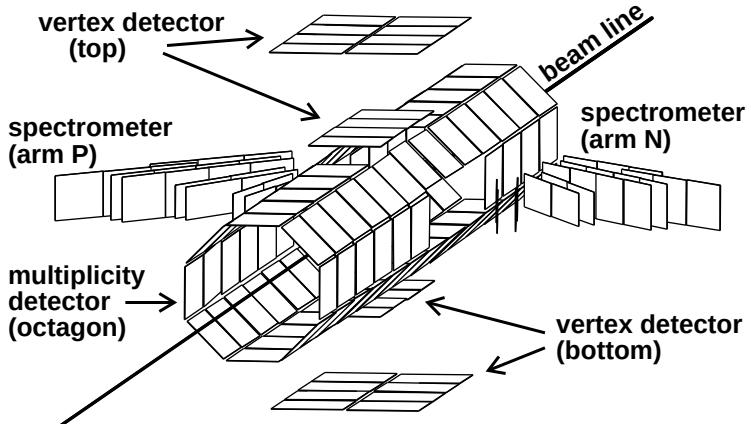

Fig. C.1: The central part of the PHOBOS detector with subsystems used in the reconstruction of the vertex position. Only the silicon sensors of the Octagonal Multiplicity detector, Vertex detector and eight first planes for two Spectrometer arms are shown.

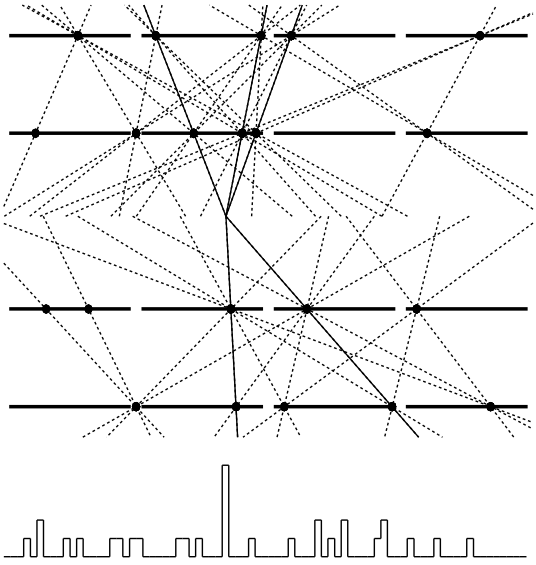

Fig. C.2: Reconstruction of the vertex position using all combination of hits registered in the Vertex detector. Dashed lines represent false combinations of hits, continuous lines correspond to primary particles. The histogram of the number of tracks extrapolated to a fixed y value as a function of z (at the bottom of the picture) is used to find the position of the vertex. In order to keep the figure more clear, all hits are assumed to be in the same row in x and the combinations pointing to very large $|z|$ are not drawn.

and provide information on position of the hit in y and z. Although the strips are divided in x, this segmentation is too coarse to give any chance to determine vertex position X_v with a precision comparable with the beam size.

In the vertex search all combinations of vertex hits are treated as track candidates and their extrapolated z positions at fixed y are entered to a histogram (Fig. C.2). The segmentation of sensors in x helps to reduce the number of false hit combinations: only those pointing to the beam line are considered (i.e. the hits from the same row in x). We expect a maximum of the histogram at the true position of the vertex Z_v. This procedure is repeated for several values of fixed y and several histograms are created. The histogram for which the maximum in z is the most distinctive is used to obtain the best estimate of Y_v and Z_v.

Obviously, this method may find a primary vertex, when some particles originating from it pass both the inner and the outer layer of the Vertex detector. The geometry of this subdetector limits the acceptance range to $|Z_v| < 24$ cm.

The number of random hit combinations is large, thus it is possible that lines defined by several hit pairs point to the same z value and the highest maximum does not coincide with the real vertex position. This happens mostly for events with very low multiplicities, but a false vertex is also found if the real vertex position is outside the Vertex detector acceptance. In such a case primary particles traverse only one silicon sensor; they enter it at small angles and usually leave hits in several consecutive strips. This information gives a chance to reconstruct the vertex position using single hits. The idea of this method of vertex reconstruction is presented in Fig. C.3. A signal in an isolated strip can be left only by a particle emerging from a collision that occurred within a range of z given by $\Delta z = 2rdz/dr$, where r is the transverse distance from the beam axis to the strip, dz is the length of the strip in z, and dr is the sensor thickness. For the multiple-strip hits, left by particles emitted at smaller angles, there are two ranges of possible vertex positions. The vertex position can be estimated from a single hit with an error $\sigma_{hit} = \Delta z/2\sqrt{6}$. In case of the Vertex detector this gives $\sigma_{hit} = 3.3$ cm and $\sigma_{hit} = 6.9$ cm, for hits in the inner and outer layer, respectively. With more hits from primary particles the error might decrease below 1 cm. However, for events with large $|Z_v|$, the acceptance of the Vertex detector treated as a single layer detector is small and large number of hits from primary particles is not possible. In addition hits that are left by other than primary

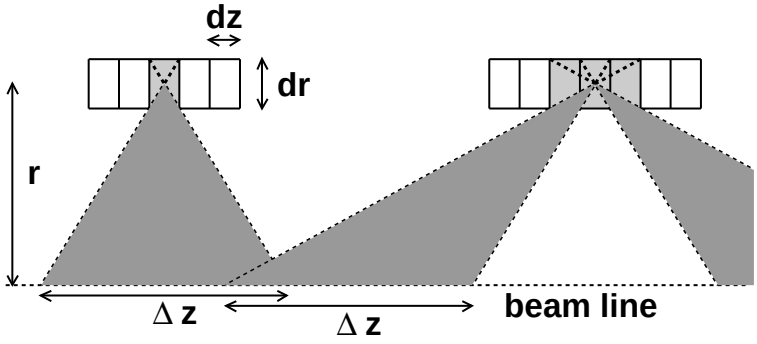

Fig. C.3: Examples of hits from primary particles leaving signals in one (left) or three (right) active elements of the silicon detector and the ranges of possible vertex positions, Δz, defined by simple geometrical calculations.

particles make such reconstruction less reliable, thus this method of the vertex reconstruction does not provide useful results in the PHOBOS experiment.

C.2 Reconstruction using the Spectrometer

The PHOBOS Spectrometer consists of two arms with 16 layers of silicon sensors placed inside the magnet normally producing a magnetic field of 2 Tesla. However, the first 8 layers of silicon sensors (shown in Fig. C.1) are in an area where the field is very weak and the charged particles follow trajectories that can be approximated by straight lines. It is sufficient to reconstruct two primary tracks and calculate their crossing point to obtain the vertex position in 3 dimensions (X_v, Y_v, Z_v). The accuracy of the vertex reconstructed in the Spectrometer is limited mostly by the size of the pads in the silicon sensors (1×1 mm^2 or 0.427×6 mm^2 in the first 6 layers). In reality the reconstruction is more difficult due to the presence of background tracks (mostly from secondary interactions). Two algorithms of vertex reconstruction using straight line track segments were thus developed.

In the *Spectrometer 3D* method, the vertex position is defined as the point for which the sum of distances from the extrapolated tracks is minimal. In an iterative procedure, tracks too distant from the calculated vertex (eg. secondary particles) are removed and the vertex position is recalculated.

The *Spectrometer 2D+1D* algorithm uses the points of closest approach of all track pairs; their coordinates are entered into a 2-dimensional $(x - z)$ and a 1-dimensional (y) histogram. The positions of the maxima in both histograms define the approximate vertex position. The final vertex position is defined by the mean values of x, y, and z, calculated using only the points that are compatible with the beam orbit and close enough to the approximate vertex.

For events with very low multiplicities (in $p+p$ collisions) sometimes there is only one track reconstructed in the Spectrometer. Together with the information about the beam orbit it can be used to estimate the vertex position even if all other methods fail. However, any independent confirmation of such vertex position is highly desired.

C.3 Reconstruction using the Octagonal Multiplicity detector

The largest fraction of primary particles (about 50%) is registered in the Octagonal Multiplicity detector consisting of 92 sensors with 0.27×0.86 cm^2 pads placed around the beam pipe and extending over 1 m. In this detector primary particles are traversing only one silicon sensor and we can not reconstruct their direction.

The first possibility for using this subdetector for vertex reconstruction offers the method

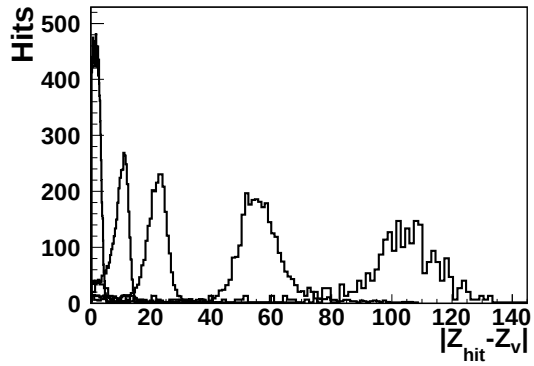

Fig. C.4: Distributions of the distances between the primary vertex and the hits for several different values of the normalized energy loss ΔE_{norm} (MC simulations). The histograms (from left to right) were obtained for ΔE_{norm} equal 1.2, 3, 6, 15 and 30.

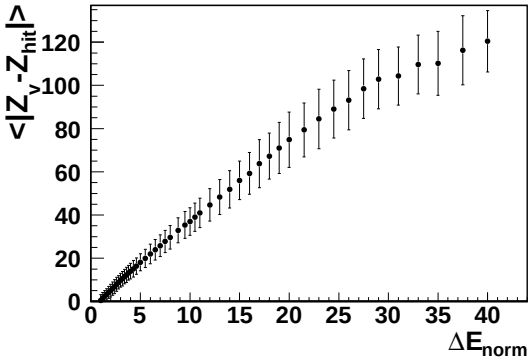

Fig. C.5: The mean distance of the hit from the vertex, $|Z_{hit} - Z_v|$, as a function of the normalized energy loss, ΔE_{norm} (MC simulations). The error bars represent the values of the width, $\sigma(|Z_{hit} - Z_v|)$, of the distributions of $|Z_{hit} - Z_v|$ distances obtained for fixed values of ΔE_{norm}.

based on geometrical properties of the hits, described above for the Vertex detector. The sensors of the Octagon are placed at r=4.5 cm from the beam line, but the pad size, dz=0.27 cm, is relatively large and thus the geometrical approach can not be precise, as σ_{hit}=15 cm. For events with large number of primary tracks this error is reduced even more than 10 times, however there are better methods of estimation of the path length in the silicon than such simple geometrical considerations.

The silicon sensors used in the PHOBOS detector not only register the passage of a charged particle, but also measure the deposited ionization energy, ΔE, which is proportional to the length of particle trajectory inside the silicon. In order to correct for varying thickness of the silicon sensors we are using the normalized energy loss ΔE_{norm}=$\Delta E/\Delta E_{MIP}$, where ΔE is the actual deposited energy and ΔE_{MIP} is the energy loss for a minimum ionizing particle at normal incidence. We can thus use ΔE_{norm} to estimate the distance of the hit from the vertex (Fig. C.4). Probability, $P(\Delta E_{norm}, |Z_{hit} - Z_v|)$, for a particle that loses the energy ΔE_{norm} to be emitted from the vertex at Z_v is obtained from the Monte Carlo simulations, with accurate calculations of ionization energy losses, but in which effects of electronics noise, energy sharing between pads, digitization and merging of signals from different particles are not included. This function is non-zero in two z ranges, symmetric with respect to Z_{hit}.

The density of primary particles is the largest near the vertex, they enter silicon at relatively large angles thus for majority of hits the uncertainty of vertex position estimation is 3-6 cm. However, useful information is provided also by hits at large distances, $|Z_{hit} - Z_v|$ up to 100 cm. Histograms similar to those shown in Fig. C.4 are used to determine the dependence of the distance $|Z_{hit} - Z_v|$ on the energy loss ΔE_{norm} shown in Fig. C.5.

The uncertainty of this energy loss based extrapolation from a single hit is always smaller than the one obtained from the simple geometrical arguments described earlier. The main problem in the estimation of the vertex position arises from hits left by background particles, multi-pad hits with a dead pad in the middle or incomplete hits at the edges of the sensors.

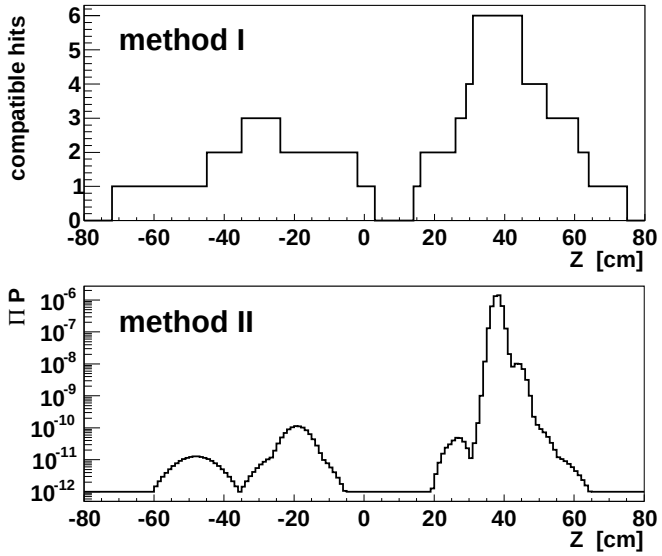

Fig. C.6: Examples of histograms used to determine the position of the vertex in two versions of the algorithm of vertex reconstruction from the hits in the Octagon. The event has the vertex at Z_v=40 cm and 6 primary tracks with hits in the Octagon. Secondary particles production and detector effects are not included in MC simulations.

They do not point to the true vertex, but to a completely different z value. Some of them may be rejected in the hit selection procedure, described in details in Ref. [268], which however effectively removes only the noise hits. In the presence of background hits good reconstruction results are obtained with maximum likelihood methods using a probability function of one variable, z. For each potential vertex position z it is possible to estimate the probability, that a hit at Z_{hit} was left by a primary charged particle emitted from z. These individual probabilities can be combined into a global function of z, the maximum of which gives the most probable position of the vertex.

In the *method I* the compatibility of the distance $|z - Z_{hit}|$ and the measured ΔE_{norm} is tested, and according to the result of this test the hit probability becomes 1 or 0. For each z considered the sum of probabilities for all hits is calculated, and the value of such sum corresponds to the number of charged primary particles that could have been emitted from this z position.

In the *method II* the single hit probability function, $P(\Delta E_{norm}, Z_{hit} - z)$, is obtained using properly normalized histograms similar to those shown in Fig. C.4. Then, at each tested hypothetical vertex position z, a product ΠP, of the values of this probability density function for all hits is calculated. As in such product values equal 0 must not appear, the probability function P has a predefined minimal value P_{min} even for such z positions, which are not compatible with the measured ΔE_{norm}. The implementation of this procedure, which includes special measures necessary to avoid numerical problems with multiplication of a large number of very small values (underflow) is described in detail in Ref. [268].

The global probability functions obtained in both methods for the same event are presented in Fig. C.6. Even for a few primary tracks traversing the Octagon, the maximum is distinctive and the vertex position is determined quite precisely.

At this point it has to be stressed, that any method using the hits in the Octagon may provide only an estimate of the vertex position in z. Other coordinates of the vertex, (X_v and Y_v), have to be set to zero or to the center of the beam orbit. Although by creating probability functions for different values of (X_v, Y_v) more distinctive maximum might be found, but only if the deviations from (0, 0) were of the order of a few cm, such approach could improve the X_v and Y_v estimates.

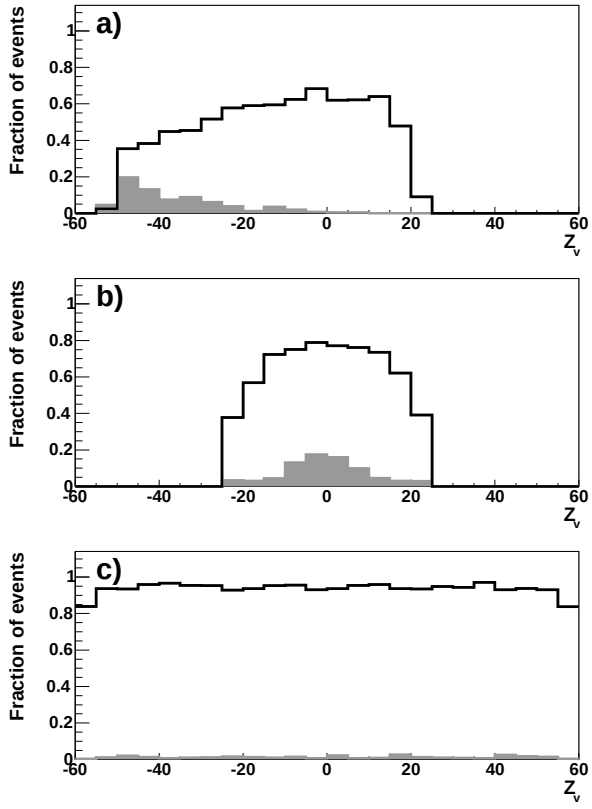

Fig. C.7: The efficiency of the vertex reconstruction for $Au+Au$ collisions at $\sqrt{s_{NN}} = 200$ GeV defined as fraction of events for which the distance between the reconstructed and true vertices does not exceed 0.5 cm, 0.1 cm and 3 cm for *Spectrometer 2D+1D* (a), *Vertex detector* (b), and *Octagon methods* (c). The additional events with incorrectly reconstructed vertex are represented by the shaded area. In MC simulations event vertices Z_v are distributed uniformly in the range -60 cm to 60 cm.

C.4 Accuracy and efficiency of vertex reconstruction algorithms

In the case of the PHOBOS experiment it is not possible to select a single vertex reconstruction algorithm, which would be the best one for all purposes. If the vertex position needs to be known in all tree dimensions with a high precision, obviously the methods using the information from the Spectrometer are best. However, the Spectrometer has small acceptance and to achieve good efficiency less precise methods have to be used as well.

In the study of the properties of vertex reconstruction methods their results obtained for Monte Carlo simulations of the PHOBOS detector response for $Au+Au$ collisions at the highest RHIC energy, $\sqrt{s_{NN}} = 200$ GeV, are compared. Later the collisions of lighter systems ($Cu+Cu$, $d+Au$ and $p+p$) are also taken into account.

The capability of vertex reconstruction depends strongly on the position of the real vertex and the multiplicity of the event. The efficiency of the reconstruction is shown in Fig. C.7 as the fraction of $Au+Au$ events for which the reconstructed vertex is close to the real one. The vertices are considered close, when their distance is smaller than $\sim 5\sigma_{v_z}$, where σ_{v_z} is the typical reconstruction error of the method considered. All methods reach their highest efficiency at $Z_v = 0$, about 60% for the *Spectrometer method*, 80% for the *Vertex detector method* and about 95% for the *Octagon method*. When the real event vertex is outside the acceptance range of a method it is quite probable that a false vertex is found inside the acceptance range. The fraction of such events is shown in Fig. C.7 as a shaded histogram showing the positions of the wrong Z_v estimates. This problem is less severe for the *Spectrometer method*, as in most cases the wrong reconstruction means only that the vertex position error is larger than 0.5 cm, but still not bigger than a few cm. The *Vertex detector method* quite often finds a vertex near $z = 0$ when the real position Z_v is far from zero, $|Z_v| > 25$ cm. To identify such events the *Octagon method* can be used, as it then gives completely different vertex position than the

Table C.1: The vertex position accuracy ([cm]) and efficiency for $Au + Au$ collisions at $\sqrt{s_{NN}} = 200$ GeV in the vertex range limited to $|Z_v| < 10$ cm. Two centrality ranges are defined using the number of charged primary particles hitting the Octagonal Multiplicity detector.

Method	15% most central events				30% most peripheral events			
	$\sigma(X_v)$	$\sigma(Y_v)$	$\sigma(Z_v)$	eff.	$\sigma(X_v)$	$\sigma(Y_v)$	$\sigma(Z_v)$	eff.
Spectrometer 3D	0.015	0.022	0.020	100%	0.350	0.100	0.300	4%
Spectrometer 2D+1D	0.025	0.022	0.030	100%	0.150	0.150	0.250	7%
Vertex det.	-	0.015	0.006	100%	-	0.030	0.023	28%
Octagon	-	-	0.500	100%	-	-	1.100	85%

Table C.2: The efficiency of the vertex reconstruction algorithms for different collision types. The vertex range was limited to $|Z_v| < 10$ cm. The mean number of charged primary particles with hits (in any subdetector) indicates the multiplicity of analyzed events.

Colliding System	$\sqrt{s_{NN}}$ [GeV]	$< N_{ch} >$	Efficiency		
			Spectrometer 2D+1D	*Vertex*	*Octagon*
Au+Au	200	947	64.2%	76.8%	94.4%
Au+Au	19	322	57.5%	72.7%	89.3%
Cu+Cu	200	296	49.0%	64.9%	88.9%
d+Au	200	66	12.4%	39.9%	86.4%
p+p	200	16	1.4%	6.4%	53.4%

Vertex detector method.

The accuracy of the methods is studied for events restricted to the range $|Z_v| < 10$ cm, in which all methods work most efficiently. Such comparison is presented in Table C.1, separately for central and peripheral $Au + Au$ collisions. In central events, with large multiplicities, all methods are 100% efficient and the vertex position errors are small. The most accurate estimate of the vertex position, but only Y_v and Z_v gives the *Vertex detector method*. The *Spectrometer methods* are less precise, especially in z direction, and *Spectrometer 3D method* has smaller errors $\sigma(X_v)$ and $\sigma(Z_v)$ than the *Spectrometer 2D+1D method*.

For peripheral events only the *Octagon method* has a large efficiency (85%), whereas both *Spectrometer methods* are inefficient (4-7%). The error of the vertex position increases for all methods, about a factor of 2 for the *Octagon method* and more than a factor of 10 for the *Spectrometer 3D* method. The *Vertex detector method* is able to reconstruct several times more events than the *Spectrometer methods* and still gives the most accurate vertex position. For events with small multiplicities the *Spectrometer 2D+1D method* is more efficient and accurate than the *Spectrometer 3D method*, which is more sensitive to incorrectly reconstructed tracks.

In order to confirm results from Monte Carlo simulations presented in Table C.1 using real data, the values of $\sigma(Z_{method} - Z_{vertex\_method})$ were calculated for *Spectrometer 3D*, *Spectrometer 2D+1D* and *Octagon methods* using events, in which all methods have found the vertex (about 50% of Au+Au events). The most accurate *Vertex detector method* can be used as a substitution of the real vertex position as it is much more accurate than any other method. In the case of both *Spectrometer methods* the errors agree very well, only the error for the *Octagon method* is different, about 20% smaller for the real data than for the Monte Carlo simulations.

Comparison of efficiencies of vertex reconstruction methods for different energies in Au+Au

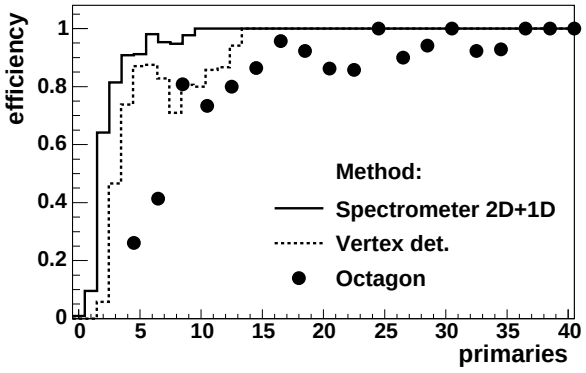

Fig. C.8: The vertex reconstruction efficiency as a function of the number of primary charged particles registered in the subdetector used by *Spectrometer 2D+1D*, *Vertex detector* and *Octagon methods*.

collision and for lighter colliding systems is shown in Table C.2. For collisions of heavier nuclei ($Au + Au$ or $Cu + Cu$) the efficiencies of the precise *Spectrometer* and *Vertex detector methods* are close to 50% or higher. If a deuteron is one of the projectiles, the efficiency drops much faster for the *Spectrometer method*, than for the *Vertex detector method*. For $p + p$ collisions only small fraction of vertices can be found correctly by precise methods. The *Octagon method* has always the highest efficiency of more than 86% for nucleus+nucleus collisions and more than 50% for $p + p$ interactions.

The efficiencies of the vertex reconstruction methods used in the PHOBOS experiment reflect the acceptance of subdetectors used by the reconstruction algorithms. To compare the "reconstruction power" of the methods using one, two or several layers of silicon we calculate their efficiencies as a function of the number of primary particles that were registered in the appropriate subdetector and point to the real vertex (Fig. C.8). The high quality of the information from reconstructed tracks causes that *Spectrometer 2D+1D method* can find the vertex in 50% of events, in which only two primary particles traverse the Spectrometer; when 5 such tracks are available, this method is almost 100% efficient. For the *Vertex detector method*, the minimal number of primary particles is 3 and 100% efficiency is reached for 15 such tracks. The *Octagon method* needs at least 5 primary particles and is more than 80% efficient if 10 primary particles are registered in the Octagon.

C.5 Vertex reconstruction in $p + p$ collisions

The vertex reconstruction in the PHOBOS experiment is efficient and precise only for events with large multiplicities. In $p + p$ interactions there are rarely enough tracks registered in the acceptance of the Spectrometer or the Vertex detector and the only method that may provide vertex information for large fraction of events is the *Octagon method*. It can be used to verify the vertex position obtained from other methods or can be applied if all other methods fail, giving the vertex position in z with an error $\sigma(Z_v) = 1.6$ cm. In the last case it is important to know that the reconstructed vertex was found in approximately correct position - not many cm away. In Fig. C.9 the efficiency of the vertex reconstruction is shown as a function of vertex position for two cases: when the vertex range was limited to either $|Z_v| < 120$ cm or $|Z_v| < 60$ cm. The fraction of correctly reconstructed vertices is approximately the same, however there is quite different number of events in which a vertex was found in a wrong position. For the wider vertex range we can see many such events near $z = 50$ cm. In this part of the Octagon detector more hits from secondary particles created in the massive PHOBOS magnet are registered, and they may mimic a vertex in this area. This problem may be to a large extent overcome when the vertex range is limited to $|Z_v| < 60$ cm, either by short beam bunches or by a trigger

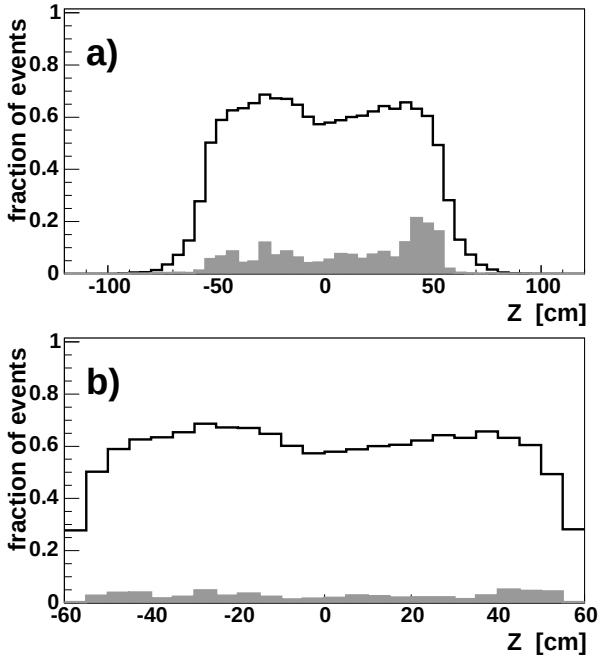

Fig. C.9: The efficiency of the *Octagon method* of vertex reconstruction (histograms) in $p + p$ collisions at $\sqrt{s_{NN}}$=200 GeV as a function of the vertex position, Z_v, for the true vertex position limited to ±120 cm (a) and ±60 cm (b). Accepted events have $|Z_{oct} - Z_v| < 5$ cm. The shaded areas show the distribution of Z_{oct} positions for remaining events, in which the vertex was reconstructed, but in a wrong position.

accepting only collisions close to $z = 0$. The fraction of incorrectly reconstructed vertices drops in this case below 3%.

Some improvement of the vertex position for $p + p$ interactions can be achieved when at least one particle is reconstructed in the Spectrometer. If it is compatible with the beam orbit it may determine the vertex position Z_v with an error smaller than 1 cm - accuracy not possible to achieve with the *Octagon method*.

Section summary

The PHOBOS experiment was designed as one of two "small" experiments at RHIC, thus the capabilities of the Vertex detector - a subdetector designed for vertex reconstruction - are very limited. In the Conceptual Design Report the reconstruction of the vertex position only along the beam was foreseen. During preparations of the off-line software the reconstruction using the information from the Vertex detector was extended to two dimensions (Z_v and Y_v) and two methods based on tracks from Spectrometer were added. Coordinates of the vertex in three dimensions are provided by vertex reconstruction methods using tracks from the Spectrometer, although they suffer from a very limited acceptance of this detector. Later, to enable the analysis of events with low multiplicities (peripheral, low energy $Au + Au$ collisions, $p + p$ interactions) the novel *Octagon method*, using information from a single layer silicon detector, was created. After extensive studies and software developments the vertex reconstruction methods reached high efficiency and accuracy considerably surpassing earlier expectations.

D Reconstruction of the number of charged particles

The PHOBOS Multiplicity detector registers charged particles, usually hitting only one silicon sensor, in almost the full solid angle. Several methods for the estimation of the multiplicity of charged particles and their emission angles are described in this Appendix. They are used either in the reconstruction of inclusive charged particle density or, on event-by-event basis, in correlation studies. In addition, for particles traversing the Spectrometer the momentum can be measured and identification is possible.

The PHOBOS Multiplicity detector deployed in such studies includes an octagonal tube covering pseudorapidity range $|\eta| < 3$, and six ring detectors extending the pseudorapidity measurement to $|\eta| < 5.4$. Acceptance of this detector is shown in Fig. D.1. The information from the Vertex detector and from first layers of the Spectrometer is also used in some analyzes. Details on the detector geometry and properties of the silicon sensors are given in Section 3.1.

Particles traverse the sensors of the Multiplicity detector at an angle that depends on their pseudorapidity. The length of the track in the silicon sensors of the Octagon, and thus the energy deposited, varies significantly with location. Particles may also traverse more than one pad, especially if they enter the sensor at a small angle. Usually at the beginning of the reconstruction procedure, hits in neighboring pads (in z direction) are merged. Next the total deposited energy is divided by $cosh(\eta)$ and by the thickness of the sensor, so that the mean value of the signal is normalized to the same energy for all primary particles ($\Delta E \approx 80$ keV). In order to reject noise signals and hits from background particles not originating from the primary vertex, only pads containing more than 75% of this energy are counted as occupied.

D.1 Hit counting method

In this method pads with signals are not merged; only those with low signals are rejected. The number of occupied pads in a pseudorapidity bin, $N_{pads}(\eta)$, has to be corrected for occupancy effects, as for example in the most central $Au + Au$ collisions, about 1.6 particles traverse each pad at midrapidity. Such correction is calculated assuming that probability of n particles traversing the same pad follows a Poisson distribution. The mean occupancy can be then obtained from the ratio of occupied and unoccupied pads in a given η bin. The contributions from not rejected secondary particles, are estimated from Monte Carlo simulations including all detector effects. A systematic error of about 10% includes uncertainties in the occupancy correction and the background estimation.

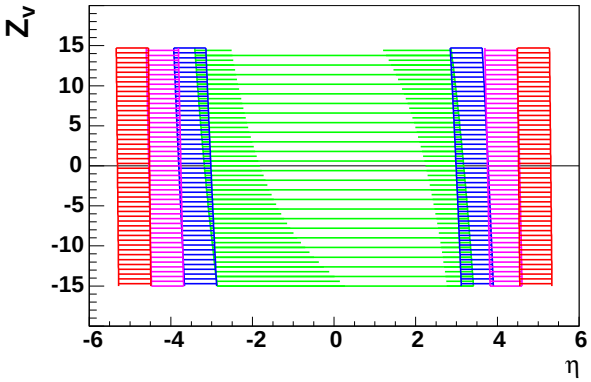

Fig. D.1: Acceptance of the PHOBOS Multiplicity detector in η for different Z_v vertex positions. The range $3 < |\eta| < 5.5$ is covered by the rings, the central part is measured by the octagon. The area with fewer horizontal lines corresponds to Spectrometer or Vertex detector windows, where the acceptance of the Multiplicity detector is limited to 50% or 75%.

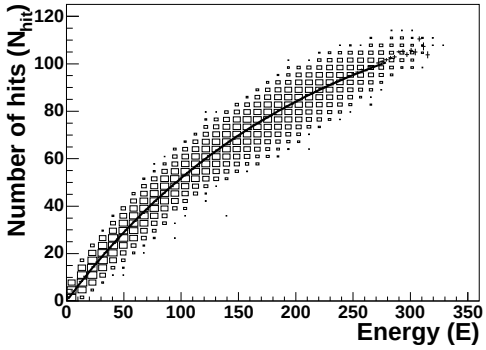

Fig. D.2: Fitting of the dependence of the number of registered hits on the ionization energy deposited by charged particles in the silicon sensors of the octagon using the formula $\langle N_{hit} \rangle = N_{max}(1 - e^{-E/E_{max}})$ (for the bin $-0.5 < \eta < 0$, Au+Au collisions at $\sqrt{s_{NN}} = 200$ GeV). The average energy per particle is given by E_{max}/N_{max}.

D.2 Energy loss method

In the pads traversed by two or more particles, the energy loss is integrated and the average signal is increased (doubled, tripled etc.). If the sum of energy losses in all pads in an η bin is calculated and divided by the mean energy loss for one particle an estimate of the number of particles is obtained. In the reconstruction of the $dN_{ch}/d\eta$ distribution the average energy loss per track, ΔE_{tr}, and the fraction of primary particles to all particles (primary+secondary) are determined as functions of η using GEANT simulations for HIJING events. Systematic errors for this method are of the order of 10%, similar to these for the *hit counting method*. Within the systematic errors the results of both reconstruction procedures agree, and the published $dN_{ch}/d\eta$ distributions are calculated as an error-weighted average of both methods [3].

D.3 Event-by-event multiplicity reconstruction

The energy loss registered in the silicon is correlated with the number of particles traversing a pad. However, the ionization energy losses follow a Landau distribution with a very long tail. In addition particles with low momenta deposit much more than the average energy; thus on the event-by-event basis a simple method of dividing the registered energy by the mean energy loss per particle is not precise enough. Especially in the case of very large signals in a single pad it may be equally probable that the hit was due to a single particle with a large ionization or that it is a sum of contributions from several particles. In the correlation studies, presented in Section 4, a more cautious approach is thus needed.

In the forward-backward correlations study [24], before a hit is accepted two thresholds are applied: a low energy loss cut intended to remove background hits and a high energy loss cut (η dependent) that removes particles with very small momenta. The average energy loss per particle was not taken from the Monte Carlo simulations, but obtained from the experimental data by fitting the dependence of the number of hits on the total energy loss in the η bin considered (see Fig. D.2).

In the two-particle correlation analysis [36], it was necessary to determine the number of particles contributing to each hit. In the case of events with small multiplicity, for example in peripheral $Cu + Cu$ collisions (in which the occupancy is below 4%), we assume that the experimental dE/dx distribution corresponds to the probability function $p_1(dE/dx)$ of registered energy loss dE/dx from a single particle. Starting from p_1, similar probabilities $p_i(dE/dx)$ for the cases of i particles hitting the pad were calculated. For more central events one obtains the experimental distribution $p(dE/dx)$ which is a sum of $p_i(dE/dx)$ probabilities with different weights w_i. The mean number of particles hitting a pad in which energy loss $dE/dx = e_{hit}$ was

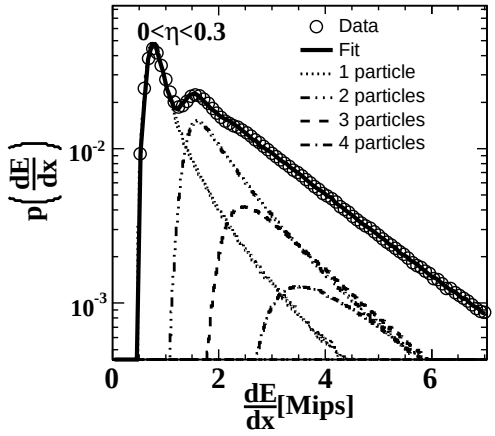

Fig. D.3: The ionization energy loss distribution, dE/dx, for the hits registered in the Octagon at $0 < \eta < 0.3$ (open circles) fitted by a sum of predicted dE/dx distributions for various numbers of particles traversing a single pad (dashed lines). The distribution was obtained for the most central $Au + Au$ collisions (3%).

registered is then calculated as:

$$N(e_{hit}) = \sum_i \; i \; w_i \; p_i(e_{hit}) \; / \; \sum_i w_i \; p_i(e_{hit}) \tag{D.1}$$

The above procedure is valid when the emission angles of primary particles are similar. Thus in the two-particle analysis described in Section 4.3, it was performed for many narrow bins with $|\Delta\eta| = 0.3$. An example of the dE/dx distribution with its contributions is shown in Fig. D.3.

D.4 Tracklet method

In addition to the charged particle measurement in a very wide η range using the Multiplicity detector, the PHOBOS detector is capable of providing similar information in a limited acceptance based on hits registered in the Spectrometer and in the Vertex detector. Although the acceptance of these detectors is broader than two η units, we reconstruct only $dN_{ch}/d\eta|_{|\eta|<1}$. In this reconstruction the *tracklets*, tracks of charged particles defined by the primary interaction point and two hits in consecutive layers of the detector, are used. For each hit the pseudorapidity, η, and azimuthal angle, ϕ, is calculated and a pair of hits from different layers is accepted if they are sufficiently close. In the case of the Spectrometer the total angular distance $D = \sqrt{\delta\eta^2 + \delta\phi^2}$ has to be smaller than 0.015, while for the Vertex detector $|\delta\eta| < 0.04$ and $|\delta\phi| < 0.3$ are required. These selection criteria are not identical because of different size of pads in the silicon sensors of these two detectors.

In the reconstruction procedure a fraction of primary particles is lost, but some background is added. The main sources of reconstruction inefficiencies are "dead" pads and small gaps between the sensors, through which some particles may traverse a layer without leaving a hit. The selection criteria are not very restrictive, thus *tracklets* not only from primary particles, but also from random combinations of hits or from particles from decays or secondary interactions, are accepted. The background fraction depends on occupancy in the detector and varies from 1% to 15% across the Spectrometer. In order to correct for these two effects and for the overall limited acceptance in azimuthal angle, results of *tracklets* reconstruction for GEANT simulations of HIJING events are used. They allow us to calculate the corrections as a function of vertex position, Z_v, and the centrality of the collision. The final estimate of $dN_{ch}/d\eta|_{|\eta|<1}$ is obtained by averaging over Z_v in each centrality bin. The systematic error of this estimate includes the uncertainty of reconstruction efficiency, combinatoric background subtraction and

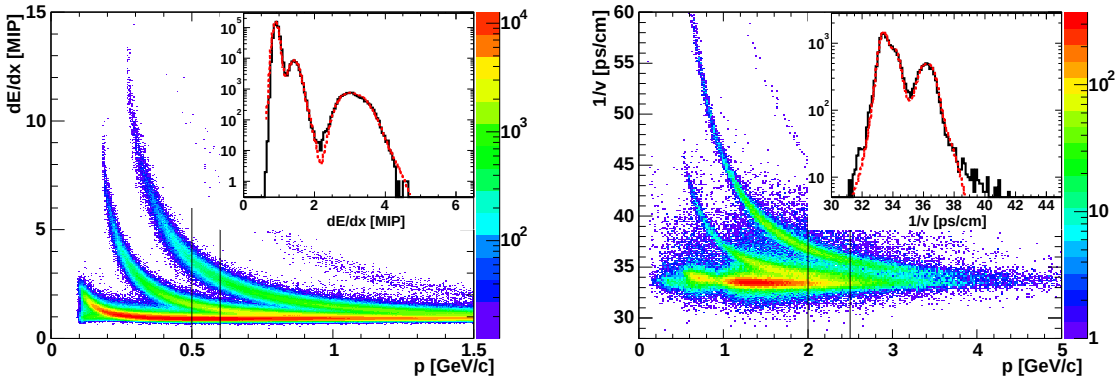

Fig. D.4: Identification of charged particles measured in the PHOBOS Spectrometer, using the ionization energy loss, dE/dx, registered in the silicon sensors (left) or according to the inverse velocity, $1/v$, obtained for particles reaching the Time of Flight detector. Dependences of dE/dx and $1/v$ as a function of total momentum for positively charged particles (π^+, K^+ and protons) are shown. The lines indicate the selected momentum slices to plot the insets.

contributions from decays. The total systematic error is 4.5% for the Spectrometer and 7.5% for the Vertex detector. More details can be found in Ref. [5].

D.5 Reconstruction of particles in the Spectrometer

The PHOBOS Spectrometer was designed to measure precisely a small fraction of charged particles emitted at mid-rapidity. The standard acceptance range $0 < \eta < 0.5$ can be extended by proper selection of the primary vertex range to $\eta \approx 2$. In the particle reconstruction procedure [2] first straight track segments in the first 6 layers and curved segments in other layers, placed in the high magnetic field, are separately found. Later the segments are matched and the momentum of the particle is fitted. Several cuts are applied in order to reject false track candidates and particles from secondary interactions. The particle identification uses ionization energy losses measured in silicon sensors or the velocity of particles obtained from the TOF detector (Fig. D.4). Detail information on identification capabilities are given in Section 3.1.

Particles reconstructed in the Spectrometer were used in the studies of particle spectra, particle ratios, correlations with a trigger particle, etc. In the analysis of charged particles density the *tracklet method* is more appropriate, because acceptance of the Spectrometer is larger in this case.

Section summary

In the PHOBOS detector primary charged particles are registered in almost the full solid angle using a single layer Multiplicity detector. Several methods of reconstruction were developed that enable us to reconstruct $dN_{ch}/d\eta$ distribution and study multiplicity correlations. Results from different reconstruction algorithms, including *tracklet method*, are consistent within their systematic errors. A small fraction of charged primary particles is fully reconstructed and identified using the information from the Spectrometer and TOF detectors. They are used in several studies performed by the PHOBOS Collaboration.

E Monte Carlo simulations for the PHOBOS Experiment

In high energy experiments measurements are performed using electronic devices and complicated systems, thus the collected information is far from that which can be compared with theoretical models. A reconstruction procedure with several steps is thus necessary before any useful data are obtained.

In the PHOBOS experiment this is done by a computer program called PhAT (PHOBOS Analysis Tool). The detector is not a perfect device and the reconstruction procedure is not 100% efficient, thus the necessary information may be either deformed or not registered at all. Registered ionization signal is always altered by electronic noise and digitization, particle trajectories are modified by multiple scattering. A particle may miss a sensor or traverse it through a defective pad without leaving a registered hit, random hits may be connected into a false "ghost" track or the identification procedure may give a wrong result. Some particles may be thus not detected or their properties are incorrectly reconstructed. In the analysis appropriate corrections for a limited detector acceptance and inefficiencies of reconstruction have to be applied. Such corrections are usually obtained from simulations of the response of the detector and results of reconstruction obtained for a known sample of events. Using the simulations it is possible also to estimate the background contribution and errors of reconstructed observables.

In addition to studying the performance of the detector and reconstruction procedures simulations are very useful to determine how the detector affects more complicated event properties. This is done using specially prepared or modified events, which have desired properties, and comparing their parameters with those obtained from reconstruction. In the PHOBOS experiment such studies were most extensively used in the analysis of elliptic flow.

The basic performance studies can be done using relatively few events, sometimes only a few thousands. There are however analyzes in which the number of Monte Carlo events should be, if possible, even larger than the number of real events. This is difficult to achieve because the real collisions of nuclei occurs with frequency of hundreds Hz, while using one computer it is possible to simulate only a few $Au + Au$ events per hour. Of course if a farm of a few hundreds computers is used, much larger number of simulated events can obtained, but still it is impossible to fulfil all requirements. In the years 2000-2005 PHOBOS experiment has registered about 1,300,000,000 triggers, while from the PHOBOS Monte Carlo simulations only about 245,000,000 events were obtained in a longer time, the years 2000-2008 (see Fig. E.1). Even if we take into account the fact that not all triggered events contain useful data, the experimental statistics is in many cases much bigger than that from the PHOBOS Monte Carlo.

The problem with small statistics from full GEANT based simulations may in some cases be overcome by much simpler special simulations (toy model simulations). They are however always prepared for a specific study, not registered in the PHOBOS database and are thus not counted together with the official PHOBOS Monte Carlo simulations.

E.1 General concepts of PHOBOS Monte Carlo

In the PHOBOS experiment the Monte Carlo simulations are performed in three basic steps:

- generation of events with required characteristics, usually from a generator of heavy ions

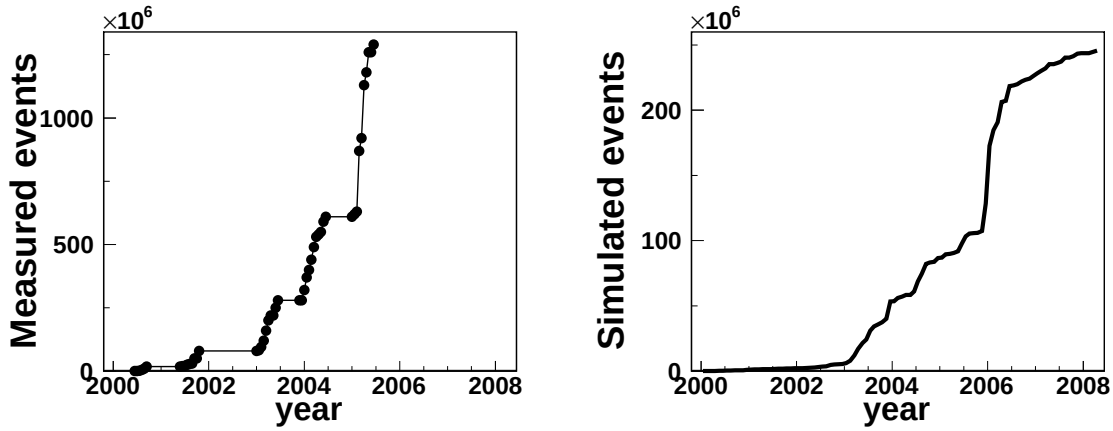

Fig. E.1: The number of real events registered by the PHOBOS experiment (left) and the number of simulated Monte Carlo events of all types (right). In both cases the integrated total number of events obtained up to the time shown on x axis is plotted. Note: the scales of y axis are different.

collisions;

- simulation of the detector response using detailed description of the detector geometry and materials, based on GEANT 3.11 package [269], which gives signals registered by the detector (hits) according to the acceptance, but without effects due to electronics;

- smearing procedure that transforms the hits to the signals in the format obtained from the measurements and introduces inaccuracies from electronics (noise, bad channels); it substitutes to the GEANT digitization step but includes also basic reconstruction.

Separation of the first task is most natural, as events generators are available as standalone programs. In addition, by saving the files with generated events, it is possible to reuse them for simulations with different conditions (vertex range, detector geometry, simulation options). Output from this step is stored in a file using a PHOBOS specific format (ADAT file).

The simulation step is the most complicated and CPU time consuming. An ADAT file and a few others files containing information on the PHOBOS detector are read and as the ouptut a PhoMCHits file is produced. Usually the generated events are used in the simulations only once, but they can be reused, for example in simulations with different vertex range.

Also the smearing step may be executed on the same events more then once as several types of smearing are possible. Standard smearing produces a PhoSmMCHits file, but in addition a more extensive reconstruction may be performed. Its results are stored in the format of ROOT trees in PhoMCAnt file.

After each step of PHOBOS Monte Carlo simulations information from it is registered in the simulations database. This enables us to see immediately the progress of production and later to search for simulations of required type.

A simplified diagram of the processing chain is shown in Fig. E.2 and below each step of PHOBOS Monte Carlo simulations is described in more detail.

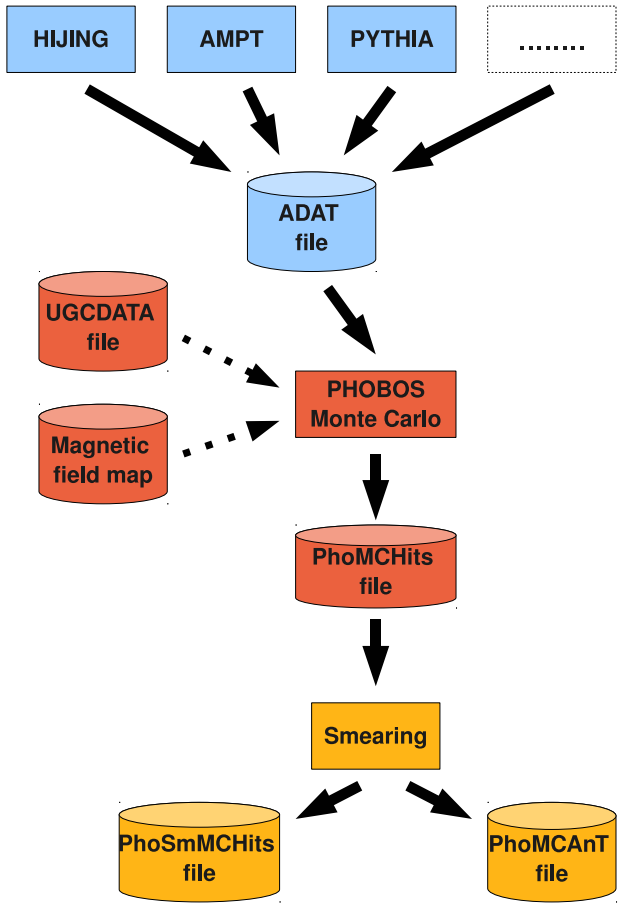

Fig. E.2: The diagram of the PHOBOS Monte Carlo simulations. The programs (boxes) and files (cylinders) are marked by different colors according to the step in which they are used or produced: generation (blue), simulation (red) and smearing (yellow). Thick black arrows show the transfer of Monte Carlo data, dotted arrows denote reading of additional information.

E.2 Generation of events

In the generation step several packages provided by the authors of the models are used. The events were obtained from HIJING [155, 156], AMPT [157], VENUS [270] and PYTHIA [180] generators, but several other model were also tried. The HIJING generator was the most frequently used, the fraction of events from each generator used in the simulations is shown in Fig. E.3. In order to accommodate all possible generators their output was always transformed into the the same compact custom format of events (ADAT). This format uses text files, thus the events generated in toy models or even entered by hand in the text editor can be used. While the file is archived on tape it is automatically compressed, thus the use of text format does not increase the usage of resources.

Most of the generators can be used to obtain events with collisions of different nuclei, from the heaviest $Au + Au$ (in the case of RHIC) to $p + p$. As shown in Fig. E.4 the fraction of events with $Au + Au$ collisions is similar to those for $d + Au$ and $p + p$, while there are fewer $Cu + Cu$ events. Smaller number of events with collisions of nuclei (heavier than deuteron) is due to the fact that such simulations require much longer CPU time per event. Using the same computer resources it is possible to simulate 50 times more $p + p$ events than $Au + Au$ events. If the pie chart shown in Fig. E.4 was representing CPU time usage, $Au + Au$ events would become dominant, while the CPU time fraction for $p + p$ would drop to 2% and for $d + Au$ and $Cu + Cu$ was about 10%.

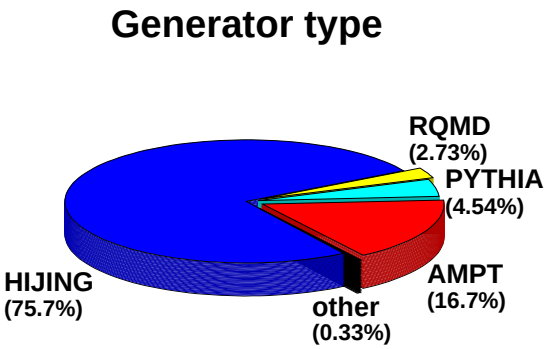

Fig. E.3: The fraction of events from several different event generators used in the PHOBOS Monte Carlo simulations.

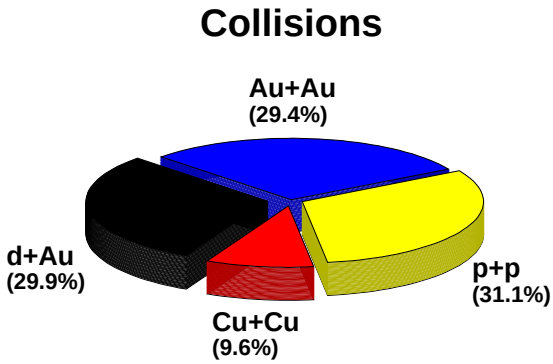

Fig. E.4: The fraction of events used in the PHOBOS Monte Carlo simulations divided according to the type of colliding system.

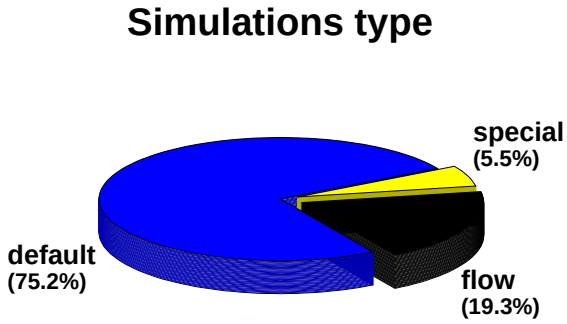

Fig. E.5: The fraction of events used in the PHOBOS Monte Carlo simulations divided according to their type: the events from an event generator without modifications (default), events with predefined type of flow and events with other types of modifications (special).

The events supplied by the original generators are possibly close to real events and are thus very useful in majority of studies. However, quite often some modifications, most frequently a specific type of the elliptic flow, are required. Events with such features, sometimes different than in the data, are necessary in studies of reconstruction methods and for the evaluation of their systematic errors. Several more frequently used modifications were implemented as an extension of the standard event generators, for example the events from HIJING with required elliptic flow can be generated without any additional processing or intermediate output. In Fig. E.5 it is shown that the fraction of events taken directly from the generators is the largest (75%) and the flow is the most frequent modification.

Generation of events for the simulations is moderately CPU time consuming, but of course it depends on the generator program (a factor of 10 is possible) and centrality of collisions requested. Usually this step takes less than 20% of time necessary for the whole procedure.

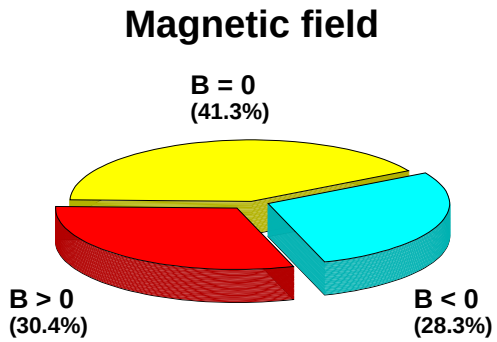

Fig. E.6: The fraction of events obtained from the PHOBOS Monte Carlo simulations divided according to the type of magnetic field: for the magnet switched off ($B = 0$) or for each of polarities.

E.3 Simulations of the detector response

The simulation program PMC (PHOBOS Monte Carlo) was the earliest part of the PHOBOS software. It is written in FORTRAN and was originally linked only with the GEANT 3.11 package. The standard reconstruction and analysis program PhAT (written in C++) was created much later, and from the very beginning was based and integrated with the ROOT package (newly released at that time). In order to unify the software an interface PMC-PhAT was written. It enables us to start PMC from a ROOT (PhAT) session and transfer the results of simulations directly to the code included in PhAT.

During the initialization PMC reads a geometry description and a magnetic field map (described below). Then it either reads the input file in the ADAT format or generates particles in a simple procedure implemented internally. When primary particles are defined PMC transfers the control to the standard GEANT procedures which propagate the particles through the detector, simulating all physical processes including decays and secondary interactions. Output file is created by the PMC on the basis of the information supplied by GEANT.

Regardless of the real number of particles in the event, PMC provides to GEANT only one primary particle at a time, and collects the information from its simulation to be output when all particles are already processed. This approach was necessary because of large memory requirements (especially for the computers available before the year 2000) for tracking of the secondary particles, created inside the massive iron yoke of the PHOBOS magnet. Their number was especially large, as in PMC we decided to simulate secondaries very precisely, lowering most of the standard GEANT thresholds for creating secondary particles and tracking them. Without these special setting our simulations would be not accurate enough, as we have found that the level of background hits would be then underestimated.

The information on the geometry and materials in the PHOBOS detector is stored in UGCDATA text files. The active or inactive volumes are described there by commands with parameters compatible with these needed in the calls to standard GEANT 3.11 subroutines. In a similar way the materials used in the detector elements are defined. In addition several more commands recognized only by PMC are introduced. At first the parameters describing the volumes were entered in a text editor. Later, most of them were extracted automatically from the technical drawings created in the Autocad program. The geometry definition contained in a file was found more convenient and flexible than the standard GEANT approach: the fixed code with calls to GEANT subroutines. Simulations with different geometries can be done using the same binary program, only the name of the UGCDATA file has to be changed.

The second file read at the initialization stage of PMC is the magnetic field map. It contains

the values of magnetic field vectors defined in a grid of points covering mostly the area of the Spectrometer and the magnet yoke, but extending as far as the field is non-negligible. Spacing in the grid is flexible - it is more coarse in the areas, where the field is weaker and changes less rapidly. The format of the map allows us to define both a very simple magnetic field (used in simulations for design studies of the detector) and the complete map from measurements. In PMC several magnetic field maps covering separate areas can be read and used in the simulations. This is useful for special simulations in the area extending to the Zero Degree Calorimeters, which are placed behind RHIC magnets. In the PHOBOS experiment the magnet could be switched off or work at one of two polarities. Although real measurements were done mostly with the magnet switched on, over 40% of events were simulated without the magnetic field (see Fig. E.6). Simulations for $B = 0$ are less CPU time consuming (about 70% of the time needed for $B \neq 0$) and the presence of the magnetic field has negligible effects for multiplicity studies.

In the chain of Monte Carlo production the simulations are the most time consuming part and usually take more than 80% of total CPU time. Full simulation of one very central $Au+Au$ event takes up to one hour. Interestingly, this CPU time was similar in all years from 1995-2008, even if computers, on which the first simulations for the PHOBOS experiment were performed, were about 100 times slower than in the year 2008. However, the first description of the detector geometry was very simple, it included active elements of the detector and very few support structures. Later many inactive elements were added to the geometry file and their description became more realistic, but at the same time more complicated. Larger number of volumes increases the CPU time, the main reason of increased computation time is tracking of secondary particles. Their number is now larger than at the beginning not only because of adding more material in the geometry definition, but also due to the change of tracking parameters - lowering of the standard cut values for stopping of particles (which results in an increase of the number of secondary particles). This was necessary for accurate simulation of ionization energy losses which is very important for particle identification in the silicon. Fortunately, performance of new computer processors increased concurrently with these growing requirements, thus more accurate simulations are possible.

E.4 Smearing

In this step PhoMCHits files created by the PMC program are read, their content is copied to the output PhoSmMCHits files, but also new information is added. The main tasks performed in this step are:

- the energy losses of the charged particles are transformed into signals registered by the detector elements (for example pads in the silicon sensors), if more particles hit the same element their contributions are added;
- gains and pedestals appropriate for a given element are simulated, the electronic noise is added to the signal, the signal is converted from analog to digital and finally processed in the same way as the signal measured in the real data;
- the basic reconstruction of hits in the silicon sensors (including merging of neighbor pads) is performed;
- centrality of the collisions is determined (for $A + A$ events);
- several procedures of vertex reconstruction (described in Section C) are executed;

- the standard tracking in the Spectrometer is performed, if creation of PhoMCAnt files is requested.

The CPU time requirements for this step are the lowest, but the amount of data transferred from and to disks is the largest.

E.5 Automatization of simulation procedures

At the beginning of performance studies of the PHOBOS detector relatively small number of events was sufficient for the estimation of the detector acceptance or tests of the reconstruction software. Simulations could be obtained by running a few batch jobs on one or a few computers.

Later, for more detailed analyses much larger MC event samples became necessary. Typical simulation request has grown from a few thousands to sometimes even a few millions of events. Such large requests could be fulfilled because the computing power of RHIC Computing Facility (RCF) [271, 272] has increased and several hundreds of processors became available to the PHOBOS experiment. Large requests are split into many smaller jobs in order to be run on many computers and to complete each of them in a reasonable time. At the same time several hundreds of jobs are running and many of them are finishing every day. Some fraction of jobs fail due to problems like a lost network connection (especially frequent in the first years of RCF operations). All completed jobs need to be tested and these which are not successfully completed are restarted once more. In order to keep track of generated and simulated events the information on requested samples is kept in a logbook and entered to a computer database.

The simulations, which at the very beginning could be done by running simple jobs, soon required automatization of many tasks. After a few years of development the procedure that minimizes the human intervention has been established:

- newly arrived simulation request is entered in the logbook, the run number (or a whole range of run numbers) is assigned to it and it is scheduled for production;
- the input files from the chosen event generator are selected for the request; usually a new set of events is generated, but sometimes the sample generated earlier can be reused;
- before starting requested simulations, they are divided into runs (for each input file), runs are divided into small jobs for which execution time is below 100 hours (a single job may simulate from 50-200 events of the most central $Au + Au$ collisions to 10000 events of $p+p$ interactions); one common macro for all simulation jobs is created and a few control files for each job are generated using a script;
- the jobs prepared in the previous step are submitted for execution; several different job manager systems were used (PBS, LSF, Condor) and in each case different control files are necessary;
- during execution the jobs not only create the output files, but also store the information in the database of simulation runs;
- the progress of the simulations or even single jobs can be monitored in several ways: by checking the entries in the database, by examining the job log files or even by inspection of the computers on which the jobs are running; there are several tools (scripts) that display only selected information in a compact form;
- the state of the jobs is continuously monitored using a script collecting the information and presenting a summary as a WWW page; any problems that require some action can be easily spotted; this information is very useful to optimize usage of the available computers, especially when many hundreds jobs are running;

- each run with all jobs finished undergoes a test in which failed jobs are detected and the correctness of all output files is examined; appropriate script selecting the failed jobs that need to be rerun is automatically created and a human decision is needed only to confirm this action; if the run is accepted as completed, appropriate scripts are used to transfer the output files to the permanent storage on tapes in HPSS (High Performance Storage System) and to remove from disk no more needed input files with generated events;
- smearing jobs for each run are started after it is accepted as completed, one job per each previously produced PhoMCHits file is necessary;
- results of smearing are also tested, first in short jobs reading each created PhoSmMCHits and PhoMCAnt file, then by a single script analyzing results of those earlier tests for the whole run;
- after successful verification of produced files they are transfered to tapes in HPSS and the information in the database of simulation runs is updated.

The production of the MC data encountered several difficulties due to limited computer resources. Obviously, the CPU time available was never sufficient, thus large requests required many days or weeks. For smearing a limiting factor was the bandwidth of the network or delays in the access to the disks. The disk space available for the simulation jobs after a longer period of running with 100% efficiency was sometimes also not sufficient and prompt testing and removing of finished runs was necessary to avoid potential problems. Only the space available in HPSS was never exhausted.

Section summary

Running of PHOBOS Monte Carlo simulations is a task that was maintained for many years. It has started with preparations of the detector design, became more intensive with the first measurements at RHIC and is continued after last experimental data has been taken. It will eventually stop when the last analysis of the PHOBOS data is finished. During 15 years of using the PMC program it was extensively modified and enhanced, many procedures for running simulations were developed, adjusted to changing computer resources and automatized. All these efforts enabled us to produce nearly 250,000,000 events of various types used in all studies performed by the PHOBOS Collaboration.

F Kinematic properties of the clusters

In the original approach a cluster is defined as an object (particle) with some momentum (longitudinal and transverse) that decays isotropically into some number of finally observed particles. Identification of clusters is possible only if it is assumed that they are identical with known resonances. Even then identification is questionable when many alternative combinations of clusters are possible. However, the biggest problem is due to the fact that the list of resonances is incomplete, thus full kinematic reconstruction is practically never possible. This is why experimental studies of clusters are limited to estimation of their effective parameters: the size (number of particles produced in the decay) and the width in pseudorapidity (or rapidity). Still, if the cluster is a real object, the effective parameters are determined by the more basic ones, like the mass, momentum and decay mode. Studies of cluster decays for many choices of these basic parameters presented in this Appendix are used to determine which values of the cluster width in pseudorapidity are realistic.

In the analysis of decays of clusters we assume that they have the mass $M_{cluster}$ and momentum $\vec{P}_{cluster}$, but really important are the transverse and longitudinal components $P_{T,cluster}$ and $P_{z,cluster}$. In the case of particles from decays their number and types are fixed by the decay mode, while their transverse momentum and pseudorapidity depend also on cluster basic parameters. In the tests the basic parameters of the clusters are not completely free, because they should be adjusted appropriately to describe properties of events, especially the rapidity (or pseudorapidity) and transverse momentum distributions. The $dN/d\eta$ distribution measured for $Au + Au$ collisions at $\sqrt{s_{_{NN}}} = 200$ GeV, or rather a fit to it (Fig. 3.3), can be reproduced by generation of $P_{z,cluster}$ from an appropriately defined distribution, as this parameter is not otherwise constrained (assuming that the total momentum conservation can be neglected). For the experimental $p_{_T}$ distributions, parameterizations obtained in fits to the PHENIX data [172] are used:

$$\frac{dN_\pi}{dp_{_T}}(p_{_T}) = \frac{p_{_T}}{-1.0 + exp(\sqrt{p_{_T}^2 + m_\pi^2}/0.229)} \tag{F.1}$$

$$\frac{dN_K}{dp_{_T}}(p_{_T}) = \frac{p_{_T}}{1.0 + exp(\sqrt{p_{_T}^2 + m_K^2}/0.293)} \tag{F.2}$$

$$\frac{dN_p}{dp_{_T}}(p_{_T}) = \frac{p_{_T}}{-1.0 + exp(\sqrt{p_{_T}^2 + m_p^2}/0.392)}. \tag{F.3}$$

The transverse momentum of a final particle is a sum of $\vec{P}_{T,cluster}$ and the transverse component of its decay momentum, $\vec{p}_{decay}$. For clusters with $P_{T,cluster}$=0 the average transverse momentum of decay products is $\langle p_{_T} \rangle \approx 0.786\ p_{decay}$, where p_{decay} depends on the mass of the cluster and the number and masses of decay products. By selecting appropriate mass of the cluster we can easily obtain correct $\langle p_{_T} \rangle$. However, it is impossible to reproduce experimental $p_{_T}$ distribution using identical clusters with $P_{T,cluster}$=0 as the experimental $p_{_T}$ distribution has a long tail of large values, while the shape of p_{decay} is different: it is peaked at maximal allowed value for two-particle decay, has a maximum in the middle of the allowed range for 3-particle decay. Longer tail appears in decays into more particles, but a reasonable reproduction of the $p_{_T}$ distribution requires that non-zero values of $p_{T,cluster}$ are allowed.

In Fig. F.1 several examples of the $p_{_T}$ distributions obtained for selected decays are shown.

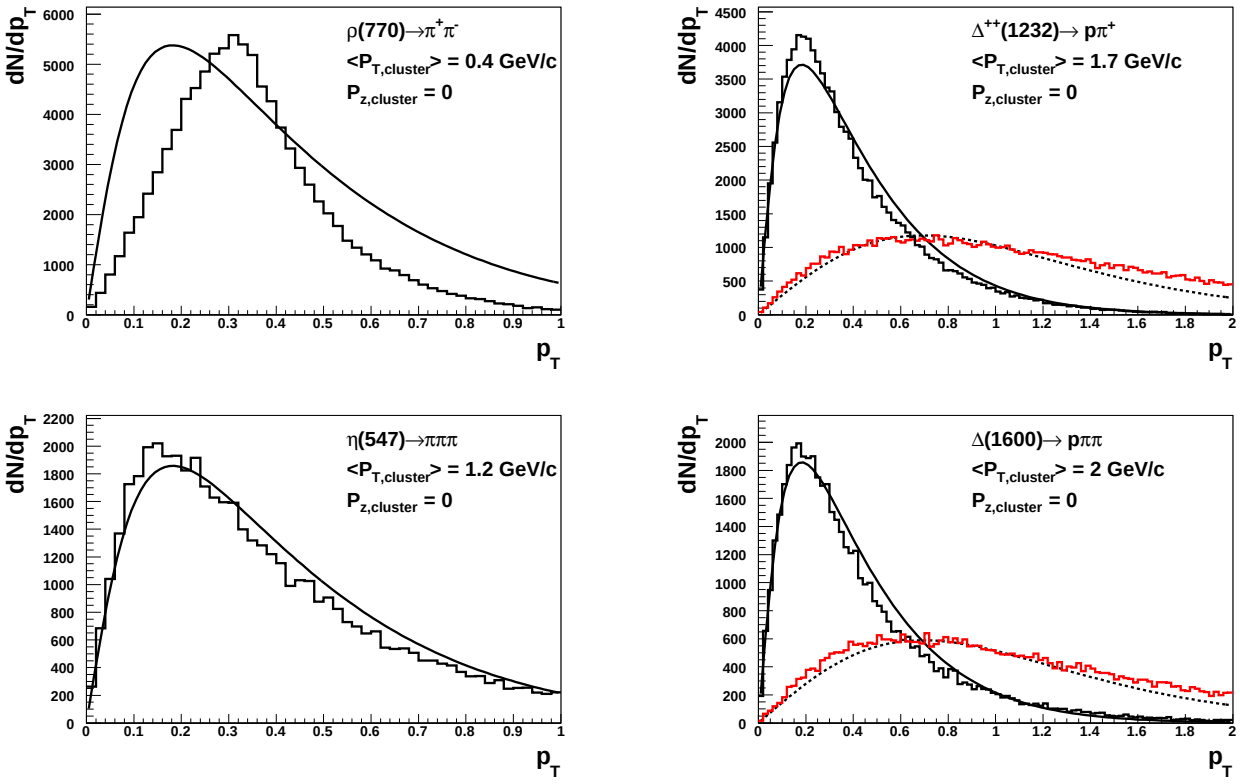

Fig. F.1: Transverse momentum distributions (arbitrary units) of particles from $\rho(770) \to \pi^+\pi^-$, $\Delta^{++}(1232) \to p\pi^+$, $\eta(547) \to \pi\pi\pi$ and $\Delta(1600) \to p\pi\pi$ decays: pions (black histograms) and protons (red histograms) compared to the experimental p_T distribution (lines: continuous for pions, dashed for protons). Parent particle transverse momentum was generated from the function defined in Eq. F.4, using $\langle P_T \rangle$=0.4 GeV/c for $\rho(770)$, $\langle P_T \rangle$=1.7 GeV/c for $\Delta^{++}(1232)$, $\langle P_T \rangle$=1.2 GeV/c for $\eta(547)$, $\langle P_T \rangle$=2.0 GeV/c for $\Delta(1600)$.

It was assumed that the clusters (resonances) have the transverse momentum distribution:

$$\frac{dN_{cluster}}{dP_{T,cluster}}(P_{T,cluster}) = P_{T,cluster} \exp(-2P_{T,cluster}/\langle P_{T,cluster} \rangle) \tag{F.4}$$

The experimental distributions are very well reproduced in decays into 3 particles, the worst agreement is for the decay $\rho(770) \to \pi^+\pi^-$ for which $\langle P_T \rangle$ is the same, but the width is smaller. However, it is necessary to keep in mind that the reproduction of the inclusive p_T distribution in each decay that may happen in collisions of nuclei is not mandatory. Contrary, in some decays $\langle P_T \rangle$ and width are smaller, in other decays larger and the experimental distribution is a sum of many different distributions. Considering a specific decay the value of $\langle P_{T,cluster} \rangle$ that bast reproduces inclusive p_T distribution may be different than that which is present in real events. Results obtained for such $\langle P_{T,cluster} \rangle$ should be treated as a first guess and not as very precise and unquestionable.

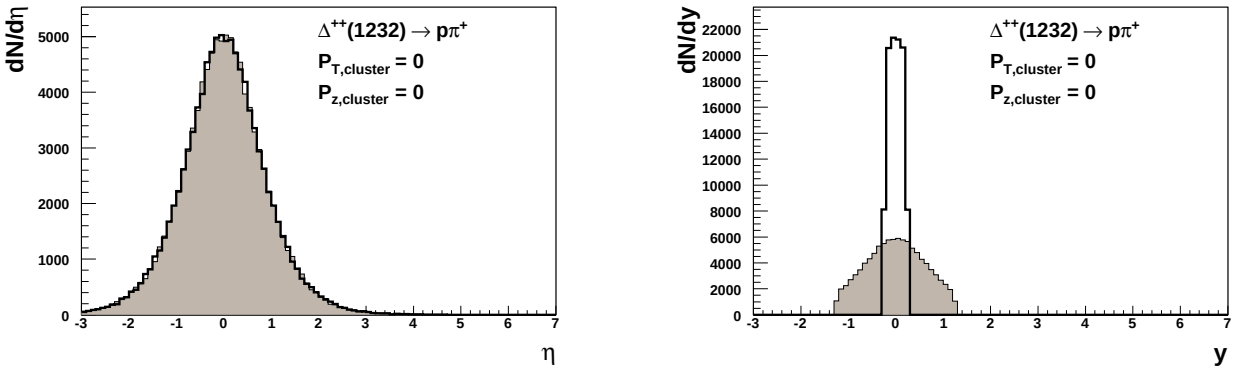

Fig. F.2: Single particle $dN/d\eta$ and dN/dy distributions (arbitrary units) for pions (filled histogram) and for protons (empty solid line histogram) from $\Delta^{++}(1232) \to p\pi^+$ decay. The decaying particles have P_T=P_z=0. Note: in the decay at rest $dN/d\eta$ does not depend on particle type thus the histograms for protons and pions are practically identical.

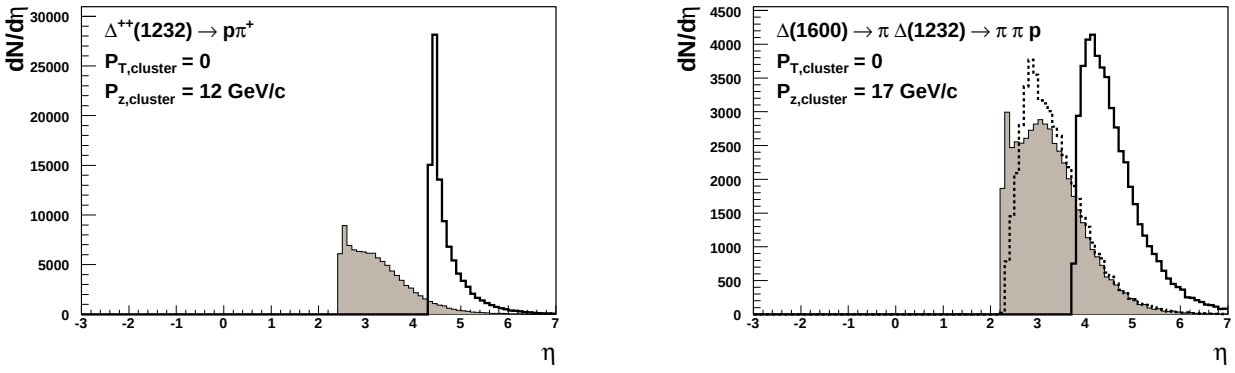

Fig. F.3: Single particle $dN/d\eta$ distributions (arbitrary units) for pions (filled or dashed histogram) and for protons (empty solid line histogram) from $\Delta^{++}(1232) \to p\pi^+$ and $\Delta(1600) \to \pi\Delta(1232) \to \pi\pi p$ decays. The decaying particles have P_T=0 but P_z=12 GeV/c ($\Delta^{++}(1232)$) or P_z=17 GeV/c ($\Delta(1600)$).

F.1 Properties of particles from resonance decays

Most of the studies in this Appendix are performed for clusters with a realistic $\langle P_{T,cluster} \rangle$, but first the special case, $P_{T,cluster} = 0$ is discussed. If in addition the longitudinal momentum $P_{z,cluster} = 0$, the pseudorapidity distribution of particles from decays does not depend on any other parameter: their mass or momentum obtained in the decay, p_{decay}. As an example the decay $\Delta^{++}(1232) \to p\pi^+$ is presented in Fig. F.2. In the same figure also the dN/dy distributions for pions and protons are shown - and they are distinctly different, This can be easily predicted using simple kinematical calculations, as the y values for a particle with the mass m are in this case limited to:

$$|y| \; < \; y_{max} = \frac{1}{2} \ln \frac{\left(\sqrt{p^2_{decay,max} + m^2} + p_{decay,max} \right)^2}{m^2}. \tag{F.5}$$

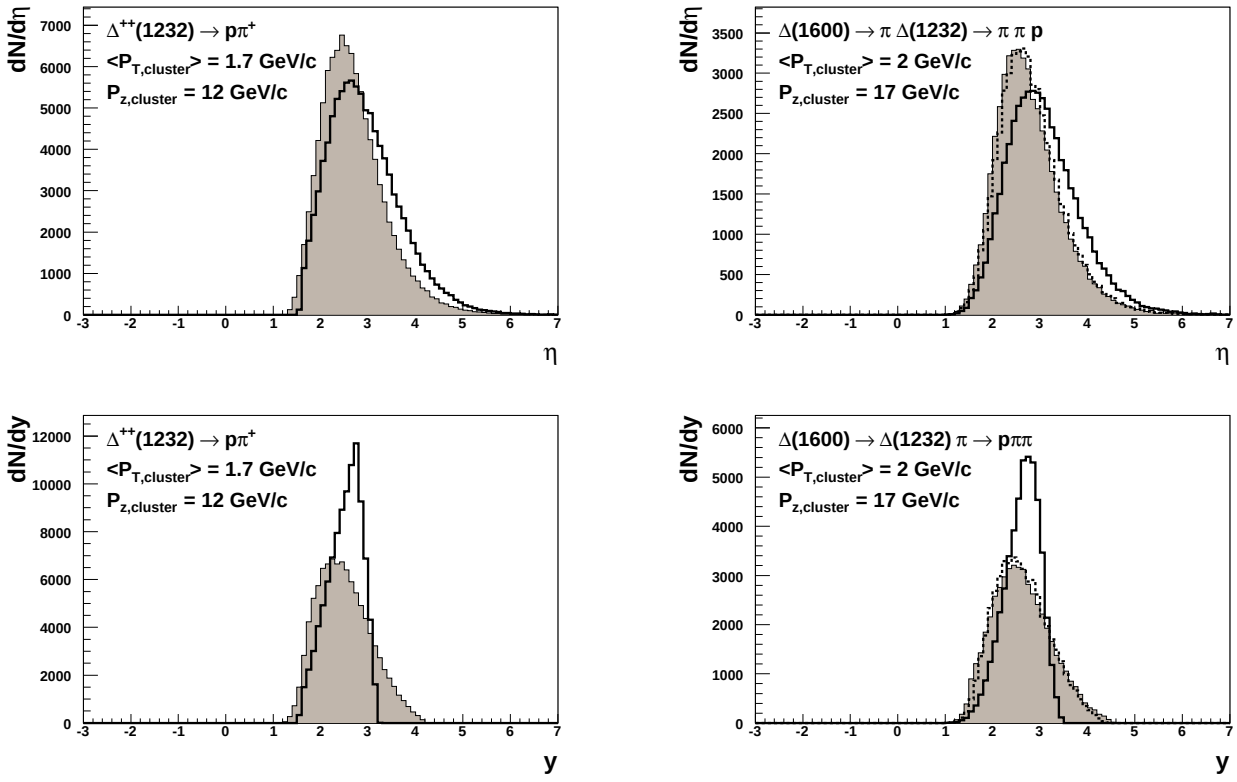

Fig. F.4: Single particle $dN/d\eta$ and dN/dy distributions (arbitrary units) for pions (filled or dashed histogram) and for protons (empty solid line histogram) from $\Delta^{++}(1232) \to p\pi^+$ and $\Delta(1600) \to \pi\Delta(1232) \to \pi\pi p$ decays. The decaying particles have $\langle P_T \rangle$=1.7 GeV/c and P_z=12 GeV/c ($\Delta^{++}(1232)$) or $\langle P_T \rangle$=2 GeV/c and P_z=17 GeV/c ($\Delta(1600)$).

For pions and protons from the analyzed decay $p_{decay,max}$ is the same, but masses are much different thus the distribution for protons is much narrower.

In the case when the cluster has some longitudinal momentum, here selected so that particles from decay have $\eta \approx 3$, the shape of $dN/d\eta$ distribution changes. In Fig. F.3 such distributions are shown for decays of $\Delta^{++}(1232)$ and $\Delta(1600)$. In this case not only the distributions for pions and protons have different widths, but also the average η for protons is almost 2 units larger than for pions. The $dN/d\eta$ distributions of the first and the second pion in the cascade decay of $\Delta(1600)$ do not overlap, but the difference is very small. There is also another, direct 3-body decay of $\Delta(1600) \to \pi\pi p$ possible, but distributions for protons and pions are qualitatively very similar to that shown in Fig. F.3.

Interestingly, introduction of the longitudinal momentum of decaying resonance does not modify the shape of the dN/dy distribution. Such modification corresponds to a transformation, in which rapidity is only shifted by a constant value.

Results obtained in Fig. F.3 are quite surprising, but were obtained for a very specific case. From now in all calculations clusters are assumed to have the transverse momentum distribution defined by Eq. F.4 and the value of $\langle P_{T,cluster} \rangle$ selected so that the experimental value of $\langle p_T \rangle$ is reproduced (but quite often also the shape of p_T distributions agrees).

For the two resonances presented previously, $\Delta^{++}(1232)$ and $\Delta(1600)$, appropriate $\langle P_T \rangle$ values are 1.7 GeV/c and 2 GeV/c, respectively. For decays with such initial parameters of

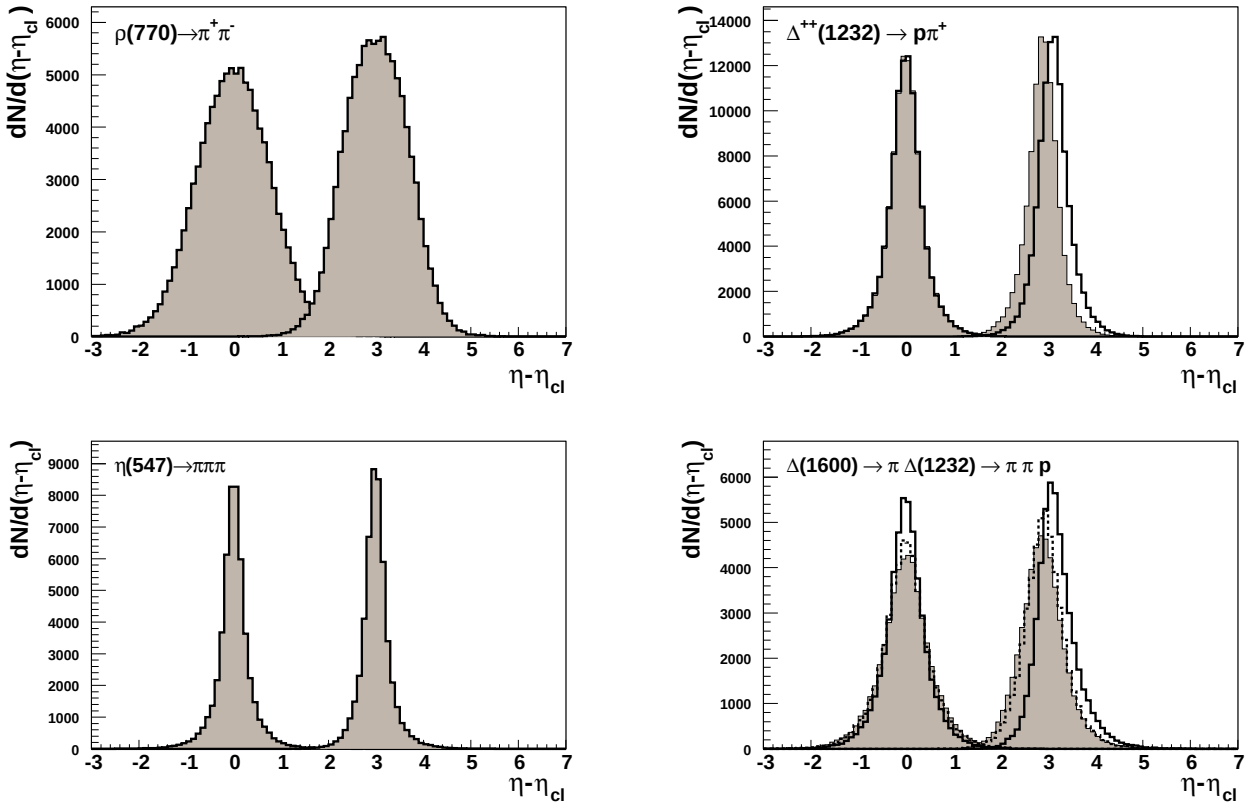

Fig. F.5: Single particle $dN/d(\eta - \eta_{cl})$ distributions (arbitrary units) for particles from decays of $\rho(770)$, $\Delta^{++}(1232)$, $\eta(547)$ and $\Delta^{++}(1600)$. The P_T distribution of decaying particles was selected so that experimental p_T distributions of final particles are approximately reproduced. Two values of longitudinal momentum for each decaying particle were used: P_z=0 (for all resonances) or P_z=8 GeV/c (for $\rho(770)$), P_z=12 GeV/c (for $\Delta^{++}(1232)$), P_z=5.5 GeV/c (for $\eta(547)$) and P_z=17 GeV/c (for $\Delta^{++}(1600)$). Note: in the case of $P_z > 0$ the distribution is shifted 3 units to the right, where the clusters are approximately located.

resonances both $dN/d\eta$ and dN/dy distributions are significantly modified (Fig. F.4). The pseudorapidity distributions for protons and pions are now very similar and centered at almost the same η value. Also the shape of them is much more symmetric. The dN/dy distribution for protons is wider than this shown in Fig F.2. Generally, non-zero value $\langle P_{T,cluster} \rangle$ makes the distributions of particles from decay more similar for different particle types and emission angles.

F.2 Cluster width in resonance decays

The single particle distributions presented in Fig. F.4 provide information how much different values of η or y have particles from decays of similar resonances, but can not be used for calculation of the cluster width. In this case we have to calculate the width of the distribution of $\eta - \eta_{cl}$ (or $y - y_{cl}$) using the estimates of cluster position in each decay. Such an estimate is a well defined value in the case of y_{cl}, but pseudorapidity of the decaying particle may be quite different than the η values of decay products. Moreover, reconstruction of cluster

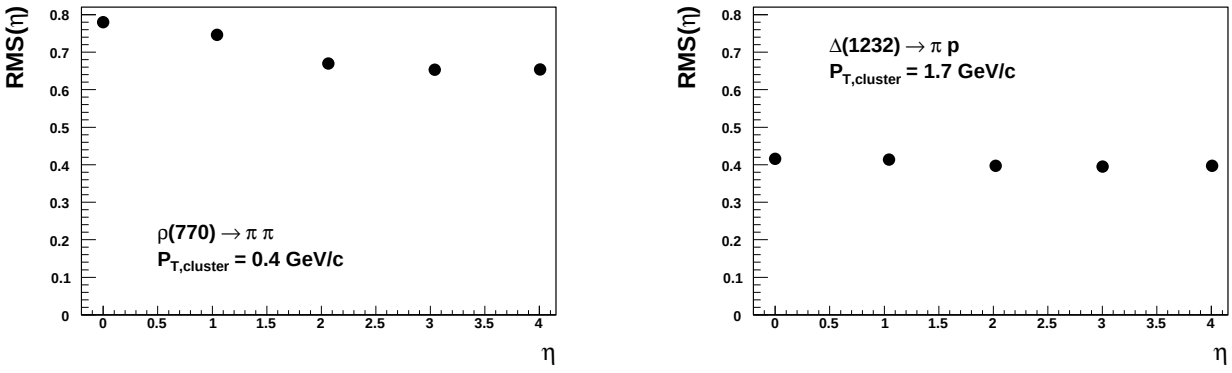

Fig. F.6: The width $RMS(\eta - \eta_{cl})$ of the $dN/d(\eta - \eta_{cl})$ distribution in the decays into two particles as a function of the cluster position in pseudorapidity.

parameters in experiment can be done only using correlations between particles. It is thus better to approximate the center of the cluster by the mean value of η (or y) of particles from decays:

$$\eta_{cl} = \frac{1}{n_{cl}} \sum_{i=1}^{n_{cl}} \eta_i, \tag{F.6}$$

where n_{cl} is the number of charged products of the decay and η_i denotes pseudorapidity of these particles.

In Fig. F.5 distributions for particles from decays of several resonances are shown. Longitudinal momenta are selected so that particles with either $\eta \approx 0$ and $\eta \approx 3$ are produced in the decays, thus both the dependence on the type of decay and the pseudorapidity of the cluster can be examined. The first striking observation is a much larger width of $\rho(770)$ than for other resonances. This is due to the assumption that the experimental $p_{_T}$ distribution has to be reproduced. For $\rho(770)$ particle the value of $P_T = 0.4$ MeV/c is sufficient, as pions have large values of $p_{T,decay}$, contrary to $\eta(547)$ decay in which $p_{T,decay}$ is small and thus $P_T = 1.2$ MeV/c is necessary to reproduce experimental $\langle p_{_T} \rangle$. As a result pions from $\rho(770)$ decay are emitted almost isotropically, while these from $\eta(547)$ decay follow approximately the direction of flight of their parent and thus their values of η are very close. This indicates that a different criterion for selection of P_T of the resonance should be used, as discussed later.

For all resonances the distributions at larger η shown in Fig. F.5 are slightly narrower. It is confirmed in Fig. F.6 where two examples of the dependence of cluster width on the cluster position are shown. Clusters at $\eta \approx 0$ are the widest, with increasing η_{cl} the width decreases and for $\eta > 2$ becomes constant. For wider clusters (like $\rho(770)$) such decrease is more significant and may reach ∼20%, for narrow clusters (like $\Delta^{++}(1232)$) the dependence of the width on η_{cl} is much weaker.

In the decays of resonances the width depends also strongly on the number of detected particles. If some particles are neutral, and thus undetected, the average separation or remaining particles is smaller, and the cluster constructed from charged particles becomes effectively narrower. In the case of $\Delta(1600)$ resonance, when only 2 out of 3 particles in the decay are charged, the width decreases up to 20%.

In the tests presented before it was requested that experimental value of $\langle p_{_T} \rangle$ has to be reproduced in each resonance decay. Such requirement leads to a much larger $P_{T,cl}$ for a light

Decay	Fraction Γ_i/Γ	K	$\langle P_{T,cl}\rangle$ GeV/c	$\sigma(\eta)$		$\sigma(y)$
				$\eta_{cl} \approx 0$	$\eta_{cl} \approx 3$	
$\eta(547) \rightarrow \pi^+\pi^-\pi^0$	23%	3	0.744	0.42	0.36	0.29
		2		0.36	0.31	0.25
$\rho(770) \rightarrow \pi\pi$	100%	2	0.915	0.62	0.53	0.52
$\omega(782) \rightarrow \pi^+\pi^-\pi^0$	89%	3	0.924	0.56	0.48	0.43
		2		0.49	0.42	0.43
$\eta'(958) \rightarrow \pi^+\pi^-\eta^0$	45%	2	1.060	0.33	0.31	0.22
$\phi(1020) \rightarrow K^+K^-$	49%	2	1.107	0.20	0.19	0.11
$\Delta(1232) \rightarrow \pi p$	100%	2	1.270	0.42	0.42	0.28
$\Delta(1600) \rightarrow \pi\pi p$	75-90%	3	1.543	0.53	0.50	0.39
		2		0.43	0.43	0.31

Table F.1: Cluster width for several decays of resonances into at least 2 charged particles. In the case of decays into 3 particles the width calculated from both 2 and 3 particles are usually given. The initial $\langle P_{T,cl}\rangle$ is calculated according to Eq. F.7, width is obtained from a gaussian fit. Clusters with large pseudorapidities ($\eta_{cl} \approx 3$) are obtained by setting $P_{z,cl}$ to and appropriately selected value.

resonance $\eta(547)$ than for a heavier $\rho(770)$. This disagrees with an experimental observation that $\langle p_T\rangle$ of particles increases with particle mass. Therefore it seems more reasonable to use a mass dependent initial transverse momentum of the decaying particle. It is thus assumed that $\langle P_{T,cl}\rangle$ can be calculated using a formula:

$$\langle P_{T,cl}\rangle(m_{cl}) = 0.76 m_{cl} + 0.33 \tag{F.7}$$

where m_{cl} is the mass of the particle and the parameters of this linear relation are chosen to give $\langle P_{T,cl}\rangle$ for π, K and p consistent with distributions described by Eqs. F.1, F.2 and F.3, respectively.

Results of calculations of the cluster width for a selection of resonance decays is presented in Table F.1. The resonances in such decays produce clusters much narrower than these from isotropic decays at rest. The widest resonance ($\rho(770)$) has the width 0.62, while the narrowest ($\phi(1020)$) only 0.2. The ϕ meson is however not a good representative, as it decays into particles with masses that summed are almost equal to the mass of the parent.

F.3 Cascade decays and effects of polarization

Results presented earlier in this Section were obtained for resonances decaying in a single step or at most in two steps (for $\Delta(1600)$). However, as from two-particle correlations study large cluster sizes were obtained, decays into more than three particles should be considered. A probable decay pattern in this case is a cascade decay with emission of pions in each step. The $\Delta(1600)$ resonance gives an example for for the mass difference between intermediate steps in such a cascade; in simulations of large clusters it is reasonable to assume that the energy available for emission of one pion is 300-350 MeV. For simplicity, it was assumed that "resonances" present in the decay have the above mentioned mass difference and are not necessarily present in the Particle Data Group tables [71]. The width of clusters increases with the number of

steps in a cascade decay; large difference is observed for a single decay and a cascade with two steps (width in $\Delta(1232)$ and $\Delta(1600)$) decays is 0.42 and 0.53, respectively), but then each additional pion emitted increases the width of the cluster by ∼2-3 %. Even for large clusters the effective width does not significantly exceed 0.6. Wider clusters are possible if the energy available for each emitted pion is much larger than 350 MeV.

Another effect that affects the cluster width is non-isotropic distribution of particles from a decay due to polarization of the parent particle. A transverse polarization increases the width; a longitudinal polarization leads to a decrease. It was analyzed for the cascade decay $\Delta(1900) \rightarrow \pi\pi\pi p$ in which $\Delta(1600)$ and $\Delta(1232)$ created in the first and second steps are polarized. For polarization schemes that maximize or minimize the modification relative to the isotropic decay a difference of less than 10% was found. This means that polarization effects are small or even negligible, especially as only in a fraction of decays they may be present.

Section summary

Assumption of an isotropic decay of clusters at rest leads to the reconstructed width in pseudorapidity of about 0.9. However, under the realistic assumption that resonances, the natural candidates for clusters, have non-negligible transverse momentum, the width for several of them (with the masses below 2 GeV) is in the range 0.2-0.6.

The majority of effects which influence the cluster width lead to its decrease; the width at large $|\eta|$ is smaller, the lack of reconstruction of neutral particles causes up to 20% narrowing of clusters. Wider clusters are expected for resonances that decay in cascade decays with many steps. A modification of the cluster width may also appear if decaying particles are polarized. However, a potential increase of the cluster width, due to the above mentioned effects, is limited to a few %.

References

[1] B. B. Back *et al.* (PHOBOS), Phys. Rev. Lett. 85 (2000) 3100.
[2] B. B. Back *et al.* (PHOBOS), Phys. Rev. Lett. 87 (2001) 102301.
[3] B. B. Back *et al.* (PHOBOS), Phys. Rev. Lett. 87 (2001) 102303.
[4] B. B. Back *et al.* (PHOBOS), Phys. Rev. Lett. 88 (2002) 022302.
[5] B. B. Back *et al.* (PHOBOS), Phys. Rev. C65 (2002) 031901.
[6] B. B. Back *et al.* (PHOBOS), Phys. Rev. C65 (2002) 061901.
[7] B. B. Back *et al.* (PHOBOS), Phys. Rev. Lett. 89 (2002) 022301.
[8] B. B. Back *et al.* (PHOBOS), Phys. Rev. Lett. 91 (2003) 052303.
[9] B. B. Back *et al.* (PHOBOS), Phys. Rev. C67 (2003) 021901.
[10] B. B. Back *et al.* (PHOBOS), Phys. Rev. Lett. 91 (2003) 072302.
[11] B. B. Back *et al.* (PHOBOS), Phys. Rev. Lett. 93 (2004) 082301.
[12] B. B. Back *et al.* (PHOBOS), Phys. Lett. B578 (2004) 297.
[13] B. B. Back *et al.* (PHOBOS), Phys. Rev. C70 (2004) 011901.
[14] B. B. Back *et al.* (PHOBOS), Phys. Rev. C70 (2004) 021902.
[15] B. B. Back *et al.* (PHOBOS), Phys. Rev. C70 (2004) 051901.
[16] B. B. Back *et al.* (PHOBOS), Phys. Rev. C70 (2004) 061901.
[17] B. B. Back *et al.* (PHOBOS), Phys. Rev. Lett. 94 (2005) 082304.
[18] B. B. Back *et al.* (PHOBOS), Phys. Rev. Lett. 94 (2005) 122303.
[19] B. B. Back *et al.* (PHOBOS), Phys. Rev. C71 (2005) 021901.
[20] B.B. Back *et al.* (PHOBOS), Phys. Rev. C72 (2005) 031901.
[21] B.B. Back *et al.* (PHOBOS), Phys. Rev. C72 (2005) 051901.
[22] B.B. Back *et al.* (PHOBOS), Nucl. Phys. A757 (2005) 28.
[23] B.B. Back *et al.* (PHOBOS), Phys. Rev. C73 (2006) 031901.
[24] B. B. Back *et al.* (PHOBOS), Phys. Rev. C74 (2006) 011901.
[25] B. B. Back *et al.* (PHOBOS), Phys. Rev. C74 (2006) 021901.
[26] B. B. Back *et al.* (PHOBOS), Phys. Rev. C74 (2006) 021902.
[27] B. Alver *et al.* (PHOBOS), Phys. Rev. Lett. 96 (2006) 212301.
[28] B.B. Back *et al.* (PHOBOS), Phys. Rev. Lett. 97 (2006) 012301.
[29] B.B. Back *et al.* (PHOBOS), Phys. Rev. C75 (2007) 024910.
[30] B. Alver *et al.* (PHOBOS), Phys. Rev. C75 (2007) 054913.
[31] B. Alver *et al.* (PHOBOS), Phys. Rev. Lett. 98 (2007) 242302.
[32] B. Alver *et al.* (PHOBOS), Phys. Rev. C77 (2008) 014906.
[33] B. Alver *et al.* (PHOBOS), Phys. Rev. C77 (2008) 061901.
[34] B. Alver *et al.* (PHOBOS), Phys. Rev. Lett. 102 (2009) 142301.
[35] B. Alver *et al.* (PHOBOS), Phys. Rev. C80 (2009) 011901.
[36] B. Alver *et al.* (PHOBOS), Phys. Rev. C81 (2010) 024904.
[37] B. Alver *et al.* (PHOBOS), Phys. Rev. Lett. 104 (2010) 062301.
[38] B. Alver *et al.* (PHOBOS), Phys. Rev. C81 (2010) 034915.
[39] B. Alver *et al.* (PHOBOS), Phys. Rev. Lett. 104 (2010) 142301.
[40] K. Woźniak *et al.* (PHOBOS), Proc. of the XXV ISMD, eds. Bruncko, Sandor and Urban. World Scientific Publishing, 1996, 297.

[41] K. Woźniak *et al.* (PHOBOS), Proc. of the XXX ISMD, eds. T.Csorgo, S.Hegyi and W. Kittel, World Scientific (2001) 458. (also: arXiv:hep-ex/0102012).
[42] K. Woźniak *et al.* (PHOBOS), Proc. of TIME2005, Nucl. Instr. and Meth. A566 (2006) 185.
[43] K. Woźniak *et al.* (PHOBOS), Proc. of QM2004, J. Phys. G 30, (2004) S1377.
[44] K. Woźniak *et al.* (PHOBOS), Proc. of QM2006, Int. J. Mod. Phys. E 16 (2007) 2187.
[45] K. Woźniak *et al.* (PHOBOS), HSQCD2008 conf., arXiv: 08009.2893v1 [nucl-ex] (2008).
[46] K. Woźniak *et al.* (PHOBOS), Proc. of EPS HEP 2009, PoS (EPS-HEP 2009) 037.
[47] K. Woźniak *et al.* (PHOBOS), Proc. of 45th Rencontres de Moriond, La Thuile, 2010, arXiv:1005.1478v1 [nucl-ex].
[48] E. Shuryak, Phys. Rep. 61 (1980) 71.
[49] J. Engels, F. Karsch, I. Montvay and H. Satz, Phys. Lett. B101 (1981) 89.
[50] F. Karsch, Nucl.Phys. A698 (2002) 199.
[51] M. Cheng *et al.*, Phys. Rev. D81 (2010) 05451034.
[52] J. D. Bjorken, Phys. Rev. D27 (1983) 140.
[53] B. B. Back *et al.* (E917), Phys. Rev. Lett. 86 (2001) 1970;
L. Ahle *et al.* (E802), Phys. Rev. C60 (1999) 064901;
J. Barette *et al.* (E877), Phys. Rev. C62 (2000) 024901.
[54] H. Appelshäuser *et al.* (NA49), Phys. Rev. Lett. 82 (1999) 2471.
[55] I. G. Bearden *et al.* (BRAHMS), Phys. Rev. Lett. 93 (2004) 102301.
[56] J. L. Klay *et al.* (E895), Phys. Rev. C68 (2003) 054905.
[57] D. J. Gross and F. Wilczek, Phys. Rev. Lett. 30 (1973) 1343.
[58] H. Politzer, Phys. Rev. Lett. 30 (1973) 1346.
[59] T. Matsui and H. Satz, Phys. Lett. B178 (1986) 416.
[60] M. Jacob, Nucl. Phys. A583 (1995) 13.
[61] D. Lissauer and E. V. Shuryak, Phys. Lett. B253 (1991) 15.
[62] H. Satz, Phys. Rep. 403-404 (2004) 33.
[63] M. C. Abreu *et al.* (NA50) Phys. Lett. B477 (2000) 28.
[64] B. Alessandro *et al.* (NA50), Eur. Phys. J. C39 (2005) 335.
[65] M. C. Abreu *et al.* (NA38), Eur. Phys. J C14 (2000) 443.
[66] M. Gyulassy and L. McLerran, Nucl. Phys. A750 (2005) 30.
[67] I. Arsene *et al.* (BRAHMS), Nucl. Phys. A757 (2005) 1.
[68] J. Adams *et al.* (STAR), Nucl. Phys. A757 (2005) 102.
[69] K. Adcox *et al.* (PHENIX), Nucl. Phys. A757 (2005) 184.
[70] B. I. Abelev *et al.* (STAR), Phys. Rev. C79 (2009) 064903.
[71] C. Amsler *et al.* (Particle Data Group), Phys. Lett. B667 (2008) 1 (also: http://pdg.lbl.gov/).
[72] T. Gburek *et al.* (PHOBOS), J. Phys. G35 (2008) 104131.
[73] A. Adare *et al.* (PHENIX), Phys. Rev. Lett. 98 (2007) 232301.
[74] B. I. Abelev *et al.* (STAR), Phys. Rev. C80 (2009) 041902.
[75] A. Capella1 and E. G. Ferreiro, Eur. Phys. J. C42 (2005) 419.
[76] L. Grandchamp, R. Rapp and G. E. Brown, Phys. Rev. Lett. 92 (2004) 212301.
[77] K. Golec-Biernat and M. Wüsthoff , Phys. Rev. D59 (1998) 014017.
[78] A. M. Staśto, K. Golec-Biernat and J. Kwieciński, Phys. Rev. Lett. 86 (2001) 596.
[79] L. McLerran and R. Venugopalan, Phys. Rev. D49 (1994) 2233.

[80] L. D. McLerran and R. Venugopalan, Phys. Rev. D49 (1994) 3352.
[81] J. P. Blaizot and F. Gelis, Nucl. Phys. A750 (2005) 148.
[82] K. Itakura, Nucl. Phys. A774 (2006) 277.
[83] F. Gelis, E. Iancu, J. Jalilian-Marian and R. Venugopalan, arXiv: 1002.0333v1 [hep-ph].
[84] D. Kharzeev and E. Levin, Phys. Lett. B523 (2001) 79.
[85] J. Adams *et al.* (STAR), Phys. Rev. C71 (2005) 044906.
[86] J. Adams *et al.* (STAR), Phys. Rev. Lett. 91 (2003) 262302.
[87] C. Adler *et al.* (STAR), Phys. Rev. Lett. 90 (2003) 82302.
[88] J. Adams *et al.* (STAR), Phys. Rev. Lett. 91 (2003) 072304.
[89] J. Adams *et al.* (STAR), Phys. Rev. Lett. 93 (2004) 252301.
[90] B. I. Abelev *et al.* (STAR), Phys. Rev. Lett. 97 (2006) 152301.
[91] S. Afanasiev *et al.* (PHENIX), Phys. Rev. C 80, 054907 (2009)
[92] I. Arsene *et al.* (BRAHMS), Phys. Rev. Lett. 93 (2004) 242303.
[93] J. Y. Ollitrault, Phys. Rev. D46 (1992) 229.
[94] C. Adler *et al.* (STAR), Phys. Rev. Lett. 87 (2001) 182301.
[95] S. S. Adler *et al.* (PHENIX), Phys. Rev. Lett. 91 (2003) 182301.
[96] J. Adams *et al.* (STAR), Phys. Rev. Lett. 95 (2005) 122301.
[97] C. Pinkenburg *et al.* (E895), Phys. Rev. Lett. 83 (1999) 1295.
[98] P. F. Kolb, P. Huovinen, U. Heinz and H. Heiselberg, Phys. Lett. B 500 (2001) 232.
[99] C. A. Oglive, Nucl. Phys. A698 (2002) 3c.
[100] R. Stock, J. Phys. G30 (2004) S633.
[101] D. Teaney, Phys. Rev. C68 (2003) 034913.
[102] P. Huovinen, P. F. Kolb, U. Heinz, P. V. Ruuskanen and S. A. Voloshin, Phys. Lett. B503 (2001) 58.
[103] J. Rafelski, Phys. Rep. 88 (1982) 331.
[104] J. Rafelski and M. Danos, Phys. Lett. B192 (1987) 432.
[105] B. I. Abelev *et al.* (STAR), Phys. Rev. C77 (2008) 44908.
[106] E. Andersen *et al.* (WA97), Phys. Lett. B449 (1999) 401.
[107] F. Antinori *et al.* (NA57), Nucl. Phys. A698 (2002) 118c.
[108] B. I. Abelev *et al.* (STAR), Phys. Rev. C79 (2009) 34909.
[109] K. Redlich and A. Tounsi, Eur. Phys. J. C24 (2002) 589.
[110] *et al.* I. G. Bearden *et al.* (BRAHMS), Phys. Rev. Lett. 94 (2005) 162301.
[111] I.C.Arsene *et al.* (BRAHMS), Phys. Lett. B687 (2010) 36.
[112] M. Gaździcki and M. I. Gorenstein, Acta Phys. Pol. B30 (1999) 2705.
[113] F. Becattini, J. Cleymans, A. Keränen, E. Suhonen and K. Redlich, Phys. Rev. C64 (2001) 024901.
[114] R. D. Pisarski and F. Wilczek, Phys. Rev. D29 (1984) 338.
[115] A. Barducci, R. Casalbuoni, G. Pettini, and R. Gatto, Phys. Rev. D49 (1994) 426.
[116] M. Stephanov, K. Rajagopal and E. Shuryak, Phys. Rev. Lett. 81 (1998) 4816.
[117] R. C. Hwa, Z. Phys. C38 (1988) 277.
[118] Zhen Cao and R. C. Hwa, Phys. Rev. C54 (1996) 2600.
[119] K. C. Chase and A. Z. Mekjian, Phys. Lett. B379 (1996) 50.
[120] H. Heiselberg and A. D. Jackson, Phys. Rev. C63 (2001) 064904.
[121] M. Stephanov, Phys. Rev. D81 (2010) 054012.
[122] L.Van Hove, Z. Phys. C27 (1984) 135.

[123] K. Rajagopal, in Quark-Gluon Plasma 2., ed. R. C. Hwa, World Scientific, 1995.
[124] V. V. Begun, M. I. Gorenstein, M. Hauer, V. P. Konchakovski, and O. S. Zozulya, Phys. Rev. C74 (2006) 044903.
[125] F. Becattini, A. Keränen, L. Ferroni and T. Gabbriellini, Phys. Rev. C72 (2005) 064904.
[126] M. Stephanov, K. Rajagopal and E. Shuryak, Phys. Rev. D60 (1999) 114028.
[127] H. Heiselberg, Phys. Rep. 351 (2001) 161.
[128] A. Anselm and M. G. Ryskin, Phys. Lett. B266 (1991) 482.
[129] J. P. Blaizot and A. Krzywicki, Phys. Rev. D46 (1992) 246.
[130] A. Bialas and R. Peszanski, Nucl. Phys. B273 (1986) 703.
[131] P. Carruthers, H. C. Eggers and Ina Sarcevic, Phys. Rev. C44 (1991) 1629.
[132] R. C. Hwa and M. T. Nazirov, Phys. Rev. Lett. 69 (1992) 741.
[133] A. K. Mohanty and S. K. Kataria, Phys. Rev. Lett. 73 (1994) 2672.
[134] St. Mrówczyński, Phys. Rev. C66 (2002) 024904.
[135] S. Jeon, V. Koch, in "Quark-Gluon Plasma 3", eds. R.C. Hwa and X.-N. Wang, World Scientific, Singapore 2003 or arXiv:hep-ph/0304012v1.
[136] C. Pruneau, S. Gavin, and S. Voloshin, Phys. Rev. C66 (2002) 044904.
[137] G. Baym, B. Blättel, L. L. Frankfurt, H. Heiselberg and M. Strikman, Phys. Rev. C52 (1995) 1604.
[138] G. Baym and H. Heiselberg, Phys. Lett. B469 (1999) 7.
[139] G. V. Danilov and E. V. Shuryak, arXiv: nucl-th/9908027v1 (1999).
[140] R. Holyński, A. Olszewski, P. Sawicki, A. Trzupek, B. Wosiek and K. Woźniak, Acta Phys. Pol. B32 (2001) 1365.
[141] St. Mrówczyński, M. Rybczyński, and Z. Wlodarczyk, Phys. Rev. C70 (2004) 054906.
[142] W. Broniowski, contribution to: P. Steinberg, PoS (CFRNC2006) 029.
[143] M. I. Gorenstein, M. Gaździcki and O.S. Zozulya, Phys. Lett. B585 (2004) 237.
[144] V. Koch, A. Majumder and J. Randrup, Phys. Rev. Lett. 95 (2005) 182301.
[145] M. Bleicher, J. Randrup, R. Snellings and X.-N. Wang, Phys. Rev. C62 (2000) 041901.
[146] M. Gaździcki, M.I. Gorenstein and St. Mrówczyński, Phys. Lett. B585 (2004) 115
[147] M. Stephanov, Phys. Rev. Lett. 102 (2009) 032301.
[148] B. B. Back *et al.* (PHOBOS), Nucl. Instr. and Meth. A499 (2003) 197.
[149] W. T. Lin *et al.*, Nucl. Instr. and Meth. A389 (1997) 415.
[150] R. Nouicer *et al.*, Nucl. Instr. and Meth. A461 (2001) 143.
[151] R. Bindel *et al.*, Nucl. Instr. and Meth. A474 (2001) 38.
[152] R. Bindel *et al.*, Nucl. Instr. and Meth. A488 (2002) 94.
[153] C. Adler *et al.*, Nucl. Instr. and Meth. A470 (2001) 488.
[154] R.Nouicer *et al.* (PHOBOS), J. Phys. G30 (2004) S1133.
[155] X. N. Wang and M. Gyulassy, Phys. Rev. D44 (1991) 3501.
[156] M. Gyulassy and X. N. Wang, Comput. Phys. Commun. 83 (1994) 307.
[157] Z. W. Lin, C .M. Ko, B. A. Li, B. Zhang and S. Pal, Phys. Rev. C72 (2005) 064901.
[158] A. Białas and W. Czyż, Acta Phys. Polon. B36 (2005) 905.
[159] J. Benecke *et al.*, Phys. Rev. 188 (1969) 2159.
[160] G. J. Alner, *et al.*, Z. Phys. C33 (1986) 1.
[161] J. E. Elias *et al.*, Phys. Rev. D22 (1980) 13.
[162] S. Fredriksson, *et al.*, Phys. Rep. 144 (1987) 187.
[163] I. Otterlund, *et al.*, Nucl. Phys. B142 (1978) 445.

[164] A. Abduzhamilov, *et al.*, Phys. Rev. D35 (1987) 3537.
[165] K. J. Eskola, Nucl. Phys. A698 (2002) 78c.
[166] D. Kharzeev and M. Nardi, Phys. Lett. B 507 (2001) 121.
[167] D. Kharzeev, E. Levin and M. Nardi, Phys. Rev. C71 (2005) 054903.
[168] S. V. Afanasiev *et al.* (NA49), Phys. Rev. C66 (2002) 054902.
[169] M. Basile *et al.*, Phys. Lett. 92 (1980) 367.
[170] M. Basile *et al.*, Phys. Lett. 95 (1980) 311.
[171] D. E. Groom *et al.*, Eur. Phys. J. C15 (2000) 1.
[172] S. S. Adler *et al.* (PHENIX), Phys. Rev. C69 (2004) 034909.
[173] A. Dress, H. Feng and J. Jia, Phys. Rev. C71 (2005) 034909.
[174] T. H. Burnett *et al.* (JACEE), Phys. Rev. Lett. 50 (1983) 2062.
[175] I. Bearden *et al.* (NA44), Phys. Rev. C65 (2002) 044903.
[176] R. Albrecht *et al.* (WA80), Z. Phys. C45 (1989) 31.
[177] G.S.F. Stephans, *et al.* (PHOBOS), Nucl. Phys. A 774 (2006) 639.
[178] K. Eggert *et al.*, Nucl. Phys. B86 (1975) 201.
[179] A. Morel and G. Plaut, Nucl. Phys. B78 (1974) 541.
[180] T. Sjostrand, S. Mrenna and P. Skand, J. High Energy Phys. 05 (2006) 26.
[181] R. E. Ansorge *et al.* (UA5), Z. Phys. C37 (1988) 191.
[182] G.S.F. Stephans *et al.* (PHOBOS), Nucl. Phys. A830 (2009) 809c.
[183] A. Adare *et al.* (PHENIX), Phys. Rev. C78 (2008) 014901.
[184] B. I. Abelev *et al.* (STAR), Phys. Rev. C80 (2009) 064912.
[185] B. I. Abelev *et al.* (STAR), Phys. Rev. Lett. 102 (2009) 52302.
[186] B. I. Abelev *et al.* (STAR), arXiv:0912.3977v2 [hep-ex]
[187] B. I. Abelev *et al.* (STAR), Phys. Rev. Lett. 103 (2009) 172301.
[188] N. S. Amelin *et al.* Eur. Phys. J. C22 (2001) 149.
[189] T. Lappi and L. McLerran, Nucl. Phys. A832 (2010) 330.
[190] J. Adams *et al.* (STAR), Phys. Rev. C73 (2006) 064907.
[191] J. Adams *et al.* (STAR), Phys. Rev. C75 (2007) 034901.
[192] B. I. Abelev *et al.* (STAR), arXiv:0806.0513v1 [nucl-ex].
[193] J. Adams *et al.* (STAR), Phys. Rev. C72 (2005) 044902.
[194] B. I. Abelev *et al.* (STAR), Phys. Rev. Lett. 103 (2009) 251601.
[195] J. Adams *et al.* (STAR), Phys. Rev, Lett. 95 (2005) 152301.
[196] J. Adams *et al.* (STAR), J. Phys. G34 (2007) 451.
[197] J. Adams *et al.* (STAR), J. Phys. G34 (2007) 799.
[198] A. Adare *et al.* (PHENIX), Phys. Rev. C78 (2008) 044902.
[199] A. Giovannini and L. Van Hove, Z. Phys. C30 (1986) 391.
[200] G. J. Alner *et al.* (UA5), Phys. Rep. 154 (1987) 247.
[201] M. M. Aggarwal *et al.* (WA98), Phys. Rev. C65 (2002) 054912.
[202] C. Alt *et al.* (NA49), Phys. Rev. C75 (2007) 064904.
[203] C. Alt *et al.* (NA49), Phys. Rev. C78 (2008) 034914.
[204] F. Henney, Phys. Lett. B45 (1973) 469.
[205] E. L. Berger, Nucl. Phys. B85 (1975) 74.
[206] J. L. Meunier and G. Plaut, Nucl. Phys. B87 (1975) 74.
[207] C. Michael, Nucl. Phys. B103 (1976) 296.
[208] D. Drijard, *et al.*, Nucl. Phys. B155 (1979) 269.

[209] Xin-Nian Wang, Phys. Rev. D43 (1991) 43.
[210] L. Cunqueiro, E. G. Ferreiro, F. del Moral and C. Pajares, Phys. Rev. C72 (2005) 024907.
[211] J. Kapusta and A. P. Visher, Phys. Rev. C52 (1995) 2725.
[212] A. Bialas, M. Bleszyński and W. Czyż, Nucl. Phys. B111 (1976) 461.
[213] A. Bzdak and K. Woźniak, Phys. Rev. C81 (2010) 034908.
[214] S. Jeon and J. Kapusta, Phys. Rev. C63 (2000) 011901.
[215] A. Bialas, W. Czyż and W. Furmański, Acta Phys. Pol. B8 (1997) 585.
[216] R. Holyński, M. Jeżabek and K. Woźniak, Z. Phys. C31 (1986) 467.
[217] K. Woźniak, Ph.D. thesis (1988) unpublished.
[218] A. Bialas and A. Bzdak, Phys. Rev. C77 (2008) 034908.
[219] A. Bialas and A. Bzdak, Phys. Lett. B649 (2007) 263.
[220] B. Boimska and H. Bialkowska, Proc. XXXIX ISMD, Gomel, Belarus (2009), arXiv:0911.1645v1 [nucl-ex].
[221] K. Fialkowski and R. Wit, Eur. Phys. J. A (2010)
[222] R. E. Ansorge *et al.* (UA5), Z. Phys. C43 (1989) 357.
[223] A. Bzdak, arXiv:0906.2858 [hep-ph].
[224] S. Haussler, M. Abdel-Aziz and M. Bleicher, Nucl. Phys. A785 (2007) 253.
[225] J. Adams *et al.* (STAR), Phys. Rev. C71 (2005) 031901.
[226] T. K. Nayak *et al.* (STAR), Nucl. Phys. A830 (2009) 555c.
[227] S. S. Adler *et al.* (PHENIX), Phys. Rev. C76 (2007) 034903.
[228] V. L. Ginzburg and L. D. Landau, Zh. Eksp. Teor. Fiz. 20 (1950) 1064.
[229] S. Afanasiev *et al.* (PHENIX), Phys. Rev. Lett. 101 (2008) 082301.
[230] A. Adare *et al.* (PHENIX), Phys. Rev. Lett. 103 (2009) 082002.
[231] H. J. Drescher1 and Y. Nara, Phys. Rev. C76 (2007) 041903.
[232] M. J. Tannenbaum, Phys. Lett. B498 (2001) 29.
[233] K. Adcox *et al.* (PHENIX), Phys. Rev. C66 (2002) 024901.
[234] S. S. Adler *et al.* (PHENIX), Phys. Rev. Lett. 93 (2004) 092301.
[235] J. Adams *et al.* (STAR), Phys. Rev. C71 (2005) 064906.
[236] T. Anticic *et al.* (NA49), Phys. Rev. C70 (2004) 034902.
[237] T. Anticic *et al.* (NA49), Phys. Rev. C79 (2009) 044904.
[238] D. Adamová *et al.* (CERES), Nucl. Phys. A727 (2003) 97.
[239] W. Broniowski, B. Hiller, W. Florkowski and P. Bożek, Phys. Lett. B635 (2006) 290.
[240] S. Jeon and V. Koch, Phys. Rev. Lett. 85 (2000) 2076.
[241] V. Koch, M. Bleicher and S. Jeon, Nucl. Phys. A698 (2002) 261c.
[242] M. Doering and V. Koch, Acta Phys.Polon. B33 (2002) 1495.
[243] K. Adcox *et al.* (PHENIX), Phys. Rev. Lett. 89 (2002) 082301.
[244] C. Alt *et al.* (NA49), Phys. Rev. C70 (2004) 064903.
[245] J. Adams *et al.* (STAR), Phys. Rev. C68 (2003) 044905.
[246] B. I. Abelev *et al.* (STAR), Phys. Rev. C79 (2009) 34909.
[247] J. Adams *et al.* (STAR), Phys. Lett. B634 (2006) 347.
[248] A. Bialas, Phys. Let. B532 (2002) 249.
[249] V. P. Konchakovski, M. I. Gorenstein, E. L. Bratkovskaya and H. Stöcker, Phys. Rev. C74 (2006) 064911.
[250] M. M. Aggarwal *et al.* (STAR), arXiv:1005.2307v1 [nucl-ex].
[251] J. Adams *et al.* (STAR), Phys. Rev. Lett. 90 (2003) 172301.

[252] C. Alt *et al.* (NA49), Phys. Rev. C79 (2009) 044910.
[253] B. I. Abelev *et al.* (STAR), Phys. Rev. Lett. 103 (2009) 092301.
[254] J. Kapusta and A. Mekjian, Phys. Rev. D33 (1986) 1304.
[255] St. Mrówczyński, Phys, Lett. B459 (1999) 13.
[256] S. V. Afanasiev *et al.* (NA49), Phys. Rev. Lett. 86 (2001) 1965.
[257] V. Koch and T. Schuster, Phys. Rev. C81 (2010) 034910.
[258] M. M. Aggarwal *et al.* (WA98), Phys. Lett. B420 (1998) 169.
[259] M. M. Aggarwal *et al.* (WA98), Phys. Rev. C67 (2003) 044901.
[260] M. Harrison, T. Ludlam and S. Ozaki, Nucl. Instr. and Meth. A499 (2003) 235.
[261] H. Hahn, *et al.*, Nucl. Instr. and Meth. A499 (2003) 245.
[262] T. Hallman, *et al.*, RHIC II/eRHIC White Paper (2003).
[263] B. Surrow, arXiv:hep-ex/0602009v1 (2006).
[264] K. H. Ackermann *et al.* (STAR), Nucl. Instr. and Meth. A499 (2003) 624.
[265] K. Adcox *et al.* (PHENIX), Nucl. Instr. and Meth. A499 (2003) 469.
[266] M. Adamczyk *et al.* (BRAHMS), Nucl. Instr. and Meth. A499 (2003) 437.
[267] S. Manly *et al.* (PHOBOS), Nucl. Phys. A 774 (2006) 523.
[268] E. García, K. Woźniak *et al.*, Nucl. Instr. and Meth. A570 (2007) 536.
[269] R. Brun *et al.*, GEANT 3.21, Detector Description and Simulation Tool, CERN Program Library Long Write-up W5013, (1994).
[270] K. Werner, Phys. Rep. 232 (1993) 87.
[271] B. G. Gibbard and T. G. Throwe, Nucl. Instr. and Meth. A499 (2003) 814.
[272] A. W. Chan, *et al.*, Nucl. Instr. and Meth. A499 (2003) 819.